Engineering and optimization of electrode/electrolyte interfaces to increase solid oxide fuel cell (SOFC) performances

Rossen Tchakalov

PSL ★
UNIVERSITÉ PARIS

THÈSE DE DOCTORAT
DE L'UNIVERSITÉ PSL

Préparée à MINES ParisTech

Engineering and optimization of electrode/electrolyte interfaces to increase solid oxide fuel cell (SOFC) performances

--

Ingénierie et optimisation des interfaces électrode/électrolyte pour augmenter les performances de piles à combustible à oxyde solide (SOFC)

Soutenue par
Rossen TCHAKALOV
Le 29 janvier 2021

Ecole doctorale n° 621
Ingénierie des Systèmes, Matériaux, Mécanique, Énergétique

Spécialité
Sciences et génie des matériaux

Composition du jury :

Daria VLADIKOVA Professeur, Bulgarian Academy of Sciences	*Présidente*
Jean-Claude GRENIER Directeur de recherche émérite, ICMCB-CNRS	*Rapporteur*
Paolo PICCARDO Professeur, University of Genova	*Rapporteur*
Marjorie CAVARROC Ingénieur Docteur, SAFRAN Tech	*Examinateur*
Anthony CHESNAUD Chargé de recherches, MINES ParisTech	*Examinateur*
Guilhem DEZANNEAU Directeur de recherche, SPMS – CNRS	*Co-Directeur de thèse*
Alain THOREL Directeur de recherche, MINES ParisTech	*Directeur de thèse*

MINES ParisTech | PSL ★

Thank you…

Many thanks to everybody who has made this work possible. Thanks to the great scientists for the basis of this wonderful and complex subject. Thanks to homo-sapiens for starting to work with ceramics almost 30 000 years ago, and making me feel like a monkey when I did not understand why the cells break.

I would like to humbly thank the members of the jury for their implication in my work, their time, their instructions and the discussion during the defense. Daria, thank you for your continuous encouragement and for being the best president. Paolo, thank you for the fun times but also for your serious work as *rapporteur*. Jean-Claude, thank you for accepting to be a part of my thesis even though my 250 pages almost scared you. I hope there was not too much "blabla". Marjorie, thank you for your everlasting enthusiasm and your pieces of advice to improve my work. My thanks are extended to the other actors without who the defense would have been far more difficult, thank you Anne Françoise, Marie-Helene, Claudine Veronique, Lucien, Jerome, for your assistance and most of all for your patience.

My supervisors, my teachers, my guides, thank you from the bottom of my heart for your teachings. I have learned so much from you in both science but also human relations. You have always believed in me and coped with my "strong personality". Alain, I was so happy to go to Bulgaria with you. You have been a bottomless well of knowledge and I am proud to have been your student. Anthony, you were the first pillar at the CdM and I will always cherish our coffees and discussions. Guilhem, you are one of the first to have believed in me and without you, I would not be writing this right now. You have been more than a teacher, you have been a friend and a father figure on so many occasions.

Thank you Jean-François and thank you Francesco for your help whenever it was needed and for your good mood. Thanks to all the wonderful people at Centre des matériaux to have made my work place a cozy place (Sylvain, Catherine, Zak, Yann, Vladimir, Vincent, Frank, Fabrice, Maria, Jean-Chris, Antoine, Kevin, Gérard, Lynh Thy Patrice, Greg, René, Vasco, Fred, Julie, Stephanie, Régis, Michel,…)

Thanks to all the wonderful people at Centrale who have accepted me as one of their own ever since my first day of internship before my thesis. Thank you for making me feel like at home

whenever I came to Centrale (Thierry, Christine V, Christine B, Pascale G, Pascale S, Pierre, Agnes, Brahim, Pierre Eymeric, Nicolas, Hubert, Charles, Raphaël, the late JMK, Vincent, Franz, Fabienne, Claire…)

Thanks to my PhD Buddies you have all been so great and I have grown so much with you. Thank you Sebo, Alex, Bastien, Jonathan, Jean-Mich, Patrizio, David, Hugo D, Ben, Amar, Chiraz, Vitoria, Chenyi, Milad, Henry… So much have been discussed, so many opinions have been shared, so much coffee has been drunk.

A special thanks to the BFF, Chloé and Lenny as well as Clément I would like to present to you my special thanks. Seeing you was one of the reasons to go to work with positive thinking. Thanks, friends.

Another special thanks to Hugo, the second-best co-bureau one may want ;). You were also one of my pillars during my thesis. We have followed each other's Dunning–Kruger effect curves and we have evolved together. I hope we can both achieve our Ikagi and talk about it.

Thank you Erwan (Ewané), thank you for being my friend ever since the first year of University (It has been a while…) but particularly thank you for being there during the redaction, during the defense preparation, and finally during the presentation with me.

All my love and thanks to my new families. Christian, Corrine, Lucie, Quentin thank you for your interest in my work, your continuous support and your trust in me. Cedric, Naemi, Yoyo thank you for your love, and the happy times we have together. I am so happy that all our clans have merged.

To my Mom, my Bro and my Dad I can hardly express all my limitless gratitude. Your unconditional love, support, and trust are the only reason I am here today. I could always count on you have always made me feel special. Thank you…

To my muse, the love of my life, my partner, my better half. You have been next to me for every moment and I know now that we can confront every difficulty together. Every day is a blessing as long as I am with you. And thanks to your little C3 for the trips to work together.

Contents

Abbreviations

AEC	Area Expansion Coefficient		MEK	MethylEthylKetone
AFC	Alkaline fuel cell		MEKET	MEK+EtOH
AS	Anode Support		MeOH	Methanol
ASR	Area Specific Resistance		MIEC	mixed ionic and electric conductor
ATPB	Active Triple Phase Boundary		OCV	Open circuit voltage
BM	Ball milling		ORR	oxygen reduction reaction
B-V.	Buttler Volmer		PAFC	Phosphoric acid fuel cell
cermet	Ceramic-metallic composite		PCFC	Proton Conducting Fuel Cell
CGO	Gadolinium doped ceria		PEG	PolyEthileneGlicol
DGM	Dusty gas model		PEMFC	Proton exchange membrane fuel cell
DMFC	Direct methanol fuel cell		PET	PolyEthileneTaftalate
EDS	Energy Dispersive X-ray Spectroscopy		PVB	PolyvinylButiral
EFCF	European Fuel Cell Forum		R.G.	Relative Gap
EIS	Electrochemical impedance spectroscopy		SDC	Scandium Doped Ceria
EMF	Electromotive force		SEM	Scanning electron microscopy
EtOH	Ethanol		SOFC	Solid oxide fuel cell
HT	High Temperature		TEC	Thermal expansion coefficient
IPCC	Intergovernmental Panel on Climate Change		TEM	Transmission electron microscopy
IT	Intermediate Temperature		TGA	ThermoGravimetric Analysis
LSCF	Lanthanum strontium cobalt ferrite		TPB	Triple Phase Boundary
LSM	Lanthanum strontium manganite		UNEP	United Nations Environment Program
LST	Lanthanum strontium titanate		YST	Yttrium strontium titanate
LT	Low Temperature		YSZ	Yttrium stabilized zirconia
MCFC	Molten carbonate fuel cell			

General introduction

Contents

I.   Sustainable development context

In the past five decades, researchers have widely studied the impact of human activity on the environment and in particular on climate change which has been a global concern since the first world summit. This concern has resulted in the creation of the United Nations Environment Program (UNEP) in 1972 establishing laws and guidelines to tackle the pollution caused by the industrialization of the 20th century [1]. Another important milestone reflecting the will to limit the impact of human activity on the environment is the creation of the Intergovernmental Panel on Climate Change (IPCC - United Nations body for assessing the science related to climate change) in the late 80s [2], providing regular scientific assessments as well as adaptations and mitigation options. Those organisms are some of the numerous initiatives taken in order to control the human and limit footprint on the environment [3] [4] [5] [6].

However, the recent climate predictions [7] reveal that even further changes must be made. Several scenarii have been developed, anticipating the consequences of a global temperature increase and any rising above 1,5°C would have a dramatic impact on a planetary scale. Desertification, ice melting, and species extinction are some of the already observed phenomena [8] [9] [10].

With the world population growth [11] as well as the improvement of the global standards of living, the energy demand is increasing at a dramatic rate. The worldwide global energy consumption has increased by more than 70% in less than 30 years (120% increase worldwide electricity consumption) [12]. Despite the strive to reduce carbon dioxide and the emission of

other, the energy mix remains still highly dependent on fossil resources like coal, oil, or gas as well as uranium for nuclear energy. The dependency on fossil fuels or uranium also creates potential geopolitical tensions due to their uneven distribution. This context reveals the unprecedented urgency for green sustainable energy production, storage, and distribution.

In this context, the "power to gas" concept and more precisely the utilization of hydrogen gas as an energy vector is receiving a lot of interest in nowadays society. The development of fuel cell and electrolyzer technology has been strongly supported by governmental and private aids around the world in order to promote renewable energy storage and hydrogen-fueled mobility. Companies such as McPhy have seen their stock price multiplied in several months in 2020 and have attracted a multitude of contracts for hydrogen mobility [13] and green hydrogen production [14], despite the global economic crisis due to the Covid19 pandemic. Air Liquide has stared in 2016 their program Blue Hydrogen "whose goal is to gradually decarbonize its production of hydrogen dedicated to energy applications" [15] and have ever since participated in the development of hydrogen mobility [16] [17].

II.   Energy and fuel cells

As mentioned in the previous paragraph, the production of green hydrogen and its utilization as fuel requires electrochemical devices such as electrolyzers and fuel cells. In this work, we will concentrate on fuel cell operation, but it is interesting to note that an electrolyzer can be compared to a fuel cell functioning in reverse.

A fuel cell is an electrochemical device allowing the direct conversion of electrochemical energy, provided from the oxidation of a reacting compound used as fuel into electrical energy and heat. Because there is no combustion process involved, fuel cells are not limited by Carnot efficiency and can reach higher efficiency values than thermal engines. Furthermore, the electrical work is directly converted from the reaction enthalpy, thus reducing the number of transformations and consequently reducing energy losses.

Sir William Robert Grove, is one of the first scientists to study the chemistry behind fuel cells functioning by demonstrating water dissociation and formation in his "gas voltaic battery" (Figure 1). In the first half of the 19th century, Grove showed that steam can be dissociated into

Hydrogen and Oxygen by electrolysis and that this process is reversible. Ever since fuel cell technology has attracted considerable interest [18].
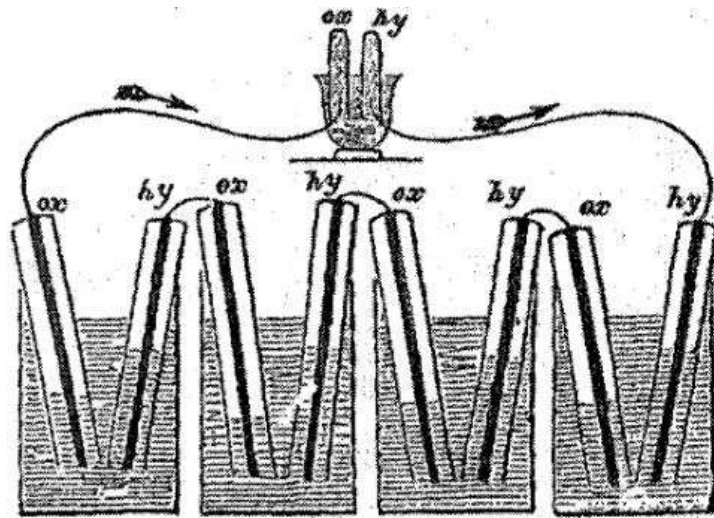
Figure 1 Sir William Robert Grove's "gas voltaic battery" [23]

High power fuel cell systems and stacks have been built in the 1920s by William W. Jacques and Emil Baur reaching 30 kW [19]. Practical applications development started in the 30s by Thomas Francis Bacon whose fuel cells were to be used in the Royal Navy's submarines during the second world war. In 1958, Bacon presented his alkaline fuel cells which, thanks to their reliability, attracted the attention of the company Pratt and Whitney and were installed aboard the Apollo spacecraft. It was at the same time that GE also developed fuel cell technology for NASA and McDonnell Aircraft during the GEMINI program. They also provided the fuel cell for one of the first fuel cell-powered vehicles: a 15 kW tractor from Allis Chalmers (figure 2 and [20]). In the 60s different types of fuel cells, such as solid oxide fuel cells (SOFC) [21] (cf. ANNEX - I) have started to emerge changing the operating temperature, component materials, and fuel. Since then development has continued taking into account an increase in power density and durability, as well as lowering costs. In the 21st-century fuel cells have been integrated into numerous domains, especially in transportation (automobiles, buses, tractors, trains, and ships) and stationary use (homes, hospitals, schools, etc.) [22].

Figure 2 Allis Chalmers fuel cell tractor (source image: Smithsonian institute [24])

In this study, we will focus on SOFC technology which attracts a lot of interest due to several advantages compared to other types of fuel cells. The use of oxide ceramic materials reduces drastically corrosion issues and inconveniences linked to the management of liquid electrolytes. The high temperature boosts electrode kinetics, thus allowing to achieve high power densities with low to none use of noble catalysts such as Pt. Moreover the high-quality heat allows to perform internal reforming making the utilization of carbon-based gases as fuel possible and highly efficient compared to their use in thermal engines. The heat can also be coupled with other technologies, thus increasing the efficiency of the fuel cells by cogeneration. However, SOFC presents some important disadvantages such as relatively low durability (several tens of thousands of hours) induced by the high-temperature operation as well as electrode material alteration or poisoning.

III.   Project

Our general objective is to enhance the electrochemical performances (current and power density) of a single solid oxide fuel cell by engineering geometrically macroscale architectured electrode/electrolyte interfaces (fig 2), thus expanding the equivalent exchange surface area. This expansion should develop a larger number of active triple phase boundaries (ATPB), allowing to sustain more simultaneous electrochemical reactions, resulting in an increase in power density. A

16

previous study confronts experimental data with numerical simulation and brings forward an underestimation of the power increase calculated by the numerical model [28] [29].
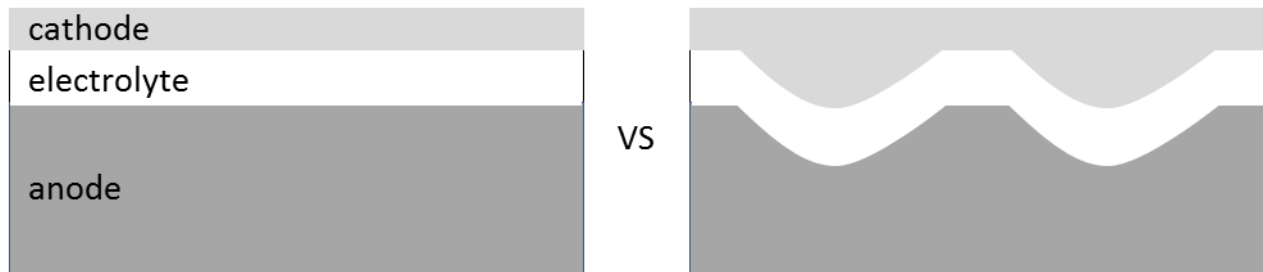
Figure 3 Concept

This work is conducted following three axes: fabrication, structural characterization. A low cost and reproducible fabrication protocol for anode supported button cells with planar or architectured electrode/electrolyte interfaces are established using common ceramics engineering techniques such as tape casting. Structural analyses are performed using scanning electron microscopy (SEM), using secondary and backscattered electrons for the microstructural assessments as well as the measurement of the layers thicknesses and integrity observations, and dispersive X-ray spectroscopy for the chemical distribution and singularity analysis. Electrochemical measurements like electrochemical impedance spectroscopy (EIS) and polarization curves analysis are conducted to control the performances and compare the architectured cells to equivalent planar ones.

In the first chapter of this document, some general information such as basic fuel cell principles, types, and materials are reviewed. This is followed by a discussion on different potential pathways to increase SOFC performances such as interface architecting, supported by a brief bibliographic survey on the subject. In this chapter, a technical discussion on the project objectives will be conducted. The second chapter offers a detailed presentation of the fabrication protocol, as well as its validation. The third chapter is dedicated to the structural and microstructural analysis of the cells including porosity and layer thickness. The fourth chapter is focused on electrochemical measurements in order to characterize the fabricated fuel cells. Here fuel cells with architectured electrode/electrolyte interfaces are compared to equivalent planar cells and a discussion on the influence of the architecture is proposed. Finally, a discussion on the obtained results as well as the perspectives will be carried out.

References

[1]   U. N. Environment, 'UNEP', *UN Environment*. http://www.unenvironment.org/node (accessed Aug. 20, 2019).

[2]   'IPCC — Intergovernmental Panel on Climate Change'. https://www.ipcc.ch/ (accessed Aug. 20, 2019).

[3]   'What is the Kyoto Protocol? | UNFCCC'. https://unfccc.int/kyoto_protocol (accessed Aug. 20, 2019).

[4]   'COP21', *Gouvernement.fr*. https://www.gouvernement.fr/en/cop21 (accessed Aug. 20, 2019).

[5]   'UNITED NATIONS Climate Change Summit'. https://www.un.org/en/climatechange/ (accessed Aug. 20, 2019).

[6]   'Climate change initiatives and partnerships', *UNEP*. http://www.unenvironment.org/explore-topics/climate-change/about-climate-change/climate-change-initiatives-and-partnerships (accessed Aug. 21, 2019).

[7]   'Global Warming of 1.5 ^{o}C —'. https://www.ipcc.ch/sr15/ (accessed Aug. 20, 2019).

[8]   Martin, 'UN Report: Nature's Dangerous Decline "Unprecedented"; Species Extinction Rates "Accelerating"', *United Nations Sustainable Development*, May 06, 2019. https://www.un.org/sustainabledevelopment/blog/2019/05/nature-decline-unprecedented-report (accessed Aug. 20, 2019).

[9]   'Arctic Sea Ice News and Analysis | Sea ice data updated daily with one-day lag'. https://nsidc.org/arcticseaicenews/ (accessed Aug. 20, 2019).

[10]   'Land and Drought | UNCCD'. https://www.unccd.int/issues/land-and-drought (accessed Aug. 20, 2019).

[11]   'World Population Prospects - Population Division - United Nations'. https://population.un.org/wpp/Graphs/Probabilistic/POP/TOT/900 (accessed Aug. 20, 2019).

[12] 'World Energy Consumption Statistics | Enerdata'. https://yearbook.enerdata.net/total-energy/world-consumption-statistics.html (accessed Aug. 20, 2019).

[13] 'Nouveau contrat - Mobilité hydrogène', *McPhy*, Jul. 30, 2020. https://mcphy.com/fr/communiques/nouveau-contrat-mobilite-hydrogene/ (accessed Aug. 24, 2020).

[14] 'Nouveau contrat | Stations et électrolyseur grande capacité', *McPhy*, Aug. 03, 2020. https://mcphy.com/fr/communiques/nouveau-contrat-stations-et-electrolyseur-grande-capacite/ (accessed Aug. 24, 2020).

[15] 'Hydrogen energy', *Air Liquide*, Apr. 28, 2016. https://www.airliquide.com/science-new-energies/hydrogen-energy (accessed Aug. 24, 2020).

[16] 'L'énergie hydrogène pour les véhicules', *Air Liquide Energies*, Dec. 12, 2016. https://energies.airliquide.com/fr/transport-propre-transport-passagers/lenergie-hydrogene-vehicules (accessed Aug. 24, 2020).

[17] 'Air Liquide va construire la première station hydrogène haute pression destiné...' https://fr.media.airliquide.com/actualites/air-liquide-va-construire-la-premiere-station-hydrogene-haute-pression-destinee-aux-camions-longue-distance-en-europe-6776-1ba6d.html (accessed Aug. 25, 2020).

[18] J. M. Andújar and F. Segura, 'Fuel cells: History and updating. A walk along two centuries', *Renewable and Sustainable Energy Reviews*, vol. 13, no. 9, pp. 2309–2322, Dec. 2009, doi: 10.1016/j.rser.2009.03.015.

[19] C. Stone and A. E. Morrison, 'From curiosity to "power to change the world®"', *Solid State Ionics*, vol. 152–153, pp. 1–13, Dec. 2002, doi: 10.1016/S0167-2738(02)00315-6.

[20] 'Allis-Chalmers Fuel Cell Tractor', *National Museum of American History*. https://americanhistory.si.edu/collections/search/object/nmah_687671 (accessed Aug. 22, 2019).

[21] J. Weissbart and R. Ruka, 'A Solid Electrolyte Fuel Cell', *J. Electrochem. Soc.*, vol. 109, no. 8, pp. 723–726, Jan. 1962, doi: 10.1149/1.2425537.

[22] 'Fuel Cell Applications - an overview | ScienceDirect Topics'. https://www.sciencedirect.com/topics/engineering/fuel-cell-applications (accessed Aug. 22, 2019).

[23]   P. G. Grimes, 'Historical pathways for fuel cells', *IEEE Aerospace and Electronic Systems Magazine*, vol. 15, no. 12, pp. 7–10, Dec. 2000, doi: 10.1109/62.891972.

[24]   'Home', *Smithsonian Institution*. https://www.si.edu/home (accessed Aug. 22, 2019).

[25]   O. Z. Sharaf and M. F. Orhan, 'An overview of fuel cell technology: Fundamentals and applications', *Renewable and Sustainable Energy Reviews*, vol. 32, pp. 810–853, Apr. 2014, doi: 10.1016/j.rser.2014.01.012.

[26]   G. Chen, Y. Gao, Y. Luo, and R. Guo, 'Effect of A site deficiency of LSM cathode on the electrochemical performance of SOFCs with stabilized zirconia electrolyte', *Ceramics International*, vol. 43, no. 1, Part B, pp. 1304–1309, Jan. 2017, doi: 10.1016/j.ceramint.2016.10.082.

[27]   S. C. Singhal, 'Solid Oxide Fuel Cells: Past, Present and Future', in *Solid Oxide Fuels Cells: Facts and Figures: Past Present and Future Perspectives for SOFC Technologies*, J. T. S. Irvine and P. Connor, Eds. London: Springer London, 2013, pp. 1–23.

[28]   M. Geagea, 'Nouvelles architectures de surfaces d'échanges de piles à combustible de type SOFC pour l'amélioration de l'efficacité électrochimique', Apr. 2017, Accessed: Aug. 23, 2019. [Online]. Available: https://pastel.archives-ouvertes.fr/tel-01901236.

[29]   F. Delloro and M. Viviani, 'Simulation study about the geometry of electrode-electrolyte contact in a SOFC', *Journal of Electroceramics*, vol. 29, no. 3, pp. 216–224, Nov. 2012, doi: 10.1007/s10832-012-9766-8.

Chapter I
SOFC state of the art

Cathode (ex: LSCF)
$O_2 + 4e- = 2O^{2-}$

Electrolyte (ex: YSZ)

Anode (ex: Ni/YSZ)
$2H_2 + 2O^{2-} = 2H_2O + 4e-$

$(N_{2(g)})$

$(Air)\ O_{2(g)}$

e^-

O^{2-}

e^-

$(CO_{2(g)})\ H_2O_{(g)}$

$(CH_{4(g)})\ H_{2(g)}$

cathode

electrolyte

anode
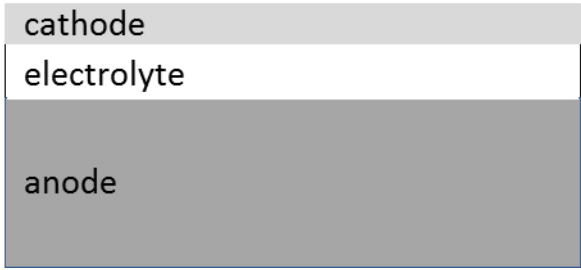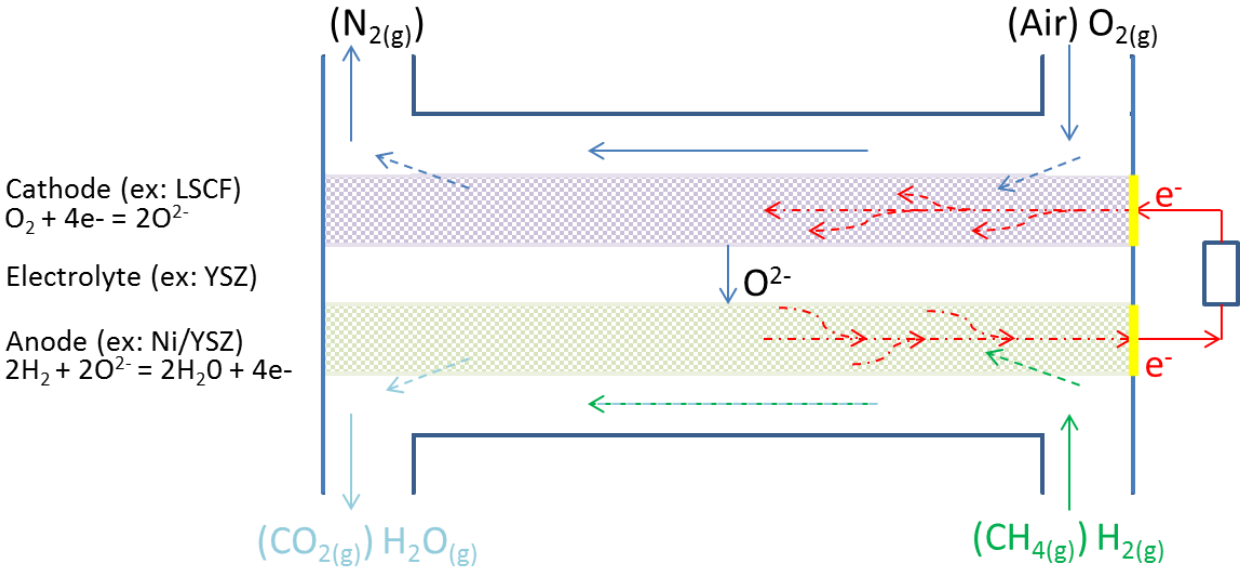
VS

Chapter I abstract

The first chapter of this document is dedicated to a bibliographic study of the results of theoretical and experimental research on SOFCs' operation, of interest for the present study.

In the first part, the basic principles of the fuel cells are presented including thermodynamics and electrochemistry overview. A simplified schematics of a SOFC allows visualizing the global cell operation, displaying the electrochemical reactions in each electrode, the gas diffusion, and charge transport directions (figure I – abstract – 1). In the second and the third part of the chapter, we present a brief literature review on the used materials and microstructures as well as on the different possibilities to increase the electrochemical performances of SOFC.

In the present work we propose a geometrical modification of the electrode/electrolyte interfaces to extend the apparent exchange surface and by doing so to increase the number and length of active triple phase boundaries as shown in Figure I – abstract - 2. There is also a potential activation of previously nonpercolating paths, therefore increasing the further the TPB density and length. Thus, the catalytic properties of the interface are modified (compared to a planar interface) and the activation losses, as well as the ohmic losses, should decrease.

Chapitre I résumé

Le premier chapitre de ce document est consacré à une étude bibliographique des résultats de la recherche théorique et expérimentale concernant le fonctionnement des SOFC, d'intérêt pour la réalisation de l'étude.

Dans la première partie, les principes de base des piles à combustible sont présentés, y compris relevant de la thermodynamique et de l'électrochimie. Un schéma simplifié d'une SOFC permet de visualiser le fonctionnement global de la pile, en affichant les réactions électrochimiques dans chaque électrode, la diffusion des gaz et les directions de transport de la charge (figure I - abstract - 1). Dans les deuxième et troisième parties du chapitre, nous présentons une brève revue de la littérature sur les matériaux utilisés et les microstructures, ainsi que sur les différentes possibilités d'augmenter les performances électrochimiques des SOFC.

Dans le présent travail, nous proposons une modification géométrique des interfaces électrode/électrolyte afin d'étendre la surface d'échange apparente et, ce faisant, d'augmenter le nombre et la longueur de frontières de triple phase actives, comme le montre la figure I - abstract - 2. Il y a également une activation potentielle de chemins précédemment non percolants, augmentant ainsi d'autant la densité et la longueur des TPB. Ainsi, les propriétés catalytiques de l'interface sont modifiées (par rapport à une interface plane) et les pertes d'activation, ainsi que les pertes ohmiques, devraient diminuer.
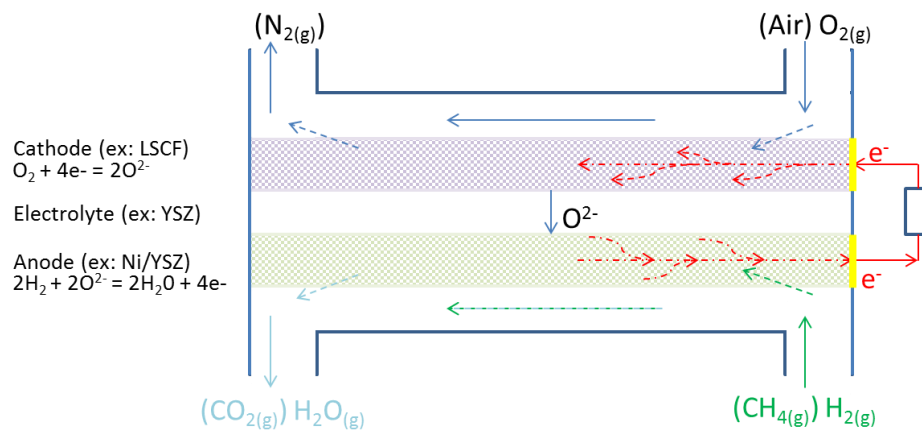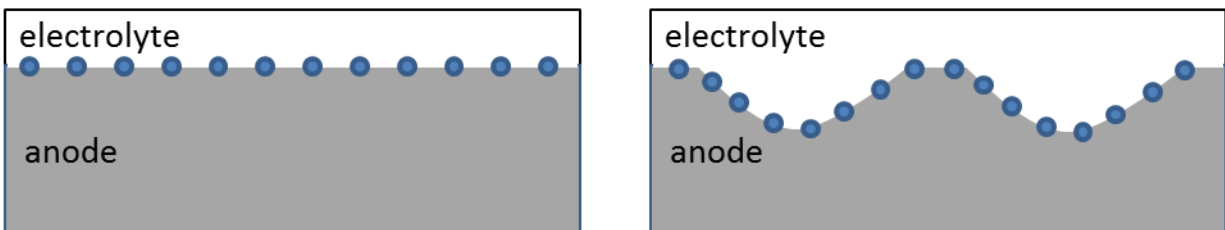

Figure I – abstract – 1 SOFC concept

Figure I – abstract – 2 Illustration of triple-phase boundary increase due to the surface area augmentation

Chapter I SOFC state of the art

Contents

I.   Introduction

In this chapter, we will review some general information such as basic fuel cell principles, types and materials as well as different potential pathways to increase SOFC performances. A condensed bibliographic survey will accompany the latter. SOFC are a type of cells composed entirely of solid materials and which operate at high temperatures (600°C -1000°C). This technology has attracted significant interest over the past few decades, due to its elevated current and power densities, superior efficiency thanks to the cogeneration of electricity and high-quality heat, as well as its capacity to internally reform methane and other carbon-based fuels. Those are some of the reasons for which SOFC presents an ideal candidate for high energy output needs as in industry or housing application as well as heavy transportation.

The development of SOFC technology debuted in the late 1930s with the work on ion-conducting oxides of Emil Bauer and Hans Preis. Their work was based on earlier studies made by Walther Nernst on ceramics material composed of 85% ZrO_2 and 15% Y_2O_3 also called "Nernst Mass". Since then the subject has known moderate advancement, but the high electrical resistance of the used materials, as well as the mechanical and the thermal-induced complications, have limited the research and development expansion. The Westinghouse's cathode-supported tubular SOFC became one of the first SOFC power systems in the 80s and 90s. Since the SOFC development and commercialization has gained considerable attention. The research and application progress has been covered on multiple occasions in books and publications [1], and conferences, symposia, and conferences such as the European Fuel Cell Forum (EFCF [2]).

II.   SOFC overview

The functioning of a solid oxide fuel cell is equivalent to that of other types of fuel cells where the electrochemical energy from fuel oxidation (equation I-1) is directly transformed into electrical current. A single cell is composed of three principal compartments: two porous electrodes in which the redox reactions occur (equations I-2 and I-3), separated by a dense, ion-conducting electrolyte (figure I-3). The high operating temperature is necessary to activate the ion conduction of the electrolyte. The latter is dense and electrically insulating, to avoid gas and electronic short circuit. Thus the electrons are exchanged through an external circuit which results in an electrical current generation.
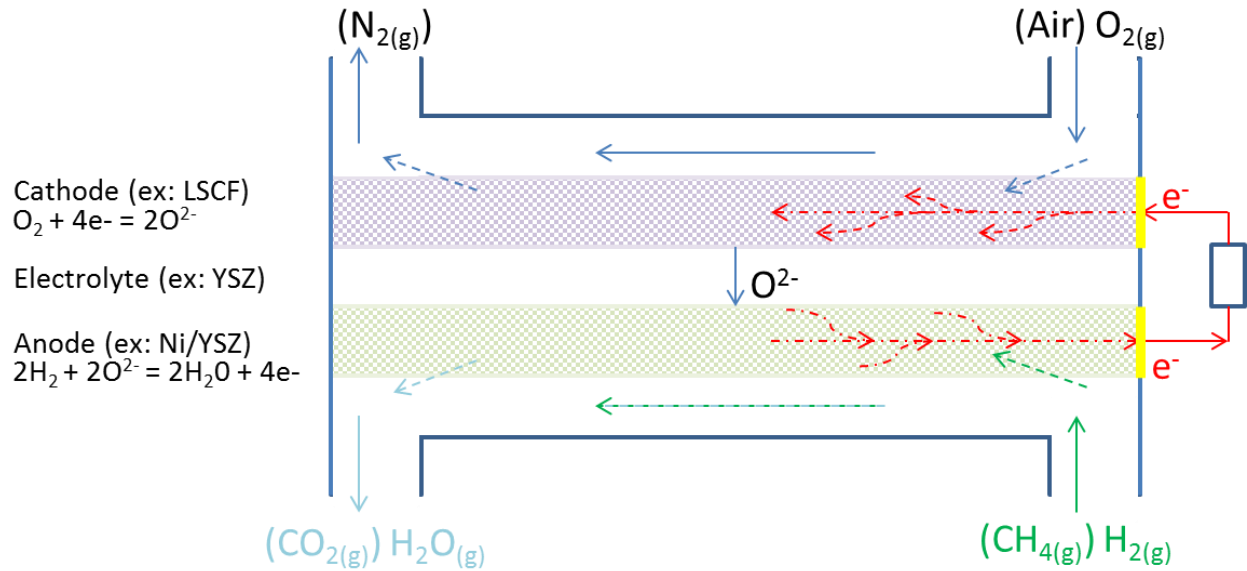
Figure I - 3 SOFC concept

One of the SOFC advantages is the capacity to use carbon-based gases as fuel (eq I-2 b and d). The reaction with methane is particularly efficient because of the intern reforming (eq. I-2c) producing *in situ* two supplementary fuels. Using fuel cells to generate electricity from methane has a notable advantage over combustion-based technologies as mentioned earlier, due to the lack of Carnot efficiency limitation. Its use, however, is associated with greenhouse gas emissions (CO_2) and it can provoke carbon coking which is one of the principal anode degradations mechanisms.

$$H_{2(g)} + \frac{1}{2}O_{2(g)} \leftrightarrow H_2O_{(g)} \tag{I-1}$$

$$H_2 + O^{2-} \leftrightarrow H_2O + 2e^- \tag{I-2a}$$

$$CH_4 + 4O^{2-} \leftrightarrow CO_2 + 2H_2O + 8e^- \tag{I-2b}$$

$$CH_4 + H_2O \leftrightarrow CO + 3H_2 \tag{I-2c}$$

$$\begin{cases} CO + O^{2-} \leftrightarrow CO_2 + 2e^- \\ H_2 + O^{2-} \leftrightarrow H_2O + 2e^- \end{cases} \tag{I-2d}$$

$$\frac{1}{2}O_2 + 2e^- \leftrightarrow O^{2-} \tag{I-3}$$
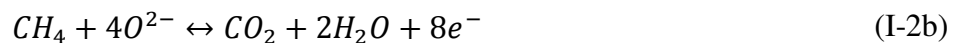
In this work, we will focus on the utilization of hydrogen gas as a fuel.

II.A.   Theoretical overview

II.A.1. Free Gibbs energy and reversible potential

As the basic principle of operation is the transformation of internal electrochemical energy, a focus on the thermodynamic aspect is necessary. Every chemical reaction is associated with a free Gibbs energy depending on the chemical activities of the components as well as their chemical bond energy, and the operation conditions (eq I-4).

$$\Delta_r G = \Delta_f G^0 + RT \times ln\left(\frac{a_{ox}}{a_{red}}\right) \tag{I-4}$$

Where $\Delta_f G^0$ is the standard Gibbs energy calculated by using the gas formation energy at atmospheric pressure, R is the gas constant, T is the operating temperature, a_{ox} and a_{red} are respectively the oxidant and reducer activities.

The electrical potential of the reaction is proportional to the free Gibbs energy and depends on the number of exchanged electrons (eq I-5). By developing this expression, we obtain the Nernst relation, which allows expressing the system's electrical potential or its electromotive force as a function of the gas concentration i.e. partial pressure (eq I-6).

$$E_{rev} = -\frac{\Delta_r G}{nF} \tag{I-5}$$

$$E_{rev} = E_{rev}{}^0 + \frac{RT}{nF} \times ln\left(\frac{P_{H_2O}}{P_{H_2}P_{O_2}^{0,5}}\right) \tag{I-6}$$

Where E_{rev} is the reversible potential E°_{rev} is the standard reversible potential, P_i is the partial pressure of the element i.

In the case of water vapor formation the reversible potential is: $E_{rev} = 1.17V$ at 800°C with the use of humidified hydrogen as a fuel (pH$_2$=0.97 bar, pH$_2$O=0.03 bar) and air as oxygen source (pO$_2$=0.2 bar).

II.A.2. Irreversibilities and actual cell potential

Thermodynamics provides an insight into the behavior of a system in an equilibrium state. Within the fuel cell, a multitude of electrical, chemical, and diffusion processes occur while it is operating. Each of them influences the global electrical generation impacting the cell voltage by inducing irreversibility causing it to decline as the current increases. Outside the equilibrium, the notion of overpotential η is introduced (Equation I-7) to characterize the potential losses in the fuel cell.

$$\eta = E_{rev} - E(i) \qquad\qquad (I\text{-}7)$$

Those losses can be resumed in four principal categories which allow establishing the polarization equation (eq I-8) :

- Fuel cross-over and internal currents
- Activation losses
- Ohmic losses
- Concentration losses

$$E(i) = E_{rev} - \eta_{act,a} - \eta_{act,c} - \eta_{pol} - \eta_{conc,a} - \eta_{conc,c} \qquad\qquad (I\text{-}8)$$

Where E is the actual cell voltage, $\eta_{act,a}$ is the anode activation overpotential, $\eta_{act,c}$ is the cathode activation overpotential, η_{pol} is the polarization overpotential, $\eta_{conc,a}$ is the anode concentration overpotential and $\eta_{conc,c}$ is the cathode concentration overpotential.

II.A.2.a)   Activation losses

The activation overpotential is caused by the energy requirements to initiate the electrochemical reactions and more precisely, by the reduction kinetics at the anode and the sluggishness of the ORR at the cathode. At low current density, it is the predominant factor for voltage losses and it follows the Butler-Volmer equation (equations I-9 and I-10).

$$j_{el} = j_{0,el} * \left[e^{\frac{\alpha RT}{nF}\eta_{act,el}} + e^{\frac{-(1-\alpha)RT}{nF}\eta_{act,el}} \right]$$ (I-9)

$$\eta_{act,el} = -\frac{R*T}{\alpha_{el}*n*F}\ln(j_{0,el}) + \frac{R*T}{\alpha_{el}*n*F}\ln(j_{el})$$ (I-10)

Where j_0 is the exchange current density rate, j is the current density, α is the charge transfer coefficient. The subscript "el" designates the considered electrode and j_0, as well as α, depend on the electrode material, microstructure, and chemical activity.

II.A.2.b)   Ohmic losses

Provoked by internal resistance majorly due to the electrolyte ionic transportation resistance, as well as interface contact resistance and also hindered electronic conductivity in the electrodes. Thus, an equivalent series resistance is considered and used in ohmic low as shown in equation I-11.

$$\eta_{pol} = R_{ohm} \times i$$ (I-11)

Where R_{ohm} is the total cell resistance including ionic resistance of the electrolyte but also of the electrodes, electronic, and contact resistance.

II.A.2.c)   Concentration losses

Concentration losses are caused by the decrease in the concentration of the reacting gasses, due to an insufficient gas supply rate in respect to their consumption. Hence, concentration losses are predominant at high current densities and it is possible to define a limiting current corresponding to the supply rate.

$$\eta_{conc,el} = -\frac{R*T}{n*F}\ln\left(1 - \frac{i}{i_l}\right)$$ I-12

Where i_l is the limiting current defined as the current where the partial pressure of the considered gas becomes zero as in equation I-14:

$$P_2 = P_1(1 - \frac{i}{i_l})$$ I-13

Combining equations I- (8,9,11 and 12) we can plot the polarization curve of the fuel cell as shown in figure I – 4. We distinguish three domains on the curve where one of the overpotentials is predominant.
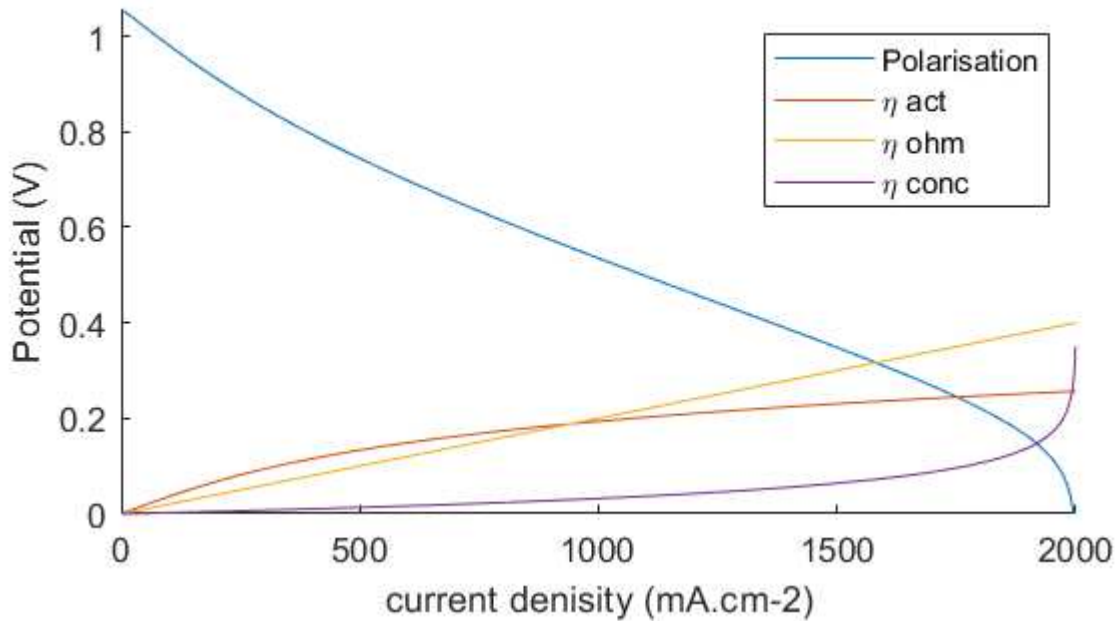
Figure I - 4 Typical polarization curve with the contributions corresponding to the activation, ohmic and concentration overpotentials

II.B. SOFC composition

As mentioned previously, a single fuel cell is generally composed of a porous anode and cathode separated by a dense electrolyte. Each component has a different role and its materials and microstructure must be adapted to ensure an optimal cell operation.

In this work, two types of fuel cells (Type I and type II cells) are fabricated differentiated by their electrolyte and electrode compositions.

II.B.1. Electrolyte

II.B.1.a) *Definition*

The term "Solid Oxide Fuel Cell" is derived from the utilization of a solid oxide material for the electrolyte. This component ensures the gas and electronic separation of the electrodes as well as

the ionic transfer necessary to preserve the electroneutrality of the cell. Its position in contact with both a reducible atmosphere at the anode side and an oxidizing atmosphere at the cathode side imposes excellent chemical stability. Thus, the electrolyte has very strict requirement specifications:

- Thermal and chemical stability in reducing and oxidizing atmospheres
- Good ionic conductivity and negligible electronic conductivity
- Dense microstructure
- Thermal and chemical compatibility with both electrodes

Oxygen ion transport in most oxide electrolyte materials is carried out through lattice oxygen vacancies. The specific ion conductivity (S/cm) is influenced by the concentration of those vacancies. Generally fluorite or perovskite oxides with low valence element substitution (also called doping), present increased vacancy concentration due to the Van der Waals potential mismatch between the cations (Figure I - 5).
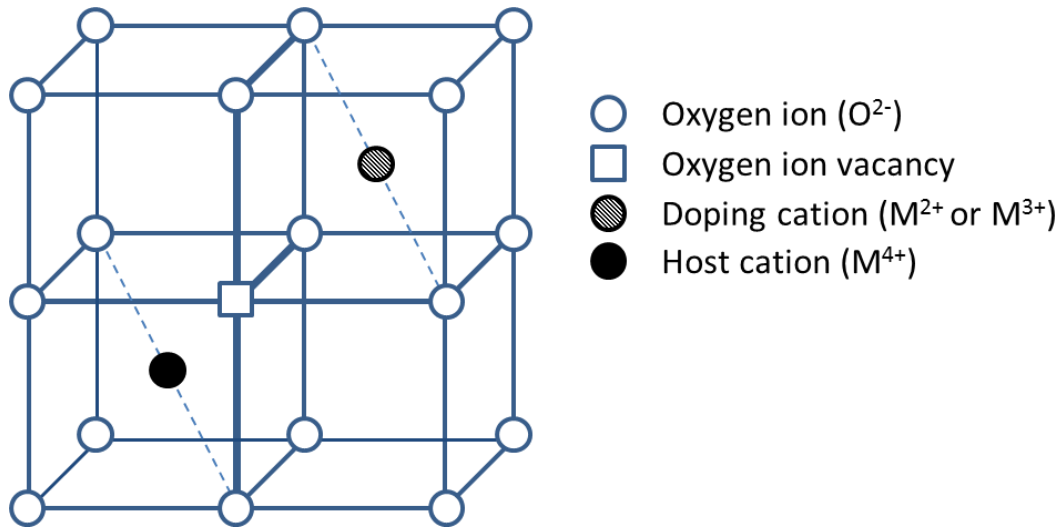
Figure I - 5 Doped fluorite oxide structure [3]

The vacancy creation can be represented with the Kroger Vink notation illustrated here by the example of Yttria Stabilized Zirconia – YSZ (equation I-15). This example is particularly relevant as YSZ is the state of the art electrolyte material for SOFC technology and is used in this project.

$$Y_2O_3 + 2Zr_{Zr}^\times \rightarrow 2Y'_{Zr} + 3O_O^\times + V_O^{\bullet\bullet} + 2ZrO_2 \qquad \text{I-15}$$
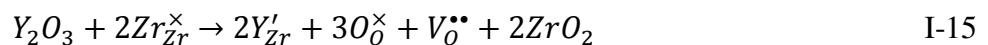
II.B.1.b)   Electrolyte Materials

Zirconia and its stabilized form.

Thanks to its chemical stability as well as its mechanical and thermal properties, zirconium oxide is a material of choice in multiple domains. It is widely used in the biomedical field as prosthesis material for dental prosthesis, hip replacement or coating, etc. It can be found in chemistry as sintering supports, in high energetic grinding devices such as ball-milling jars and balls, as raw material for jewelry and other crystal applications with eventually a monocrystalline transformation (crystal growth). Its application can stretch from mechanical utilizations such as valves, seal rings, cutters, etc, to high precision functional electronic components such as oxygen detectors.

Material doping is necessary for certain applications. Yttria doping has a dual effect on the zirconia structure. As mentioned it enhances the ionic conductivity but also stabilizes the cubic crystalline structure of the material. The latter is necessary because ZrO_2 displays martensitic allotropic transformation in the temperature interval from 700°C to 1100°C [4]. The monoclinic form ($P2_1/c$ space group, figure I - 6), stable at ambient temperature, is transformed into a quadratic or cubic fluorite form at high temperature. This transformation is accompanied by a sudden volume variation which can be problematic during cell operation or sintering. Substitution of some zirconium sites with yttrium cations induces a structural relaxation that allows stabilizing the cubic form at ambient temperature, avoiding any volume variations with the temperature other than thermal expansion.
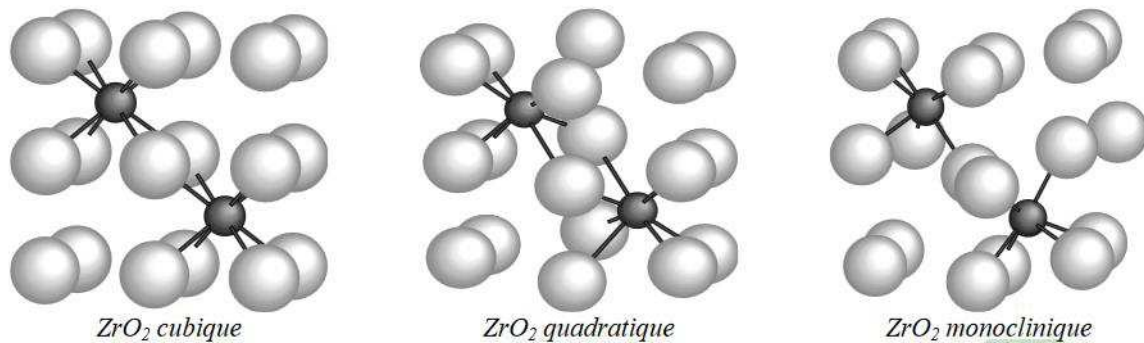

Figure I - 6 Zirconia crystalline structures [5]

In this study, for all types of cells, dense YSZ is used as electrolyte material.

Doped Ceria (CGO).

Doped ceria is considered one of the most promising alternatives of YSZ as electrolyte material due to its high ionic conductivity (as shown later in figure I – 10) at lower temperatures. It is also compatible with electrode materials such as LSCF and Ni which will be reviewed later on. However, its utilization remains relatively limited for high-temperature SOFC, because of its alteration in reducing atmosphere, leading to slight electron conductivity [6].

In our case, a dense CGO layer is deployed as a barrier layer between YSZ and LSCF based cathode in the type II cells, to prolong the fuel cell durability.

II.B.2. Anode

In most cases, a SOFC is based on a thick anode supporting a thin electrolyte and cathode. This geometry allows optimizing the internal resistance, without hindering much the durability.

In the anode supported configuration, two parts of the electrode can be identified: the supporting anode and the functional layer. Both of these parts need to exhibit excellent electronic conductivity to transport the produced electrons towards the current collector and since it is the fuel electrode, the anode must be stable in reducing atmosphere.

II.B.2.a)   Functional layer

The anode function is to provide an excellent catalytic environment for the fuel oxidation reaction ($H_2 + O^{2-} \leftrightarrow H_2O + 2e^-$). As we study the oxidation reaction, one can note that three substances of different nature (electrons, O^{2-} ions, gas molecules) are involved. Each of them is conducted by percolating adequate media and the reactions may occur at the crossing of these three conductors. These reactional sites are called triple-phase boundaries (TPB illustrated in figure I – 7) and their density is crucial for the efficiency of the functional electrode. Thus, the requirements for the anode are:

- Chemical affinity towards the fuel
- Thermal and chemical stability at reducing atmosphere
- Good electron conductivity
- Porous microstructure

- Thermal and chemical compatibility with the electrolyte

Historically, the electrode materials were either precious metals such as Au, Pt, or Pd or transition metals such as Ni, Fe, or Cu [7]. Although they are ideal electronic conductors and some of them excellent catalysts towards hydrogen oxidation, their TEC often mismatches with that of the electrolyte material. Their utilization also limits the TPB distribution uniquely at the electrode/electrolyte interface. Moreover, precious metals are expensive and rare, whereas one of the advantages to work at high temperature is the better reactional kinetics and thus they may be substituted by less expensive materials. Hence, porous ceramic-metallic composites (cermet) have been introduced as anode material, using a metal with excellent catalytic properties and oxygen conducting ceramics, often of the same material as the electrolyte. One of the main advantages of such materials is the volumetric distribution of the TPBs, thus increasing drastically their density. The presence of the electrolyte material in the anode allows modifying the cermet TEC bringing it closer to the one of the electrolyte.
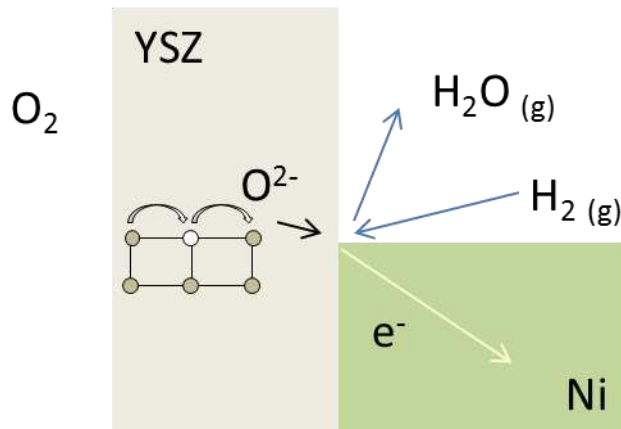
Figure I - 7 Anode triple-phase boundary

The state of the art anode material is a cermet, composed of Ni and YSZ, corresponding to the YSZ electrolyte. Nickel is an excellent catalyst for hydrogen oxidation as well as steam reforming of methane and its ideal electronic conductivity allows it to act as a current collector. However, its TEC is relatively high compared to this of YSZ $(TEC_{Ni} = 13.3 \times 10^{-6} \ K^{-1}; TEC_{8YSZ} = 10.5 \times 10^{-6} K^{-1})$ and it exhibits microstructure coarsening during sintering and cell operation. A carefully determined quantity of YSZ in the

anode allows coping with the above-mentioned hindrances. It allows decreasing the anode mean TEC converging towards the one of the electrolyte and it improves the electrode-electrolyte adhesion. A YSZ matrix strengthens the structure, limits the Ni particle aggregation, and provides the needed extension of the active TPB concentrated layer. Hence, the composition of the cermet needs to be carefully adjusted to maintain the nickel percolation, profit from properties of the YSZ matrix, and maximize the TPB concentration. Some research is conducted to find new oxide materials which are briefly reviewed in the next subchapter, although Ni-YSZ remains the most commonly used material.

II.B.2.b)   *Supporting Anode*

The supporting anode provides the mechanical strength to the fuel cell. Due to its relatively important thickness (100 - 1000µm), an optimal porosity is crucial the avoid limitation of the gas diffusion towards the functional layer as it is described in part III.A.2.b of this chapter concerning the microstructure optimization of the anode.

Here, for both layers and in both types of cells, we use a Ni:YSZ cermet with carefully controlled microstructure and porosity.

II.B.3. Cathode

The cathode is where the oxygen reduction reaction (ORR) occurs ($\frac{1}{2}O_2 + 2e^- \leftrightarrow O^{2-}$). Thus, it has a similar requirement to those of the anode.

- Chemical affinity towards oxygen
- Thermal and chemical stability at reducing atmosphere
- Good electron conductivity
- Porous microstructure
- Thermal and chemical compatibility with the electrolyte

The cathode needs to maintain good compatibility with the electrolyte taking into account the thermal expansion coefficient and the interfacial adhesion. It needs to have good thermal stability to avoid alterations in the microstructure (coarsening, fractures) and should enable adequate gas diffusion. Another crucial parameter is the chemical stability towards the electrolyte material and the oxidizing atmosphere considering that the oxygen reduction reaction (ORR) occurs in this

electrode. The cathode must exhibit an excellent electronic conductivity to distribute the incoming electrons towards the triple-phase boundaries. Identical to the anode functional layer, in this electrode, the concentration of TPB is also a major parameter to be considered. Even more so, as the ORR is sluggish and is often the limiting factor for SOFC efficiency.

Anew, noble metals can be used as electrode materials, especially Pt which is a good catalyst for oxygen reduction, ideal electrical conductor, and chemically stable at the operating temperature. However, as it is for the anode, an increase of the TPB density and a cost reduction are aimed and thus alternative materials have been introduced. Usually, perovskite materials (Figure I – 8) with good electronic conductivity and ion conductivity such as lanthanum manganite ($La_{1-x}M_xMnO_3$ where M = Sr, Ca) are used. The substitution of the A site with a lower valence element (La^{3+} with Sr^{2+} in this case) forces a charge compensation from the B site element (Mn^{3+} becomes Mn^{4+}) thus increasing drastically the electronic conductivity of the material. The state of the art material is an LSM-YSZ mixed conducting composite presenting high TPB density, an adequate mean TEC, and good electrode-electrolyte compatibility.
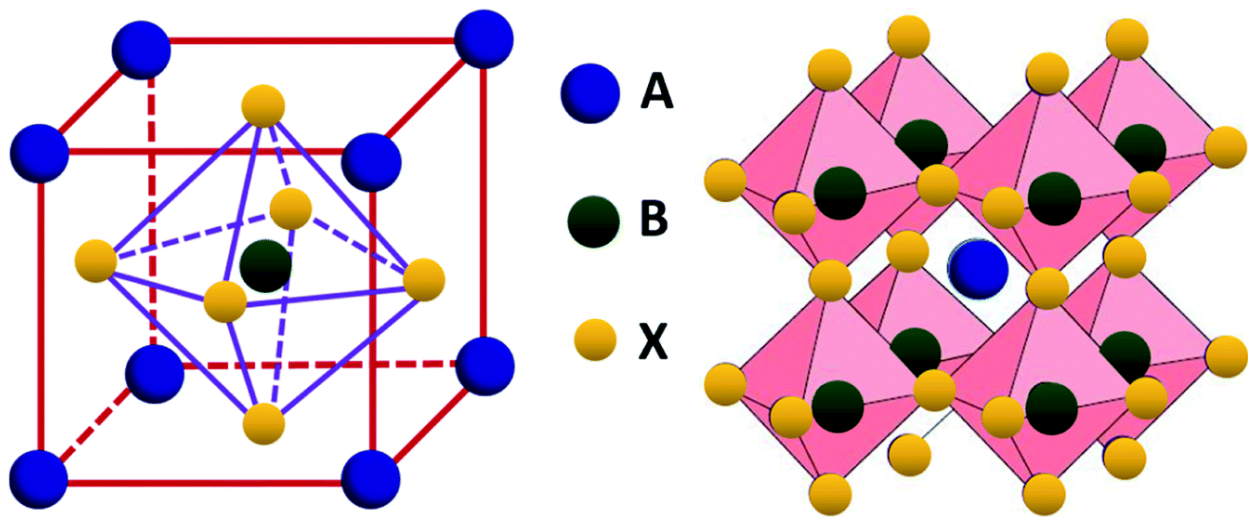

Figure I - 8 Perovskite structure [8]

Mixed ion-electron conducting (MIEC) perovskites, such as $La_{1-x}Sr_xCo_{1-y}Fe_yO_3$ (LSCF) are also developed to promote larger reacting surfaces, especially for intermediate temperature SOFC. Thanks to the ionic conductivity, those materials exhibit a faster ORR kinetics compared to LSM,

especially in a composite with an ionic conducting material, but usually have lesser chemical and microstructural stability. For example, a chemical reaction between LSCF and YSZ is observed at high temperature (above 800°C) producing an insulating phase $ZrSrO_3$ (Figure I – 9 [9]). This reaction can be limited by the presence of an intermediate CGO layer. However, this requires supplementary fabrication steps and materials, which can increase the fabrication price. Nevertheless, in some cases, the gain in performances outweighs the cost increase.
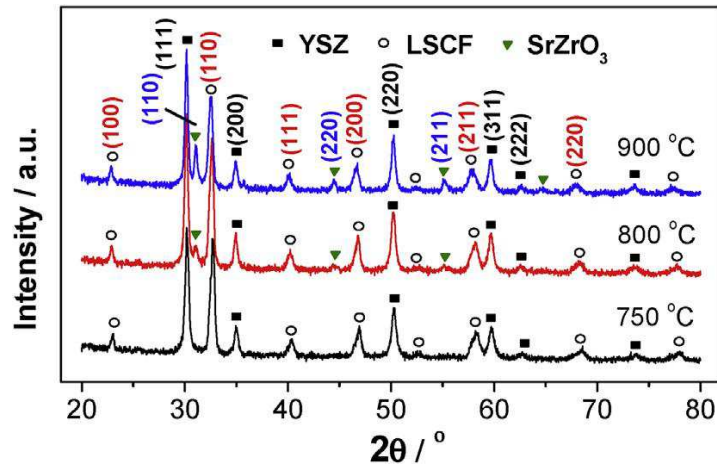
Figure I - 9 XRD LSCF/YSZ contact SrZrO3 formation [9]

As mentioned, in this study we fabricated two types of cells differentiated by their cathode composition. For type I cells, an LSM:YSZ composite is used, and for type II cells, a LSCF:CGO composite is applied.

III.   Bibliographic survey on performance enhancement for SOFCs

Several paths of SOFC, amelioration are studied in ordered to contribute to SOFC attractiveness: 1) lifespan, 2) pollution resistance, 3) catalytic activity, 4) thermal, mechanical, chemical compatibility and stability, and 5) electrochemical performances. Numerous pathways are currently investigated by the research community starting on a single cell level (new materials, microstructure, geometry, or design) way up to complex hybrid systems involving the synergy of numerous technologies [10] [11] [12] [13].

In this chapter, some single solid oxide fuel enhancement techniques are reviewed. They are coarsely categorized in terms of the scale of modification from the conventional design. Many of the modifications can be considered as multiscale, but for the sake of simplicity, only three sections are considered here. In the first part, nanoscale alterations are considered such as alternative materials and/or TPB concentration increase. The two electrode and electrolytes are considered separately, although usually, the use of alternative materials concern the entire cell (ex: use of CGO as intermediate temperature electrolyte, CGO:Ni cermets and CGO:LSCF composites). The second part of this subchapter will concern microscale modification. Here some electrochemical enhancement techniques such as infiltration, exsolution, and impregnation are mentioned as well as the impact on performances of microstructure variations (ex: pore and grain size). The last part will focus on "macroscale" engineering such as electrode-electrolyte interface architecting, layer optimization, and pore structure as well as cell design.

III.A. Materials and microstructure

Adapting the material composition of the elements of the cell is crucial to assure first-rate performances including power density, lifespan, fuel flexibility, and in some cases functioning reversibility. As mentioned previously, the most commonly used materials are Ni:YSZ cermets for the anode, YSZ or CGO for the electrolyte, and perovskite mixed conductors or composites for the cathode such as LSM or LSM:CGO. Although those materials have been proven to have good electrochemical and catalytic performances, they are potential subjects to composition alteration, poisoning, mechanical or microstructural degradation. Ni:YSZ cermets have several well-known deteriorations processes such as sulfur poisoning, carbon coking, Ni grain growth at sintering, and redox cycling [14]. YSZ has excellent chemical, mechanical and thermal stability, and a good pure ionic conductivity at high temperature (> 700°C) [15],[16]. The exponential decrease of this conductivity with the temperature requires either a high-temperature functioning or the use of thin electrolyte layers (~10 µm). One of the YSZ compatible cathode materials is LSM which exhibits a good mixed conductivity and chemical stability, but a low catalytic activity towards oxygen reduction reaction (ORR).

III.A.1.Electrolyte

The ohmic losses in the fuel cell voltage are mainly caused by the electrolyte resistivity. Thus, to increase the electrochemical performance of a single fuel cell, the resistivity needs to be lowered.

An enhancement of the global efficiency of the cell can also be considered, by lowering the operating temperature. Two pathways can be explored: 1) increasing the conductivity by either increasing the operating temperature or by using more performant materials, or 2) decrease the thickness of the electrolyte layer thus reducing the transport distance of the ions.

In the late 80s, Steele [17] has presented a practical comparison method of ion-conducting materials by specific conductivity as a function of reciprocal temperature. This method consists of fixing a target-specific resistivity and determine the maximum electrolyte layer thickness to meet this resistivity (figure I – 10). This study has been a guide towards electrolyte development for the last 30 years, promoting material and design innovations.

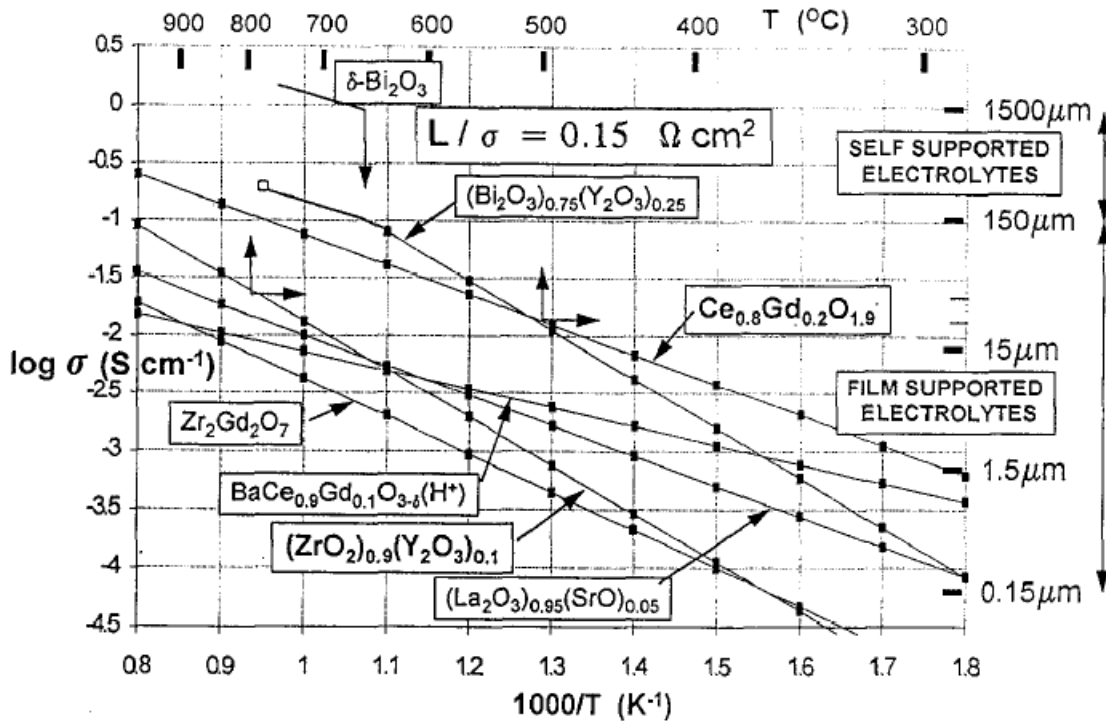Figure I - 10 Oxygen transport conduction of oxide materials Steele et al. [17]

III.A.1.a)   Materials

Based on figure I – 10, numerous studies on oxides with high ionic conductivity have been carried out, revealing some potential alternatives to YSZ. Sc-doped zirconia exhibits a higher ion conductivity than YZS, but the cost and aging of the material present drawbacks to its use for SOFC technology

Bismuth-based electrolyte materials have the highest ion conductivity but their decomposition above 800°C and in reducing atmosphere is problematic for the fabrication and the functioning of HT-SOFC. Doped lanthanum gallium perovskite materials (LGSM) have been considered as an alternative material for LT-SOFC. Despite their good ionic conductivity (0.14 Ω^{-1}.cm^{-1} at 800°C), chemical instability, and incompatibility with perovskite or metallic electrodes as well as poor sinterability restrain their use. However, some advances in its stabilization have been reported and its use as electrolyte-supported cells remains interesting [18]. LGSM has been used in a Ni:LDC anode supported cell as an electrolyte film by Bozza et al. [19], exhibiting good electrochemical performances (maximum power density of 0.79 W.cm^{-2} at 700°C).

The most popular electrolyte alternative for intermediate and low-temperature SOFC are doped ceria based materials. Gadolinium-doped ceria (CGO or GDC) has usually a higher ion conductivity than YSZ at intermediate temperature (σ ($Ce_{0,9}Gd_{0,1}O_{1,95}$) = 0.025 Ω^{-1}.cm^{-1} compared to σ (YSZ) =0.005 Ω^{-1}.cm^{-1} at 600°C), thus being an excellent candidate. Its main drawback is a reduction of Ce^{4+} to Ce^{3+} in reducing atmosphere, causing electronic conductivity and lattice expansion potentially resulting in microcracks. A detailed description of the reducing process is reviewed by Mogensen et al. [6], providing also practical application information for SOFC devices. They review some studies of compatibility between CGO and other SOFC materials such as the works of Tompsett et al. [20] and Sammes et al. [21] which reveal a chemical reaction between CGO or CeO_2 and YSZ at prolonged high-temperature thermal treatment. An insulating cubic phase is formed in YSZ:CGO composites which might hinder the electrochemical properties of the material. Nevertheless, the phase creation is observed after treatment of 72h at 1300°C which is by far longer than any sintering duration of those materials. Furthermore, CGO presents good chemical stability in an oxidizing atmosphere and compatibility with cathode materials such as LSCF (cf. Chap 1 - I.B.3). Thus, one may consider a bilayered CGO/YSZ electrolyte as is the case of Brahim et al. [22] where the researchers studied the electrochemical performances of a thin bilayered electrolyte elaborated by a sputtering technique.

A thin CGO barrier layer between the YSZ electrolyte and LSCF based cathode is very commonly used by cell manufacturers such as Forschungszentrum Jülich [23], Fiaxell SOFC Technologies [24], SOFCMAN [25], and many others to promote durability, cathode adhesion, and electrochemical performances.

III.A.1.b)   Microstructure

Studies of bi-layered electrolytes to improve IT-SOFC performances are reviewed by Shri Prakash et al. [26], considering several material couples other than CGO/YSZ. Extremely high performances bilayer electrolytes with erbium stabilized bismuth oxide (ESB) have been reported by several teams. Joh et al. [27] obtained a maximum power density of 2.1 W.cm^{-2} at 700°C and 1.6 W.cm^{-2} at 650°C with ESB/YSZ bilayers and Wachsman et al. [28] as well as Ahn et al. [29] demonstrate a maximum power density close to 2 W.cm^{-2} at 650°C using ESB/CGO bilayers. A maximum power density of 3.27 W.cm^{-2} was registered by Ishihara et al. [30] with a modified Ni(Fe) alloy-SDC anode and an LGSM/SDC bilayer electrolyte. The strategy of using a bilayer electrolyte shows a lot of encouraging results and, as mentioned, it is vastly used in the industry (especially CGO/YSZ).

Electrolyte thickness and design are predominant factors for SOFC performances enhancement. The oxygen ion transportation is an energy activated process which is principally responsible for the polarization overpotential of a cell. Thus the correlation between the layer quality (microstructure, thickness, interfaces) and the electrochemical performances needs to be to evaluate its influence on the effect of the architecturation.

III.A.1.c)   In this work

Based on the literature review, two types of electrolytes are used.

- Simple 8YSZ layer type I cells
- 8YSZ electrolyte layer followed by a CGO10 barrier layer

III.A.2. Anode

Electrode optimization is crucial for overall SOFC efficiency amelioration. This may be achieved by: 1) enhancing the durability of the anode which is prompt to microstructural or chemical degradation, thus lowering increasing the global rentability of the cell, 2) enhancing the catalytic properties by which the electrochemical performances can be increased and eventually the operating temperature may be decreased. The utilization of composite materials is already an optimization of the electrodes by transforming the reactional zone from a 2D surface at the electrolyte/electrode interface to a 3D volume called Anode Functional Layer (AFL). Thus, a decrease in the activation can be achieved by offering a superior number of active sites.

To improve SOFC lifespan and fuel flexibility, anode degradation by carbon deposition (coking) or other poisonings (sulfur) as well as microstructural alterations caused by the reducing atmosphere or the high operating and sintering temperature, alternative anode materials are widely studied. Their use to replace the conventional Ni-YSZ cermet can cope with some of the issues enhancing the overall SOFC performances. Additionally, fabrication technics such as infiltration, exsolution, and impregnation are developed to enhance the electrochemical performances by modifying the nano or microstructure of the electrode.

III.A.2.a)   Materials

One of the strategies is to use poison-resisting mixed ion electron-conducting oxides (MIEC) anodes which have also the advantage to present extended TPB, passing from 1D TPB to a 2D surface TPB which increases drastically number of reactional sites. Some researchers used doped titanate perovskites, due to their stability in redox conditions and their good electronic conductivity. Strontium titanate ($SrTiO_3$) is one of the most popular examples which is frequently doped with elements such as La, Cr, Fe, Mn, Cu, Sc, etc in order to increase its conductivity (from $10^{-5} - 10^{-1}\,\Omega^{-1}.cm^{-1}$ to $1 - 10^3\,\Omega^{-1}.cm^{-1}$). Flores *et al*. [31] review the latest advances in this field and provide an exhaustive list of titanates along with their electrical conductivity and temperature of application. Some lanthanum-doped strontium titanates ($La_xSr_{1-x}TiO_3$) stand out with high electric conductivity (100 $S.cm^{-1}$ at 1200 °C and 600 $S.cm^{-1}$ at 600 °C). Ma and Tietz [32] present a comparison between La and Y doping for $SrTiO_3$ (LST and YST respectively) in which their conductivity and their thermal and chemical compatibility with YSZ are tested. LST exhibits better conductivity, whereas YST has better chemical compatibility with YSZ and both of the materials are suitable candidates for alternative anode material. YST-YSZ composites have also been studied and characterized by He *et al*. and by Marina *et al* [33], showing that LST has adequate thermal, electric and electrocatalytic properties for SOFC electrode use. Miller and Irvine [34] focused on doping the B site of LST by various compounds ($La_{0.33}Sr_{0.67}Ti_{0.92}X_{0.08}O_{3+\delta}$ where X = Al^{3+}, Ga^{3+}, Fe^{n+}, Mg^{2+}, Mn^{n+}, and Sc^{3+}) altering the electrocatalytic activity as well as the conductivity. Numerous related studies have been conducted supporting the potential benefit of titanates usage [35], [36], [37], [38], [39], [40]. Although the titanate perovskites show good chemical stability towards anode degradations, they are yet to achieve the electrochemical performances of Ni:YSZ cermets.

Other materials have been considered as Ni:YSZ substitutes such as Cu:CeO$_2$ cermets as well as Cu with Sm-doped ceria [41]. In their work, Costa-Nunes and al. [42] demonstrated excellent performances of Cu-CeO$_2$ or Cu–Co–CeO2–YSZ anodes for H$_2$, CO, and syngas. Ceria-based anodes with Cu exhibited very high resistance to sulfur poisoning as shown by He, Gorte et Vohs [43] who did not observe any degradation when introducing up to 450 ppm of H$_2$S. Huang and Goodenough studied the electronic conductivity and anode performance in H$_2$, H$_2$ containing 5% H$_2$S and CH$_4$ of the double perovskite Sr$_2$MgMnO$_{6-\delta}$. They demonstrated good electrochemical performances and stability (over P$_{max}$=0,8 W.cm^{-2} in H$_2$ and H$_2$/H$_2$S and P$_{max}$=0,44 W.cm^{-2} in CH$_4$) [44], [45].

Although some alternative materials offer good resistance to poisoning, they rarely can match Ni catalytic activity towards H$_2$ and its excellent conductivity. Thus, to maintain electrochemical performances, the transition metal remains an important element for SOFC functioning. Some authors put forward the use of rare earth doped ceria as a substitute for YSZ in Ni-based cermets especially for low-temperature SOFC due to its good ionic conductivity. For example, nickel and gadolinium doped ceria cermets (Ni:CGO) have exhibited coke resistance with CH$_4$ on several occasions [46], [47] and potential use to increase triple-phase boundary concentration by infiltration or impregnation.

III.A.2.b) *Microstructure*

A multitude of papers has been published on electrode microstructure optimization based on either experimental data, analytical calculations, or numerical simulations demonstrating a considerable influence on SOFC performances. The dominating parameters are usually equivalent to the anode and the cathode such as porosity, pore size, grain size, TPB concentration, and accessibility.

Porosity optimization

Jo *et al.* [48] conduct a study on the physical parameters of a single cell using an electrochemical model. They determine that in a non-graded electrode, the optimum porosity is 42 %vol and the optimum pore radius is 2.4 μm. In the case of a graded electrode, the optimum porosity and pore size are 30 % and 2.2 μm respectively. In their work, the authors demonstrate that grading the porosity of the anode has a consequent effect on the maximum power density, achieving

approximately 70 % increase (1200 mW.cm^{-2} for a cell with a nongraded anode and 2000 mW.cm^{-2} for an equivalent cell with a graded anode).

Ni *et al*. [49] work on a similar study, also demonstrating optimal pores radius (3 μm) and optimal porosity (40 %) as well as operating temperature and choice of supporting element influence on electrochemical performances.

An excellent review of porous ceramics manufacturing by tape casting, published by Nishihora *et al*. [50] provides very interesting information on porosity tailoring as well as a multitude of references. Du *et al*. [51] review the utilization of freeze casting for SOFC fabrication, presenting very interesting possibilities of porosity tailoring, opening a promising pathway towards the increase of SOFC performances. An example of excellent performance increase is published by Chen *et al.* [52], where the authors apply freeze casting to fabricate high-performance low-temperature SOFC with tailored electrode porosity. Thus, they observe a significant increase in the maximum power density varying from 402 mW.cm^{-2} for untailored cell, 732 mW.cm^{-2} for sole anode pores tailoring and 1440 mW.cm^{-2} for both electrodes tailoring.

In our study, we use gradual porosity for the anode and in some cases for the cathode.

Infiltration/Impregnation

The infiltration method has gained interest in the past two decades. It allows separating the sintering of the different materials in an electrode in order to reduce chemical and mechanical alterations. The technique consists of three principal stages of fabrication. A porous skeleton is laid over the electrolyte by a classical deposition technique such as screen printing, spin coating, or tape casting and it is sintered. An electrode material solution (usually nitrates) is infiltrated in the prepared porous structure, followed by a thermal treatment to obtain the wanted phase. Historically the method has been first used for anode YSZ based cermet with either Ni or Cu infiltrated particles [53].

Catalyst nanoparticles infiltration has been used by Emir Dogdibegovic *et al*. [54] to achieve high performances in metal-supported solid oxide fuel cells. They have experimented with five catalysts and several of their cells show reproducible performance at 1.50 W.cm^{-2} at 700 °C. The

maximum cell power obtained by the team is 2,85 W.cm⁻² at 800°C for a PrO$_x$/SCSZ/SDCN$_{40}$ cell.

Futamura *et al*. [55] used the impregnation method to render an alternative anode material as performant as the classical Ni cermets having higher durability and fuel utilization. They have co-impregnated a Ce$_{0.9}$Gd$_{0.1}$O$_2$ (CGO) - Sr$_{0.9}$La$_{0.1}$TiO$_3$ (LST) composite with noble metal/CGO catalyst nanoparticles (Rh, Pt, and Pd) as well as Ni/CGO nanoparticles. Thus they were able to demonstrate adequate performance for the alternative anode. The Ni/CGO impregnation is especially performant from an electrochemical point of view (~1.0 V at 0.2 A.cm⁻² with 3 % - humidified H2 fuel). However, all of the co-impregnated anodes cells show slightly lower I-V performance compared to the conventional Ni/ScSZ for highly humidified H$_2$.

The impregnation method is also used by Han *et al.* [56] on anodes for tubular systems, introducing nanoscale Fe and Ni catalysts particle into a Ni:YSZ anodes. Their cells do not have a very high power density but they observe a slight increase after impregnation (from 0,38 to 0,40 and 0,48 W.cm⁻²).

Nielsen *et al*.[57] seek to improve the durability of SOFC by using an alternative anode material La$_{0.4}$Sr$_{0.4}$Fe$_{0.03}$Ni$_{0.03}$Ti$_{0.94}$O$_3$ infiltrated with Ni:CGO catalyst particles. They report high power density at intermediate temperature (0.650 W.cm^{-2} at 0.7 V and 700 °C) thus exhibiting competitive performance and potentially elevated durability due to the lower temperature.

Exsolution

Exposure to a redox atmosphere (fuel or oxygen) can alter an electrode material composition resulting in either degradation or enhancement of the properties. Thenglong Zhu et al. [58] demonstrate exsolution and nucleation of Ni$_{0.5}$Fe$_{0.5}$ particles in Sr$_{0.95}$(Ti$_{0.3}$Fe$_{0.63}$Ni$_{0.07}$)O$_{3-d}$ electrode used to replace Ni-based cermets. The exsolution yields a competitive anode polarization resistance dividing by up to 4 compared to the more classical material SrTi$_{0.3}$Fe$_{0.7}$O$_{3-\delta}$ without nanoparticles.

III.A.2.c)   In this work

Based on the literature review, two types of anodes are used.

- Simple Ni:YSZ cermet with a 44:56 volume ratio is tested on the cells type O with elevated porosity (> 35 %)

- Graduate Ni:YSZ cermet composed of a functional layer and of an anode support layer differentiated by the elevated porosity in the anode support (> 35 %)

III.A.3.Cathode

The cathode activation polarization and sluggishness of the oxygen reduction reaction are some of the main factors responsible for SOFC electrochemical losses. Optimizing the air electrode is one of the most important levers to increase cell performances. Here the requirements are equivalent to those of the anode functional layer, i.e. good electron conductivity, oxygen catalysis, high triple-phase boundary concentration and accessibility, chemical and mechanical stability in an oxidizing atmosphere, and high temperature.

III.A.3.a)   Materials

Considerable research has been conducted for optimal cathode material, taking into account the complex requirements, but also the cost-efficiency. The most common composite, widely used in research and industry is LSM/YSZ laid over a YSZ electrolyte. This composite exhibits good electrochemical performances thanks to its adequate electron and ion conductivity. However, the catalytic properties of LSM towards the ORR are limited and an alternative needs to be developed.

Electron conducting perovskites such as the state of the art material LSM, are frequently used directly or combined in a composite with an ion-conducting material. San Ping Jiang [59] has published in 2008 an interesting review on the development of LSM perovskites as cathode material for SOFC in which the influence of the stoichiometry on the conductivity, the thermal expansion coefficient as well as activation energy is studied.

An excellent literature survey on the perovskite cathode materials has been published by Kaur *et al*. [60]. In this work electronic and ionic conductivities are cataloged for a multitude of materials such as La, Sr or Pr based materials as well as Nd, Gd, Sm, and Y based materials with or without cobalt doping, The authors have also mapped some fuel cell performances related to the cathode materials comparing, in particular, the ASR and the power density of the cells revealing.

promising performances observed with Pr or Nd containing materials such as $La_{0.35}Pr_{0.15}Sr_{0.5}FeO_{3-\delta}$ and $Nd_{0.5}Sr_{0.5}Co_{0.5}Fe_{0.5}O_{3-\delta}$.

As seen previously, mixed ion electron-conducting (MIEC) materials are considered such LSCF, because of their intrinsically elevated TPB length. LSCF also presents superior catalytic activity potentially increasing the electrochemical performances. In a composite with CGO, it represents an excellent cathode material candidate, except for its reactivity with YSZ, which can be limited by the presence of a CGO barrier layer. Numerous studies on different stoichiometries of lanthanum strontium cobalt ferrite cathode materials ($La_{1-x}Sr_xCo_{1-y}Fe_yO_{3-\delta}$ with x~0.4 and y~0.2) have been carried out, some of them reviewed by Jiang *et al.* [9], taking into account the electronic and ionic conductivity as well as thermal expansion coefficient and catalytic properties. Among these materials, the $La_{0.6}Sr_{0.4}Co_{0.2}Fe_{0.8}O_{3-\delta}$ (LSCF48) stoichiometry presents a relatively elevated electron conductivity ($\sigma_{el} = 280\ S.\,cm^{-1}$ at 800°C) and acceptable thermal expansion coefficient ($TEC = 15.3\ \times 10^{-6}\ K^{-1}$).

III.A.3.b)   Microstructure

Optimization of the cathode microstructure is essential to obtain adequate electrochemical performances. As it is for the anode, the microstructure of the cathode concerns the concentration of the percolating triple-phase boundaries, meaning the percolation of the three conducting media (pores, electron conductor, ion conductor).

Hee Kim *et* al. [61], have demonstrated interesting results of current density increase by fabricating cells with bi-layer LSCF based cathodes. The application of a "functional" layer composed of LSCF:CGO composite and a current collecting layer composed of LSCF allowed the authors to decrease the global cell impedance compared to a cell with a single LSCF:CGO layer cathode by approximately 30 %.

Porosity optimization.

Tsai *et al.* [62] have demonstrated that an apparent gas diffusion limitation becomes important for LSM:YSZ cathode with a porosity lower than 30 %.

In the previously quoted work by Chen *et al.*[51]*,* on the utilization of freeze-casting to obtain a tailored electrode porosity, the authors demonstrated a significant effect of the cathode pore

tailoring. The maximum power density of their cells is doubled comparing a non-tailored cathode porosity and tailored cathode porosity (732 mW.cm^{-2} and 1440 mW.cm^{-2} respectively).

Huang et al.[63] adopt the infiltration method to enhance an LSCF-CGO cathode by infiltrating it with nanoscale $La_{1-x}Sr_xCoO_{3-\delta}$ (LSC). They report two times higher maximum power density for the infiltrated cells compared to the conventional ones.

The infiltration method is also used by Manuel Brito et al. to increase the performances and durability of solid oxide reversible cells. $La_{0.6}Sr_{0.4}Co_{0.2}Fe_{0.8}O_{3-\delta}$ (LSCF) - $(CeO_2)_{0.8}(SmO_{1.5})_{0.2}$ (SDC) composite cathode scaffolds were infiltrated with SDC nanoparticles.

He et al. [64] published a numerical investigation demonstrating the importance of microstructural optimization of an LSCF based cathode. In their study, a cell with an optimized cathode may exhibit a 40 % increase in the total reaction current.

Impregnation:

S.P. Jiang [65] has published a review of the utilization of wet impregnation as an alternative method for the fabrication of high performances electrodes of SOFC. In this work, a multitude of examples can be founded concerning anode for and cathode impregnation such as CeO_2 impregnation of porous LSM as cathode material [66]. Palladium impregnation of LSCF cathode was employed by Sahibzada et al. [67] allowing to lower 3-4 times the cathodic impedance. Yamahara et al. studied cobalt-impregnation of LSM cathode supported SOFC [68], and reported a significant augmentation of the maximum power density compared to a similar cell without impregnation (270 mW.cm^{-2} and 130 mW.cm^{-2} respectively).

Exsolution

Lattice strain-enhanced exsolution has been proposed by Han et al. [69] for perovskite thin films. The authors achieved a high degree of exsolution (1100 particle/µm) of nanoparticles (~5 nm), thus opening a very promising path towards catalytic enhancement for perovskite material based electrodes such as LSCF.

III.A.3.c)   In this work

Based on the literature review, three types of cathodes are tested in this work.

- Graduate LSM:YSZ composite cathode composed of a functional layer with a materials volume ratio equal to 1:1 and of a gas diffusion layer with a materials volume ratio 8:2 and increased porosity (15 % additional porosity)
- A simple layer LSCF48:CGO10 composite cathode with a 1:1 volume ratio

III.B. Cell design

Optimization in single-cell design meaning layer thickness or interface engineering is a promising way to enhance the efficiency of SOFC devices. For example, as reviewed in the previous subchapter, the electrolyte thickness and design has a considerable effect on the cell performances.

III.B.1.DM-Cell

An innovative fuel cell design has been proposed, proven, and patented by Alain Thorel's team named dual membrane fuel cell (dmFC) [70]. The new cells are composed of a combination of an oxygen ion and proton-conducting fuel cells with a mixed ionic conducting central membrane (figure I − 11). The concept has received a lot of interest and was studied in the IDEAL-Cell European project during which, early generation cells were conceived and tested, exhibiting encouraging results (~100 mA.cm^{-2} at 700 °C).
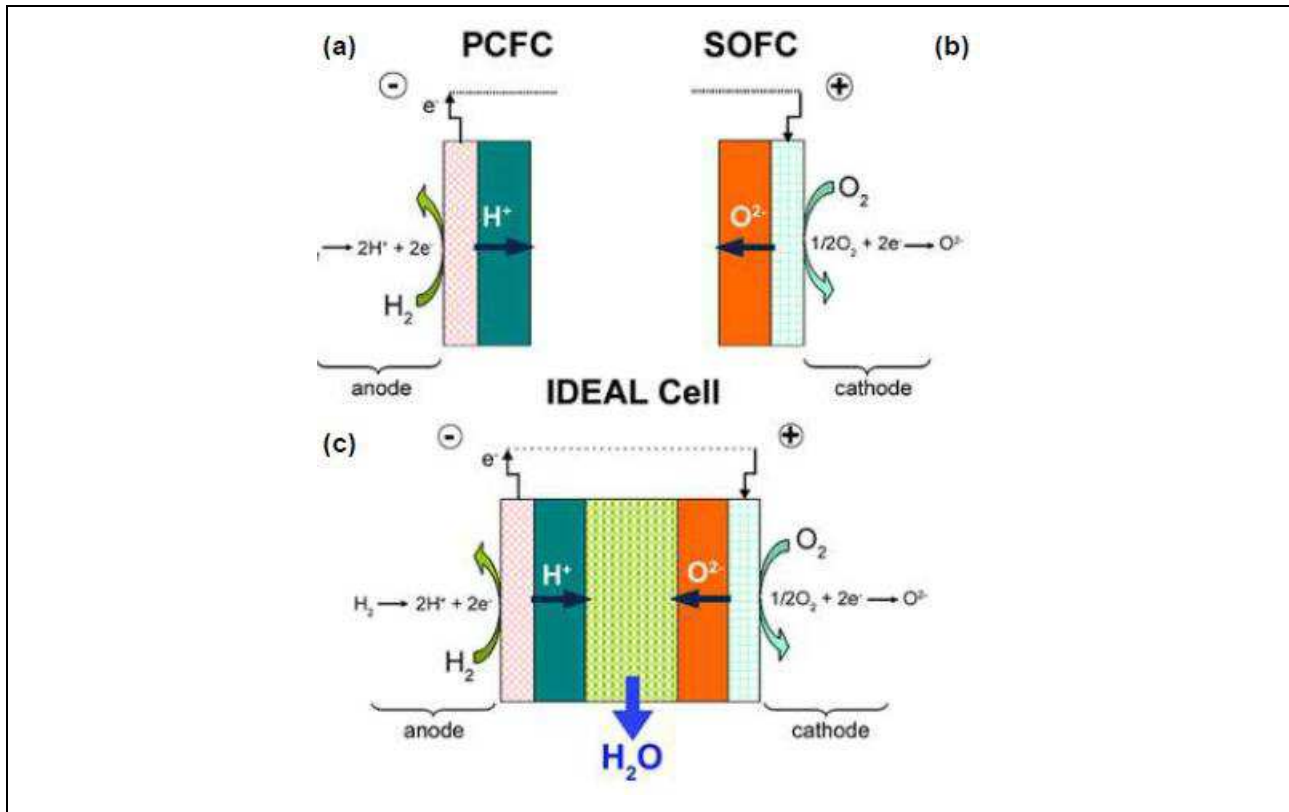
Figure I - 11 Ideal cell concept [70]

III.B.2.Interfaces active surface area extension

A surface extension is a regularly used method to increase effective performances in an interfacial exchange system. It can be observed in natural systems developing colossal exchange surfaces such as pulmonary alveoli (145 m²) and intestines (32 m² [71]). It is used in many technological fields such as heat exchangers [72], catalysts [73], batteries [74], supercapacitors [75], etc.

In the SOFC field, interface area expansion implies an increase in the electrode functional layers, and potentially the number of active triple phase boundaries. Hence, architecting the electrode/electrolyte interfaces is a promising pathway toward an increase in SOFC performances and the idea has been suggested on several occasions as in R. Ihringer's work [76]. However, the fabrication of thus prepared cells can reveal to be challenging due to complex material phenomena such as sintering, material oxidation, and reduction, thermal expansion, residual stress, etc. Several researchers have studied the impact of surface modification on SOFC cells exhibiting interesting fabrication methods as well as electrochemical results.

Konno *et al*. have studied the effect of mesoscale structuring of the anode/electrolyte interface in their work published in 2010 [77] followed by a similar work on the cathode/electrolyte interface published by Iwai *et al*. [78]. In their works, they demonstrate an increase in the performances proportional to the surface area extension. However, the studies are performed on electrolyte supported fuel cells which allows neglecting the variation in the ohmic resistance induced by the interface architecture.

In 2017 Cebollero *et al*. [79], established a laser micro-patterning of a YSZ electrolyte surface to enlarge the cathode/electrolyte interface area. They demonstrate a reliable texturing process with a nanosecond laser, with which they have achieved a 30 % surface expansion. The electrochemical impedance spectroscopy they realized on their cells reveals an overall resistance decrease compared to the one corresponding to the cells with planar interfaces, matching the surface expansion.

A numerical modeling and experimental work have been initiated in our team on the subject. During the Ph.D. work of Maya Geagea [80], a preliminary study on architectured SOFC has been established accompanied by a functioning simulation based on previous work established by Viviani and Delloro [81]. In their paper, the authors investigate the influence on the performances of the microstructure and pattern geometry of a half cathode-electrolyte architectured cell. During M. Geagea's work, an unexpected mismatch between analytical and numerical prediction and experimental data is observed. The experimental electrochemical performances of the preliminary architectured cells exceed by at least two times the predicted ones.

IV.   Objectives

This Ph.D. project aims to refine and to continue the up quoted work providing a reliable and cost-effective fabrication protocol for cells with planar and architectured interfaces. To increase our understanding of the interfacial phenomena occurring in achiterctured cells, cells with architectured anode/electrolyte and electrolyte/cathode interfaces are electrochemically compared to planar cells with equivalent microstructure.

We predict that the architecturation which will increase the effective surface will consequently, increases the number of TPBs as illustrated in figure I – 1. There is also a potential activation of previously non-percolating paths, as illustrated in figure I – 13, therefore increasing the further

the TPB density. Thus, the catalytic properties of the interface are modified (compared to a planar interface) and the activation losses should decrease.
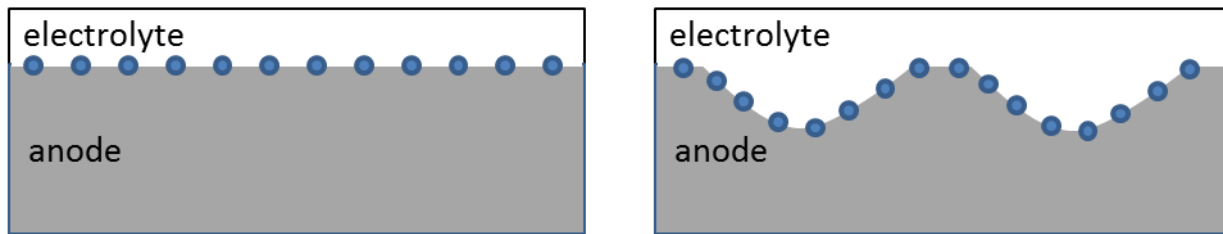

Figure I - 12 Illustration of triple-phase boundary increase due to the surface area augmentation
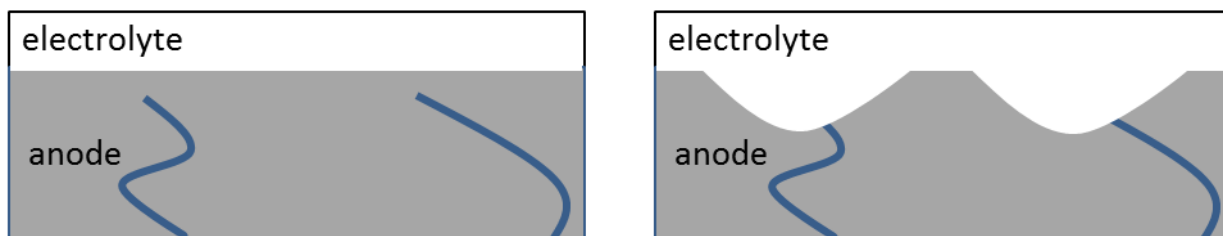

Figure I - 13 Illustration of triple-phase boundary activation due to the surface area augmentation

In their work Delloro and Viviani suggest that the penetration of the dense ion-conducting electrolyte in the porous anode can lead to the creation of a "highway for ions", resulting in lower resistivity and an increase in the electrochemical performances. However, in a single interface architecturing, the electrolyte would represent a variable thickness, which would result in a higher resistivity at the thicker spots. Thus, a comparison between the effects is necessary to predict and understand the variation in the electrochemical performances.

Henceforth, the main objective of this Ph.D. work is to study the impact of the interfacial architecturing on the electrochemical performances. To achieve this goal, a three-way approach is adopted: 1) establish a reliable fabrication protocol for planar and architectured fuel cells allowing the creation of comparable objects, 2) a microstructural and electrochemical analysis of the fabricated cells, and 3) establish a numerical model using actual cell parameters.

IV.A. Fabrication

During M. Geagea's thesis, a non-optimized fabrication protocol was used, hindering the reproducibility of the measurements. However, the results are very encouraging and suggest a lack of understanding of the phenomena occurring at the cell interfaces.

A reproducible fabrication protocol is necessary to confirm the observed results and to vary different cell parameters to promote comprehension. The first objective of this thesis is to establish such a protocol using common ceramics fabrication techniques at cost efficiency, potentially applicable to the industry. First, the elaboration of fuel cells with planar interfaces and correct electrochemical performances needs to be managed. Subsequently, an architecturing method could be applied during the fabrication process to shape equivalent planar and architectured cells. The architecturing method should provide the possibility to modify the anode/electrolyte as well as the electrolyte/cathode interfaces.

Before proceeding with the cell fabrication, some technical constraints need to be advised. The raw ceramics preparation is based on the tape-casting technique which imposes several major considerations such as material choosing and engineering, slurry characterization, minimization of the tape residual stress, and deformations during the thermal treatment. In their book on tape casting, Mistler and Todd [82] have provided an extensive understanding of the technique as well as practical guidelines for successful casting. Additionally, literature from Forschungszentrum Jülich [83] has helped to establish the casting protocol as well as the thermal treatment and to anticipate ceramics deformations.

The fabrication protocol is further detailed in Chapter II of this document.

IV.B. Cell characterization and electrochemical testing

A characterization protocol including optical and electronic microscopy, profilometry is applied to control the cell microstructure and architecture. It allows extracting pertinent parameters (layer thickness, pore and grain size, patterns dimensions) necessary for the cells studying and the development of the numerical model. Extensive electrochemical measurements such as polarization measurements and electrochemical impedance spectroscopy in various conditions are carried out to compare the fuel cells and to study in detail the effect of the architecturing.

IV.C. Modeling

A numerical model, allowing to simulate planar or architectured cell operation, is initiated in COMSOL Multiphysics software, based on the work of Delloro and Viviani and integrating cell parameters extracted from the characterization protocol. In this model, an adaptation of the previous works is carried out to comply with the variation of the cell materials. However, the model is unfinished and thus it is not presented in this work.

IV.D. Results and discussion

As mentioned, a lack of understanding of the interfacial phenomena is the potential reason for the mismatch between theory and experience. This project attempts an advancement toward this understanding the experimental data.

References

[1]   S. C. Singhal and K. Kendall, 'Solid oxide fuel cells', in *Proceedings of the 3rd International Symposium, vols*, 2003, pp. 89–11.

[2]   'efcf 2: O-Library'. https://past.efcf.com/index.php-id=2154.html

[3]   *Nonstoichiometric Oxides*. Elsevier, 1981.

[4]   G. MOULIN, J. FAVERGEON, and G. BÉRANGER, 'Zircone - Céramique fonctionnelle', *Ref : TIP597WEB - 'Technologies biomédicales'*, Oct. 10, 2008. https://www.techniques-ingenieur.fr/base-documentaire/42606210-biomateriaux/download/n3210/zircone.html

[5]   R. Bachelet, *Couches minces d'oxydes élaborées par voie sol-gel, épitaxiées et nanostructurées par traitements thermiques post-dépôt*. Limoges, 2006.

[6]   M. Mogensen, N. M. Sammes, and G. A. Tompsett, 'Physical, chemical and electrochemical properties of pure and doped ceria', *Solid State Ionics*, vol. 129, no. 1, pp. 63–94, Apr. 2000, doi: 10.1016/S0167-2738(99)00318-5.

[7]   J. Weissbart and R. Ruka, 'A Solid Electrolyte Fuel Cell', *J. Electrochem. Soc.*, vol. 109, no. 8, pp. 723–726, Jan. 1962, doi: 10.1149/1.2425537.

[8]   Z. Yi, N. H. Ladi, X. Shai, H. Li, Y. Shen, and M. Wang, 'Will organic–inorganic hybrid halide lead perovskites be eliminated from optoelectronic applications?', *Nanoscale Adv.*, vol. 1, no. 4, pp. 1276–1289, Apr. 2019, doi: 10.1039/C8NA00416A.

[9]   S. P. Jiang, 'Development of lanthanum strontium cobalt ferrite perovskite electrodes of solid oxide fuel cells – A review', *International Journal of Hydrogen Energy*, vol. 44, no. 14, pp. 7448–7493, Mar. 2019, doi: 10.1016/j.ijhydene.2019.01.212.

[10]   S. Inac, S. O. Unverdi, and A. Midilli, 'A parametric study on thermodynamic performance of a SOFC oriented hybrid energy system', *International Journal of Hydrogen Energy*, vol. 44, no. 20, pp. 10043–10058, Apr. 2019, doi: 10.1016/j.ijhydene.2019.01.247.

[11]   A. Perna, M. Minutillo, E. Jannelli, V. Cigolotti, S. W. Nam, and K. J. Yoon, 'Performance assessment of a hybrid SOFC/MGT cogeneration power plant fed by syngas from a biomass down-draft gasifier', *Applied Energy*, vol. 227, pp. 80–91, Oct. 2018, doi: 10.1016/j.apenergy.2017.08.077.

[12]   Y. D. Lee, K. Y. Ahn, T. Morosuk, and G. Tsatsaronis, 'Exergetic and exergoeconomic evaluation of an SOFC-Engine hybrid power generation system', *Energy*, vol. 145, pp. 810–822, Feb. 2018, doi: 10.1016/j.energy.2017.12.102.

[13]   I. Rossi, A. Traverso, and D. Tucker, 'SOFC/Gas Turbine Hybrid System: A simplified framework for dynamic simulation', *Applied Energy*, vol. 238, pp. 1543–1550, Mar. 2019, doi: 10.1016/j.apenergy.2019.01.092.

[14]   M. S. Khan, S.-B. Lee, R.-H. Song, J.-W. Lee, T.-H. Lim, and S.-J. Park, 'Fundamental mechanisms involved in the degradation of nickel–yttria stabilized zirconia (Ni–YSZ) anode during solid oxide fuel cells operation: A review', *Ceramics International*, vol. 42, no. 1, Part A, pp. 35–48, Jan. 2016, doi: 10.1016/j.ceramint.2015.09.006.

[15]   A. ROLLE, V. THORETON, C. PIROVANO, O. LAFON, and R.-N. VANNIER, 'Conducteurs ioniques par ions oxyde', *Ref : TIP053WEB - 'Physique Chimie'*, Jan. 10, 2015. https://www.techniques-ingenieur.fr/base-documentaire/sciences-fondamentales-th8/fondamentaux-en-chimie-42106210/conducteurs-ioniques-par-ions-oxyde-af6711/ (accessed Sep. 11, 2019).

[16]   V. V. Kharton, F. M. B. Marques, and A. Atkinson, 'Transport properties of solid oxide electrolyte ceramics: a brief review', *Solid State Ionics*, vol. 174, no. 1, pp. 135–149, Oct. 2004, doi: 10.1016/j.ssi.2004.06.015.

[17]   B. C. H. Steele, 'Oxygen transport and exchange in oxide ceramics', *Journal of Power Sources*, vol. 49, no. 1, pp. 1–14, Apr. 1994, doi: 10.1016/0378-7753(93)01789-K.

[18]   M. Lo Faro and A. S. Aricò, 'Electrochemical behaviour of an all-perovskite-based intermediate temperature solid oxide fuel cell', *International Journal of Hydrogen Energy*, vol. 38, no. 34, pp. 14773–14778, Nov. 2013, doi: 10.1016/j.ijhydene.2013.08.122.

[19]   F. Bozza, R. Polini, and E. Traversa, 'High performance anode-supported intermediate temperature solid oxide fuel cells (IT-SOFCs) with La0.8Sr0.2Ga0.8Mg0.2O3−δ electrolyte films prepared by electrophoretic deposition', *Electrochemistry Communications*, vol. 11, no. 8, pp. 1680–1683, Aug. 2009, doi: 10.1016/j.elecom.2009.06.029.

[20]   G. A. Tompsett, N. M. Sammes, and O. Yamamoto, 'Ceria–Yttria-Stabilized Zirconia Composite Ceramic Systems for Applications as Low-Temperature Electrolytes', *Journal of the American Ceramic Society*, vol. 80, no. 12, pp. 3181–3186, 1997, doi: 10.1111/j.1151-2916.1997.tb03247.x.

[21]   N. M. Sammes, G. A. Tompsett, and Z. Cai, 'The chemical reaction between ceria and fully stabilised zirconia', *Solid State Ionics*, vol. 121, no. 1, pp. 121–125, Jun. 1999, doi: 10.1016/S0167-2738(98)00538-4.

[22]   C. Brahim, A. Ringuedé, E. Gourba, M. Cassir, A. Billard, and P. Briois, 'Electrical properties of thin bilayered YSZ/GDC SOFC electrolyte elaborated by sputtering', *Journal of Power Sources*, vol. 156, no. 1, pp. 45–49, May 2006, doi: 10.1016/j.jpowsour.2005.08.017.

[23]   'SOFC reaches 11 years in Jülich lifetime test', *Fuel Cells Bulletin*, vol. 2019, no. 3, p. 14, Mar. 2019, doi: 10.1016/S1464-2859(19)30125-7.

[24]   'Fiaxell SOFC Technologies - Cells'. https://fiaxell.com/products/specialty-inks-powders-and-cells/cells (accessed Jan. 28, 2020).

[25]   'SOFCMAN'. http://www.sofcman.com/asc.asp.

[26]   B. Shri Prakash, R. Pavitra, S. Senthil Kumar, and S. T. Aruna, 'Electrolyte bi-layering strategy to improve the performance of an intermediate temperature solid oxide fuel cell: A review', *Journal of Power Sources*, vol. 381, pp. 136–155, Mar. 2018, doi: 10.1016/j.jpowsour.2018.02.003.

[27]   D. W. Joh, J. H. Park, D. Kim, E. D. Wachsman, and K. T. Lee, 'Functionally Graded Bismuth Oxide/Zirconia Bilayer Electrolytes for High-Performance Intermediate-Temperature Solid Oxide Fuel Cells (IT-SOFCs)', *ACS Appl. Mater. Interfaces*, vol. 9, no. 10, pp. 8443–8449, Mar. 2017, doi: 10.1021/acsami.6b16660.

[28] E. D. Wachsman and K. T. Lee, 'Lowering the Temperature of Solid Oxide Fuel Cells', *Science*, vol. 334, no. 6058, pp. 935–939, Nov. 2011, doi: 10.1126/science.1204090.

[29] J. S. Ahn *et al.*, 'Development of High Performance Ceria/Bismuth Oxide Bilayered Electrolyte SOFCs for Lower Temperature Operation', *J. Electrochem. Soc.*, vol. 157, no. 3, p. B376, Jan. 2010, doi: 10.1149/1.3276503.

[30] T. Ishihara, H. Eto, and J. Yan, 'Intermediate temperature solid oxide fuel cells using LaGaO3 based oxide film deposited by PLD method', *International Journal of Hydrogen Energy*, vol. 36, no. 2, pp. 1862–1867, Jan. 2011, doi: 10.1016/j.ijhydene.2009.12.174.

[31] J. J. Alvarado Flores, M. L. Ávalos Rodríguez, G. Andrade Espinosa, and J. V. Alcaraz Vera, 'Advances in the development of titanates for anodes in SOFC', *International Journal of Hydrogen Energy*, vol. 44, no. 24, pp. 12529–12542, May 2019, doi: 10.1016/j.ijhydene.2018.05.171.

[32] Q. Ma and F. Tietz, 'Comparison of Y and La-substituted SrTiO3 as the anode materials for SOFCs', *Solid State Ionics*, vol. 225, pp. 108–112, Oct. 2012, doi: 10.1016/j.ssi.2012.03.048.

[33] 'Thermal, electrical, and electrocatalytical properties of lanthanum-doped strontium titanate', *Solid State Ionics*, vol. 149, no. 1–2, pp. 21–28, Jul. 2002, doi: 10.1016/S0167-2738(02)00140-6.

[34] 'B-site doping of lanthanum strontium titanate for solid oxide fuel cell anodes', *Journal of Power Sources*, vol. 196, no. 17, pp. 7323–7327, Sep. 2011, doi: 10.1016/j.jpowsour.2010.11.067.

[35] C. Périllat-Merceroz, G. Gauthier, P. Roussel, M. Huvé, P. Gélin, and R.-N. Vannier, 'Synthesis and Study of a Ce-Doped La/Sr Titanate for Solid Oxide Fuel Cell Anode Operating Directly on Methane', *Chem. Mater.*, vol. 23, no. 6, pp. 1539–1550, Mar. 2011, doi: 10.1021/cm103316b.

[36] A. Ovalle, J. C. Ruiz-Morales, J. Canales-Vázquez, D. Marrero-López, and J. T. S. Irvine, 'Mn-substituted titanates as efficient anodes for direct methane SOFCs', *Solid State Ionics*, vol. 177, no. 19, pp. 1997–2003, Oct. 2006, doi: 10.1016/j.ssi.2006.06.014.

[37]   V. Vashook, L. Vasylechko, J. Zosel, W. Gruner, H. Ullmann, and U. Guth, 'Crystal structure and electrical conductivity of lanthanum–calcium chromites–titanates La1−xCaxCr1−yTiyO3−δ (x=0–1, y=0–1)', *Journal of Solid State Chemistry*, vol. 177, no. 10, pp. 3784–3794, Oct. 2004, doi: 10.1016/j.jssc.2004.07.007.

[38]   D. P. Fagg, V. V. Kharton, J. R. Frade, and A. A. L. Ferreira, 'Stability and mixed ionic–electronic conductivity of (Sr,La)(Ti,Fe)O3−δ perovskites', *Solid State Ionics*, vol. 156, no. 1, pp. 45–57, Jan. 2003, doi: 10.1016/S0167-2738(02)00257-6.

[39]   K. B. Yoo and G. M. Choi, 'Performance of La-doped strontium titanate (LST) anode on LaGaO3-based SOFC', *Solid State Ionics*, vol. 180, no. 11, pp. 867–871, Jun. 2009, doi: 10.1016/j.ssi.2009.02.013.

[40]   C. D. Savaniu and J. T. S. Irvine, 'La-doped SrTiO3 as anode material for IT-SOFC', *Solid State Ionics*, vol. 192, no. 1, pp. 491–493, Jun. 2011, doi: 10.1016/j.ssi.2010.02.010.

[41]   null Park, null Vohs, and null Gorte, 'Direct oxidation of hydrocarbons in a solid-oxide fuel cell', *Nature*, vol. 404, no. 6775, pp. 265–267, Mar. 2000, doi: 10.1038/35005040.

[42]   O. Costa-Nunes, R. J. Gorte, and J. M. Vohs, 'Comparison of the performance of Cu–CeO2–YSZ and Ni–YSZ composite SOFC anodes with H2, CO, and syngas', *Journal of Power Sources*, vol. 141, no. 2, pp. 241–249, Mar. 2005, doi: 10.1016/j.jpowsour.2004.09.022.

[43]   H. He, R. J. Gorte, and J. M. Vohs, 'Highly Sulfur Tolerant Cu-Ceria Anodes for SOFCs', *Electrochem. Solid-State Lett.*, vol. 8, no. 6, pp. A279–A280, Jan. 2005, doi: 10.1149/1.1896469.

[44]   J. B. Goodenough and Y.-H. Huang, 'Alternative anode materials for solid oxide fuel cells', *Journal of Power Sources*, vol. 173, no. 1, pp. 1–10, Nov. 2007, doi: 10.1016/j.jpowsour.2007.08.011.

[45]   Y.-H. Huang, R. I. Dass, J. C. Denyszyn, and J. B. Goodenough, 'Synthesis and Characterization of Sr2MgMoO6 − δ An Anode Material for the Solid Oxide Fuel Cell', *J. Electrochem. Soc.*, vol. 153, no. 7, pp. A1266–A1272, Jan. 2006, doi: 10.1149/1.2195882.

[46]   O. A. Marina, C. Bagger, S. Primdahl, and M. Mogensen, 'A solid oxide fuel cell with a gadolinia-doped ceria anode: preparation and performance', *Solid State Ionics*, vol. 123, no. 1, pp. 199–208, Aug. 1999, doi: 10.1016/S0167-2738(99)00111-3.

[47]   'Fuel reforming and electrical performance studies in intermediate temperature ceria–gadolinia-based SOFCs', *Journal of Power Sources*, vol. 86, no. 1–2, pp. 411–416, Mar. 2000, doi: 10.1016/S0378-7753(99)00493-0.

[48]   D. H. Jo *et al.*, 'Optimization of physical parameters of solid oxide fuel cell electrode using electrochemical model', *Korean J. Chem. Eng.*, vol. 28, no. 9, p. 1844, Aug. 2011, doi: 10.1007/s11814-011-0026-4.

[49]   M. Ni, M. K. H. Leung, and D. Y. C. Leung, 'Parametric study of solid oxide fuel cell performance', *Energy Conversion and Management*, vol. 48, no. 5, pp. 1525–1535, May 2007, doi: 10.1016/j.enconman.2006.11.016.

[50]   R. K. Nishihora, P. L. Rachadel, M. G. N. Quadri, and D. Hotza, 'Manufacturing porous ceramic materials by tape casting—A review', *Journal of the European Ceramic Society*, vol. 38, no. 4, pp. 988–1001, Apr. 2018, doi: 10.1016/j.jeurceramsoc.2017.11.047.

[51]   'Freeze-casting for the fabrication of solid oxide fuel cells: A review', *Materialia*, vol. 1, pp. 198–210, Sep. 2018, doi: 10.1016/j.mtla.2018.07.005.

[52]   Y. Chen, Q. Liu, Z. Yang, F. Chen, and M. Han, 'High performance low temperature solid oxide fuel cells with novel electrode architecture', *RSC Adv.*, vol. 2, no. 32, pp. 12118–12121, Nov. 2012, doi: 10.1039/C2RA21921B.

[53]   R. Craciun, S. Park, R. J. Gorte, J. M. Vohs, C. Wang, and W. L. Worrell, 'A Novel Method for Preparing Anode Cermets for Solid Oxide Fuel Cells', *J. Electrochem. Soc.*, vol. 146, no. 11, pp. 4019–4022, Jan. 1999, doi: 10.1149/1.1392586.

[54]   E. Dogdibegovic, R. Wang, G. Y. Lau, and M. C. Tucker, 'High performance metal-supported solid oxide fuel cells with infiltrated electrodes', *Journal of Power Sources*, vol. 410–411, pp. 91–98, Jan. 2019, doi: 10.1016/j.jpowsour.2018.11.004.

[55]   S. Futamura *et al.*, 'SOFC anodes impregnated with noble metal catalyst nanoparticles for high fuel utilization', *International Journal of Hydrogen Energy*, vol. 44, no. 16, pp. 8502–8518, Mar. 2019, doi: 10.1016/j.ijhydene.2019.01.223.

[56]   Z. Han, Z. Yang, and M. Han, 'Optimization of Ni-YSZ anodes for tubular SOFC by a novel and efficient phase inversion-impregnation approach', *Journal of Alloys and Compounds*, vol. 750, pp. 130–138, Jun. 2018, doi: 10.1016/j.jallcom.2018.02.135.

[57]   J. Nielsen, Å. H. Persson, B. R. Sudireddy, J. T. S. Irvine, and K. Thydén, 'Infiltrated La0.4Sr0.4Fe0.03Ni0.03Ti0.94O3 based anodes for all ceramic and metal supported solid oxide fuel cells', *Journal of Power Sources*, vol. 372, pp. 99–106, Dec. 2017, doi: 10.1016/j.jpowsour.2017.10.066.

[58]   T. Zhu, H. E. Troiani, L. V. Mogni, M. Han, and S. A. Barnett, 'Ni-Substituted Sr(Ti,Fe)O3 SOFC Anodes: Achieving High Performance via Metal Alloy Nanoparticle Exsolution', *Joule*, vol. 2, no. 3, pp. 478–496, Mar. 2018, doi: 10.1016/j.joule.2018.02.006.

[59]   S. P. Jiang, 'Development of lanthanum strontium manganite perovskite cathode materials of solid oxide fuel cells: a review', *J Mater Sci*, vol. 43, no. 21, pp. 6799–6833, Nov. 2008, doi: 10.1007/s10853-008-2966-6.

[60]   P. Kaur and K. Singh, 'Review of perovskite-structure related cathode materials for solid oxide fuel cells', *Ceramics International*, vol. 46, no. 5, pp. 5521–5535, Apr. 2020, doi: 10.1016/j.ceramint.2019.11.066.

[61]   J. Hee Kim, Y. Park, and H. Kim, 'A bi-layer cathode based on lanthanum based cobalt- and iron-containing perovskite and gadolinium doped ceria for thin yttria stabilized zirconia electrolyte solid oxide fuel cells', *Ceramics International*, vol. 38, no. 8, pp. 6303–6310, Dec. 2012, doi: 10.1016/j.ceramint.2012.04.086.

[62]   T. Tsai, 'Effect of LSM-YSZ cathode on thin-electrolyte solid oxide fuel cell performance', *Solid State Ionics*, vol. 93, no. 3–4, pp. 207–217, Jan. 1997, doi: 10.1016/S0167-2738(96)00524-3.

[63]   Y.-L. Huang, A. M. Hussain, and E. D. Wachsman, 'Nanoscale cathode modification for high performance and stable low-temperature solid oxide fuel cells (SOFCs)', *Nano Energy*, vol. 49, pp. 186–192, Jul. 2018, doi: 10.1016/j.nanoen.2018.04.028.

[64]   'Microstructure optimization of porous mixed ionic and electronic conducting cathode for solid oxide fuel cells', *Journal of Power Sources*, vol. 478, p. 228771, Dec. 2020, doi: 10.1016/j.jpowsour.2020.228771.

[65]   S. P. Jiang, 'A review of wet impregnation—An alternative method for the fabrication of high performance and nano-structured electrodes of solid oxide fuel cells', *Materials Science and Engineering: A*, vol. 418, no. 1–2, pp. 199–210, Feb. 2006, doi: 10.1016/j.msea.2005.11.052.

[66]   S. P. Jiang, Y. J. Leng, S. H. Chan, and K. A. Khor, 'Development of (La , Sr) MnO3-Based Cathodes for Intermediate Temperature Solid Oxide Fuel Cells', *Electrochem. Solid-State Lett.*, vol. 6, no. 4, p. A67, Feb. 2003, doi: 10.1149/1.1558351.

[67]   M. Sahibzada, 'Pd-promoted La0.6Sr0.4Co0.2Fe0.8O3 cathodes', *Solid State Ionics*, vol. 113–115, no. 1–2, pp. 285–290, Dec. 1998, doi: 10.1016/S0167-2738(98)00294-X.

[68]   K. Yamahara, C. Jacobson, S. Visco, X. Zhang, and L. Dejonghe, 'Thin film SOFCs with cobalt-infiltrated cathodes', *Solid State Ionics*, vol. 176, no. 3–4, pp. 275–279, Jan. 2005, doi: 10.1016/j.ssi.2004.08.017.

[69]   H. Han *et al.*, 'Lattice strain-enhanced exsolution of nanoparticles in thin films', *Nature Communications*, vol. 10, no. 1, pp. 1–8, Apr. 2019, doi: 10.1038/s41467-019-09395-4.

[70]   A. S. Thorel *et al.*, 'Proof of Concept for the Dual Membrane Cell I. Fabrication and Electrochemical Testing of First Prototypes', *J. Electrochem. Soc.*, vol. 160, no. 4, pp. F360–F366, Jan. 2013, doi: 10.1149/2.051304jes.

[71]   H. F. Helander and L. Fändriks, 'Surface area of the digestive tract - revisited', *Scand. J. Gastroenterol.*, vol. 49, no. 6, pp. 681–689, Jun. 2014, doi: 10.3109/00365521.2014.898326.

[72]   A. G. Yazıcıoğlu, S. Aradağ, E. Aylı, G. Gülben, and S. Kakaç, '4.2 Heat Exchangers', in *Comprehensive Energy Systems*, I. Dincer, Ed. Oxford: Elsevier, 2018, pp. 40–69.

[73]   L. Lloyd, *Handbook of industrial catalysts*. New York: Springer, 2007.

[74]   M.-H. Ryou, Y. M. Lee, Y. Lee, M. Winter, and P. Bieker, 'Mechanical Surface Modification of Lithium Metal: Towards Improved Li Metal Anode Performance by Directed Li Plating', *Advanced Functional Materials*, vol. 25, no. 6, pp. 834–841, 2015, doi: 10.1002/adfm.201402953.

[75]   L. Chang and Y. Hang Hu, '2.21 Supercapacitors', in *Comprehensive Energy Systems*, I. Dincer, Ed. Oxford: Elsevier, 2018, pp. 663–695.

[76]   R. Ihringer, 'Electrolytes minces sur supports anode dans les piles à combustible SOFC', *Infoscience*, 2001. https://infoscience.epfl.ch/record/32783.

[77]   A. Konno *et al.*, 'Mesoscale-structure control at anode/electrolyte interface in solid oxide fuel cell', *Journal of Power Sources*, vol. 196, no. 1, pp. 98–109, Jan. 2011, doi: 10.1016/j.jpowsour.2010.07.025.

[78]   H. Iwai *et al.*, 'Power generation enhancement of solid oxide fuel cell by cathode–electrolyte interface modification in mesoscale assisted by level set-based optimization calculation', *Journal of Power Sources*, vol. 196, no. 7, pp. 3485–3495, Apr. 2011, doi: 10.1016/j.jpowsour.2010.12.024.

[79]   J. A. Cebollero, R. Lahoz, M. A. Laguna-Bercero, and A. Larrea, 'Tailoring the electrode-electrolyte interface of Solid Oxide Fuel Cells (SOFC) by laser micro-patterning to improve their electrochemical performance', *Journal of Power Sources*, vol. 360, pp. 336–344, Aug. 2017, doi: 10.1016/j.jpowsour.2017.05.106.

[80]   M. Geagea, 'Nouvelles architectures de surfaces d'échanges de piles à combustible de type SOFC pour l'amélioration de l'efficacité électrochimique', Apr. 2017, Accessed: Aug. 23, 2019. [Online]. Available: https://pastel.archives-ouvertes.fr/tel-01901236.

[81]   F. Delloro and M. Viviani, 'Simulation study about the geometry of electrode-electrolyte contact in a SOFC', *Journal of Electroceramics*, vol. 29, no. 3, pp. 216–224, Nov. 2012, doi: 10.1007/s10832-012-9766-8.

[82]   R. E. Mistler and E. R. Twiname, *Tape casting: theory and practice*. Westerville, OH: American Ceramic Society, 2000.

[83]   N. H. Menzler, J. Malzbender, P. Schoderböck, R. Kauert, and H. P. Buchkremer, 'Sequential Tape Casting of Anode-Supported Solid Oxide Fuel Cells', *Fuel Cells*, vol. 14, no. 1, pp. 96–106, 2014, doi: 10.1002/fuce.201300153.

CHAPTER II

Fabrication of planar and architectured SOFCs
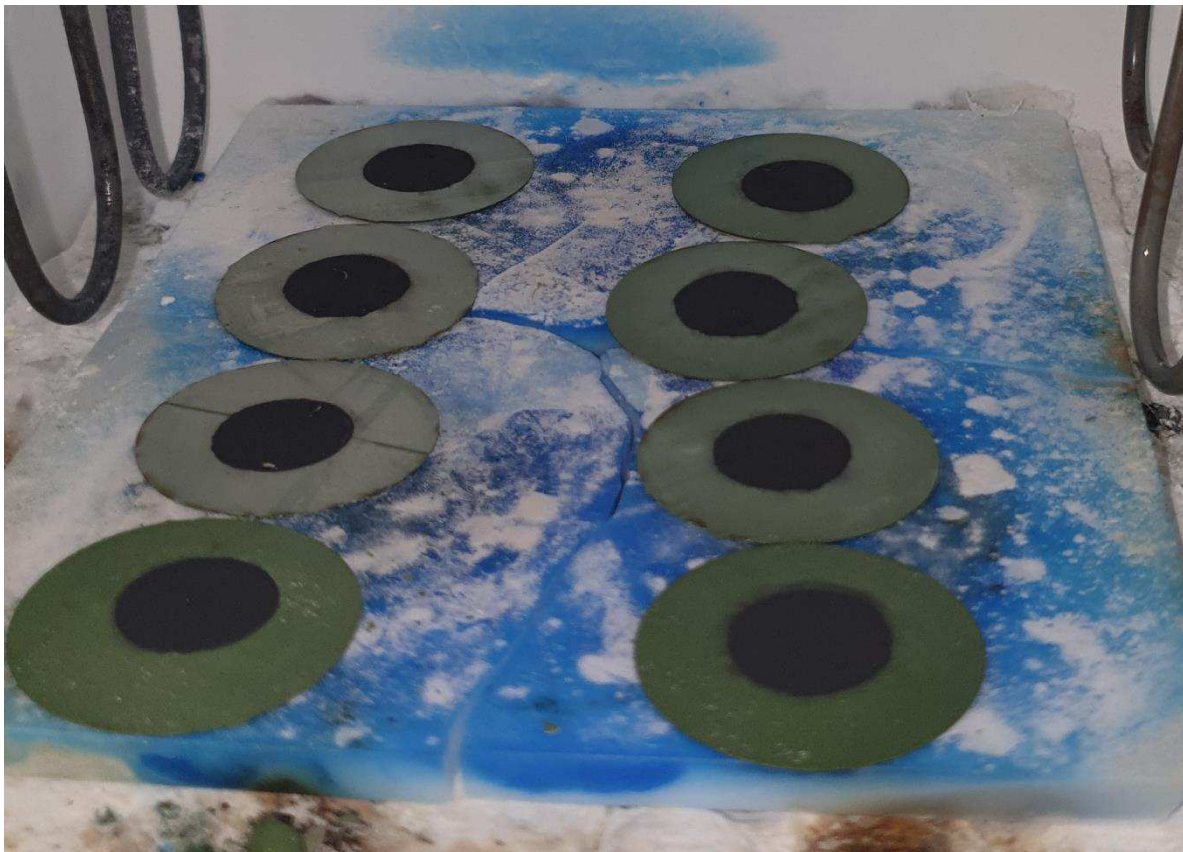
Chapter II Abstract

One of the main objectives of this study is the setting up of a protocol for performant cell fabrication, being as simple, as reliable, and as cost-effective as possible. For this reason, a minimal number of fabrication stages is aimed. In this way, the tape casting method is chosen to elaborate the raw cell components, which can be shaped as needed, assembled, and thermally treated to obtain the final object (Figure II – abstract – 1 – A). An architecturation procedure is carried out using an innovative soft template application method which consists of slightly modifying the tape casting technique (figure II – abstract – 2 A and B). Thus, the architecturation of the tapes and consequently the cell components does not require additional fabrication steps and is applicable on an industrial scale. By using this fabrication protocol, two types of fuel cells are produced differentiated by the compositions and microstructures of the electrodes as well as the presence of a barrier layer. The cells and their components composition are illustrated in Figure II – abstract – 1 B. The type I cells present an architectured anode electrolyte interface whereas the Type II cells present an architectured cathode/electrolyte interface. A rapid verification procedure is conducted on which cells allows to validate them for further structural characterization and electrochemical testing

Chapitre II Résumé

L'un des principaux objectifs de cette étude est la mise en place d'un protocole de fabrication de cellules performantes aussi simple, aussi fiable et aussi rentable que possible. Pour cette raison, un nombre minimal d'étapes de fabrication est visé. Ainsi, la méthode de coulage en bande est choisie pour élaborer les composants cellulaires crus, qui peuvent être mis en forme selon les besoins, assemblés et traités thermiquement pour obtenir l'objet final (Figure II - abstract - 1 - A). Une procédure d'architecture est réalisée en utilisant une méthode innovante d'application de templates souples qui consiste à modifier légèrement la technique de coulage en bande (figure II - résumé - 2 A et B). Ainsi, l'architecturation des bandes et, par conséquent, des composants des cellules, ne nécessite pas d'étapes de fabrication supplémentaires et est applicable à l'échelle industrielle. En utilisant ce protocole de fabrication, deux types de piles à combustible sont produits, différenciés par les compositions et les microstructures des électrodes ainsi que par la

présence d'une couche barrière. Les cellules ainsi que la composition de leurs constituants sont illustrées dans la Figure II – abstract – 2 B. Les cellules de type I présentent une interface anode/électrolyte architecturée, tandis que les cellules de type II présentent une interface cathode/électrolyte architecturée. Une procédure de vérification rapide permet de valider les cellules pour une caractérisation structurelle et des tests électrochimiques supplémentaires.

A)
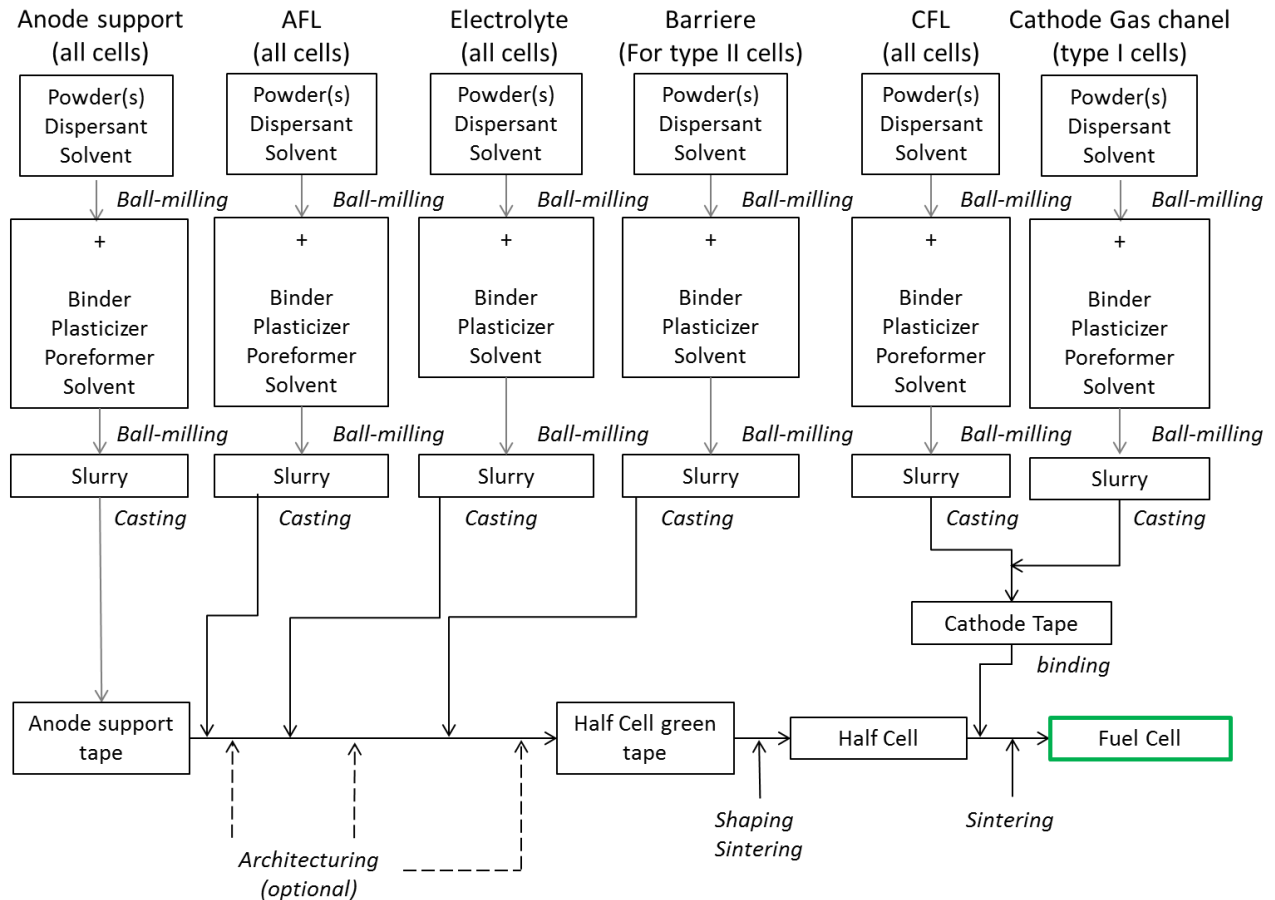
B)
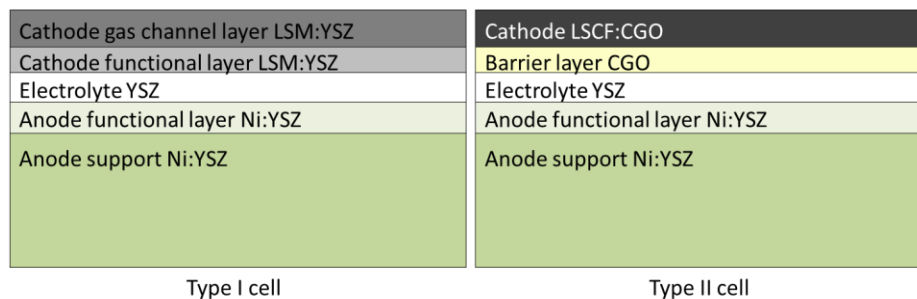
Figure II - abstract - 1 Cell fabrication: A) Fabrication protocol overview; B) Cell types overview
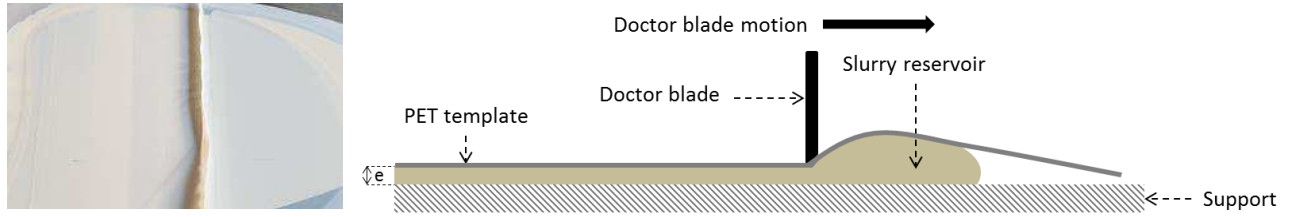
Figure II - abstract - 2 Soft template architecturation method. A) green tape architecturing using a PET1500 fabric; B) Principle schematic

CHAPTER II Fabrication of plane and architectured SOFCs

Contents

List of figures

I.   Introduction

One of the main objectives of this study is the setting up of a protocol for cell fabrication, being as simple, as reliable and as cost-effective as possible. An anode-supported flat cell configuration is chosen with or without architectured electrode/electrolyte interfaces. For the sake of clarity, the term "flat cell" will be used as opposed to tubular cell, whereas to refer to the state of the interface the terms planar or architectured cells will be employed.

As mentioned in the previous chapter, a fuel cell is a complex object made of different functional materials, with carefully controlled microstructure, that has to be intimately connected although their thermo-mechanical behavior and chemical properties are different. The fabrication protocol, which becomes more complex since architectured interfaces are integrated, must take into account these requirements for an optimized cell operation, without putting aside the economic and logistic outlooks. For this reason, a minimal number of fabrication stages is aimed. In this way, the tape casting method is chosen to elaborate the raw cell components, which can be shaped as needed, assembled, and thermally treated to obtain the final object.

In this chapter, the details of the fabrication protocol are reviewed followed by a validation study. Two types of fuel cells are fabricated differentiated by the compositions and microstructures of the electrodes as well as the presence of a barrier layer.

- Type I cells: These cells are formed by an anode support composed of an Ni:8YSZ cermet with a 44:56 volume ratio and with elevated porosity (> 35%), and an anode functional layer has intermediate porosity of approximately 20 – 25 %. The electrolyte is composed of dense 8YSZ film. The cathode functional layer is composed of LSM:8YSZ composite with a 50:50 volume ratio and intermediate porosity (~20 – 25 %), whereas the cathode gas channel layer has a higher porosity of approximately 35 – 40 %.
- Type II cells have the same anode and electrolyte composition and microstructure as type I cells. Additionally, a dense barrier layer is cast over the electrolyte composed of CGO10. The cathode material, in this case, is an LSCF:CGO composite and the porosity is approximately 20-25 %.

The type I cells allow visualizing the impact of the architecture on cells with graduated electrodes and with adequate intrinsic performances. Type II cells are fabricated to demonstrate the feasibility and pertinence of the architecturing on commercial cells.

Figure II – 1A summarizes each step of the fabrication protocol and figure II – 1B presents schematics of the three types of cells. The particularity of this protocol is the establishment of each layer, with adequate thickness and microstructure, by tape casting. Usually, screen printing is involved, which adds to the protocol complexity with additional compounds, experimental steps, and devices by the need for different compounds and devices as well as preparation time. In our protocol, the half cells are prepared by sequential tape casting and co-sintering. The cathode tape is prepared and shaped in parallel and it is bound to the sintered half-cell by a simple adhesion technique using a solvent, followed by a firing and sintering procedure.

The establishment of the protocol follows an iterative methodology, adjusting experimental parameters such as material proportions, dispersion process, or layer thickness, based on microstructural analysis and electrochemical measurements. To control the cell integrity, preliminary optical microscopy observations of the electrode and electrolyte open surfaces, as well as SEM observations of transversal fracture controlling the layer cohesion, are carried out. The final step to validate the protocol is a cell polarization measurement in operating conditions.

The detailed structural study is implemented in the next chapter (Chapter III – SOFC components characterization), in which microstructure and architecturing are characterized.

A)
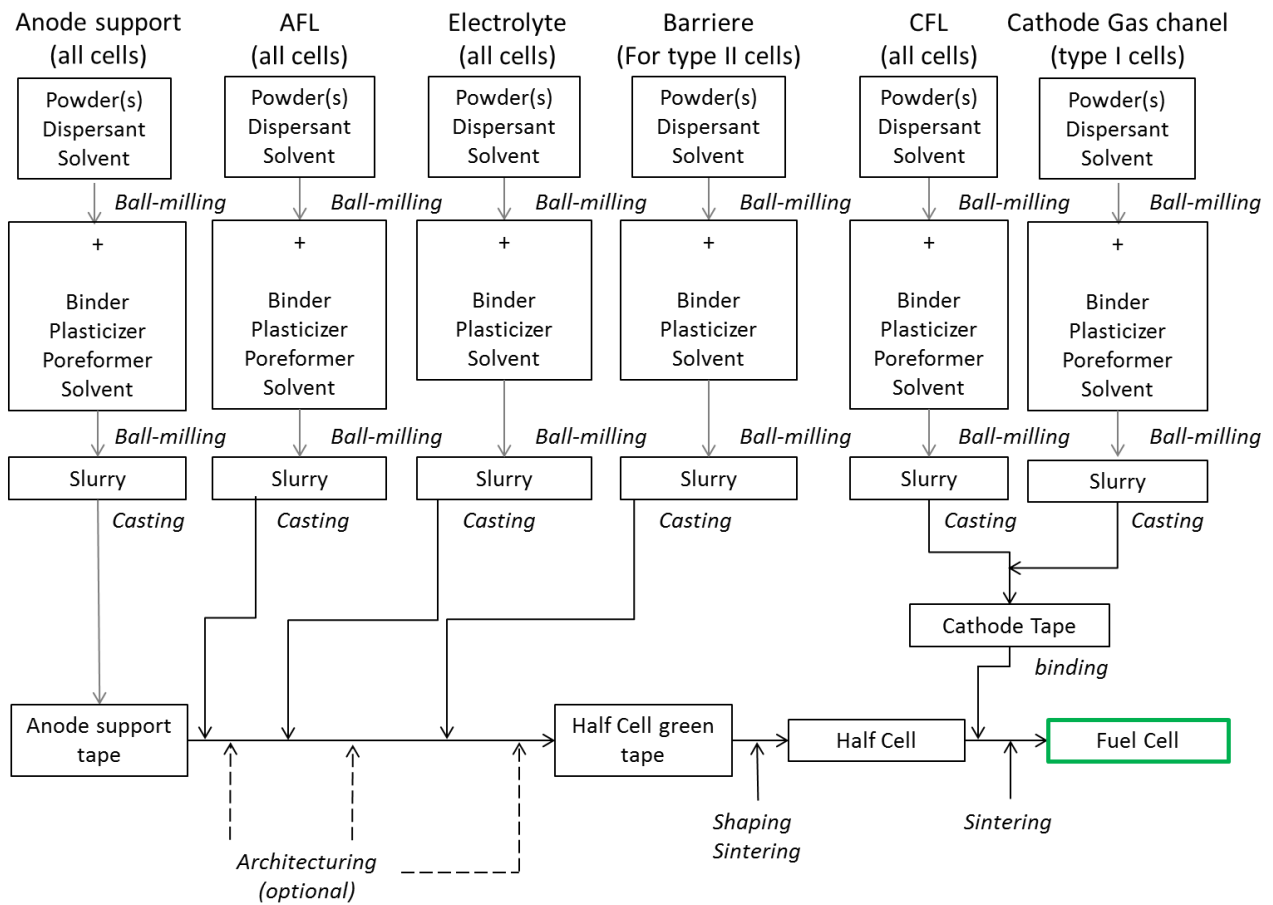
B)
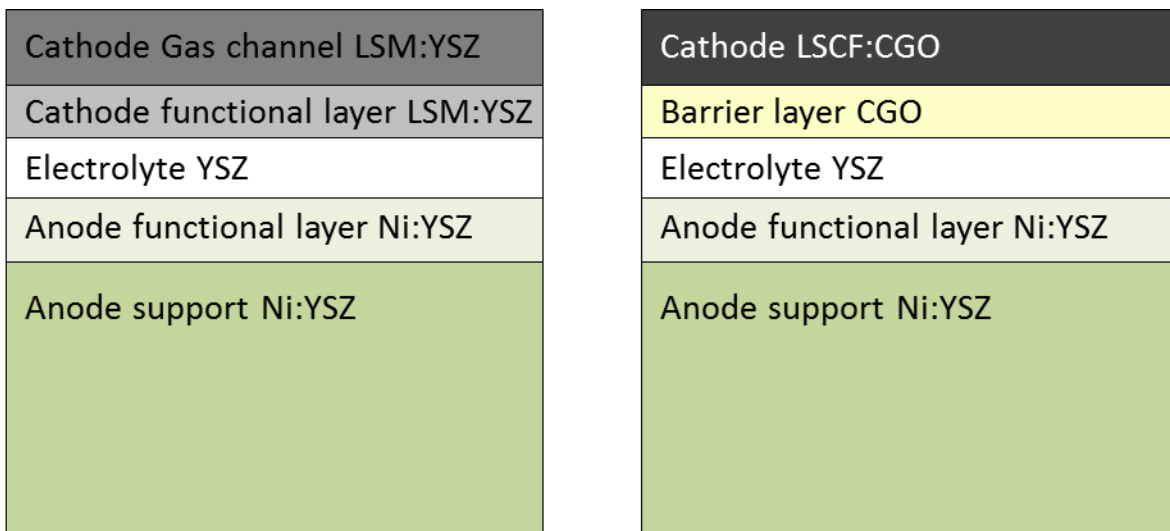
Type I cell   Type II cell

Figure II - 1 Cell fabrication: A) Fabrication protocol overview; B) Cell types overview

II.   Raw materials

Slurry composition is essential for the homogeneity and integrity of the green and sintered ceramics. It is usually composed of the ceramic powder(s) (functional materials), solvent, organic and inorganic additives which assure the powder dispersion, confer the mechanical aspect of the green tape (plasticity, strength), and influence the microstructure (porosity distribution, pore and grain size). In this subchapter, the different elements of the slurry will be described and characterized.

II.A.   Powders

The functional materials are the only ingredients of the slurry which remain after the thermal processing. Usually, the powders are chosen in order to satisfy the purpose of the final object, and the rest of the ingredients of the slurry are adapted to them. For this reason, a preliminary powder characterization is essential. Parameters such as particle size distribution and shape as well as powder density are used to determine the quantity and nature of the additives to achieve a homogeneous suspension.

In tape casting, the particle morphology and size are used to fix the quantity and nature of the binder. The green tape is essentially a homogeneous particle dispersion embedded in a binder matrix. Thus, a granulometry study and optic or electronic microscopy should be conducted preceding the slurry formulation. The particle size distribution has an important influence on the bulk microstructure due to the eventual sedimentation as well as its impact on the powder dispersion and sinterability.

Usually, a green tape bulk as compact as possible is aimed during casting to optimize the sintering process. Thus particle packing models have been developed such as Shanefield's work [1], to aid in this objective which can be particularly useful for electrolyte fabrication. The Shanefield's model demonstrates that a large particle size distribution with spherical shapes is favorable towards high bulk density. However, a fine and narrowly distributed grain size powder presents a high free surface area and consequently surface energy, proportional to the driving force of the sintering process. For the fabrication of SOFC electrodes, complementary parameters should be taken into account, such as percolation, tortuosity, and porosity, impacted by the shape and the size of the particles. Furthermore, powder storage is often followed by particle

agglomeration and humidification. Hence, control over the dispersion and milling procedure during the slurry preparation is crucial.

The powders are characterized by laser granulometry using a MASTERSIZER 2000 (Malvern Instruments) and the SEM observations are carried out with a S-FEG FEI Nova NanoSEM 450.

The laser diffraction granulometry measures the laser scattering by a powder dispersed in an adequate solvent[1] allowing to obtain the grain size distribution. The suspension is homogenized by mechanical stirring and ultrasound to break soft agglomerates. The technique provides a statistical overview of the grain size distribution (in terms of light-diffusing objects) in the powder which is complementary with a finer microscopic observation (SEM). The latter is used to study singular particle size and morphology. The combination of the two techniques provides global information needed to optimize the slurry preparation.

II.A.1. NiO

Nickel oxide, as a precursor for the metallic nickel, is mixed with YSZ in the cermet. Once reduced in presence of the fuel, Ni plays the role of an electronic conductor as well as a catalyst for the fuel oxidation. Thus, its dispersion, morphology, and volume proportion will strongly affect the fuel cell performances.

The volume proportion with respect to the ones occupied by YSZ and the pores as well as its homogenous dispersion greatly influences the electron conductivity of the cermet. A percolation threshold exists naturally below which the continuity of the electron-conducting phase in the solid is insufficient to ensure adequate electron transportation towards the external circuit. For a spherical approximation of the morphology of the grains, this threshold is close to 33% vol and can be lower in the case of other morphology. Here the Ni volume proportion is adjusted to maximize the electron conductivity of the anode (support and anode functional layer), without hindering the TPB concentration and TEC compatibility between the electrode and the electrolyte as seen in Chapter 1. The cermet electron conductivity as a function of the Ni volume proportion is described by an S-shaped curve (figure II-2 [2]). Usually, a volume proportion of 40% of the solid phase represents a good compromise. It is slightly above the percolation threshold which

---

[1] The term of solvent is used due to its dissolving properties toward the additives in slurry preparation. Its role in the laser granulomere is to suspend the particles and to vehicle them through the measurement cell of the apparatus

allows keeping a high electric conductivity, without hindering the thermomechanical compatibility with the electrolyte.

In our case, we choose a Ni volume proportion of 44% of the solid phase, which corresponds to an initial mass proportion of NiO:YSZ of 60:40 in the slurry.
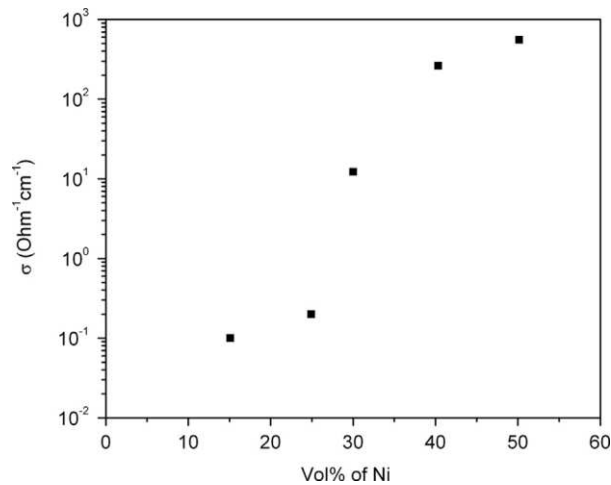

Figure II-2 Ni:YSZ cermet electron conductivity as a function of Ni volume proportion at 1000°C [2]

In this study, we use a commercial green nickel oxide (NiO), grade F powder provided by Novamet. As mentioned previously, finer powders provide better reactivity due to their higher surface energy and may enhance the active TPB concentration. For this reason, powder engineering is essential for the fabrication and adequate milling process and suitable dispersant for the slurry formulation needs to be chosen. In figure II-3, the effect of the milling process on the grain size distribution of NiO powder is presented.
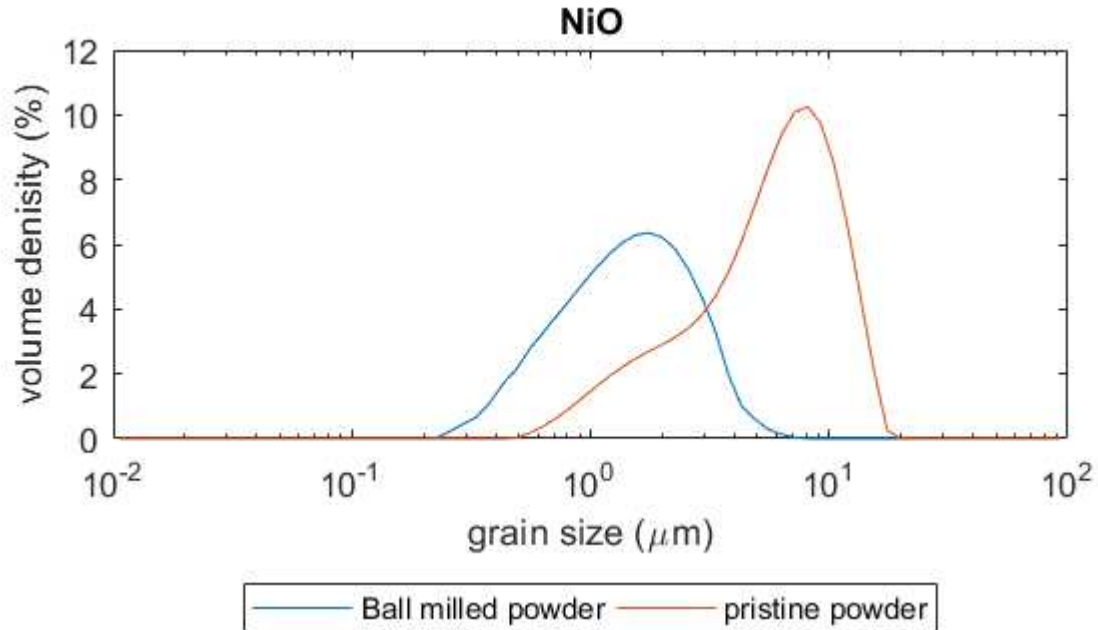
Figure II- 3 Laser granulometry in ethanol of NiO provided by Novamet. Visualization of the effect of the ball-milling procedure on the grain size distribution

The NiO pristine powder presents a large grain size distribution, showing an order of magnitude difference between the smaller and the larger particle size. The ball milling may have two distinct effects on the powder engineering which are elementary particle grinding or aggregates and agglomerates breaking. Figure II-3 indicates that the milling influences the grain size distribution by making it more homogeneous and reducing substantially the mean grain size.

To better interpret the granulometry measurement of the powders, SEM observations are performed and summarized in figure II-4.
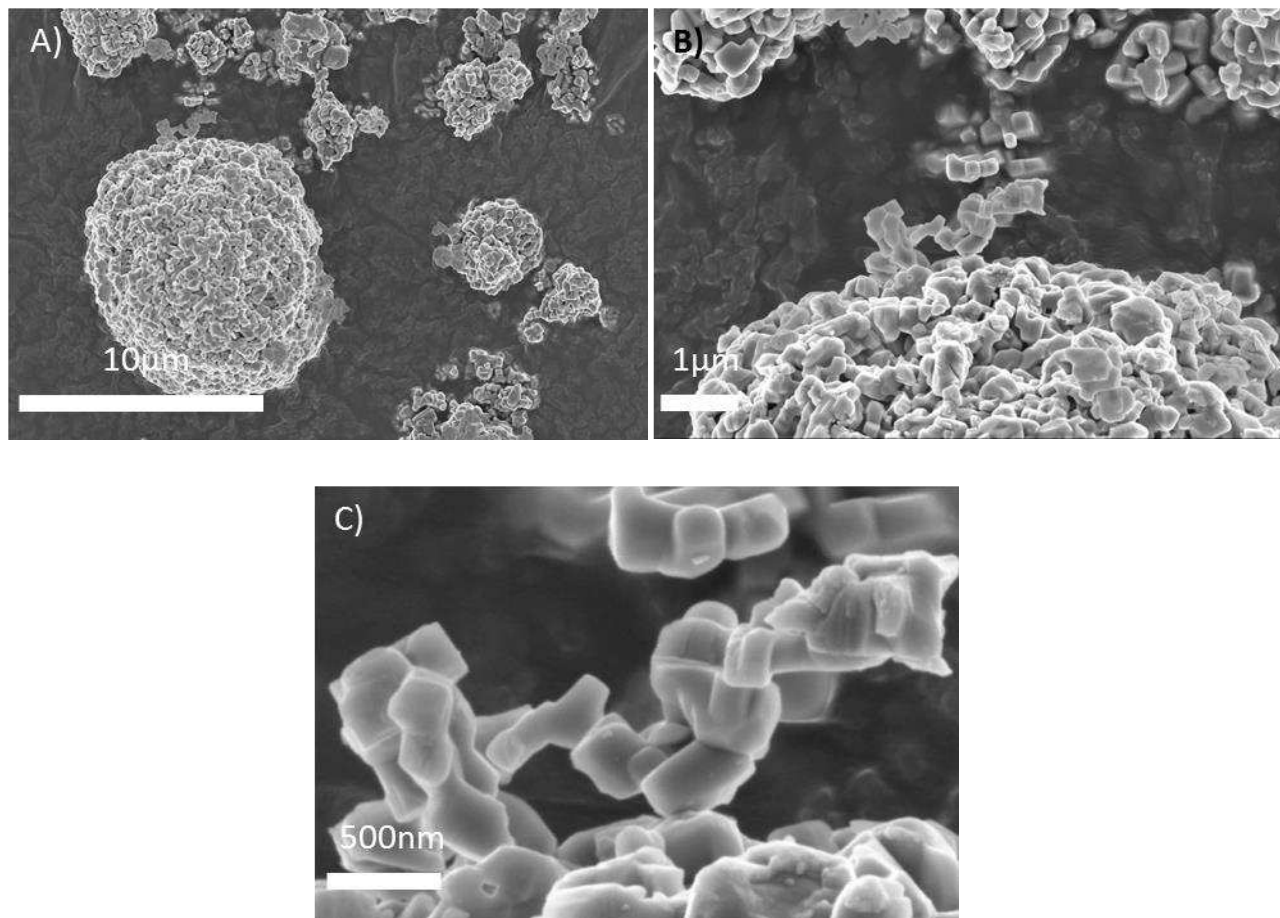
Figure II- 4 SE micrographs with an increasing magnification of NiO powder provided by Novamet

The SEM observations are consistent with the granulometry results allowing to conclude that the NiO powder is composed of agglomerates (1-10 μm) formed by fine particles (100-500 nm). Thus a ball milling procedure in an ethanol-based solvent is necessary to break the aggregates and the agglomerates and disperse the particles.

II.A.2. YSZ

YSZ powder is used for the composition of the anode cermet as well as for the electrolyte due to its physico-chemical properties, reviewed in the previous chapter. Commercial fully stabilized zirconia with 8 %mol of Y_2O_3 provided from TOSOH Japan is used in both cases. The manufacturer provides powder characteristics data (morphology parameters and physical properties) which are listed in Table II – 1.

Table II - 1 YSZ manufacturer data [3]

POWDER CHARACTERISTICS	TZ-8Y	TZ-8YS	TZ-10YS
Y_2O_3 (mol%)	8	8	10
Specific Surface Area (m^2/g)	16±3	7±2	6±2
Binder (Approx. wt.%)	-		
Appearance	Granule	Granule	Granule

TYPICAL PROPERTIES OF SINTERED BODY	TZ-8Y	TZ-8YS	TZ-10YS
Density (g/cm^3)	5.90	5.90	5.80
Bending Strength R.T. (MPa)	300	300	200
Hardness (Hv 10)	1250	1250	1250
Electric Resistance ($\Omega \cdot$cm) at 800ºC	19.8	20.3	27.3
Electric Conductivity log σ(S/cm) at 800ºC	-1.30	-1.31	-1.44

Further characterization of the powder is carried out via granulometry and scanning electron microscopy to take into account storage and other eventual alteration.

Granulometry measurements of the "as delivered" powder and ball milled powder for 12h at 300 rpm in ethanol is carried out and the results are shown in figure II-5.
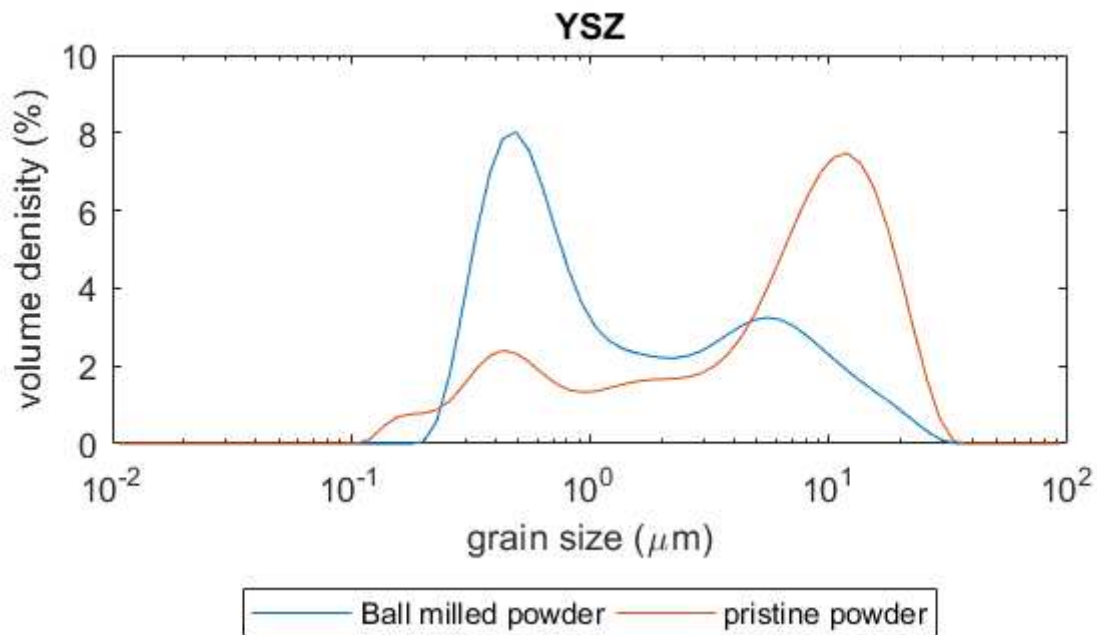

Figure II - 5 Laser granulometry of YSZ powder dispersed in 96% Ethanol. Visualization of the effect of the ball-milling procedure on the grain size distribution

The granulometry is completed with an SEM observation of the powder (figure II-6) aiding the interpretation of the results.
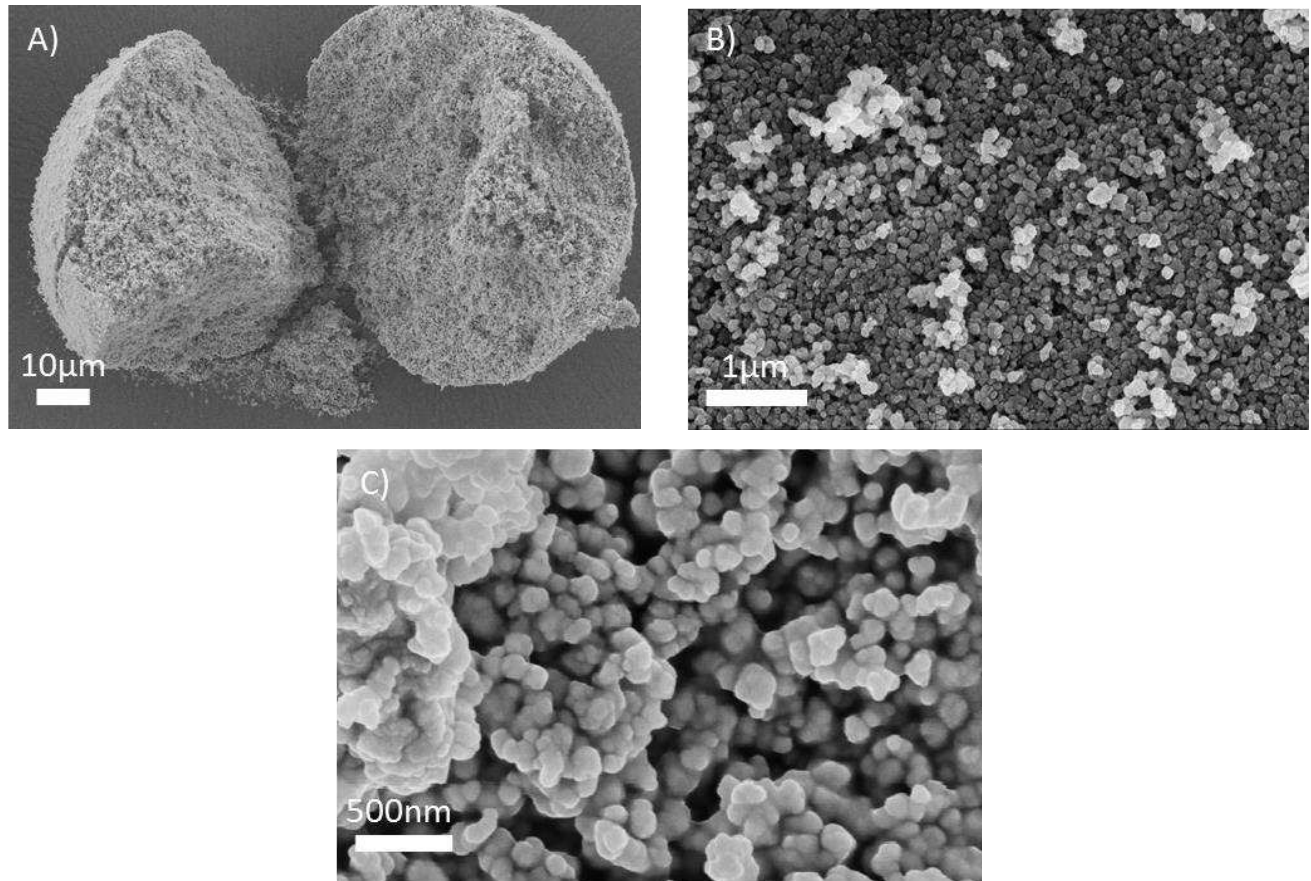

Figure II - 6 SEM micrographs with an increasing magnification of 8YSZ powder provided by TOSOH

The YSZ powder presents a large grain size distribution. The SEM observations allow us to better understand the microstructure of the powder, revealing that it is composed of fine particles (200 nm) softly agglomerated (30 µm). As it is for the Nickel oxide, the agglomerates need to be broken to facilitate the particle dispersion and promote the slurry and ceramics homogeneity. For both the anode cermet as well as the YSZ electrolyte layer, an energetic ball milling procedure is essential. On one hand, it would promote isotropic thermomechanical behavior and better electrochemical performances due to the higher TPB concentration of the cermet by avoiding particles segregation. On the other hand, it is mandatory to break down the agglomerates to fabricate electrolyte layers with an acceptable thickness (< 10 µm).

II.A.3. CGO

CGO powder is used for both the type II cell's composite cathode and the barrier layer. Its high ion conductivity [4] makes it a good candidate for electrolyte material but its instability in reducing atmosphere at high temperature (> 600°C) is unsuitable for direct application for high-temperature SOFC. Thus, it is used here as a separator between YSZ and LSCF (cathode) to promote a longer cell lifespan by limiting the reactivity between LSCF and YSZ (cf. chapter I). It also constitutes a component of the type II cell cathode composite where it enhances the ion conductivity and increase the concentration of the cathode TPBs.

In this work, we use a commercial 10% gadolinium-substituted cerium oxide powder provided by Treibacher Industries. The laser granulometry of the powder can be found in figure II-7 and the SEM observations are shown in figure II-8.
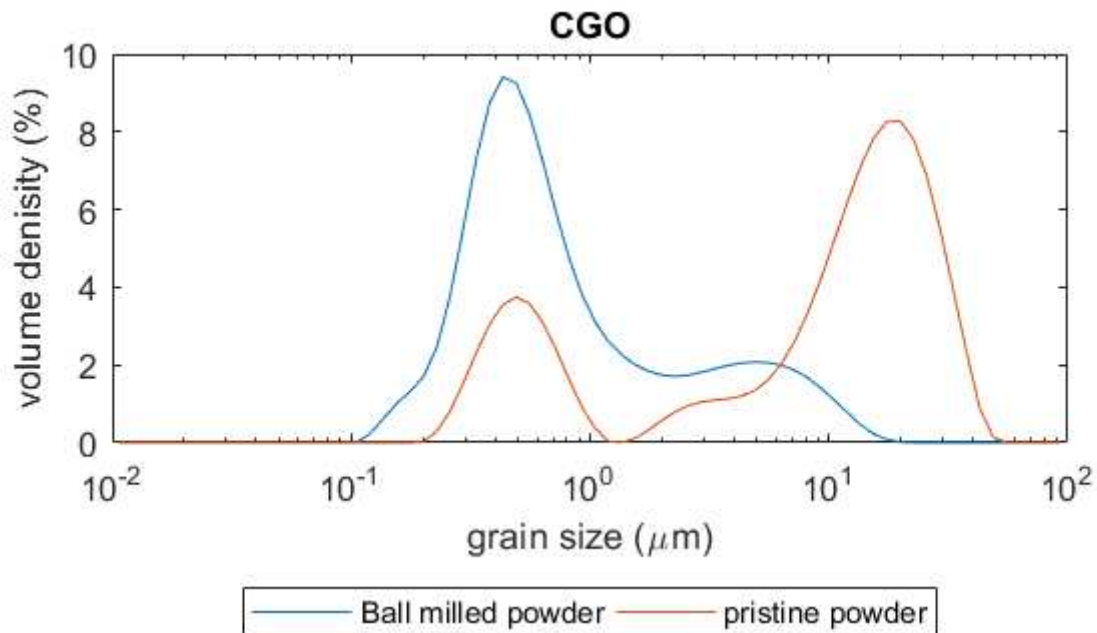

Figure II - 7 Laser granulometry of CGO10 powder provided by Treibacher. Visualization of the effect of the ball-milling procedure on the grain size distribution
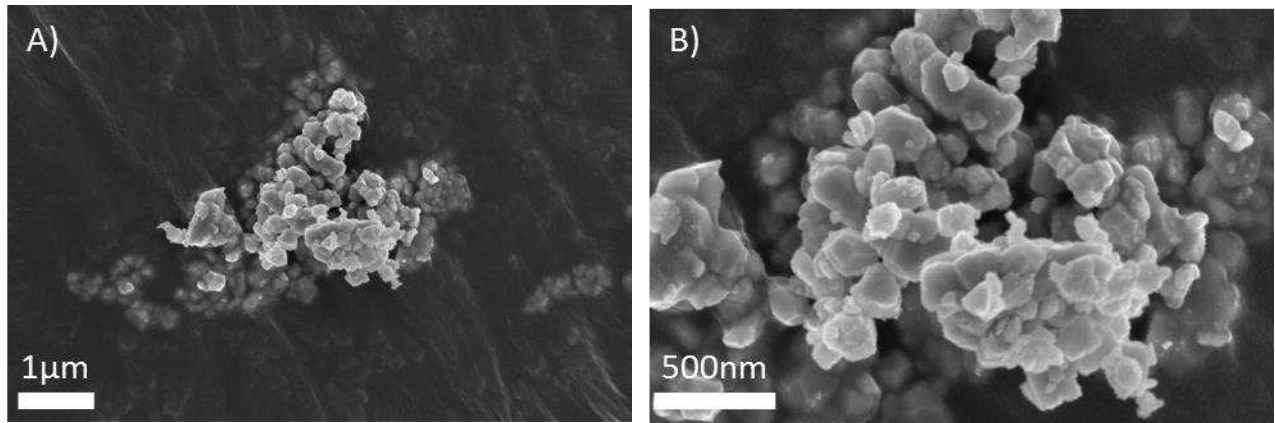
Figure II - 8 SEM micrographs with an increasing magnification of CGO10 powder provided by Treibacher Industries

The CGO powder presents the same granulometric profile as the NiO powder i.e. a bimodal grain size distribution. The same powder engineering conditions as for YSZ are valid for CGO. The presence of large agglomerates (>10 µm) would induce inhomogeneities which can hinder the thermomechanical and electrochemical behavior of the second electrolyte layer and the composite cathode. Furthermore, it is worth mentioning that the CGO barrier layer thickness is expected to be less than 10 µm and the presence of the above-mentioned agglomerates is unacceptable. Therefore, an energetic ball milling procedure is once more necessary.

II.A.4. LSM

LSM is a state of the art cathode material with good electron conductivity and chemical stability in contact with YSZ at the operating temperature. However, LSM and YSZ present a chemical reactivity at temperature higher than 1150°C forming insolating pyrochlore phases. Here a LSM powder provided from MarionTechnologies is used for Type I cells cathode composite. Figures II-9 and II-10 provide important information on the granulometric profile and the microstructure of the powder allowing to determine a milling and mixing procedure.
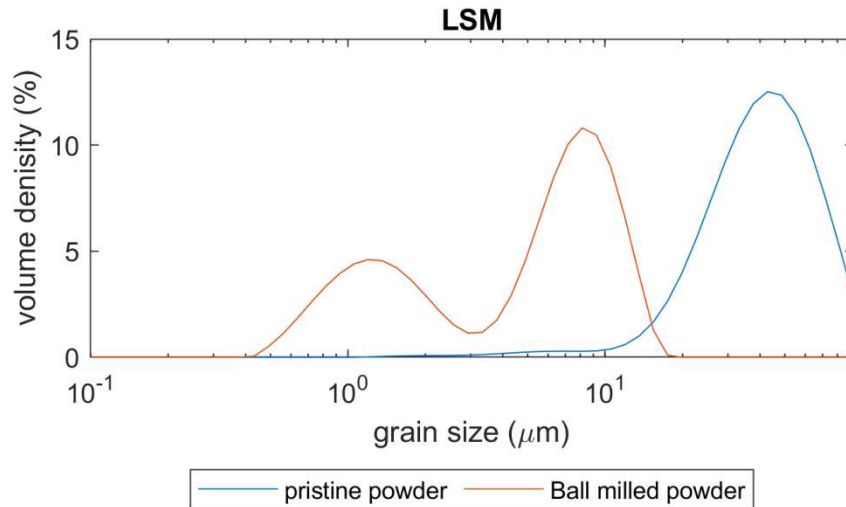
Figure II-9 Laser granulometry of LSM powder provided by Marion Technologies. A) As delivered powder; B) Ball milled for 12h at 300 rpm
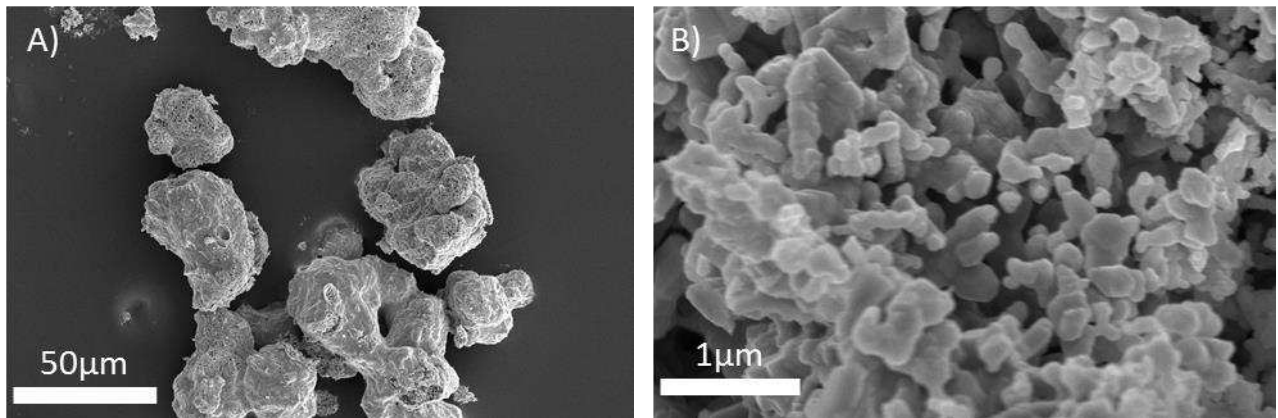

Figure II-10 SEM micrographies with increasing magnification of LSCF powder provided by Marion Technologies

As LSM is used for the CFL and eventually for the cathode gas channel, its proportion within the composite is decisive for the electrochemical performances of the cell. Fortuitously, as a state of the art material, a considerable quantity of excellent literature references can be found concerning the material ratio in the composite. In this work we use the at 1:1 volume proportion LSM:YSZ for the CFL layer and a 4:1 volume proportion LSM:YSZ for the cathode gas channel as it is presented in Cebellero et al. work on a similar project [5].

II.A.5. LSCF

For the type II cells, we use a commercial $La_{0.6}Sr_{0.4}Co_{0.8}Fe_{0.2}O_{3-\delta}$ (LSCF48) provided by Marion Technologies as an MIEC, ensuring good electron conductivity and boosted ion conductivity by the presence of CGO10. The laser granulometry of the powder can be found in figure II-11 and the SEM observation are shown in figure II-12.
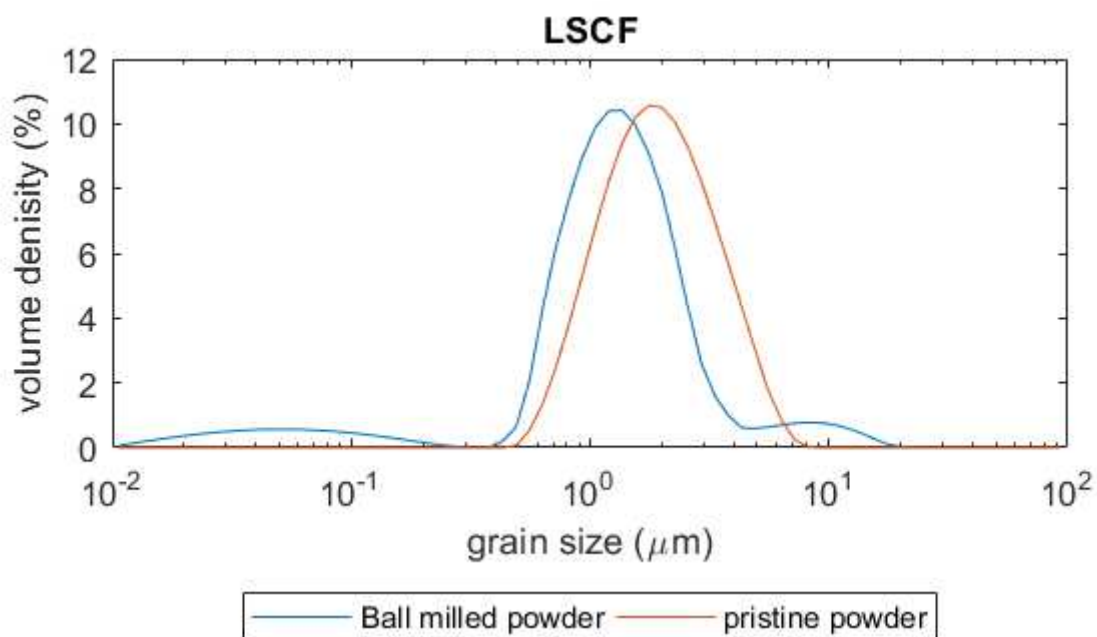

Figure II-11 Laser granulometry of LSCF48 powder provided by Marion Technologies. Visualization of the effect of the ball-milling procedure on the grain size distribution
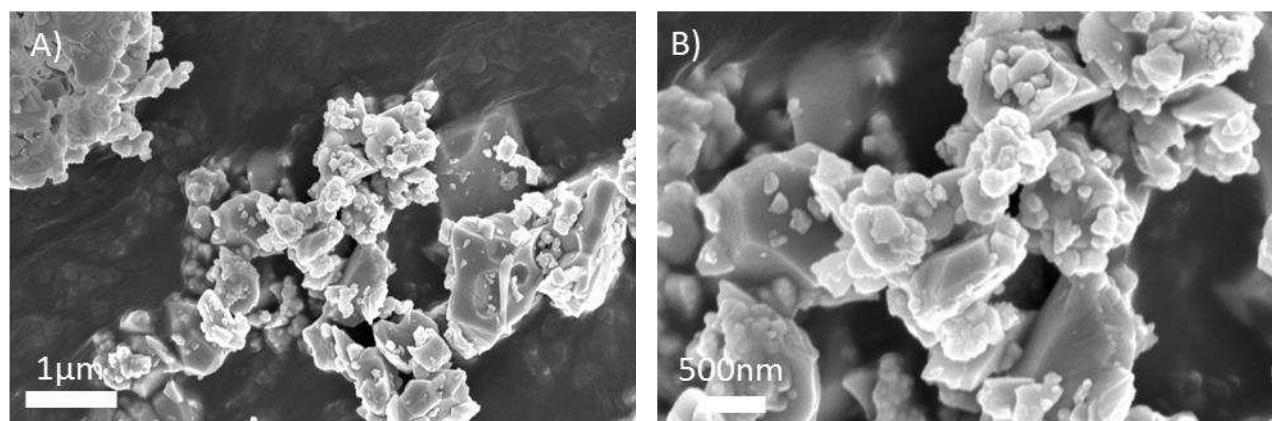

Figure II-12 SEM micrographs with an increasing magnification of LSCF powder provided by Marion Technologies

The milling process has a limited effect on the grain size distribution. Thus, a short mixing procedure (4h) has been used for the early type II cell fabrication. After SEM observation of those cells (figure II - 30), mediocre particle dispersion is visible demonstrated by CGO agglomerates. Hence, a long milling procedure is necessary to achieve a homogeneous dispersion crucial for adequate electrochemical performance. The milling procedure used previously for the other components is applied resumed in subchapter III.A.1.

II.A.6. Pore former

In some cases, such as for SOFC electrodes, controlled porosity distribution and morphology in the sintered solid is required. The elimination of a sacrificial compound, called pore former, can leave a predefined amount of vacant spaces in the ceramic serving as a gas distributor. The porosity requirements are different for each element of the cell. The anode support ensures the mechanical support of the cell, but also the gas distribution as well as the water management and the electron collection. Thus its porosity proportion needs to be elevated and composed of large pores, whereas the porosity in the electrodes functional layers, i.e. close to the electrolyte, needs to be kept optimal in order to maximize the TPB length and concentration.

During the reduction of NiO to Ni, a small size porosity is generated due to the 40% volume reduction between NiO and Ni. This porosity should also be taken into account, although it may be challenging to predict its proportion and tortuosity.

In this study, we use a synthetic graphite powder provided by Alfa Aesar with a 7-11 μm grain size (announced by the fabricant).

A SEM imaging of the raw powder reveals a large particle size distribution varying from several microns to 20-30 μm (figure II-13). Thus certain particles are excessively large and need to be broken to a grain size of 1-5 μm, to match the porosity requirements. The aimed porosity would ideally have a bimodal size distribution: a nano porosity (< 1 μm) insuring an elevated TPB concentration and a larger porosity (> 1 μm) acting as a gas conduit for fuel or oxygen distribution as well as and water and inert gases evacuation. Hence the pore former is added at the same time as the powders enduring a grain size reduction as well as dispersion.
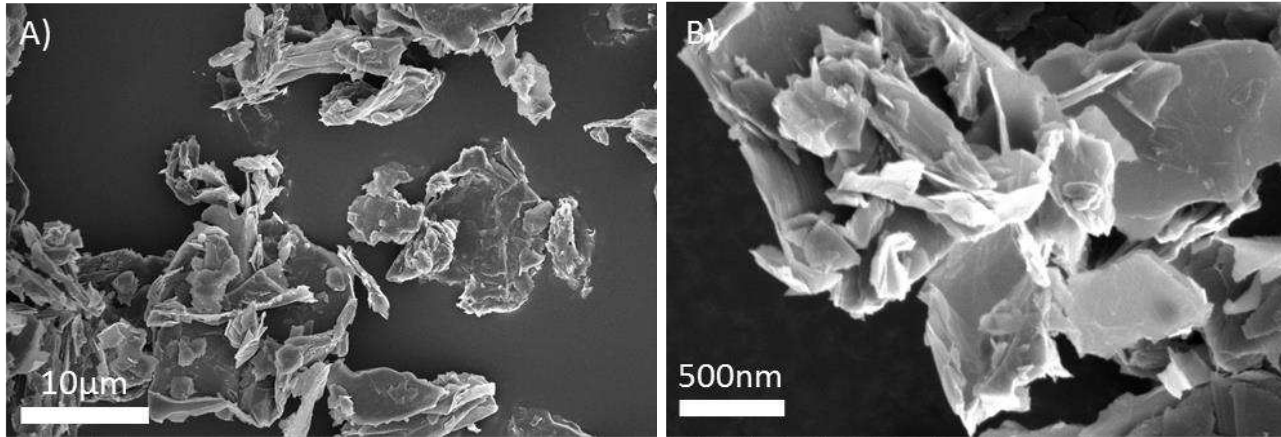
Figure II-13 SEM micrographs with an increasing magnification of synthetic graphite powder provided by Alfa-Aesar

It is important to notice that the graphite has a plate-like shape, by which the resulting pores are expected to present a similar elongated shape. However, the milling process allows us to break the agglomerates and the plates, and the energetic dispersion allowing to achieve a homogeneous and satisfactory pore size and distribution.

II.B.   Solvent and additives

II.B.1. Solvent

The solvent, also called vehicle or base, has the role to provide a liquid character for the slurry, suspend the particles and dissolve the additives. In most of the applications, the solvent and the additives are organic, but interesting results have also been observed applying aqueous-based routes [6]. A multitude of choices is available in the literature considering single chemical solvents such as ethanol (EtOH), methanol (MeOH), methyl ethyl ketone (MEK), or toluene, as well as combinations of solvents which in some cases can be at form an azeotrope such as MEK-EtOH (MEKET solvent).

Another common requirement for the tape casting solvent is its quick evaporation. This is one of the reasons manufacturers use organic solvents rather than aqueous. Evaporation impacts directly the production rate, hence it represents an essential characteristic for industrialization. However, premature evaporation of the solvent can be associated with a "skin" effect that hinders the bulk drying and can generate inhomogeneity in the tape. This phenomenon is especially relevant for

thick layers (> 100 µm) and using a fast evaporating solvent such as pure MEK (~2.5 times faster evaporation rate compared to ethanol [7]). Adding ethanol to the pure MEK vehicle can lower reasonably the evaporation, reducing the local solvent depravation which decreases the importance of the "skin" effect. A well-known azeotrope proportion of MEK-EtOH (MEKET) has been widely used for tape casting and other industrial applications, due to its dissolution capacity, reasonable evaporation rate, and good dispersing ability (partially demonstrated by the granulometric measurements).

In this study, an azeotropic mixture of MEK 60 %vol – EtOH 40 %vol is used.

II.B.2. Dispersant

As indicated by his name, the main role of the dispersant is to separate the powder particles and avoid flocculation before they are coated by the binder. There are roughly two types of dispersants using steric hindrance and/or Van der Waals repulsion. Ionic repulsion is promoted by the use of polar molecules or solvent and for steric hindrance, usually, polymers or other long-chain molecules can be used.

In this study, α-terpineol is chosen as a dispersant, which has been demonstrated to provide a sufficient steric hindrance by Maiti et al. [8] and is commonly used as a serigraphy inks vehicle.

II.B.3. Binder

The binder is chosen after the characterization of the powders to provide a binding matrix coating the elementary particles and to maintain them homogeneously dispersed. The compound is usually a polyvinyl or a polyacrylate, with long polymer chains, which provide the desired mechanical behavior to the tape, by rearranging themselves during the solvent evaporation. Thus it influences greatly the strength, flexibility, durability, etc. of the green tape and the binder nature and quantity must be strictly controlled, to avoid particle segregation or defective tapes.

The binder choice must take into consideration several parameters such as T_g (glass transformation temperature), burnout temperature, solubility, powder firing atmosphere, ash residue, and pollutants or by-products. The polymer chain length of the chosen product is another factor that should be also taken into account. The number of monomers by chain usually accessible by the molar weight, can influence the slurry viscosity, and the capacity to "charge" it with solid matter.

During this work, a PVB Butvar B98 provided by Sigma Aldrich is used (figure II-14) and its quantity is determined based on the high specific surface of the powders (> 10 m².g^{-1}), and the tests realized by M. Geagea [9].
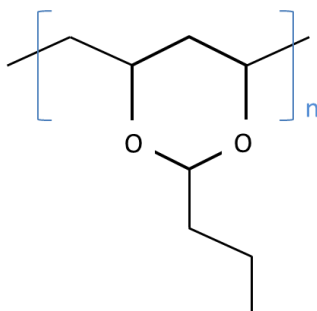

Figure II-14 (Poly)VinylButyral

II.B.4. Plasticizer

This additive could be considered complementary to the binder since its purpose is to give plastic and/or elastic behavior to the matrix, i.e. the capacity to bend without cracking. This property is imperative for the cutting or punching, rolling, laminating, and stacking of the tapes. In tape casting, there are two types of plasticizers defined by some authors as type I and type II. In their book, Mistler and Twiname [10] provide a pedagogic explanation of the two types of plasticizers illustrating their influence on the matrix mechanical properties by comprehensive graphics and mention some examples of commonly used compounds. Briefly, Type I plasticizer softens the binder chains allowing them to stretch resulting in lower T_g of the matrix, whereas Type II plasticizer lubricates the internal matrix.

A commercial ACROS Organics PEG400 is used as a type II plasticizer.

III.   Cell fabrication

III.A. Slurry

III.A.1.Preparation

Once the components have been chosen, and the needed quantities determined, the slurry may be prepared by mixing adequately the compounds. The powder characterization reveals a need for an energetic mixing process to break the particle agglomerates and homogenize the mixture.

Thus, the slurry preparation is carried out via ball milling, in zirconia or agate coated jar, and with the aid of zirconia or agate balls respectively (figure II-15A).

Two steps mixing process is carried out (figure II-15 B). During the first stage, the powders are dispersed in the solvent in presence of the dispersant. This stage is necessary to break the agglomerates and to disperse homogeneously the particles. For the second stage, the binder, the plasticizer, and eventually a pore former is added and the mixing process allows to coat the particles with the dissolved binder. The slurries compositions can be found in Tables Annex 3 to 9 in the annex.
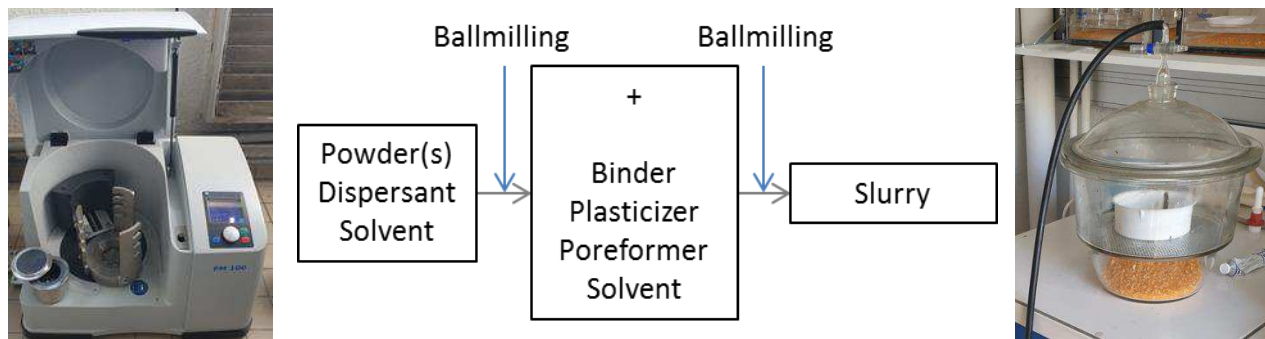
Figure II-15 Slurry preparation devices and procedure A) Retsch® Planetary ball mill PM100 and agate grinding jar. B) Mixing procedure; C) Desiccator used as a low vacuum chamber

During the mixing procedure, the slurry accumulates air which needs to be eliminated in order to avoid bubbles formation and to ensure the quality of the future tapes. A low vacuum chamber is used for this reason and the duration varies with the slurry quantity (figure II-15C). A vacuum can be also used to rectify the viscosity of the slurries by forcing the evaporation of the solvent.

III.A.2.Characterization

The rheology of the slurries is systematically characterized by a Rheology International Viscometer spindle rotation viscometer equipped with an RV4 spindle at 20 rpm. These measurement conditions are commonly observed in the literature. Some authors suggest that they provide a sheer ratio close to this of the blade during casting. Although others do not necessarily agree with the latter approximation, most authors agree that the parameters are practical due to the easy conversion in $mPa.s^{-1}$. In our case it allows above all, to compare the slurries and maintain a good reproducibility.

The viscosity control also allows us to anticipate certain adaptability of the slurries which is necessary to cope with particular conditions such as the presence of architecture patterns. In figure II – 16, we observe a mediocre electrolyte penetration within an architectured anode. This problem has been solved by slightly reducing the electrolyte viscosity, allowing it to wet the architectured surface.
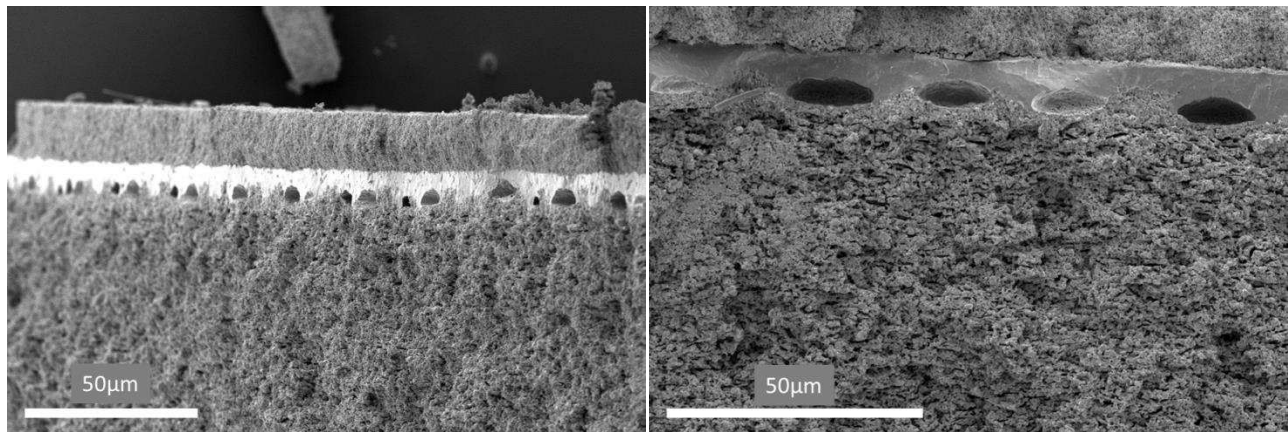

Figure II - 16 SEM observation of cavity presence at the electrode/electrolyte interface in a defective architectured cell (Sample C3A-6a-2)

A wide range of viscosity values can be found in the literature and most of them are situated between 500 cPs and 6000 cPs [10]. Taking into account the modifications, the approximate slurry viscosity values can be found in Table II-2.

Table II - 2 Slurries rheology

Slurry	Viscosity (cPs)
Anode support	4500
AFL	3500
Electrolyte YSZ	3000
Electrolyte CGO	3000
CFL	3000
Cathode gas channel	3500

III.B. Tape casting

Tape casting is well known and vastly used fabrication technique, applied in numerous domains, such as plastic, paint, and paper manufacturing as well as ceramics fabrication for various applications. Historically it was first used for ceramics by G.N. Howatt et al. [11] and was patent in 1952 as a method of producing high-dielectric insulation ceramic plates [12].

The technique consists of casting a ceramic suspension (slurry) over a relatively moving carrier surface controlling the thickness of the coating with a doctor blade (figure II-17). The thickness can vary in a large range from 10 μm to more than 1 mm, thus allowing it to be adapted for numerous components applications such as dielectric ceramics, semi-conductors, oxygen detectors, and SOFC.
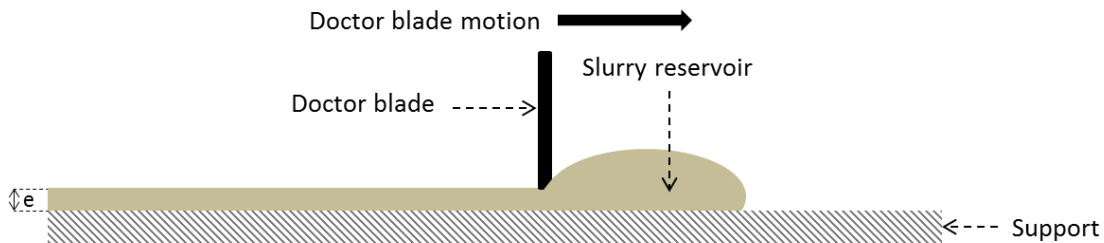

Figure II- 17 Tape casting principle schematic

The cast wet film is left to dry in either a drying chamber with or without airflow and heat or simply at open-air and room temperature. The dried tape, also called green ceramic tape, can be laminated, cut, enrolled, and stored.

Although the fabrication process appears to be quite simple, a multitude of parameters influences the final ceramics quality such as slurry composition and viscosity, casting speed and thickness, doctor blade shape, carrier nature as well as drying temperature and duration. However, this method is considered to be one of the finest approaches in elaborating large area ceramics or metal plates with regular and controlled thickness. A multitude of books and publications have been written on the subject and in this work, the R.E. Mistler and E.R. Twiname's book "Tape Casting Theory and practice" [10] has been largely used for understanding and mastering the technique.

III.B.1. Equipment

Once the slurry is prepared, de-aired and its viscosity controlled, it can be cast into raw ceramics tapes. During this study, a homemade casting bench (figure II – 18A) was used for the longer tapes and a commercial tape caster Elcometer 4349 Automate Film Applicator (figure II – 18B) for the shorter tapes. In both cases, we employed an Elcometer 3580 doctor blade equipped with micrometer screws to control the tape thickness (figure II – 18C). The tapes are cast over glass plates and/or silicon Mylar film to ensure a perfectly smooth surface and reusability of the support. In this work, the slurry reservoir is replaced by a puddle spread in front of the blade preceding the casting.

Figure II-18 Tape casting equipment. A) Homemade tape casting bench; B) Commercial Elcometer 4340 tape caster; C) Elcometer 3580 doctor blade;

III.B.2.Preliminary considerations – drying, shrinkage

Before initiating the casting procedure, rapid characterization of the drying duration and thickness reduction is necessary, especially for sequential tape casting which involves casting over dry tapes.

For this test, a small tape is cast over a previously weighted Mylar film and it is placed on a scale. The weight variation as a function of time is shown in figure II-19. Less than 20% of the solvent remains after one hour of drying which indicates an approximate waiting time before casting the next layer.
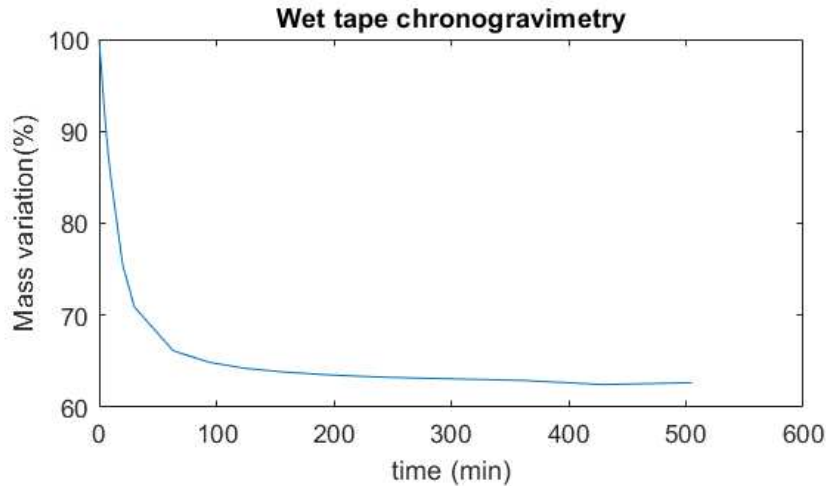
Figure II- 19 Wet tape chronogravimetry

An excessively fast evaporation rating of the solvent can provoke a skin effect on the tape free surface. This skin effect can hinder the bulk drying, inducing density, and residual stress inhomogeneity, especially for the thicker layers. In this study, a thermodynamic solution is preferred, by placing a glass plate at approximately 2 cm above the casted tape. By doing this, a locally pseudo-saturated atmosphere is created, which slows the evaporation rate maintaining the wetness of the free surface and promoting bulk drying (figure II-20).

Figure II-20 Schematic representation of the drying pseudo-chamber

Once the drying of a single layer is characterized, the shrinkage ratio needs to be determined to anticipate the final tape thickness. Being fixed on the support, the direction perpendicular to the tape surface is the only dimension in which the shrinkage is allowed. Thus, the thickness decrease should formally be equal to the solvent volume proportion in the slurry which is approximately 70%vol. This proportionality is verified by simple thickness measurements.

III.B.3. Half-cell casting

The three types of cells are elaborated by a sequential tape casting, which consists of casting multiple layers over dried previously casted tapes. The sequences of the half-cell casting are the following:

Type I

1) Three layers of anode support with wet thicknesses of 500 µm
2) Anode functional layer with a wet thickness of 50 µm
   - Potential architecturing
3) Electrolyte layer with a wet thickness of 50 µm
   - Potential architecturing

Type II

1) Three layers of anode support with wet thicknesses of 500 µm
2) Anode functional layer with a wet thickness of 50 µm
   - Potential architecturing
3) Electrolyte layer with a wet thickness of 50 µm
4) Barrier layer with a wet thickness of 50 µm
   - Potential architecturing

A schematic of the sequential casting can be found in Figure II – 21.
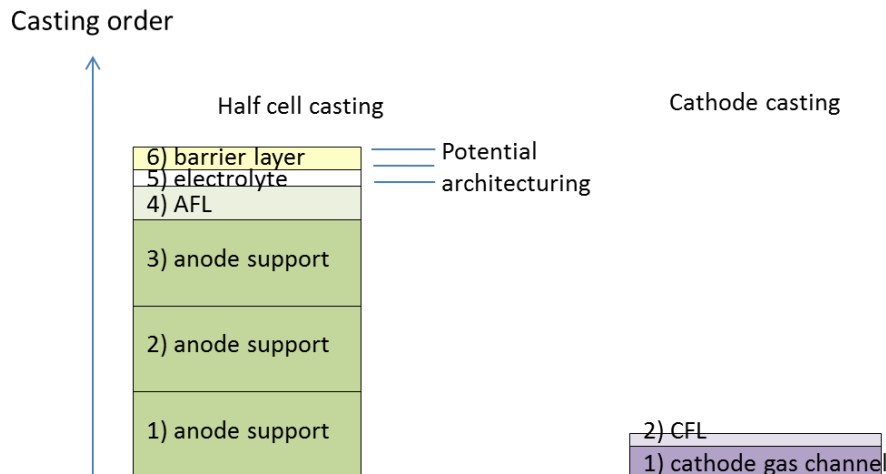
Figure II- 21 Casting order representation

The architecting of the interfaces intervenes either before or after the electrolyte (or barrier) casting.

III.B.4.Cathode casting

In this study, we fabricate two types of cells based on the materials of the cathode composite. Type I cathodes are composed of LSM/YSZ composite and Type II are composed of LSCF/CGO composite. For type I, bilayered tapes are cast. On one side a gas diffusion layer with elevated porosity and electron-conducting phase concentration (4:1 electron conductor : ion conductor). On the other side, a functional layer with a 1:1 volume fraction of the electron and ion-conducting phases is with minimum porosity. For Type II cells, on layer cathode tapes are cast with the cathode functional layer composition (LSCF:CGO with 50:50 volume proportion and intermediate porosity)

The cathode tapes are cast independently from the half-cell. A sequential casting is carried out here as it is for the half cell. The usual sintered cathode thickness is between 50-100 μm, and for this reason, a 300 μm wet thickness gas channel cathode tape is cast and dried followed by a casting of a CFL tape with a 50 μm wet thickness. Once the tape is dry, it can be stored, shaped, and used for the cell completion.

III.C. Architecturing and shaping

As the objective of the thesis is to compare architectured and planar cells, this shaping stage of the fabrication process is critical. Many potential methods of interface architecturing are considered such as template-assisted cold press stamping (figure II-22) which was used in previous work [9].
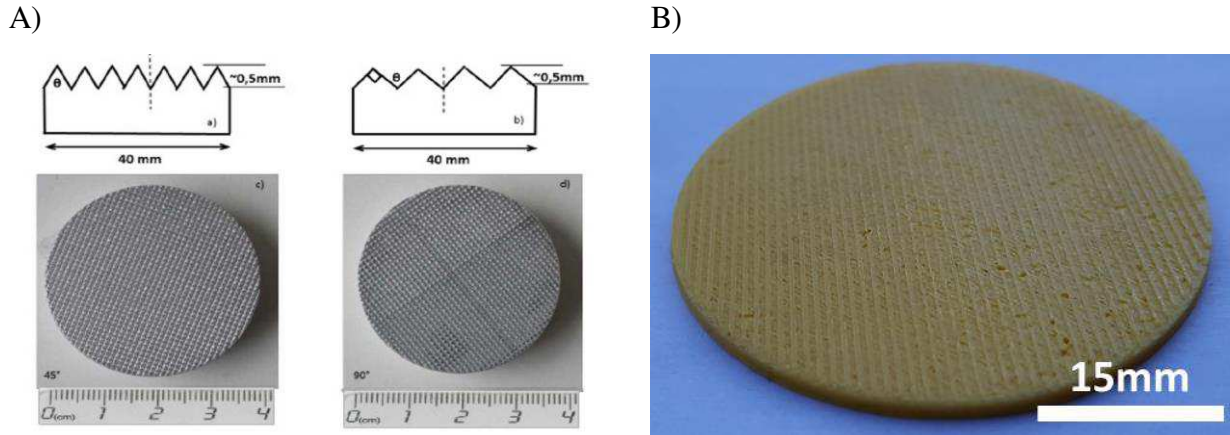
Figure II-22 Cold press architecturing templates. A) Aluminum templates with pyramidal patterns; B) 3D printed PLA template with rail patterns

Although this method has shown some preliminary results, the localized stress applied by the template over the green ceramic hinders the mechanical stability during sintering. This could result in cracks initiation and propagation reducing the reproducibility of the fabrication, as it can be observed in the up-quoted work.

During the current work, two other methods of architecturing are tested: laser engraving of green tapes and template application during tape casting.

III.C.1. Laser engraving

This method has an important potential for development due to the possibility of complex patterns engraving and industrial-scale applications. Laser engraving on ceramics can be found in many porcelain or ceramics industries. Some researchers have even applied laser architecturing of sintered fuel cells [5] [13] [14]. Although they demonstrate interesting results, the ceramics often present micro-cracks induced by the laser shock and the lack of plastic deformation as well as limited heat conduction.

In this study, laser engraving is applied to the green ceramic tapes. The engraving at this stage of the fabrication presents multiple advantages over the engraving on sintered ceramics.

- The plastic deformability of the tape, induced by the presence of the binder matrix, compensates for the laser impact

100

- The thermoplasticity of the binder eases the heat absorption avoiding fracturing due to an important thermal gradient
- The non-sintered powder is more tolerant toward material ablation thank to the lack of solid cohesion between the particles
- Tape casting and co-sintering remains possible because the following layer can be cast over the engraved surface
- A multitude of patterns can be programmed with CAO software and the different resolutions can be achieved depending on the used laser characteristics
- Architecturing and tape cutting can be combined

Electrochemical performances of cells architectured by this method are not presented in this document, but interesting results can be found in Cebollero et al. [13] as well as Iwai [14] and Konno [15] works. Nevertheless, the optical profilometry of patterns resulting from laser engraving of anode support tapes is used to develop and verify a Matlab script allowing to calculate area expansion coefficients.

III.C.2. Soft template architecturing

This second architecturing method is applied during the tape casting. A PET1500 fabric provided by Sefar (Figure II-23A) is laid over the wet tape, assisted by the passage of the doctor blade (figure II-23B), and is removed when the tape is dry.
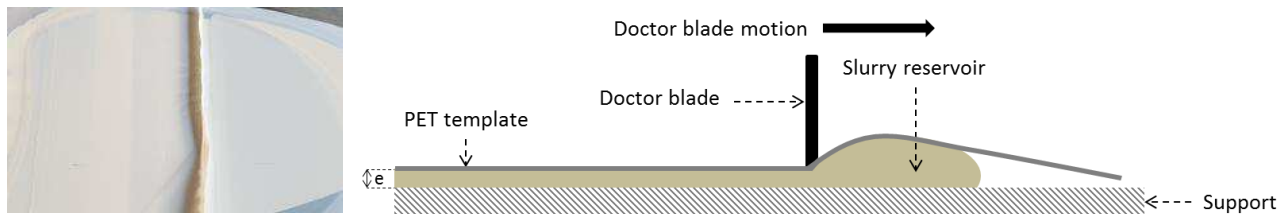

Figure II- 23 Soft template architecturation method. A) green tape architecturing using a PET1500 fabric; B) Principle schematic

This technique has the advantage to allow applying the architecture during the casting process, thus reducing the number of fabrication stages. Furthermore, the architecturing is done softly without material ablation or microstructure modification, promoting mechanical stability during sintering.

III.C.3. Tapes cutting

Once the tapes are dried and eventually architectured, they need to be cut into the shape of the final ceramic. Here, a button cell geometry is chosen and punching and blade cutting or laser cutting methods are applied. Both methods present interesting properties which are summarized in Table II-3.

Table II - 3 Pros and cons of cutting techniques		
Method	Pros	Cons
Laser cutting	Consecutive cutting Clean cut Combined architecturing and cutting	Local heating Volatility of toxic species
Punching or blade cutting	Easy application Well known and used technique	Local residual stress and tape densification Instrument quality dependency

Thus for mass production cutting, the laser seems to be a more appropriate choice due to its rapidity, reproducibility, and possible combination with an architecturing procedure. As for punctual cutting needs, punching or blade cutting remains an option.

III.D. Thermal treatment

III.D.1. Additives elimination

The thermal treatment involves two different steps: additives and pore former elimination and powder sintering.

After the solvent evaporation, the green tape is composed of more than 60 %vol of binder, plasticizer, dispersant, and pore former. These compounds need to be eliminated from the cell components to consolidate the powder grains and to form the needed porosity. Inadequate firing kinetics could cause burning and thermic gradients as well as gas pressure buildup (bubbles), hindering the integrity of the cell. Thus it is important to ensure slow combustion at the lowest possible temperature, to eliminate the binder and the other additives as well as the pore former,

allowing to slowly evacuate the produced combustion gas (CO_2) via the still largely present open porosity.

To adapt this first stage of the thermal treatment, a thermogravimetric analysis (TGA) is performed on a dry tape. The mass loss as a function of the temperature as well as the curve derivative reveals the elimination temperatures and kinetics (figure II-24). A consequent mass variation is observed between 200°C and 450°C corresponding to the organic additives elimination followed by a minor mass loss between 550°C and 650°C corresponding to the pore former elimination. The pore former must be the last to be eliminated to preserve the spaces created by its elimination.
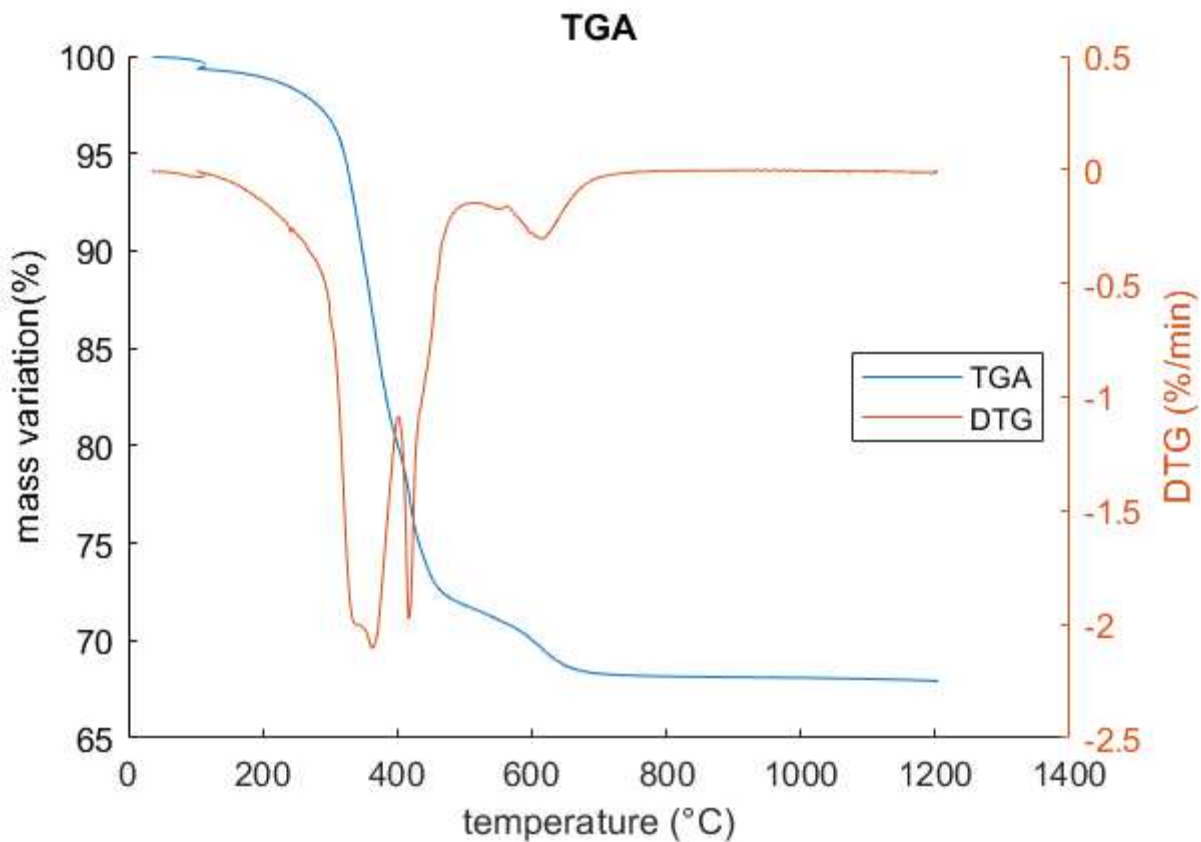
Figure II- 24 Thermogravimetric analysis of an anode support green tape in an oxidizing atmosphere (airflow at 20 ml/min)

As mentioned a slow elimination is necessary to ensure the quality of the fired ceramics. Thus, during the thermal treatment, we impose dwell periods at temperatures corresponding to a low

elimination speed. These results are used in the cell thermal treatment determination, fixing the elimination temperatures and the isotherm dwells needed for a smooth transition (Figure II – 26)

III.D.2. Sintering

Sintering is the second stage of the high-temperature thermal treatment. This process induces material consolidation by crystal grain growth and merging, aiming to reduce the global surface tension and stabilizing the system. In figure II-25 a simplified explanation of the sintering process is presented. The first step is the grain joints formation, which is less energetic than the surface tension of a solid exposed to a fluid and it is followed by low densification. The second step is grain growth (merging) resulting in grain joints and porosity elimination allowing even further superficial tension reduction and important densification rate (maximum density = 1).
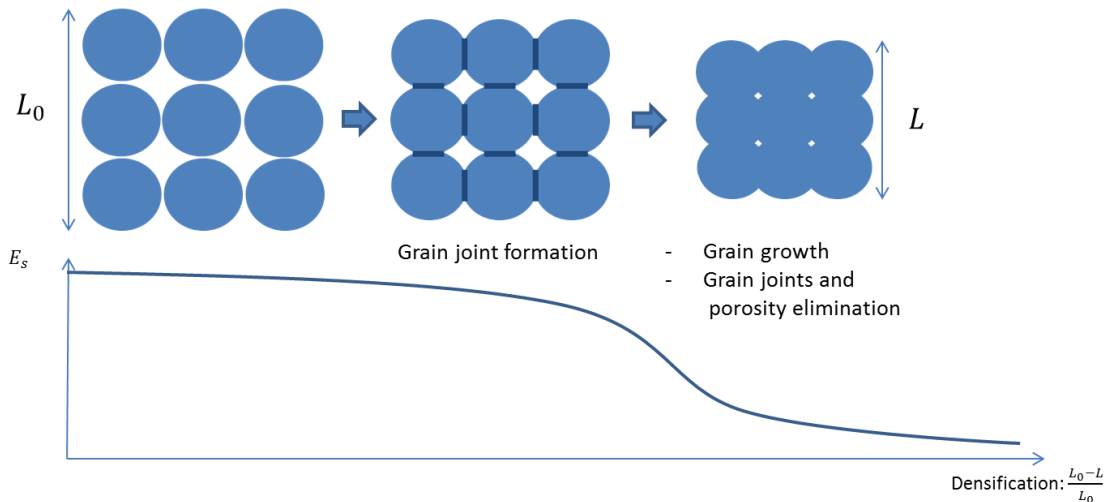
Figure II- 25 Sintering process schematic

The co-sintering of the anode and the electrolyte is a delicate phase of the fabrication susceptible to lead to cracks or other types of deformations. This is especially true in the anode supported configuration, where the anode has been cast as one or more thick layers potentially presenting sedimentation and stress gradients and delamination risks. Furthermore, the anode and the electrolyte have different thermal expansion coefficients (TEC) as well as sintering temperatures. Those parameters need to be characterized in order to anticipate the eventual deformations. As Ni:YSZ is a state of the art anode material and YSZ a state of the art electrolyte material, considerable work has been established to determine optimal sintering conditions. In the very

insightful publication by Robert Muücke *et al*. at Forschungszentrum Jülich GmbH [16], the sintering temperature of YSZ films is studied. In this work, the authors determine that a sintering temperature of 1400°C and a sintering dwell of 5h are sufficient to achieve more than 95% of density in co-sintering conditions (anode support as a substrate). This protocol is also used later by Menzler *et al.* [17] in the same team, to fabricate fuel cells extracted from sequential tape casting and coping with the flatness issues characteristic of the technique.

For the type II fuel cells, a CGO layer is cast over the YSZ electrolyte and it is co-sintered in the same conditions as described previously. We have not yet observed a reactivity between the YSZ and CGO as it is suggested that may happen at this high temperature and long duration by the previously quoted authors.

The significant sintering temperature difference between the half-cell materials and the cathode imposes a second stage of sintering. The sintering temperature for the cathode materials has been widely studied as well. For the LSM:YSZ composite we apply a sintering temperature of 1150°C as used by numerous authors such as Cebollero *et al.* [13] and Konno *et al.*[15]. For LSCF:CGO composite cathode, a sintering at 1050°C is carried out based on the study published by Leng *et al.* [18].

Based on the TGA and the bibliography, the thermal treatment for the cell elements is determined (figure II - 26) performing isotherm dwells for each compound elimination as well as for the sintering processes.
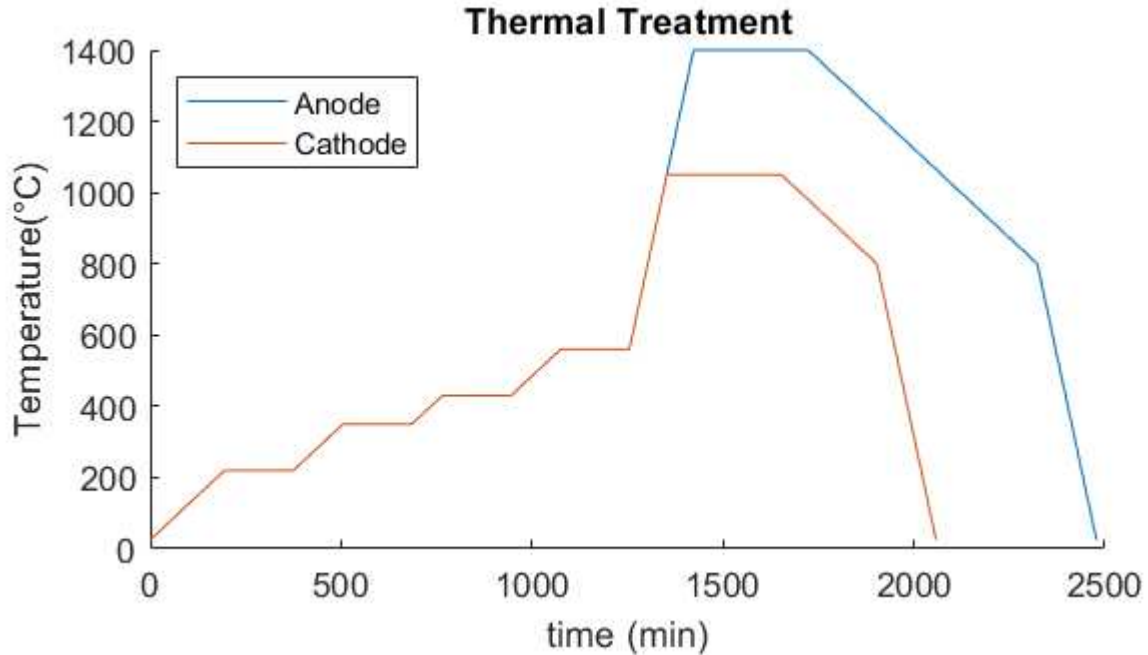
Figure II- 26 Thermal treatment

The half-cell co-sintering is an extremely delicate part of the fabrication, because of the complexity and differences of the elements (materials difference, density asymmetry). Other than crack formation and/or fracturing, one of the commonly encountered problems is the bending of the components (Figure II – 27A). The TEC mismatch of the co-sintered components, the eventual sedimentation, the residual stress in the tapes due to anisotropic drying, and casting mechanisms are all sources of mechanical deformations during the thermal treatment which are more or less controllable. We systematically observe a bending towards the anode support as shown in figure II – 28 A, although the TEC mismatch suggests that the bending should be in the other way. Thus, we may deduce that the most important contribution to this deformation is due to the residual stress in the binder matrix. Excellent discussion on cell deformation during the thermal treatment is presented by Menzler et al. [17] providing valuable information concerning the bending mechanisms.

A)   B)
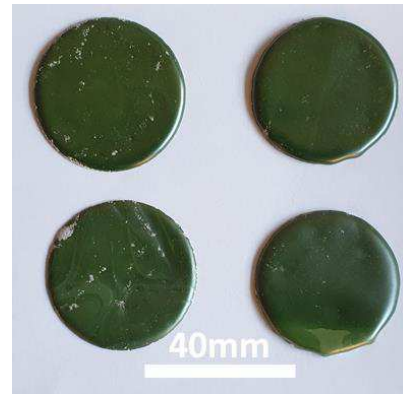
Figure II- 27 Flatness maintenance during thermal treatment. A) Sintering without weight; B) Sintering with weight

In Figure II – 27 B we show four anode/electrolyte half cells co-sintered under alumina plates weighing between 50g and 100g and 4 cm of a diameter corresponding to 400 Pa and 800 Pa respectively. They present a satisfactory flat surface, and only the edges are bent, hence their cutting (figure II – 28 A) can allow obtaining flat cells. This is achieved with a laser cutting, and as it is demonstrated in figure II – 28 B the results are satisfactory.
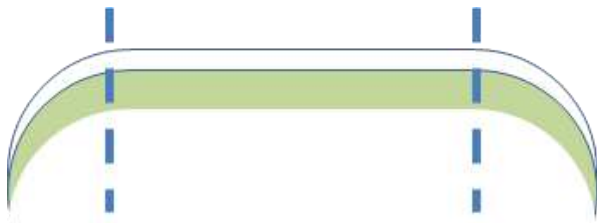
A)   B)
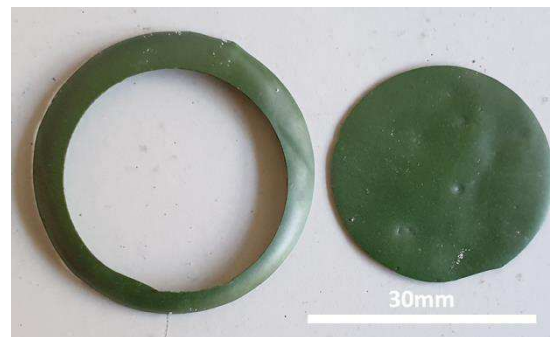
Figure II- 28 Laser cutting of half-cell edge rim. A) Schematic B) Cut half cell

III.E. Cathode deposition

The last step of the fabrication protocol is the cathode deposition over the sintered and shaped half-cell and its thermal treatment. As mentioned the cathode is realized by tape casting, and disks of the desired size are punched before being applied on the half cell. This is achieved by

locally dissolving the cathode tape and fixing it to the sintered electrolyte. The cathode is dried for 3h at 65°C and the cell is fired and sintered following the thermal treatment shown in figure II – 26 - cathode.

IV. Protocol validation and discussion

In this subchapter, the rapid validation of the fabrication protocol is carried out. The first part consists of naked-eye observations during each fabrication stage and for the final cell. However, this characterization remains superficial and strictly qualitative. To ensure reliable electrochemical measurements as well as detailed components characterization and pertinent parameter determination for the modeling, the fuel cell integrity needs to be controlled. Thus, structural control is implemented, by optical and scanning electron microscopy. An optical microscope is used to control the surface quality, allowing the detection of cracks or provide a coarse architecture characterization. SEM observations of transversal fracture demonstrate the state of the interfaces and if the cohesion between the layers is efficient. It also provides advanced information on the microstructure of the component, which is going to be discussed in the next chapter. Finally, a polarization measurement is performed to confirm the functionality of the cell. The I/V curve provides some insight into the cell quality, such as the integrity of the electrolyte which can influence the open-circuit voltage.

A detailed microstructural study is presented in the next chapter, providing information on the porosity or density of the components, their chemical distribution, and interface architecturation.

IV.A. Cell integrity

IV.A.1. Surface control

Optical observation is a simple method to confirm the structural integrity of the fuel cell, allowing to discard the samples presenting cracks or other defects (figure II – 29 A) and keep flawless samples (figure II – 29 B).
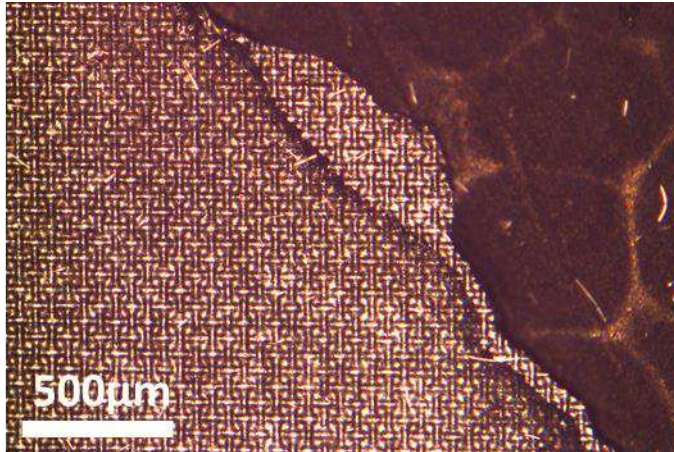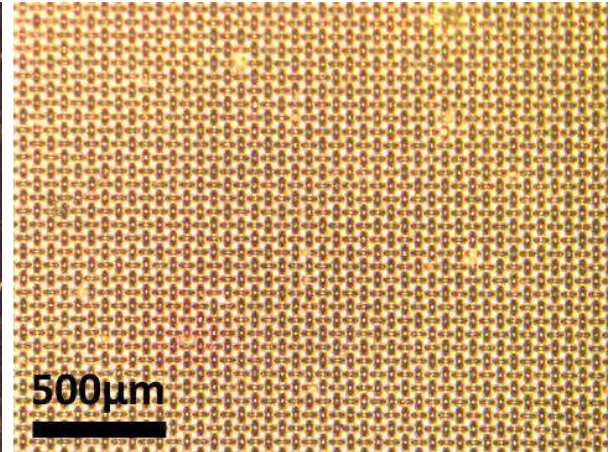
Figure II- 29 Open surface observations by optical microscope: a) cracked electrolyte; b) flawless electrolyte;

It is also practical for architecturing pattern or template observation and their coarse geometrical parameter characterizations.

IV.A.2. Layer cohesion

To ensure functionality and durability, the multiple layers of the fuel cell need to be perfectly cohesive. A cross-section SEM observation allows confirming this cohesion of the layers in both planar and architecture cells, as presented in figure II-30. The type II cell configuration is chosen here as an example, due to its more important complexity and potential delamination. Although, punctual defects are observed, such as local microscopic cavities situated near the CGO and YSZ interface or mediocre phase dispersion in the cathode, the electrolytes do not present fractures and the cells look functional, even if electrochemical measurements are necessary to confirm this.
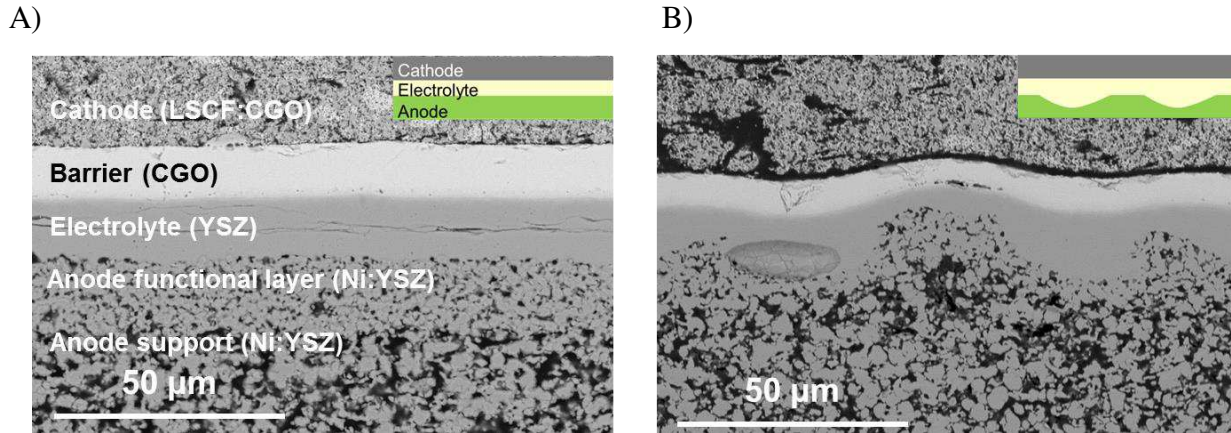
Figure II- 30 Cross sections SEM observations. A) plane cell; B) Architectured cell

These micrographs provide some important information concerning cell microstructure, which should be mentioned for the validation of the fabrication protocol.

Cermet: The lack of chemical contrast in the cermet demonstrates a good material dispersion and homogeneity, which is essential for the TPB percolation. Furthermore, the random shape of the pores as well as their distribution (size and dispersion), shows that the use of graphite as a pore former is justified.

Electrolyte: It is important to note the elevated density and the thickness of the electrolyte layers which is for both layers approximately 7 µm resulting in 14 µm global electrolyte thickness for the plane geometry. The thickness of the architectured electrolyte is more difficult to estimate due to its periodic variation between 10 µm at the "top" of the patterns and 20 µm at the "bottom". Nevertheless, the global thickness of the electrolyte remains less than 35 µm, which is the experimental limit demonstrated by B.C.H Steel [4] needed to maintain the value of $\frac{L}{\sigma} = 0.15 \, \Omega. \, cm^{-2}$. For further comparison of the fuel cell performances, a electrochemical analysis needs to be carried out, allowing to judge the equivalence of the electrolytes in the two configurations.

Cathode: In both cells, the cathode presents chemical contrast revealing particles segregation and inhomogeneity. This is an important issue, as it can hinder the reactive sites concentration and the percolation of the conducting media. Thus, an amelioration of the cathode fabrication protocol is necessary, consisting of a more energetic ball milling.

110

IV.B. Functionality

The finality of the study is to produce high-performance fuel cells. For this reason, electrochemical tests in operational or static conditions need to be performed to confirm the cell functionality concluding if the fabrication protocol is successful. Those tests can be more or less sophisticated including electrical conductivity and resistivity measurement of the components, current and power density curves, or electrochemical impedance spectroscopy (EIS) in different conditions.

The fabrication protocol can be considered as adequate as long as the fuel cells are mechanically stable and can generate electrical energy from fuel oxidation, without considerable losses and leaks (OCV ~ 1 V). A polarization measurement provides a rapid and simple way to compare the electrochemical performances of the cells.

In this work, a Fiaxell testing rig (figure II – 31 A) is used coupled with an IviumStat impedance spectrometer and a Brook Instruments debit flow meter (figure II – 31 B).

A)   B)
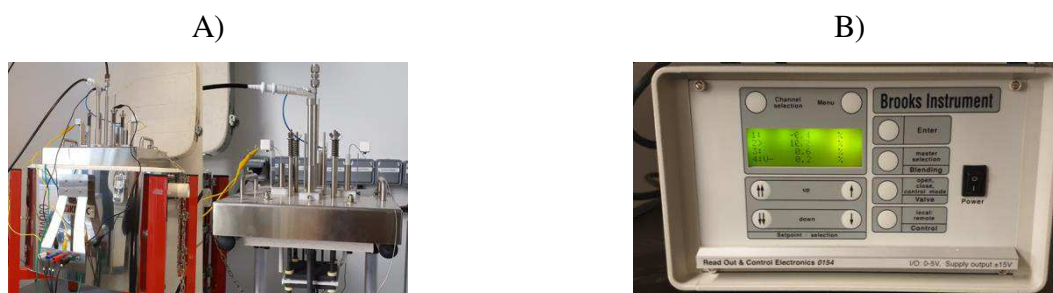
Figure II- 31 Electrochemical measurements set-up. A) Fiaxell testing rig B) Brook Instruments debit flow meter

The cell is placed between a nickel mesh at the anode side and a gold mesh at the cathode side, both having the role of current collectors. To ensure gas separation, aluminosilicate felts are shaped and positioned over the cell as shown in figure II – 32, and the excess gas is burned within the felt. Hence a local temperature gradient is possible and should be limited to avoid influencing the measurement, by temporary spacing successive measurements and controlling the gas flow.
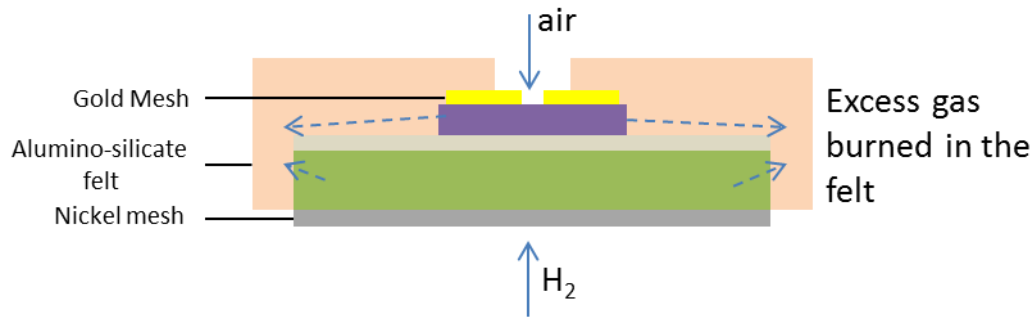
Figure II- 32 Cell testing configuration schematic

The polarization measurements are carried out according to the testing rig manufacturer recommendations: H_2 flow 100 ml/min and airflow of 300ml/min which takes into account the stoichiometric (ratio of 2,5 for the airflow/H_2 flow) as well as the surface area of the cathode ($\approx$1.5 cm^2) and results are shown in figure II – 33.
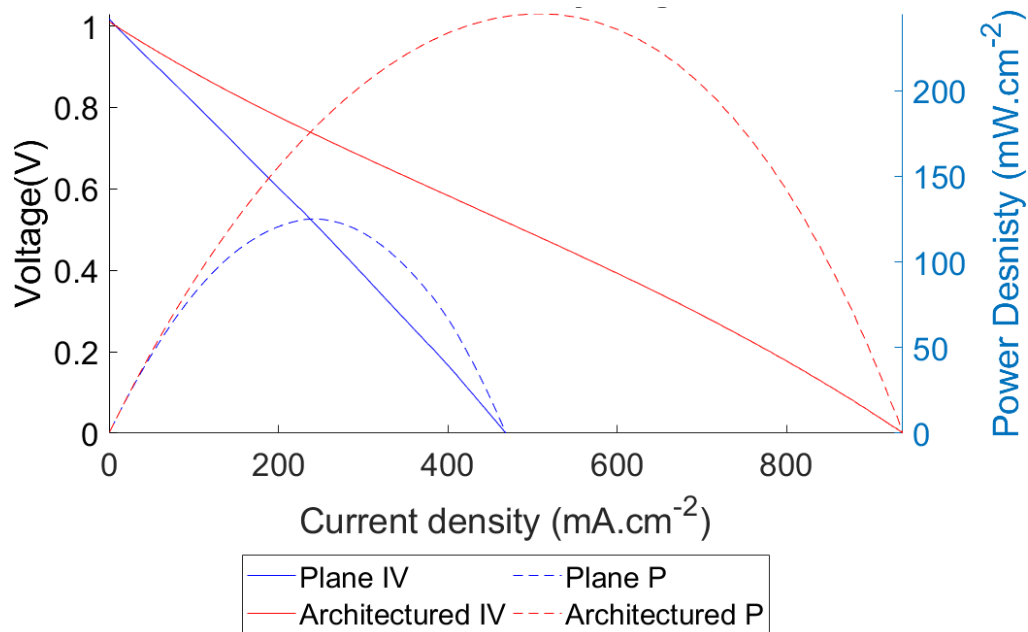

Figure II- 33 Polarization curves and associated power densities of operational planar and architectured Type II fuel cells at 790-800°C

Satisfactory cell performances are observed during these preliminary tests where the plane cell exhibits over 120 mW/cm² at 700 mV and the architectured cells exhibit 320 mW/cm² in the same gas flow conditions and at 790°C. The open-circuit voltage value of 1-1,2 V indicates that

the electrolyte layers do not present cracks and that the gases are well separated. Detailed study and comparison of the cells are presented in the next chapter, however, these results are encouraging and confirm that functioning fuel cells are produced with the established protocol.

V.   Conclusion

In this chapter, we reviewed the different steps of the fabrication protocol for planar and architectured single fuel cells. Characterization of the cells is provided at each fabrication step in order to ensure an effective progression. The specificity of this protocol is the realization of each cell component by tape casting, reducing the number of used techniques, the fabrication time, and materials. Reproducible and innovative shaping methods are applied to structure the cells and the electrode/electrolyte interfaces in particular.

Finally, simple integrity analysis and electrochemical measurements are performed to verify the functioning of the cell exhibiting satisfactory performances. Gas tightness of the electrolyte is demonstrated by elevated OCV value (above 1 V at 800°C) and acceptable overall resistance (under 5 $\Omega.cm^{-2}$) exposes adequate material composition and microstructure. However, although acceptable, global resistance should be decreased to ameliorate the cell performances.   An amelioration of the fabrication process of the cathode tapes should provide a partial solution.

Detailed microstructural analysis and electrochemical measurements for adequate cell performance comparison are described in the next chapter. The iterative methodology of the fabrication protocol establishment takes into account those characterizations.

VI. Bibliography

[1]   D. J. Shanefield, 'Particle Characteristics', in *Organic Additives and Ceramic Processing: With Applications in Powder Metallurgy, Ink, and Paint*, D. J. Shanefield, Ed. Boston, MA: Springer US, 1995, pp. 115–130.

[2]   D. W. Dees, T. D. Claar, T. E. Easler, D. C. Fee, and F. C. Mrazek, 'Conductivity of Porous Ni / ZrO2 - Y 2 O 3 Cermets', *J. Electrochem. Soc.*, vol. 134, no. 9, p. 2141, Sep. 1987, doi: 10.1149/1.2100839.

[3]   'Zirconia   Powders | https://www.tosoh.com/'.   https://www.tosoh.com/our-products/advanced-materials/zirconia-powders

[4]   B. C. H. Steele, 'Oxygen transport and exchange in oxide ceramics', *Journal of Power Sources*, vol. 49, no. 1, pp. 1–14, Apr. 1994, doi: 10.1016/0378-7753(93)01789-K.

[5]   J. A. Cebollero, R. Lahoz, M. A. Laguna-Bercero, and A. Larrea, 'Tailoring the electrode-electrolyte interface of Solid Oxide Fuel Cells (SOFC) by laser micro-patterning to improve their electrochemical performance', *Journal of Power Sources*, vol. 360, pp. 336–344, Aug. 2017, doi: 10.1016/j.jpowsour.2017.05.106.

[6]   A. Grosjean, 'Etude et réalisation par coulage en bande et co-frittage de cellules de pile à combustible à oxydes solides', phdthesis, École Nationale Supérieure des Mines de Paris, 2004.

[7]   PubChem, 'Methyl ethyl ketone'. https://pubchem.ncbi.nlm.nih.gov/compound/6569

[8]   A. K. Maiti and B. Rajender, 'Terpineol as a dispersant for tape casting yttria stabilized zirconia powder', *Materials Science and Engineering: A*, vol. 333, no. 1, pp. 35–40, Aug. 2002, doi: 10.1016/S0921-5093(01)01821-4.

[9]   M. Geagea, 'Nouvelles architectures de surfaces d'échanges de piles à combustible de type SOFC pour l'amélioration de l'efficacité électrochimique', Apr. 2017, Accessed: Aug. 23, 2019. [Online]. Available: https://pastel.archives-ouvertes.fr/tel-01901236.

[10]   'Tape Casting: Theory and Practice | Wiley', *Wiley.com*. https://www.wiley.com/en-us/Tape+Casting%3A+Theory+and+Practice-p-9781574980295

[11]   G. N. Howatt, R. G. Breckenridge, and J. M. Brownlow, 'Fabrication of Thin Ceramic Sheets for Capacitors*', *Journal of the American Ceramic Society*, vol. 30, no. 8, pp. 237–242, 1947, doi: 10.1111/j.1151-2916.1947.tb18889.x.

[12]   G. N. Howatt, 'Method of producing high dielectric high insulation ceramic plates', US2582993A, Jan. 22, 1952.

[13]   J. A. Cebollero, M. A. Laguna-Bercero, R. Lahoz, J. Silva, R. Moreno, and A. Larrea, 'Optimization of laser-patterned YSZ-LSM composite cathode-electrolyte interfaces for solid oxide fuel cells', *Journal of the European Ceramic Society*, vol. 39, no. 12, pp. 3466–3474, Sep. 2019, doi: 10.1016/j.jeurceramsoc.2019.02.049.

[14]   H. Iwai *et al.*, 'Power generation enhancement of solid oxide fuel cell by cathode–electrolyte interface modification in mesoscale assisted by level set-based optimization calculation', *Journal of Power Sources*, vol. 196, no. 7, pp. 3485–3495, Apr. 2011, doi: 10.1016/j.jpowsour.2010.12.024.

[15]   A. Konno *et al.*, 'Mesoscale-structure control at anode/electrolyte interface in solid oxide fuel cell', *Journal of Power Sources*, vol. 196, no. 1, pp. 98–109, Jan. 2011, doi: 10.1016/j.jpowsour.2010.07.025.

[16]   R. Mücke, N. H. Menzler, H. P. Buchkremer, and D. Stöver, 'Cofiring of Thin Zirconia Films During SOFC Manufacturing', *Journal of the American Ceramic Society*, vol. 92, no. s1, pp. S95–S102, 2009, doi: 10.1111/j.1551-2916.2008.02707.x.

[17]   N. H. Menzler, J. Malzbender, P. Schoderböck, R. Kauert, and H. P. Buchkremer, 'Sequential Tape Casting of Anode-Supported Solid Oxide Fuel Cells', *Fuel Cells*, vol. 14, no. 1, pp. 96–106, 2014, doi: 10.1002/fuce.201300153.

[18]   'Development of LSCF–GDC composite cathodes for low-temperature solid oxide fuel cells with thin film GDC electrolyte', *International Journal of Hydrogen Energy*, vol. 33, no. 14, pp. 3808–3817, Jul. 2008, doi: 10.1016/j.ijhydene.2008.04.034.

CHAPTER III

Components characterization and architecture analysis
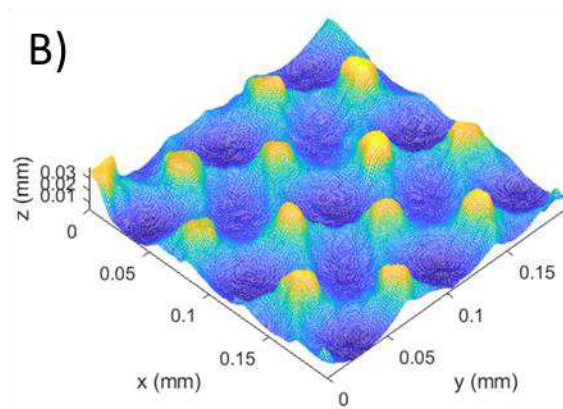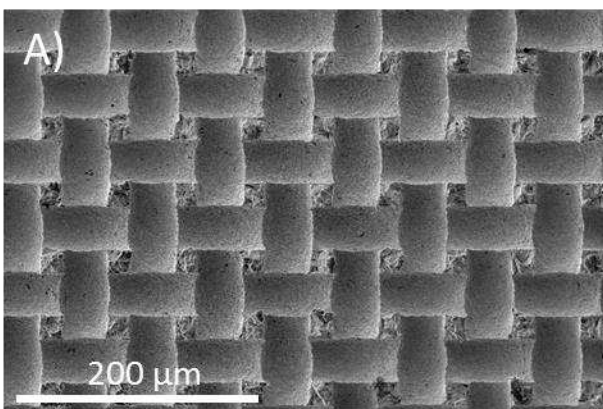
Chapter III abstract

In this chapter, we provide a detailed characterization of the cell components. This characterization includes a microstructural analysis and a chemical distribution probing. Additionally, the geometry of the architectures created by the soft template method and laser engraving are studied and characterized.

In the first subchapter, we describe the methodology used to characterize the cell components, followed by the results on the Type 1 cells (Figure III – abstract – 1) and Type II cells (Figure III – abstract – 2). The characterization is established by an extensive SEM imaging which allows measuring the thicknesses of the layers and the dimension of the porosity. The porosity analysis is carried out via a grey-scale segmentation post-treatment of SEM images realized using backscattered electrons on polished samples. An integrated energy dispersive X-ray spectroscopy detector is used to analyze the components in order to quantify the chemical dispersion and to probe any eventual singularity revealed by the chemical contrast. The third part of this chapter focuses on a geometrical characterization of the architectures. Particular attention is given to the architectures obtained by the soft template method (Figure III – abstract – 2 A and B). In this case, we calculate that the architectured effective surface is 28% larger than the equivalent planar surface and the arithmetic and harmonic mean values are 13.49 µm and 3.17 µm respectively.

The microstructural and chemical characterizations show that the materials environment at the interfaces remains unchanged between planar and architectured cells in both Types I and II cell pairs. Based on the layer thicknesses and the architecturation characterization and calculations we can compare the mean electrolyte thickness of the architectured cells to the one of the planar cells (Type I – 9.9 µm and Type II – 13.3 µm). In both cases, the mean value is superior to the planar electrolyte thickness. Thus, we may assume an equivalency between the cells keeping in mind that the approach is conservative, meaning that any potential performance increase for the architectured configuration cannot be due to a reduced impedance.

In conclusion, the Type I and Type II cells present adequate components characteristics and apparent equivalency between the architectured and planar cells based on the criteria imposed in this work. Thus, they are validated for electrochemical performance comparison.

Chapitre III résumé

Dans ce chapitre, nous présentons une caractérisation détaillée des composants cellulaires. Cette caractérisation comprend analyses microstructurales et analyses chimiques élémentaires. En outre, la géométrie des architectures créées par la méthode du template souple et la gravure laser est étudiée et caractérisée.

Dans le premier sous-chapitre, nous décrivons la méthodologie utilisée pour caractériser les composants cellulaires, puis les résultats sur les cellules de Type 1 (Figure III – abstract – 1) et les cellules de Type II (Figure III – abstract – 2). La caractérisation de l'épaisseur des couches et des dimensions de la porosité est réalisée par imagerie MEB. Concernant la porosité, un post-traitement den segmentation en échelles de gris des images MEB en contraste d'électrons rétrodiffusés sur des échantillons polis a été réalisé. Un détecteur intégré de spectrométrie dispersive en énergie de rayons X est utilisé pour analyser les composants et quantifier la dispersion chimique, et sonder toute éventuelle singularité révélée par le contraste chimique. La troisième partie de ce chapitre a porté sur une caractérisation géométrique des architectures. Une attention particulière est accordée aux architectures obtenues par la méthode du template souple sacrificiel (Figure III – abstract – 2A et B). Dans ce cas, nous calculons que la surface effective développée par l'architecture est supérieure de 28% à la surface plane correspondante, et que la moyenne arithmetique et harmnique de l'architecturation sont respectivement de 13.5 µm et 3.17µm.

Les caractérisations microstructurales et chimiques montrent que les matériaux dans l'environnement immédiats des interfaces restent inchangés entre cellules planes et architecturées pour les cellules de type I et II. Sur la base des épaisseurs des couche, et de la caractérisation et des calculs d'architecture, nous pouvons comparer l'épaisseur moyenne de l'électrolyte des cellules architecturées à celle des cellules planes (Type I - 9,9 µm et Type II - 13,3 µm). Dans les deux cas, la valeur moyenne est supérieure à l'épaisseur d'électrolyte planaire. On peut donc supposer une équivalence entre les cellules en gardant à l'esprit que l'approche est conservatrice, puisque globalement l'impédance de la configuration architecturée est supérieure à la planaire ; ainsi, tout incrément de performances qui lui est associé ne peut être attribué à une moindre résistance.

En conclusion, les cellules de type I et de type II présentent des caractéristiques de composants adéquates et une équivalence apparente entre les cellules architecturées et les cellules planes sur la base des critères imposés dans ce travail. Ainsi, elles sont validées pour la comparaison des performances électrochimiques.
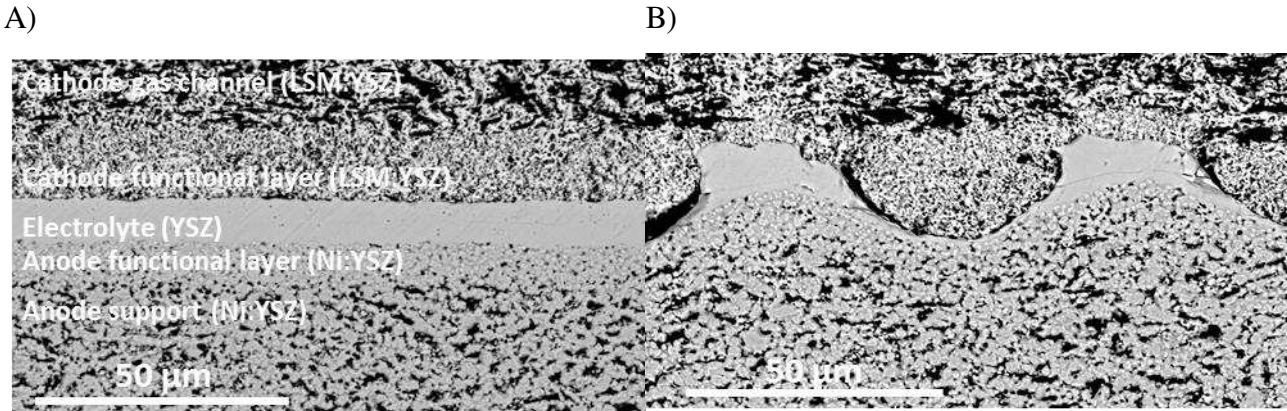
A)   B)

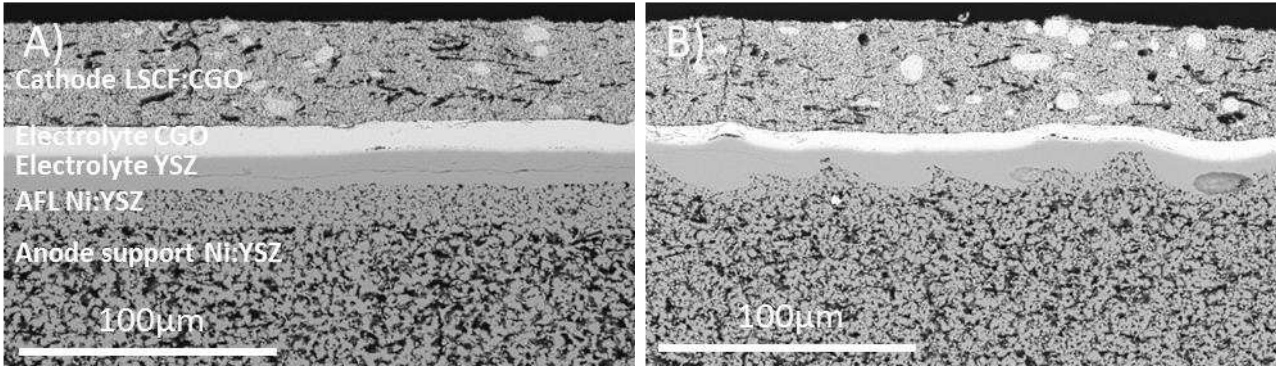Figure III - abstract - 1 Type I cross-section SEM observation. A) Planar cell; B) Cathode architectured cell

Figure III - abstract - 2 Type II cross-section SEM observation. A) Planar cell; B) Cathode architectured cell
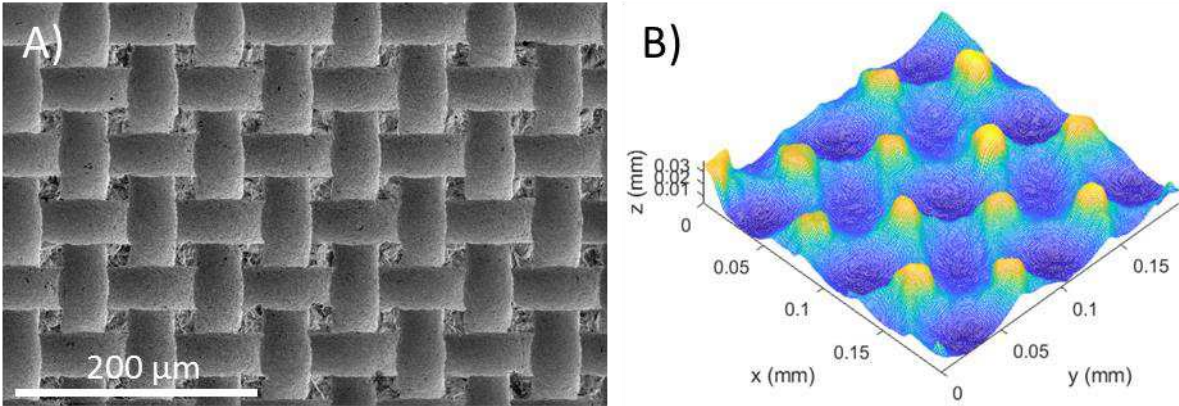
Figure III - abstract - 3 Sintered architectured anode via the soft template method : A) SEM; B) Profilometry

CHAPTER III Components characterization and architecture analysis

Contents

List of figures

Liste of tables

I.   Introduction

In this chapter, a detailed study of the fuel cells and their components is established, based on microstructural characterization and chemical analysis. The former is realized by SEM observations, and the latter consists of EDS analysis of each component composition. Several objectives motivate those analyses such as an experimental comparison between planar and architectured cells, the understanding of the electrochemical behavior at the architectured interfaces, and finally the feeding of the numerical model with realistic cell parameters. Two types of cells are analyzed: Type I and II, each presenting an architectured and a planar cell. An extended study of the architecturation is established using an optical profilometer AltiSurf500 and a Matlab-based data analysis and representation.

The next subchapter will be focused on the microstructural and chemical analysis of cell components. It is important to note that the Type I fuel cells were chronologically fabricated after the Type II cells but we have chosen this appellation due to the usage of the state of the art materials (Ni, YSZ, LSM) and the number of electrolyte layers. Hence certain fabrication optimizations have been taken into account such as the Ni concentration difference between the anode support and the AFL, the presence of a cathode gas channel layer as well as the cathode materials dispersion procedure. In the following subchapter, we will propose a detailed characterization of architecturation obtained using a soft template application and laser engraving. An original analysis method is detailed and used to extract the geometrical parameters of the two different architectures resulting from both processes.

The characterization of the cells will allow us to establish a comparison procedure based on the following criteria

- The same material environment (materials and microstructure) must be found at the interfaces of the planar and the architectured electrolytes
- The harmonic mean value of the thickness of the architectured electrolyte must be taken into account during the electrochemical performances analysis

II. Component characterization

II.A. Method

Scanning Electron Microscopy (SEM) is a powerful tool for microstructural and chemical analysis and is used in every stage of the study. It provides thorough information on grain size and distribution as well as chemical distribution, porosity characterization, interface quality, layer thickness, etc. A FEB FEI NNS450 SEM (Figure III − 1) equipped with secondary electrons detector, backscattered electrons detector, and energy dispersive X-ray spectroscopy probe has been used. Due to the low electron conductivity of certain materials, a thin (4 nm) gold-palladium layer is deposited by ion beam sputtering Figure III − 2.
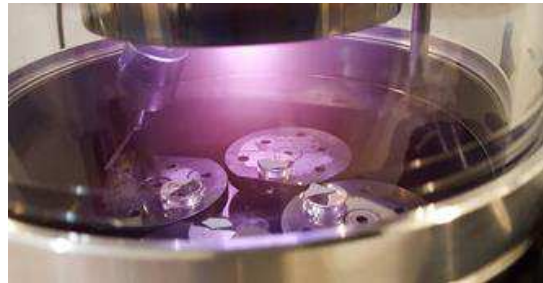
Figure III - 1 FEB FEI NNS450 SEM   Figure III - 2 Au-Pd Sputtering on nonconducting ceramics

II.A.1. Layer thickness measurement

The layer thickness is a relevant parameter for the electrodes as well as the electrolyte.

A direct proportionality between the electrolyte thickness and its resistivity was mentioned before, whereas the thickness influence in the performance of the electrodes is more difficult to establish. However, taking into account the necessity of gas distribution and the percolation of the electron-conducting phases, the functional part of the electrode layer, i.e. the part where electrode reaction indeed occurs, usually represents less than 50 µm. Additionally, the anode support provides the mechanical strength of the cell, and its thickness needs thus to be greater (typically from 250 to 500 µm).

II.A.2. Average grain size assessment

Grain size is an important characteristic, especially for electrolyte layers. For this characterization, open (without electrodes) electrolyte surfaces are analyzed with an intercept

technique, where a random measuring surface is drawn over the image, and the number of grains is counted.

This analysis is relevant for the electrolyte and the barrier layer since the grain boundaries may have a blocking effect which can induce an additional contribution to the resistance. The effect of the grain boundary is on the opposite much more difficult to quantify for electrode materials. As mentioned previously, the layer resistivity, constituting a part of the electrolyte, depends on its thickness and its microstructure (density, grain size).

Thus, grain size is an essential characteristic for both the electrolyte and the barrier layer, as grain boundary resistance is linked to the global grain boundaries area concentration and thus to the inverse of grain size. In this work, we consider that the grain boundary has essentially a blocking influence on the conductivity of the materials. Hence a significant grain size must be targeted to increase the ion conductivity of the electrolyte. Furthermore, an adequately sintered material will exhibit a thermodynamic equilibrium, i.e. a morphology steady-state, which might evolve less during operation, granting mechanical stability of the electrolyte.

II.A.3. Porosity characterization

Porosity is influenced by a multitude of factors such as the sintering process, oxide reduction, binder, and pore-former elimination. Although the quantity of additive is imposed by the fabrication protocol and the sintering and reduction mechanisms are well known, exact anticipation of the porosity characteristics can be challenging. Hence, careful characterization is necessary.

SEM observation is considered to be the most direct method for quantitative multiscale porosity study, based on image grey-level interpretation of polished or unpolished samples. However, the porosity deduction is generally impaired by the surface quality of the sample. Nevertheless, with careful sample preparation, this method provides an excellent porosity analysis. Furthermore, this method of porosity size extrapolation is valid if the material is considered as stationary (not presenting any properties gradient).

As mentioned, the basic principle is to post-treat SEM images by studying the grey level distribution in order to analyze the sample porosity. Based on the literature [1] image treatment software such as ImageJ or Gimp are used applying integrated threshold and color binarization

tools. The auto binarization usually determines the average intensity of the image and finds a threshold in a way that half of that intensity is sent to the background. This analysis is relevant for the electrode layers where the porosity optimization is an essential characteristic for adequate gas distribution.

A contrario, the electrolyte has the function to separate the electrodes, which means it needs to be perfectly dense. Furthermore, it ensures the ion conduction between the electrodes, which is facilitated by the dense microstructure as well as by the adequate average grain size, as mentioned in II.A.2.b.

For this analysis, cross-section samples are coated in epoxy resin, thoroughly polished, and rendered electrically conductive via gold-palladium sputtering. Observations via backscattered electrons accelerated at 20 kV have been analyzed with ImageJ software.

II.A.4. Chemical distribution

This characteristic is crucial for the electrodes, composed of different materials and where the material distribution influences critically the active triple phase boundaries concentration and percolation.

A chemical contrast may be observed using backscattered electrons. However, to obtain a semi-quantitative measurement, an EDS analysis is recommended. Thus, estimation of the elemental distribution is established by EDS scanning of a portion of the component in the cross-section samples. Furthermore, a line scanning is carried out perpendicularly to the surface to study the variation of composition throughout the cell.

II.B.   Type I

Type I cells are fabricated to study the impact of the architecturing on cells composed of state-of-the-art materials (Ni:YSZ anode, YSZ electrolyte, LSM:YSZ cathode as shown in Figure III – 3) and with electrodes containing a gradual porosity. The cells observed in this characterization subchapter were previously used for electrochemical performance measurement which induced elevated stress on the cell due to the mechanical pressure in the measurement setup as well the thermal gradient and variation in the cell during the measurement, oven heating, and cooling. Moreover, the polishing procedure is fairly aggressive and may alter the visible microstructure provoking layer separation and fracturing.

It is important to note that the architectured interface has the same materials environment as the planar one. Both of the interfaces are between the electrolyte and the cathode functional layer.
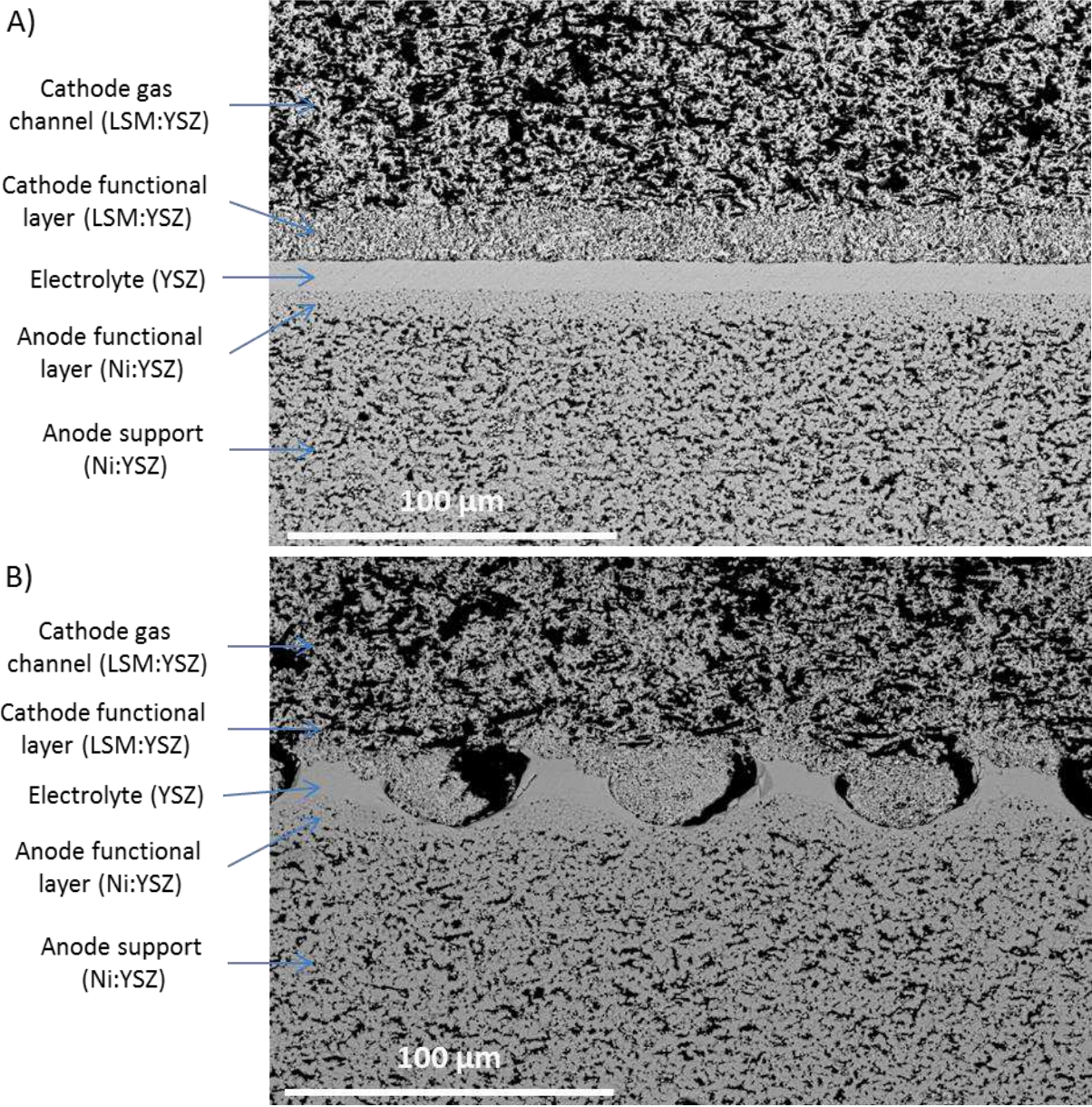

Figure III - 3 Type I cross-section observation; A) Planar cell; B) Architectured cell (cathode/electrolyte interface)

II.B.1. Electrolyte

II.B.1.a)   Electrolyte density and integrity

In figure III – 3, large scale SEM images are presented where we can observe a significant portion of the cells. There are no apparent pores in this section, and we indeed observed the same characteristics on the totality of the cell. Moreover, in both planar and architectured cases, there are no visible transversal cracks, even though the electrolyte has a very low thickness in some areas of the architectured sample. Thus, the hypothesis that architectured cells present potentially mechanical strengthening is partially supported here. The gas tightness of the electrolyte as logically deduced from the electrolyte microstructure could be further confirmed by the value of the open-circuit voltage as mentioned in the fabrication protocol validation (Chapter II. IV. Protocol validation and discussion).

As we zoom in (Figure III – 3 bis), we perceive a fracture parallel of the interface in the electrolyte in both architectured and planar cells. According to the direction of this fracture, we can assume that it is induced by the measurement setup platform pressure on the cells or the polishing procedure. We can also observe some black areas close to the architecture patterns. These may be induced by the polishing procedure.
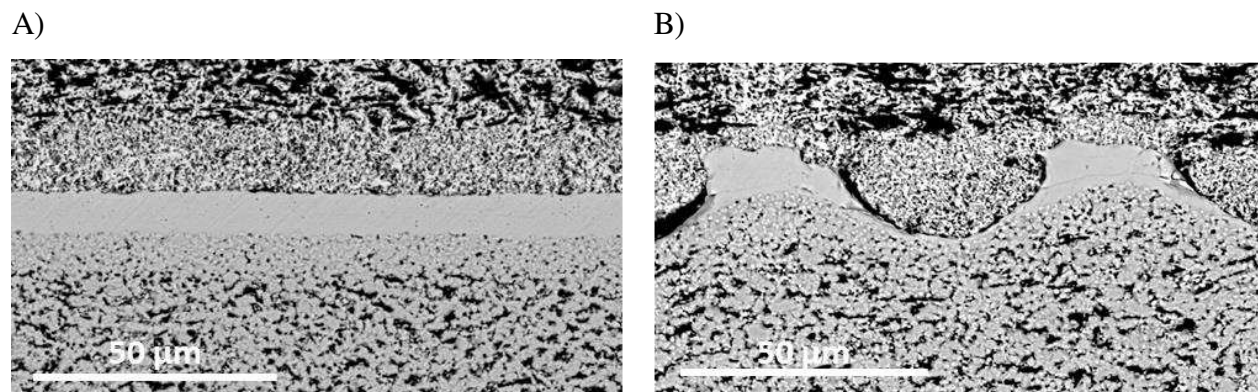
A)

B)

Figure III – 3 bis Type I cross-section observation; A) Planar cell; B) Architectured cell
(cathode/electrolyte interface)

II.B.1.b)   Electrolyte thickness

The variation of the electrolyte thickness is one of the principal parameters influencing the cell performances. Its resistance is directly proportional to its thickness and, to compare the

architectured and planar cells the minimum, the maximum, and the harmonic mean thickness need to be measured. For the minimum and maximum values, a direct measurement on the cross-section images is sufficient and the results are reported in Table III – 1. Due to the complex geometry of the architecture, the harmonic mean thickness is further studied using Matlab in the next chapter where a detailed analysis of the architecturation is provided.

Table III - 1 Type electrolyte thickness values			
	Planar	Max architectured	Min architectured
Electrolyte	9.9	14.1	3.4

The maximum and the minimum thickness values of the electrolyte of the architectured cells is significantly different from the one of the planar cell and thus, an equivalency is difficult to establish. However, as mentioned, the architecture of the interface has a complex geometry and further study is necessary to calculate the mean electrolyte.

II.B.1.c)   Grain size assessment

Using the intercept method in Figure III – 4 we can calculate the average electrolyte grain size considering the material as stationary.
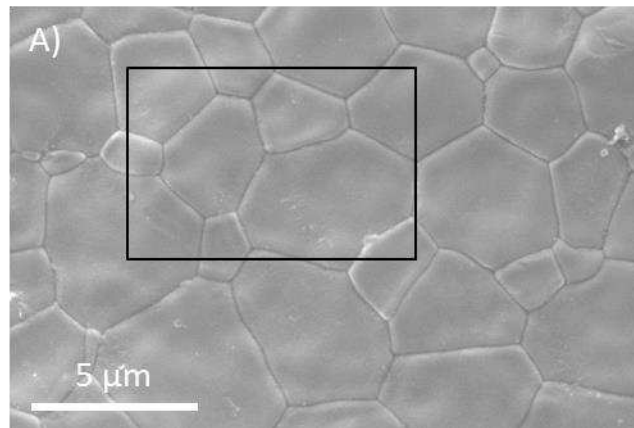

Figure III - 4 Type I electrolyte grain size assessment

In this case, the open surface is composed of a sintered YSZ electrolyte, for 5h at 1400°C. The average grain size is $2.05\,\mu m$ which represents approximately $20\,\%$ of the measured planar thickness and 60% of the minimum architectured thickness. This means that at the minimum

electrolyte thickness zones, the electrolyte is almost monocrystalline, promoting quasi-perfect conductivity condition. Even in the thicker parts of the electrolyte, the concentration of grain boundaries is limited.

II.B.2. Anode

II.B.2.a)   Anode materials distribution

In Type I cells, the anode support has a slightly more elevated concentration of Nickel in order to promote the electronic conductor percolation through the high thickness of the layer. A pore former is added in the anode support slurry to adjust the porosity to 35 %, whereas in the AFL the porosity is induced by the binder elimination and NiO reduction.

Figure III – 5 show the zones that have been chosen for the EDS analysis.
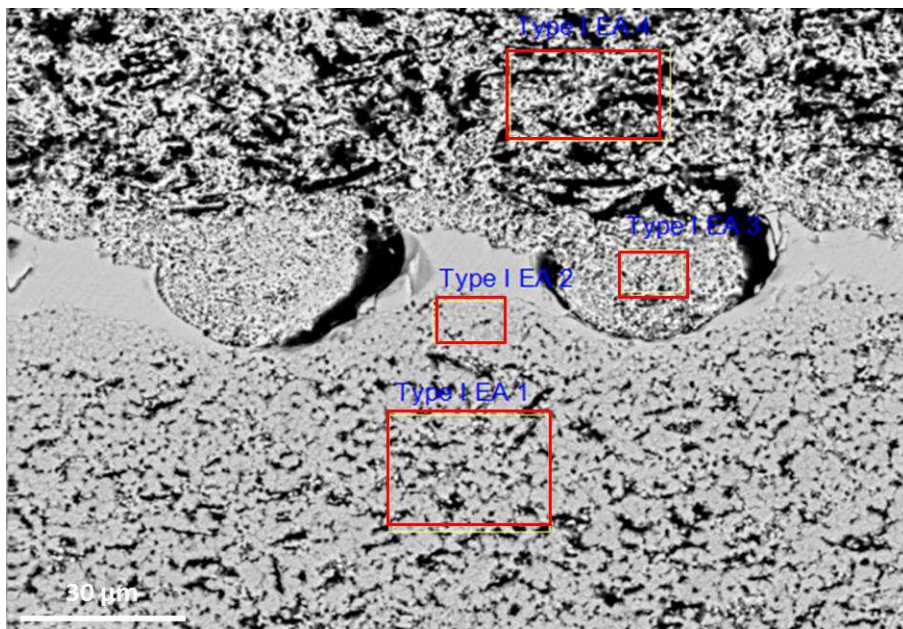
Figure III - 5 EDS scanning zones on Type I architectured cell

The anode support layer and the anode functional layers are analyzed by probing the zones EA1 and EA 2 respectively. Figure III – 6 and III – 7 show the anode layers EDS spectra and the related zone identification on the SEM image. All the potentially present elements are selected for identification and the atomic concentration (%) is reported in Table III – 3.

A)
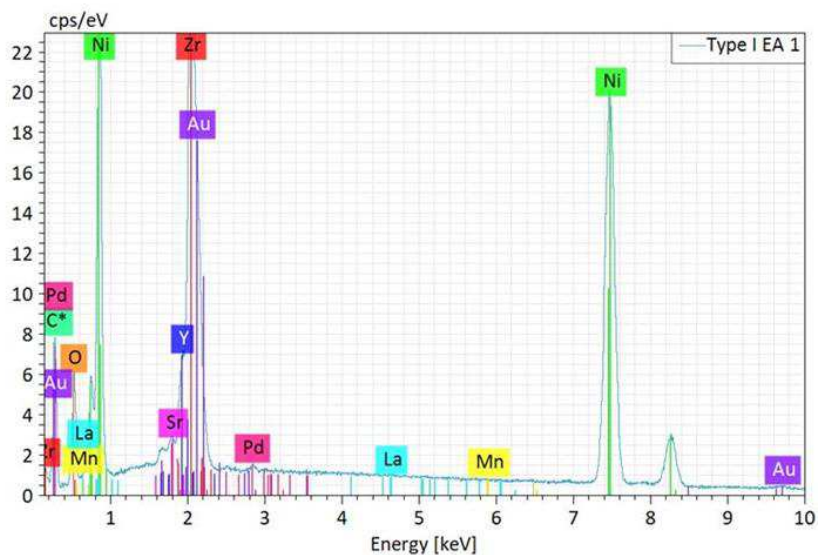
B)

Figure III - 6 EDS analysis of zone EA 1 (anode support) A) EDS Spectrum B) Scanning zone localization

A)

B)

Figure III - 7 EDS analysis of zone EA 2 (AFL) A) EDS Spectrum B) Scanning zone localization

Table III - 2 Type I cells anode composition - atomic concentration (%)								
Spectrum	C	O	Ni	Zr	Y	Mn	La	Sr
EA 1	0.0	31.7	44.6	20.3	3.4	0.0	0.0	0.0
EA 2	0.0	39.2	33.1	22.9	3.9	0.1	0.0	0.0

As expected, the nickel concentration is more elevated in the anode support than in the AFL. The slightly higher concentration in the AFL of YSZ allows the optimization of the triple-phase boundary concentration as well as the complementarity with the electrolyte.

II.B.2.b)   Anode porosity

The porosity analysis here reveals an insufficient porosity in both anode support and anode functional layer. Binarized zones for porosity analysis of the anode are shown in figure III – 8.
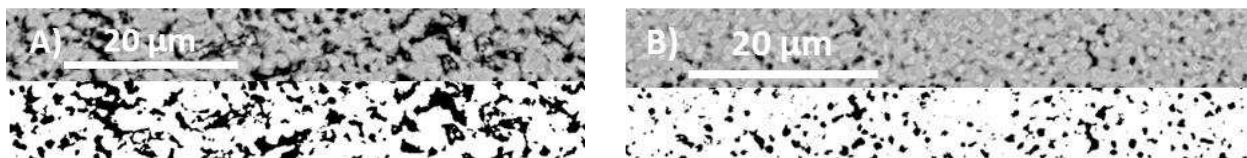
Figure III - 8 Type I cell original and binarized SEM images of anode zones for porosity analysis. A) Anode support; B) AFL

The insufficient porosity may hinder the electrochemical performances of the cells. For this reason, we have chosen to study only the cathode-electrolyte interface architecturation, maintaining similar anode properties.

II.B.3. Cathode

II.B.3.a)   Cathode materials distribution.

The two cathode layers, namely the Cathode Functional Layer (CFL) and the cathode gas channel (CGC) are composed of an LSM:YSZ composite with different material ratios. The CFL needs to present a higher number of active triple phase boundaries, and it is thus composed of a 50:50 %vol materials ratio and a decreased porosity. The CGC has the role of a current collector and gas diffusion support. Hence it has an increased quantity of electronic conductors (LSM:YSZ 80:20 %vol) and approximately 50% porosity. The EDS analysis of the cathode is visible in figures III – 9 and 11 and the results of the element atomic concentration are reported in Table III – 3.
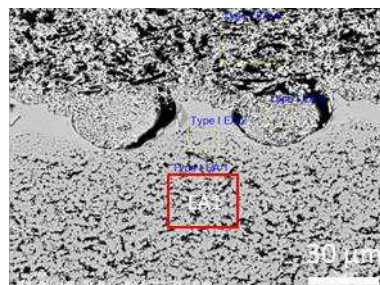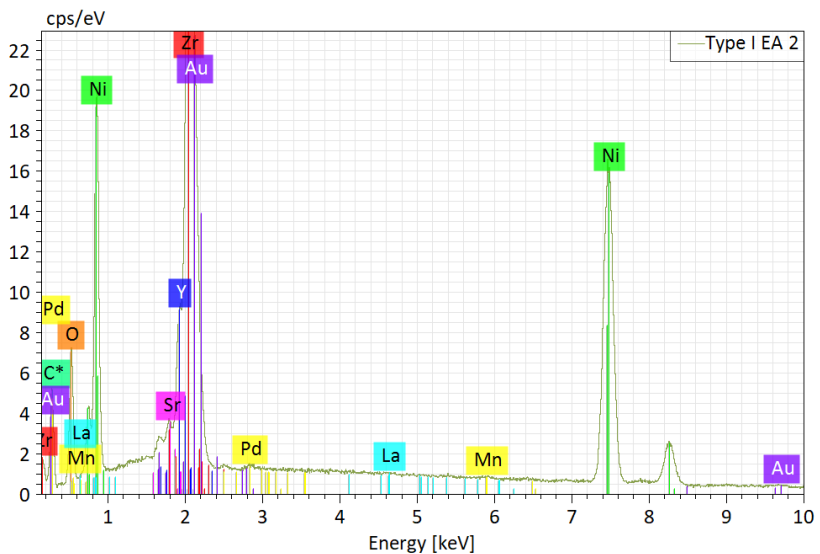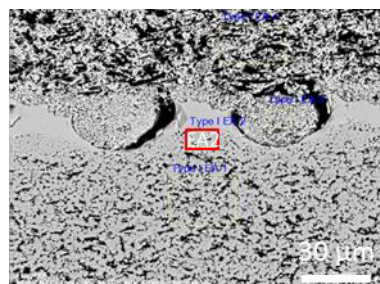
A)
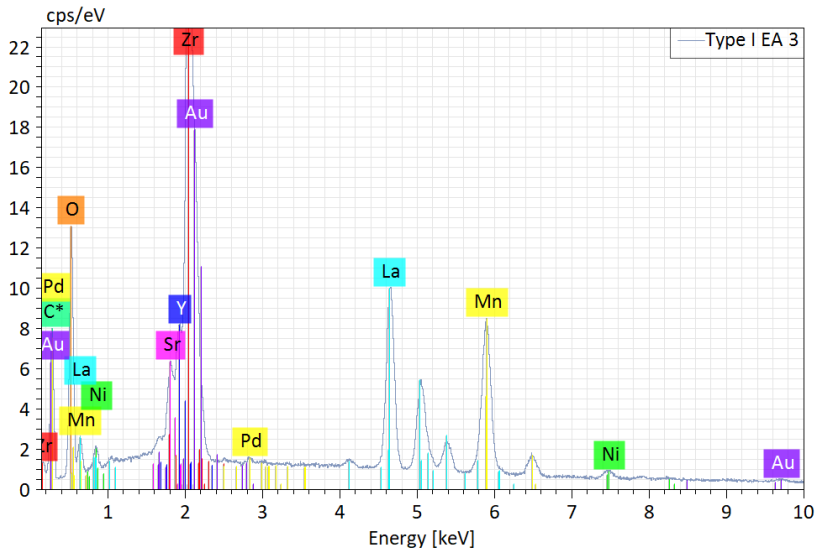
B)
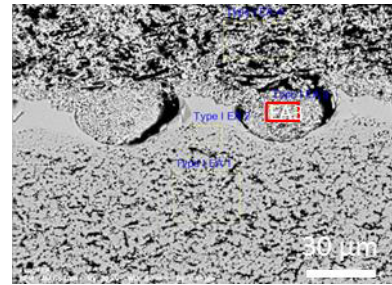
Figure III - 9 EDS analysis of zone EA 3 (CFL) A) EDS Spectrum B) Scanning zone localization

A)
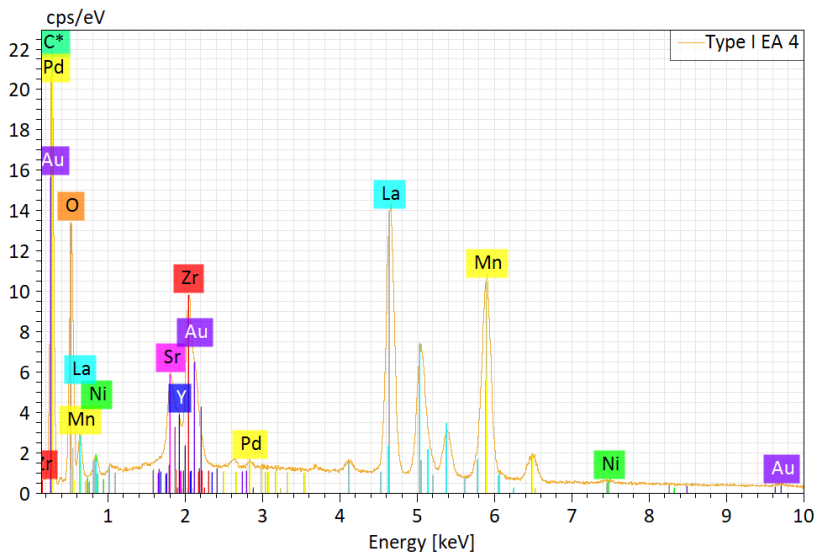
B)
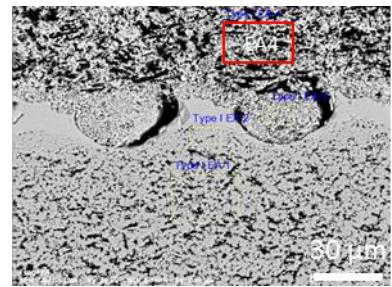
Figure III - 10 EDS analysis of zone EA 4 (Cathode gas channel) A) EDS Spectrum B) Scanning zone localization

Table III - 3 Cathode composition – atomic concentration (%)							
Spectrum	C	O	Ni	Zr	Y	Mn	La	Sr
EA 3	0.0	62.1	0.6	16.0	2.9	9.3	7.3	1.8
EA 4	0.0	58.5	0.3	6	1.1	17.2	13.7	3.2

In this case, the porosity analysis reveals elevated porosity in both CFL (34%) and CGC (57%). The slurry formulation has been established in order to achieve approximately 50% of porosity in the CGC and 30% in the CFL, which signifies that the space left during the additive elimination was slightly underestimated. Binarized zones for porosity analysis of the cathode are shown in figure III – 11.
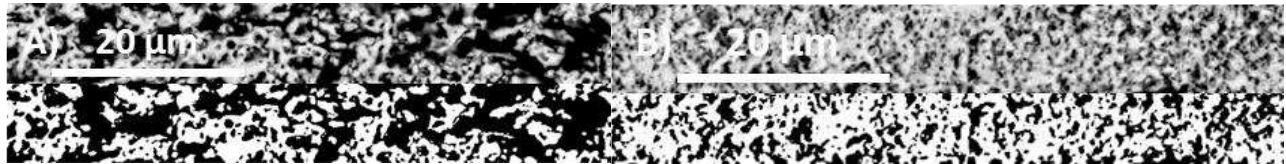
Figure III - 11 Type I cell original and binarized SEM images of the cathode for porosity analysis. A) CGC; B) CFL

II.B.4. Overview

Table III – 4 displays an overview of the measured parameters.

Table III - 4 Type I cells parameters overview					
Component	Composition (Materials and volume ratio)	Porosity (%vol)	Flat thickness (µm)	Max architectured thickness (µm)	Min architectured thickness (µm)
Anode support	Ni:YSZ 44:56	27	334±5	334±5	334±5
AFL	Ni:YSZ 44:56	11	8.4	10.8	5.2
Electrolyte	YSZ	0	9.9	14.1	3.4
CFL	LSM:YSZ 50:50	34	15.5	21.4	5.4
CGC	LSM:YSZ 50:50	57	61±5	61±5	61±5

Based on the layer thicknesses and especially the one of the electrolyte, the type I cells present a satisfactory equivalency between the architectured and the planar cells. As observed in figure III - 3, the architectured electrolyte penetrates the CFL through approximately 75 % of its thickness. In this configuration the entire interface is uniform and the triple-phase boundaries remain

homogeneously distributed. Thus, the microstructure of the cathode side of the planar and the architectured fuel cells confirm the equivalency, justifying an electrochemical comparison.

II.C. Type II

Type II fuel cells are fabricated to demonstrate the feasibility of the architecturing method for the production of industrial cells. They are composed of anode support and functional layer, an electrolyte covered by a CGO barrier layer to separate it from an LSCF:CGO composite cathode. In this study and concerning this type of cell, we concentrate on the architecturing of the anode electrolyte interface. Figure III – 13 presents the Type II cells, their layer and materials composition (Ni:YSZ anode, YSZ electrolyte, CGO barrier layer, LSCF:CGO cathode). It is important to note that the architectured interface has the same materials environment as the planar one. Both of the interfaces are between the electrolyte and the anode functional layer.
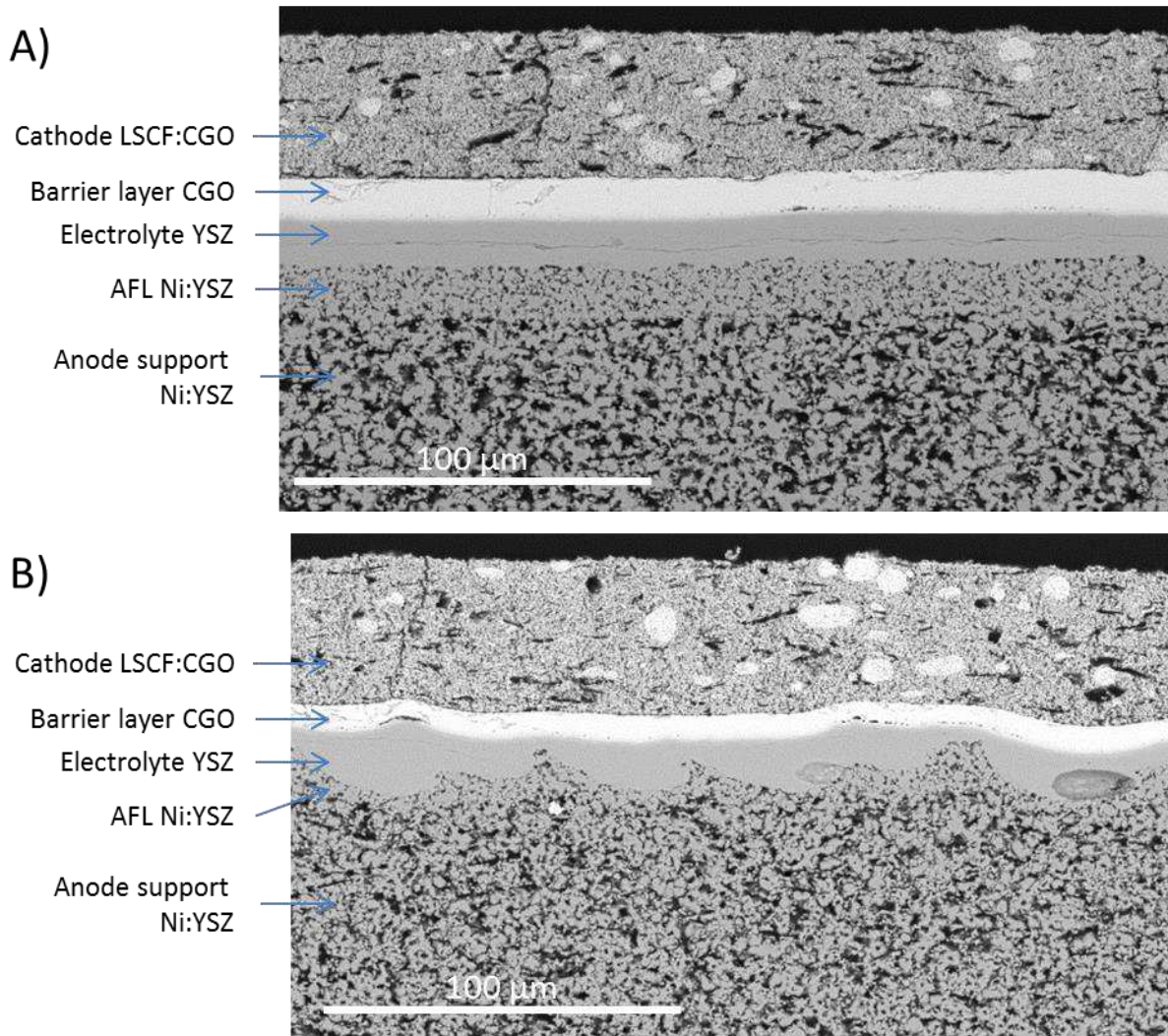
Figure III - 12 Type II cross-section observation (large scale): A) Planar cell; B) Architectured cell

II.C.1. Electrolyte and barrier layer

II.C.1.a)   Density and integrity

The electrolyte and the barrier layer have similar properties concerning ionic conduction and electronic insolation. Although the density of the barrier layer is a less stringent requirement, it promotes better ion conductivity and chemical protection than a porous microstructure. Here we also present a cross-section image of a large portion of the cell to study the integrity of the layers (Figure III – 13 A and B).

Electrolyte

As was the case for the Type I cells, the electrolyte layer does not present any fractures perpendicular to the interface. Thus, it should ensure the good electronic insolation and gas tightness of the electrodes. To confirm the hypothesis on a microscopic scale, we verify that the open-circuit voltage is close to the theoretical value (1.18 V at 800°C). However, in this case, we observe again a crack parallel to the interface through the entire length of the electrolyte in the planar cell, which is readily observed in figure III − 13 A. Based on the cell mechanical integrity after sintering and during the tests, we consider that this crack is either caused by the measurement conditions (fuel-cell testing pressure, sudden temperature variations) or during the polishing procedure. The lack or the limited presence of this type of fracture in the architectured cell supports the hypothesis that the architecture acts as bridge pillars and stabilizes the cell. The electrolyte in both cells appears to have an adequate density, as no pores are observed on the entire length. However, some closed pores and limited delamination can be observed at the electrolyte/barrier interface (figure III − 13) which may hinder the mechanical stability of the cell in the long term as well as the electrochemical performances as it induces supplementary resistivity of the materials.

A)
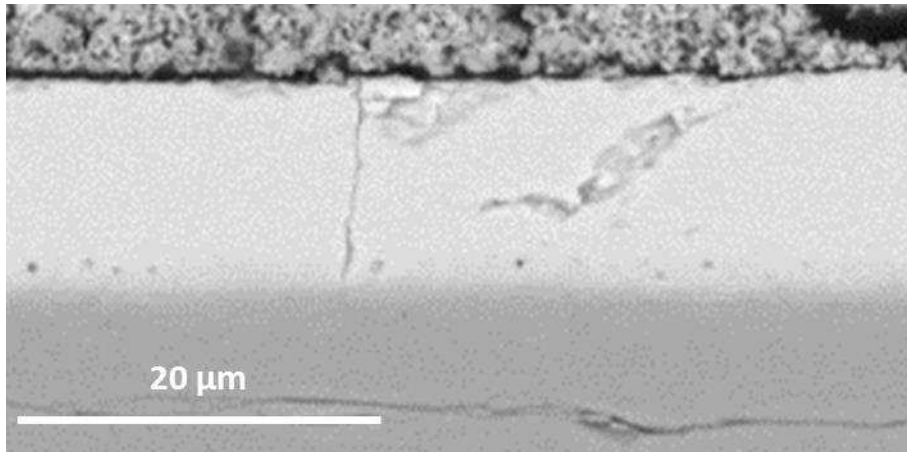
B)
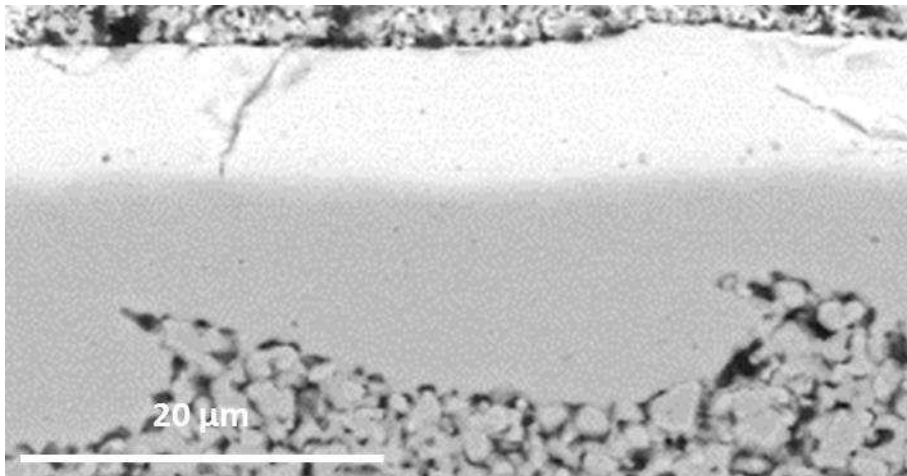
Figure III - 13 Type II cells barrier layer transversal fractures. A) Planar cell; B) Architectured cell

Barrier Layer (electrolyte CGO)

The barrier layer in this example presents several cracks perpendicular to the interface. These cracks may prove to be problematic in the long term as they could present material diffusion pathways as well as mechanical fragility. However, they do not hinder the gastightness and electron insolation of the dense block (electrolyte + barrier layer) in short term operation.

II.C.1.b)   Electrolyte and barrier thickness

To better interpret the electrochemical measurement, it is important to report the electrolyte thickness (Table III – 5) as it intervenes in the series resistance of the cell.

Table III - 5 Type II cells electrolyte and barrier layer thickness assessment					
Component	Composition (Materials and volume ratio)	Porosity (%vol)	Flat thickness (µm)	Max architectured thickness (µm)	Min architectured thickness (µm)
Electrolyte	YSZ	0	13.3	15 (±2.6)	5.4 (±0.9)
Barrier	CGO	0	11	7.2 (±0.7)	6.2 (±0.3)

The measurements reveal that the average electrolyte thickness of the architectured cells is close to the one of the planar cells. However, further study of the architecturation is necessary to calculate the harmonic mean electrolyte thickness and to establish the equivalency of the cells. .

II.C.1.c) *Grain Size assessment*

The grain size assessment here is based on observation of the free surface of the barrier layer and the electrolyte layer average grain size is deduced from the measurement on type I cells electrolyte. This is necessary because the YSZ layer is covered by the CGO layer. The scanned zones are represented in Figure III – 14 and the results are reported in Table III – 6.
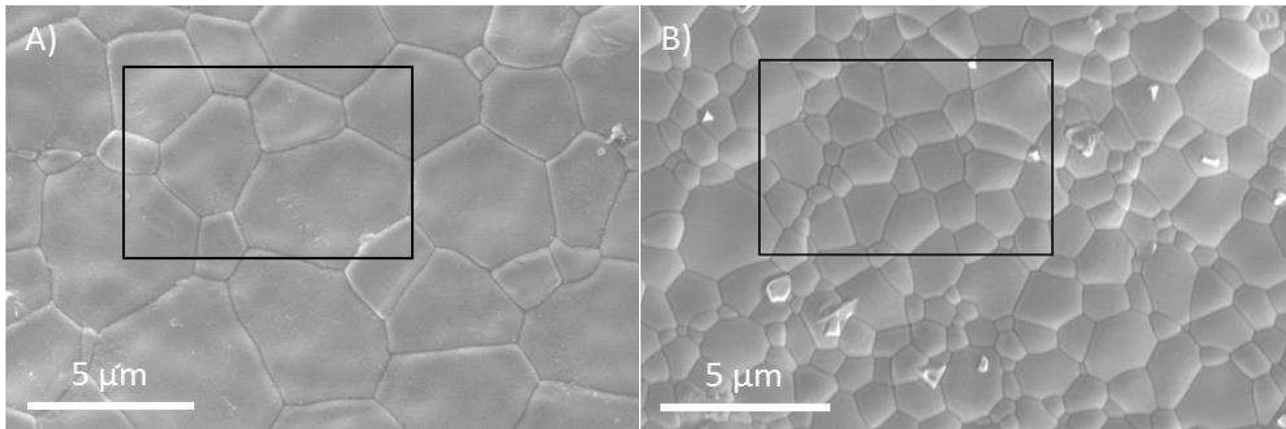
Figure III - 14 Type II cells electrolyte and barrier grain size assessment A) YSZ B) CGO

Table III - 6 Type II cells electrolyte and barrier grain size assessment A) YSZ B) CGO	
Component	Grain size (µm)
YSZ electrolyte	2.05
CGO barrier layer	0.97

The CGO grains are smaller than the YSZ grains which means that the barrier layer may present a higher resistance. However, CGO is a better ionic conductor than YSZ [2] which should partially compensate for this difference. Furthermore, the barrier layer is often thinner than the electrolyte.

II.C.2. Anode

The anode support and the AFL are established using the same materials ratio (Ni:YSZ 44:56 %vol) but with different porosity. In the anode support slurry, a pore former is added to adjust the porosity to 35 %, whereas in the AFL the porosity is induced by the binder elimination and NiO reduction.

II.C.2.a) *Phase distribution (materials)*

In figures III – 15 and 16, we may study the materials present in both the anode support and the anode functional layer. The atomic concentration (Table III – 7) and the ratio between Ni and YSZ have a minor variation between the two layers. This is because both layers were prepared with the same slurry composition solely differentiated by the presence of pore former in the anode support slurry. The lack of optimization of the nickel quantity variation in this cell is due to its fabrication prior to the Type I cells, and this factor was not yet taken into account. However, the similitude of the composition of the two layers facilitates the electrochemical study, because the only varying parameter is the porosity.

A)
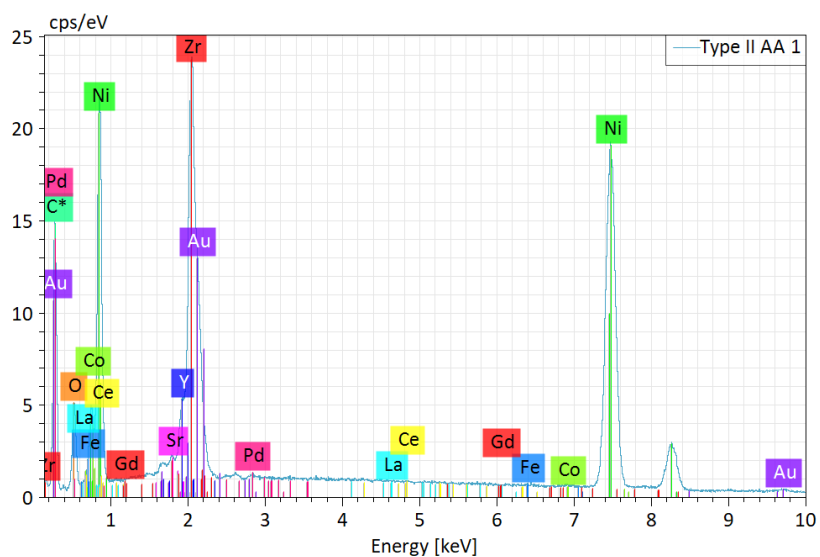
B)
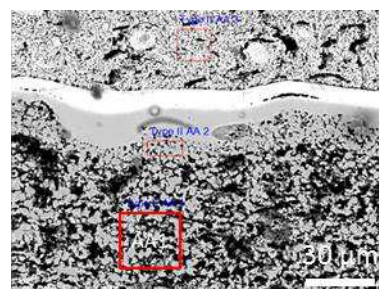
Figure III - 15 EDS analysis of zone AA1 (Anode support) A) EDS Spectrum

B) Scanning zone localization

A)
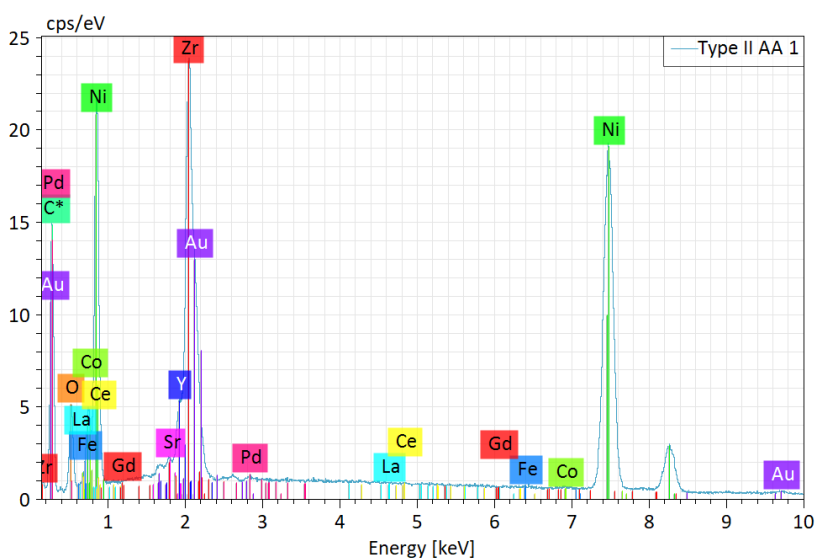
B)
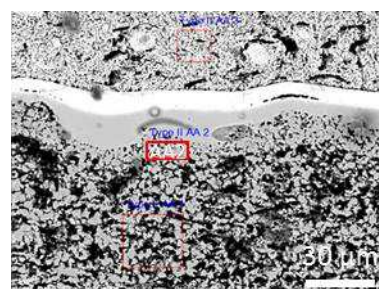
Figure III - 16 EDS analysis of zone AA2 (AFL) A) EDS Spectrum

B) Scanning zone localization

Table III - 7 Type II cells anode composition - atomic concentration (%)										
Spectrum	C	O	Ni	Zr	Y	Ce	Gd	La	Sr	Co	Fe
AA 1	0.0	28.7	49.0	18.8	3.3	0.0	0.0	0.0	0.0	0.2	0.0
AA 2	0.0	27.9	49.4	18.9	3.4	0.1	0.0	0.0	0.0	0.2	0.1

We observe some traces of cathode materials. Our hypothesis is that some material has been displaced during the polishing procedure.

II.C.2.b)   Porosity

Adequate porosity is measured for both AS and AFL (37 %vol and 18.4 %vol respectively) demonstrated here in figure III – 17.
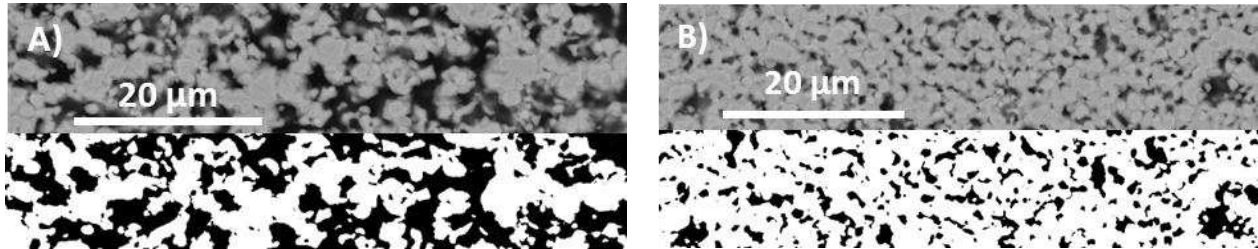
Figure III - 17 Binarized SEM images of anode zones for porosity analysis. A) Anode support; B) AFL

II.C.3. Cathode

II.C.3.a)   Materials distribution

The cathode layer is prepared by mixing LSCF and CGO powders in a 50:50 %vol ratio. In the backscatter electrons images in the SEM observation (Figures III – 18 and 19), we observe spots with different chemical contrast inside a well-dispersed matrix. Thus EDS probings of the matrix and the spots are carried out and the atomic concentration of the cathode can be found in Table III - 8.

A)
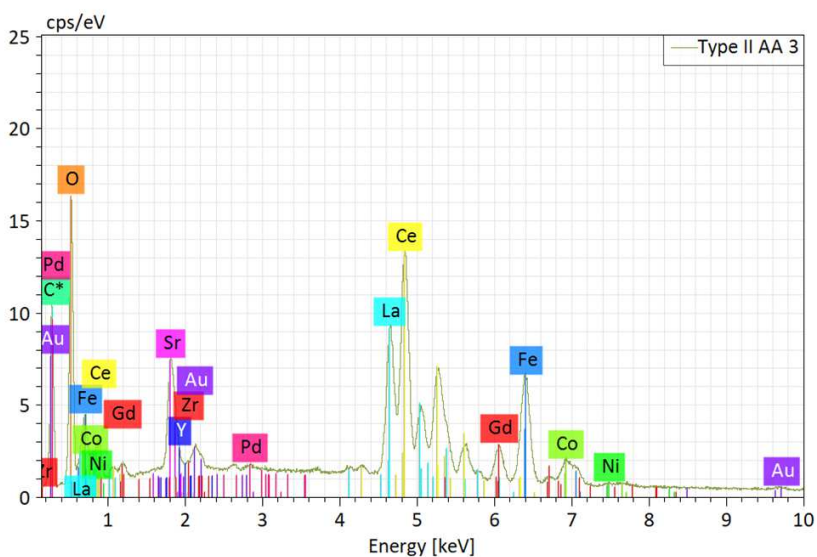
B)
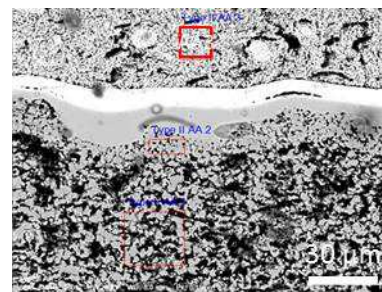
Figure III - 18 EDS analysis of zone AA3 (cathode) A) EDS Spectrum

Table III - 8 Type II cells cathode composition - atomic concentration (%)										
Spectrum	C	O	Ni	Zr	Y	Ce	Gd	La	Sr	Co	Fe
AA 3	0.0	52.4	0.5	0.0	0.0	14.3	1.6	8.6	5.3	3.7	13.7

The matrix probing reveals a fine distribution of the cathode composite.
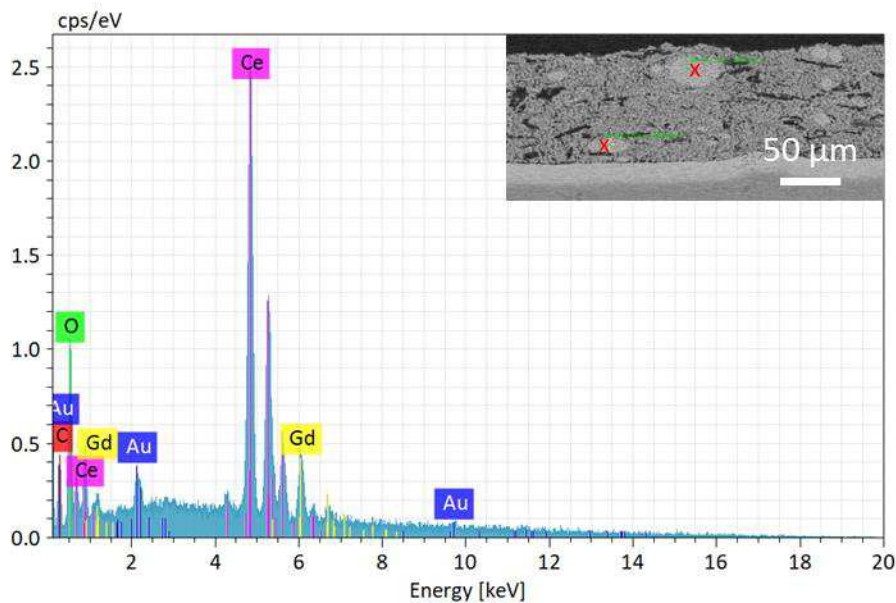
Figure III - 19 EDS analysis of segregation spots (cathode)

The probing of the segregated spots reveals that they are composed of CGO, which means that the milling/mixing procedure was not suitable during the cathode slurry preparation. Although the particle segregation may hinder the electrochemical performances, it should not be problematic for the cell comparison due to the utilization of the same cathode tape for both architectured and planar cells.

II.C.4. Overview

The microstructural parameters assessment and layer thicknesses of the Type II cells are reported in Table III – 9.

Table III - 9 Type II microstructural characterization assessment					
Component	Composition (Materials and volume ratio)	Porosity (%vol)	Flat thickness (µm)	Max architectured thickness (µm)	Min architectured thickness (µm)
Anode	Ni:YSZ 44:56	37	240 (±5)	240 (±5)	240 (±5)
AFL	Ni:YSZ 44:56	18.4	18.2	14 (±1.7)	5.7 (±1.8)
Electrolyte	YSZ	0	13.3	15 (±2.6)	5.4 (±0.9)
Barrier	CGO	0	11	7.2 (±0.7)	6.2 (±0.3)
Cathode	LSCF:CGO 50:50	28.7	38	44.6 (±0.7)	38 (±1.8)

Based on the reviewed characteristics of these cells, we may conclude that they are pseudo-equivalent and should present similar electrochemical behavior. Thus, they are suitable for electrochemical performance analysis and comparison.

III. Interface characterization

III.A. Method

Optic profilometry and data interpretation via Matlab

Architecturing the electrode/electrolyte interfaces is a core objective of this study and an analysis procedure must be established. Optical profilometry allows us to finely control the topology of an

open surface and, in our case, the architecture. In this study, an Altisurf 500 optical profilometer is used, and the results are visualized and analyzed with Altimap Topography software or Matlab.

Numerical analysis procedures and tools are developed with Matlab where the raw data is imported in order to calculate the Area Expansion Coefficient (AEC) as well as to perform a statistical study on the architecture geometry.

A comparison between a theoretical and numerical AEC calculation for simple geometries such as the laser engraved rail patterns and parallelepipedic shaped cold press template is carried out to validate the method. In table III – 10, a short overview of those results can be found, accompanied by geometric schematics and parameters as well as Matlab generated surfaces.

Table III - 10 Integration method for AEC calculation validation overview		
	Laser engraving (rail patterns)	Aluminum template (parallelepipedic patterns)
Schematic representation		
3D graphic representation		
Geometry parameters (µm)	D~240; 2L~210; H~30	D=770, 2L=300; H=570
Theoretical AEC calculation	1.0186	1.6289
Experimental AEC estimation	1.0198	1.6071
Error (%)	0.15	3.59

The low error percentage allows us to validate the calculation method, and thus it can be used on more complex architectures.

III.B. Results

During this study, two methods of architecturation are tried out: soft template architecturing method and laser engraving of green tapes. The template method is selected as the preferential method, and detailed analysis and results will be reviewed in the next subchapter. Some interesting results have been obtained using laser engraving and will be mentioned briefly afterward. However, no complete fuel cells are fabricated by this method, which should be considered for future studies.

III.B.1.Soft template architecturing

III.B.1.a)   Green tape

The preconized method of architecturing in this study is the mesh template application due to its simplicity and fewer fabrication steps. It offers a fine regular texture over the entire cell. The profilometry analysis of the architectured green tape and the sintered ceramic allows visualizing the evolution of the patterns during the thermal treatment.

The 3D surface representation of the raw tape as shown in Figure III – 20 offers an overview of the architecturation and reveals any eventual singularities. A decreased scale representation offers a more detailed view of the surface rugosity as shown in Figure III – 21.
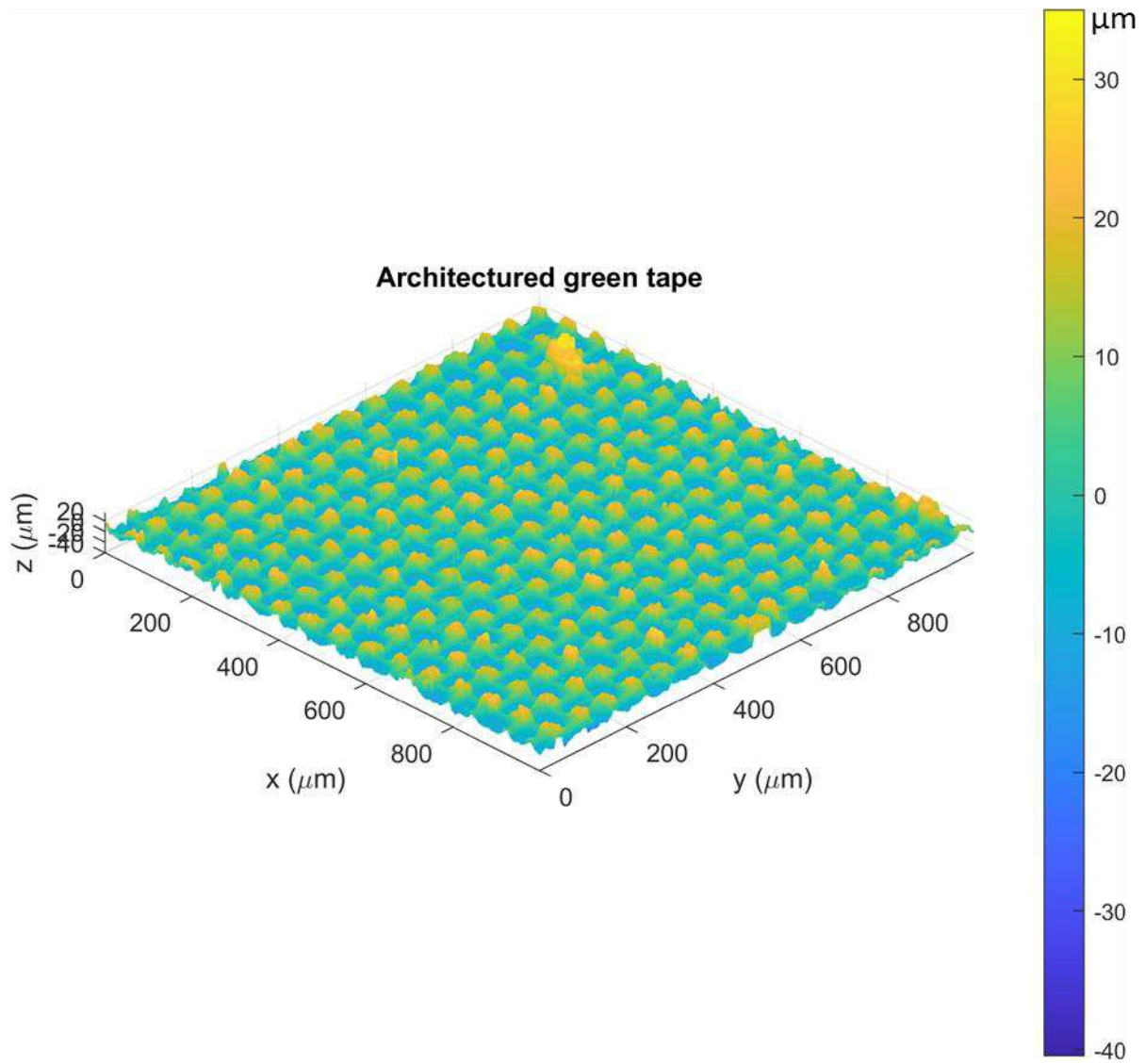
AEC=1.40

Figure III - 20 Low scale (1000 µm) 3D representation of green tape architecture
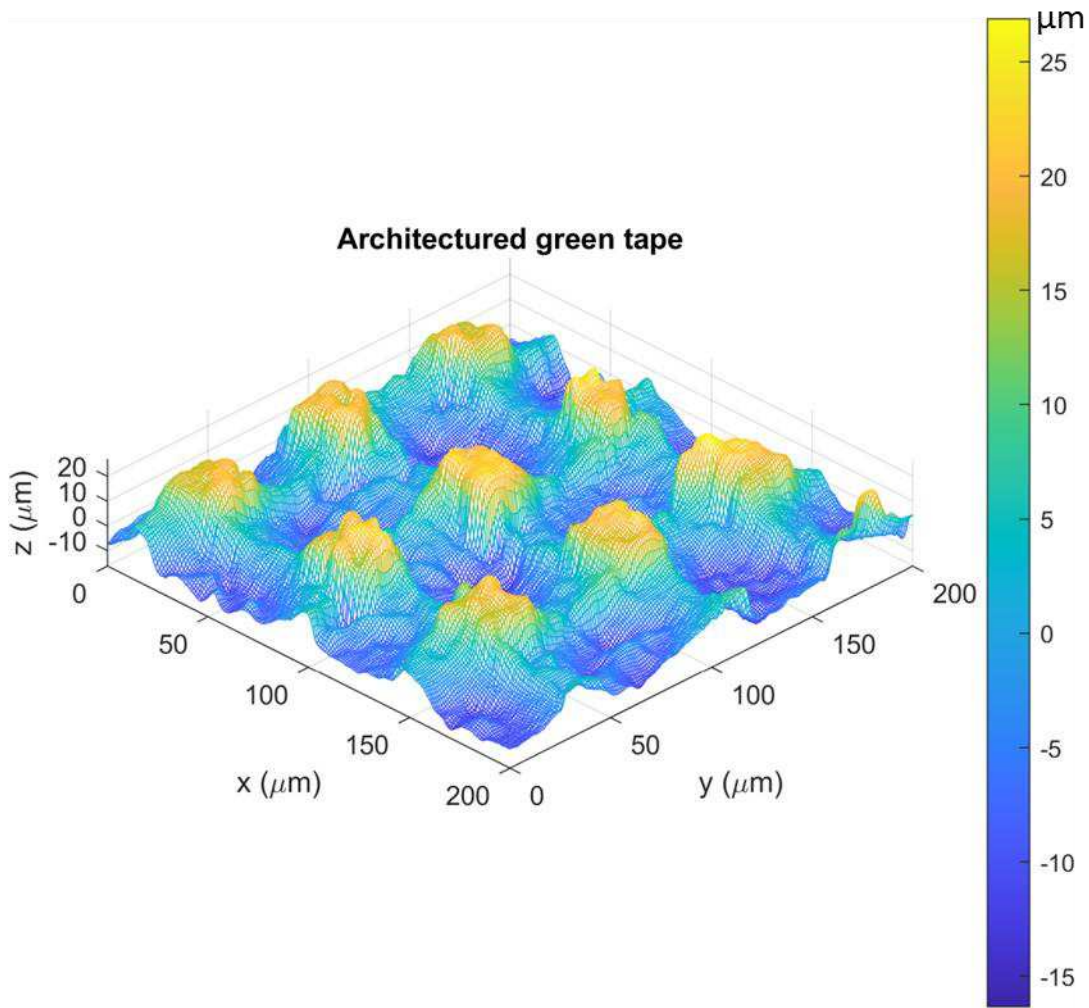
AEC = 1.40
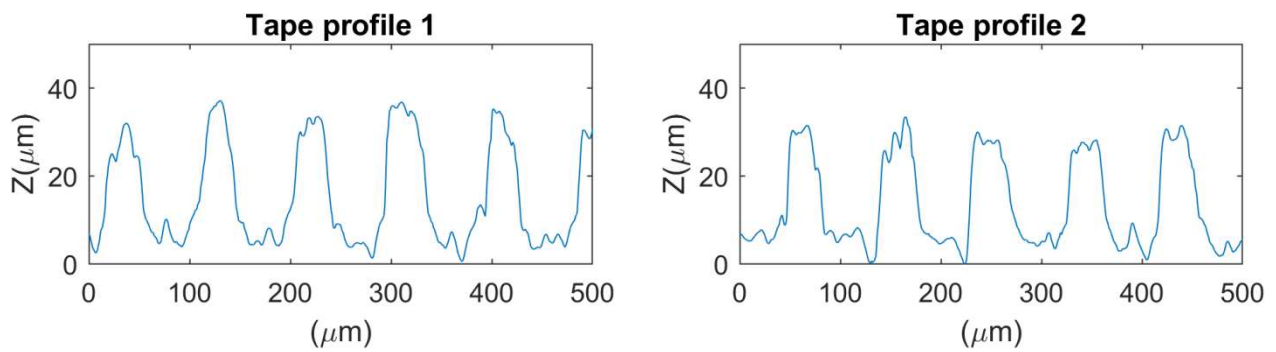
Figure III - 21 High scale (200 µm) 3D representation of green tape architecture A) 3D mesh representation of 200x200mm surface; B and C) Perpendicular profiles passing through "valleys" and 'mountains' (unequal scales for Z and XY coordinates)

A detailed geometric characterization of the architectures, as well as its variation during the sintering process, is necessary for multiple reasons:

- Anticipate wet tape thickness during fabrication
- Anticipate the final electrolyte thickness
- Facilitate the planar and architectured cells comparison
- Aid understanding of the electrochemical performances of architectured cells

However, due to the complexity of the topography, a direct study of the maxima and the minima can be challenging. For example, we observe ridge-shaped patterns between the peaks which lower the mean maxima value. Thus, the development of an analysis tool is necessary. In addition to calculating the AEC of the fuel cells, we have upgraded the Matlab script in order to calculate the mean extrema value of the Z coordinate.

The first step is to determine the global arithmetic and harmonic mean[2] Z value of the architecture. Then we can calculate the average Z of the points below and above the global mean Z representing the average minima (mean (Zmin)) and average maxima (mean (Zmax)) respectively.

- Mean (Z) corresponding to the global mean Z value of the architecture
- Mean (Zmin) = mean (Z < (mean Z)) corresponding to the mean Z value of the minima
- Mean (Zmax) = mean (Z > (mean Z)) corresponding to the mean Z value of the maxima

Secondly, we calculate the standard deviations of these three values in order to anticipate the intervals which would include a representative number of points (Table III – 11).

Table III - 11 Green tape architecture: arithmetic mean values and associated standard deviations		
	Value (µm)	Standard deviation (µm)
Mean Z	1.0168e-04	8.7622
Mean (Z<(mean(Z))	-5.998	3.3705
Mean (Z>(mean(Z))	8.45	6.8362

---

[2] Harmonic mean : $H = \dfrac{n}{\sum_{i=1}^{n}\frac{1}{z_i}}$

Based on this analysis, we deduce that 95% of the maxima of the architecture (shown in figure III − 20) are inferior to $8.45 + 2 * 6.84 = 22.12\ \mu m$ and 95 % of the minima are superior to $-6 - 2 * 3.37 = -12.74\ \mu m$ which means that the gap between maxima and minima is 36.86 µm. This means that the minimum electrolyte wet tape should not be lower than this value to avoid holes and we recommend casting it with $50\ \mu m$ wet thickness.

The second important result of the profilometry analysis is to determine the AEC. As mentioned this is done by an elementary surface integration. By using our calculation method we can determine that the AEC, in this case, is equal to 1.40. The roughness of the surface should be smoothed during the thermal treatment as a result of the additives elimination and the sintering lowering further the AEC. All the pertinent values calculated for this geometry are reported in Table III − 12.

III.B.1.b)   *Sintered ceramic*

In this subchapter, the green tape which has been characterized in III.B.1.a has been thermally treated during which the additives composing the tape have been eliminated and the functional materials have been sintered at 1400°C. As mentioned we anticipate a resulting material retraction modifying the geometry parameters. The final objective being to architecture SOFC, we will be testing sintered cells. Thus, the same characterization procedure is applied here. The ceramics surface 3D visualization with different scales can be observed in figure III − 22 and 23.
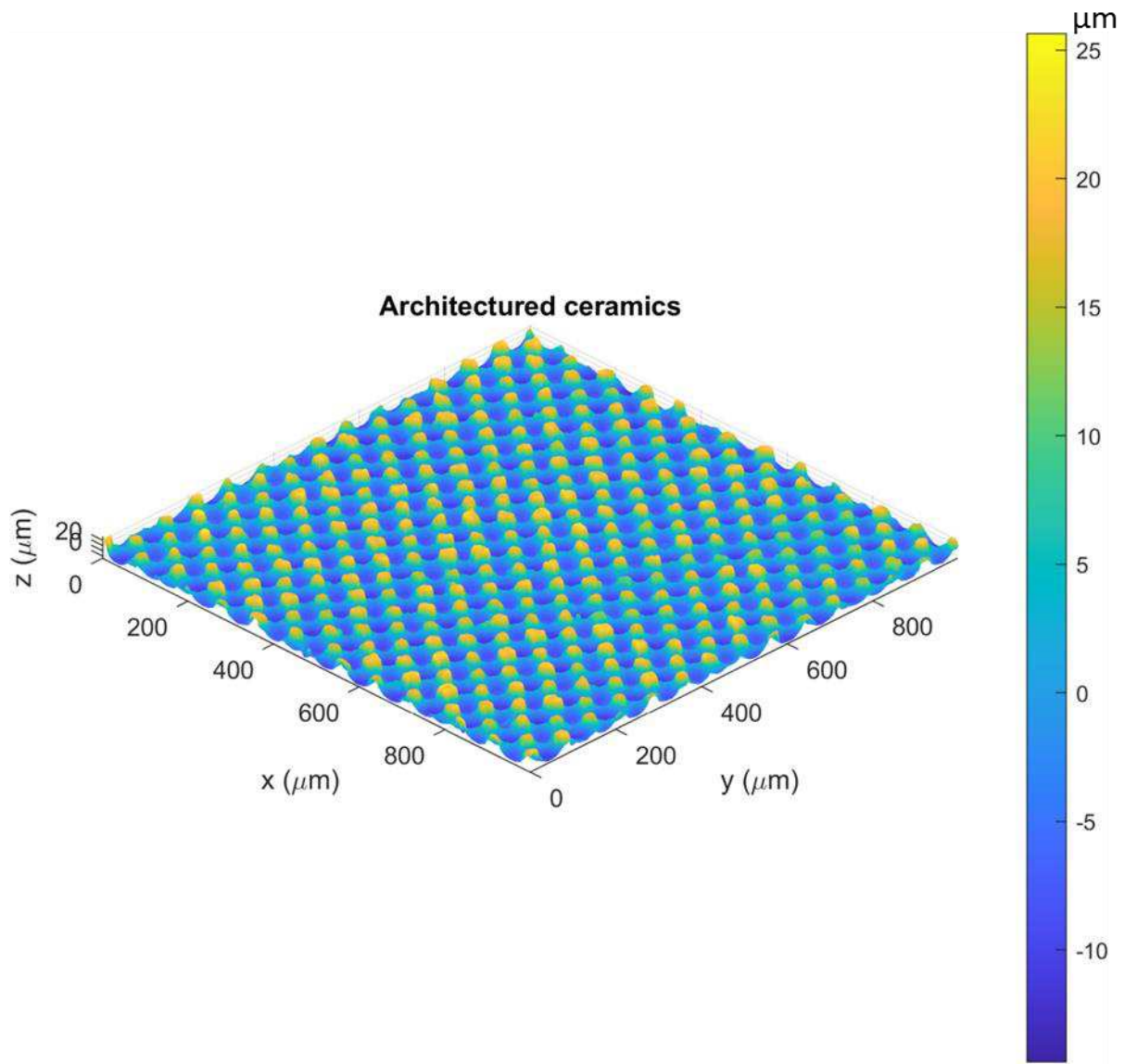
AEC = 1.28

Figure III - 22 Low scale (1000 µm) 3D representation of sintered ceramic architecture
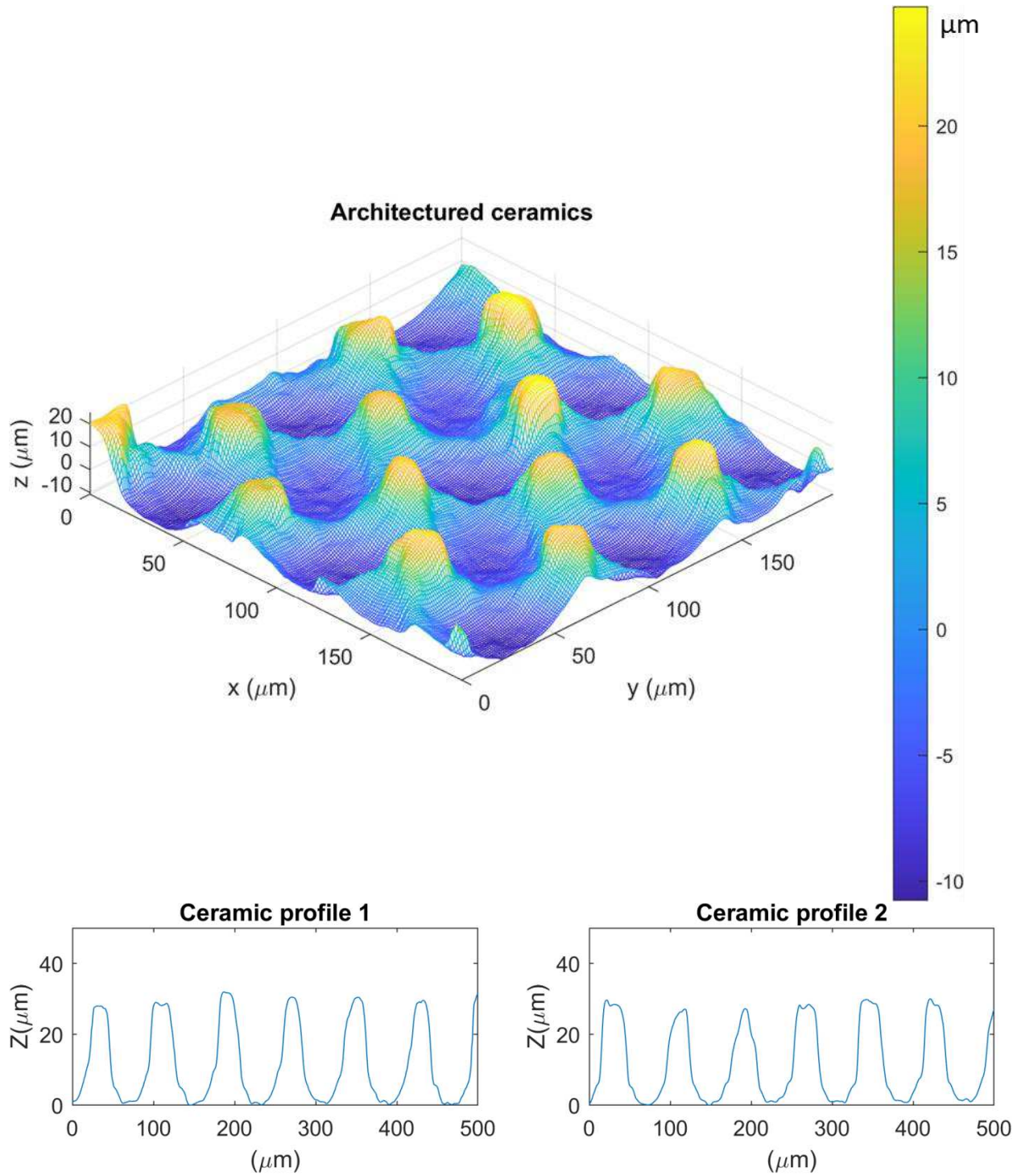
Figure III - 23 High scale (200 µm) 3D representation of sintered ceramic architecture A) 3D mesh representation of 200x200mm surface; B and C) Perpendicular profiles passing through "valleys" and 'mountains"

As expected the roughness of the surface is decreased during the thermal treatment and the material retraction is demonstrated by the number of patterns on the 200x200 µm surface. By increasing the density of patterns, the AEC should increase. However, the material retraction decreases the pattern geometrical parameters and in particular the height. In this case, we use the same methodology as for the green tape to calculate the pertinent geometrical parameters. The results of those calculations, as well as the ones concerning the green tape, are reported in Table III - 12.

Table III - 12 Pertinent Z values of the green tape (figure III – 20) and the sintered ceramic (Figure III – 22)		
	Tape (µm)	Ceramic (µm)
Mean (Z)	1.0168e-04	-5.8160e-04
Std (Z)	8.7622	8.20
Absolute Min	-40.4523	-14.37
Mean (Z<mean (Z))	-5.998	-5.299
Std (Z<mean (Z))	3.3705	2.9416
Mean (min (95% of values)	-12.72	-11.18
Absolute Max	35.01	25.64
Mean (Z>mean (Z))	8.45	8.19
Std (Z>mean (Z))	6.84	6.85
Mean (max (95% of values)	22.09	21.89
ΔZ (mean)	14.45	13.49
ΔZ 95% of the points	34.81	33.07
ΔZ (Harmonic mean)	3.7	3.17
Mean period	93.3	77.8
AEC	1.40	1.28

The AEC decrease between the green tape and the sintered ceramic is coherent with a combination of the mean Z retraction (5 % decrease) and the smoothening of the rugosity of the lateral and transversal material reduction. The lateral materials retraction is uniform and although the density of the peaks is increased their width is proportionally decreased.

In order to anticipate the influence of the electrolyte thickness variation on the resistivity of the cells, the calculation of the mean electrolyte value is necessary. However, the equivalent resistivity of parallel pathways is determined by the harmonic mean value of the resistivity of each pathway as shown in Equation 1:

For $R_1//R_2$
$$R_{eq} = \frac{R_1 \times R_2}{R_1 + R_2}$$
(1)

As the resistivity varies linearly with the thickness of the electrolyte, a calculation of the harmonic mean of the architecture is calculated and added to the minimum electrolyte value (table III – 13). The relative gap between the thicknesses is calculated in order to establish the link between the resistivity analysis and the electrolyte thickness variations.

	Planar	Min architectured	Harmonic mean + min architectured	Ratio calculated architecture thickness vs planar thickness
Table III - 13 Harmonic mean value of the architectured electrolyte thicknesses				
Type I	9.9	3.4	6.6	0.33
Type II (YSZ)	13.3	5.4 (±0.9)	8.6	0.36
Type II (CGO)	11	6.2 (±0.3)	9.5	0.14

A further investigation of the architecturing is carried out via SEM observations. Figure III – 24 shows an architectured sintered anode surface. We can observe regularly distributed patterns over a significant surface area. A lack of fractures and/or cracks demonstrates that the architecturing method does not induce additional stress on the object and is suited for large scale application.
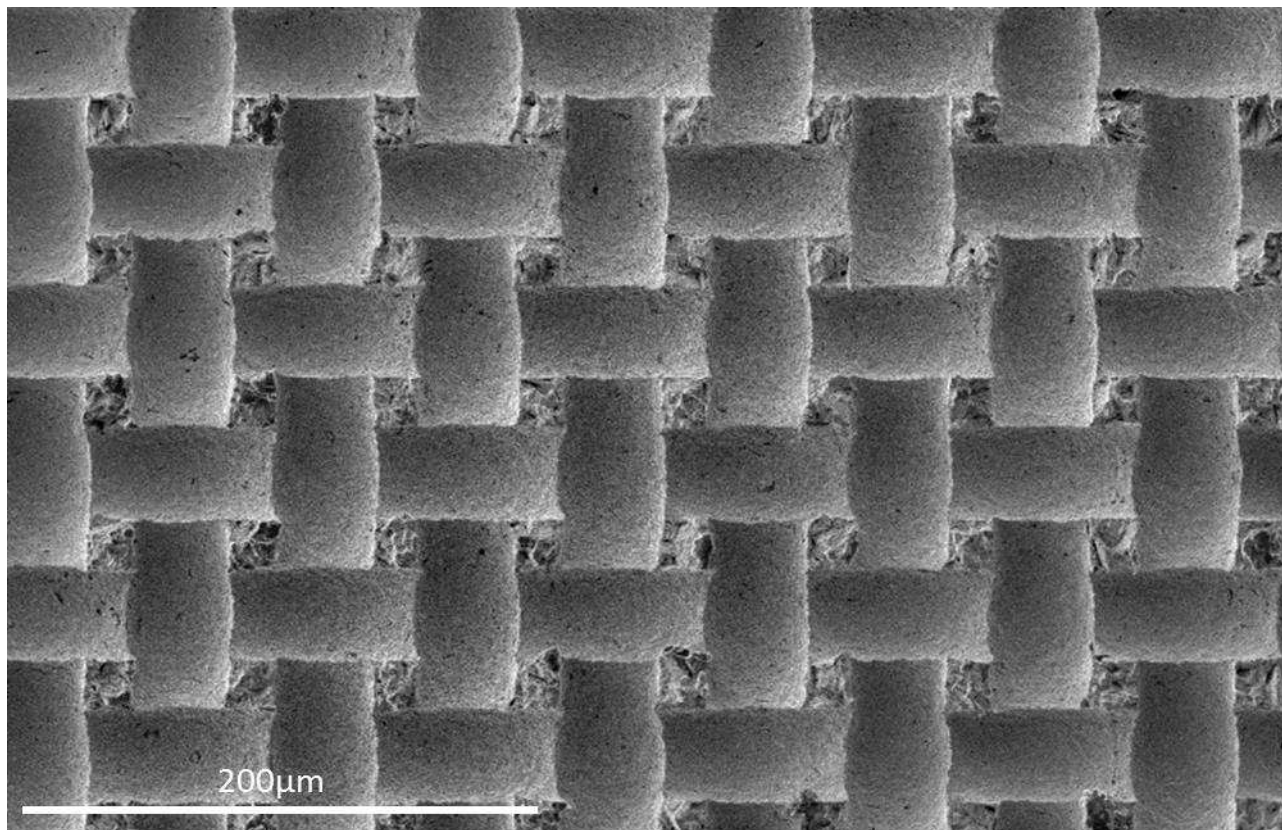
Figure III - 24 SEM of the architectured sintered anode surface

The next important characteristic of the architecturing method is the penetration and the wetting of the concerned material layers. In Figure III – 25, we show the utilization of the previously shown anode tape over which we have cast an electrolyte layer, co-sintered the half-cell, and added a cathode layer followed by a second thermal treatment. An excellent layer cohesion is visible between the architectured anode and the electrolyte and the electrolyte wets adequately the patterns. Furthermore, in this configuration, the variable electrolyte thickness presents two interesting characteristics. The first is the presence of thin areas which are beneficial for the ion conduction, thus lowering the overall cell resistance. The second is the presence of thicker areas which are potentially beneficial for the mechanical strength of the cell, acting as bridge pillars. Moreover, as mentioned, the penetration of the dense electrolyte within the porous anode may activate additional ion transportation paths lowering even more the ohmic overpotential as well as the activation overpotential.
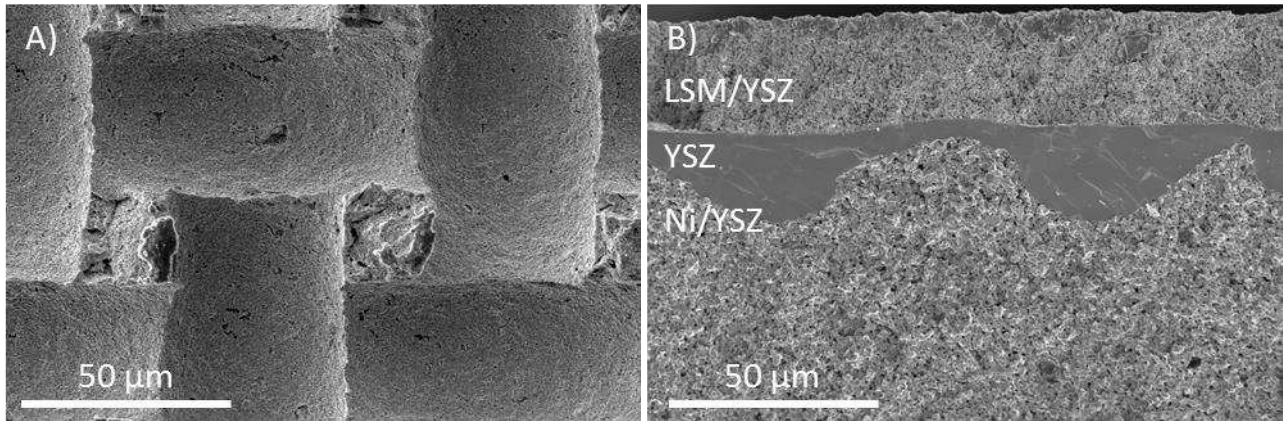
Figure III - 25 Architectured sintered open surface: Anode open surface with a porous microstructure; B) Architectured anode-electrolyte interface

In figure III – 26 A, an architectured and sintered electrolyte open surface is presented. This electrolyte has been cast and architectured over a planar anode, and the half-cell was sintered. A cathode tape is bound on the architectured electrolyte using the method described in Chapter II, and the complete cell was sintered. In this configuration, we can also observe the penetration of the electrolyte in the cathode, which offers an adequate wetting of the patterns (Figure III – 26 B). The same hypotheses are applicable as in the first case are observed, which validates the architecturing method for both interfaces.
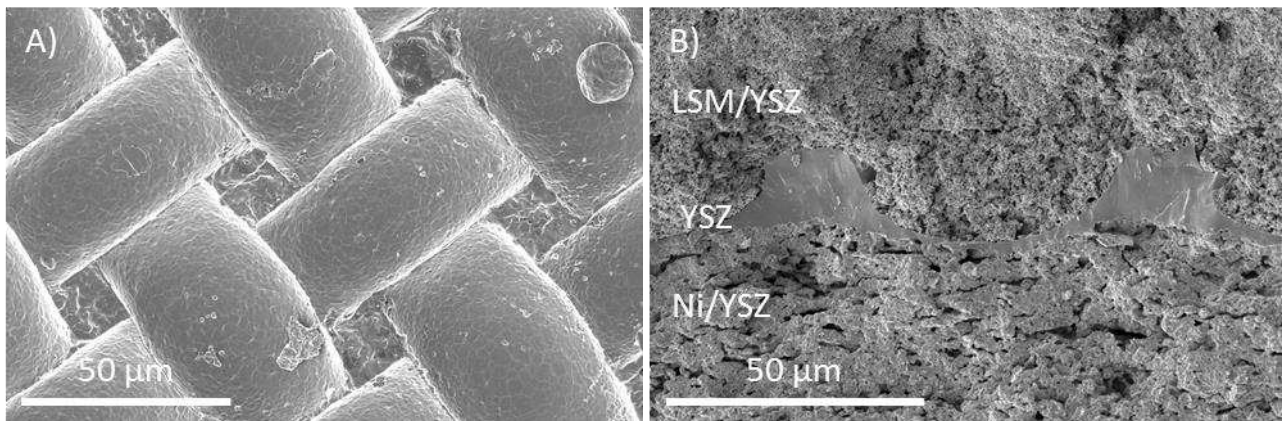
Figure III - 26 Architectured sinter electrolyte: A) Electrolyte open surface with a dense microstructure; B) Architectured cathode-electrolyte interface

In conclusion, in addition to being simple to realize, the chosen architecturing method provides excellent results where the regularity, persistence, mechanical integrity of the pattern as well as

adequate layer cohesion are demonstrated. It is also suitable for large scale application to architecture both interfaces. This method provides a considerable area expansion (close to 30%) and seems to stabilize the mechanical strength of the fuel cells.

III.B.2.Laser engraving of green tapes

Laser engraving of green tapes is achieved using a laser-engraving model Arketype JADE 6900, working with CO_2 power laser. The engraved tapes were cut and sintered following the corresponding thermal treatment. In this subchapter, we demonstrate the feasibility of opening the possibility for further study.

In figures III – 27 A and 27 B, the 3D topology of a laser architectured tape before and after sintering are presented. Both surfaces are followed by a profile line (Figures III – 27 C and 27 D respectively) which allows us to characterize the lateral periodicity parameter as well as visualize simply the height variation.

A)

B)

C)

D)
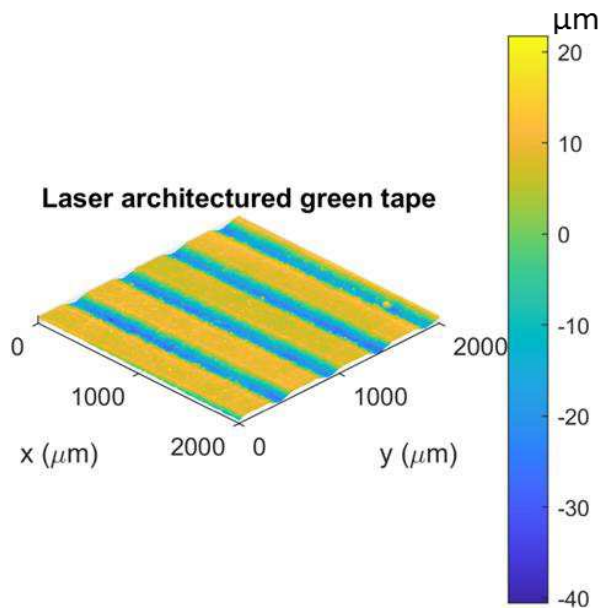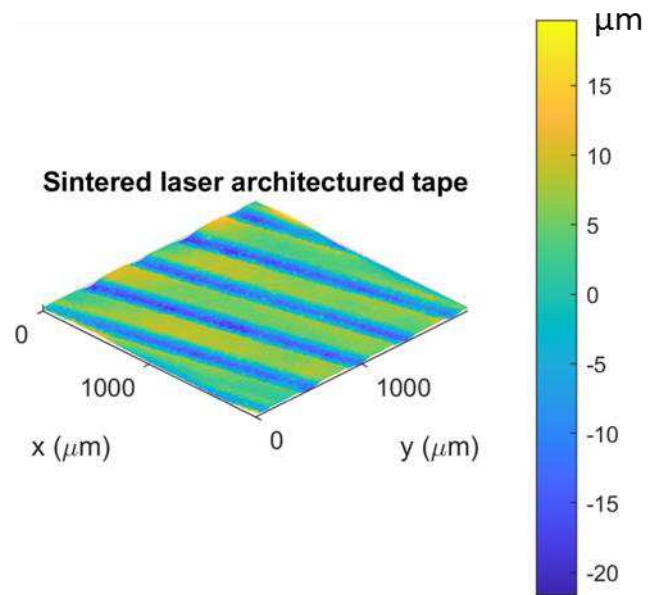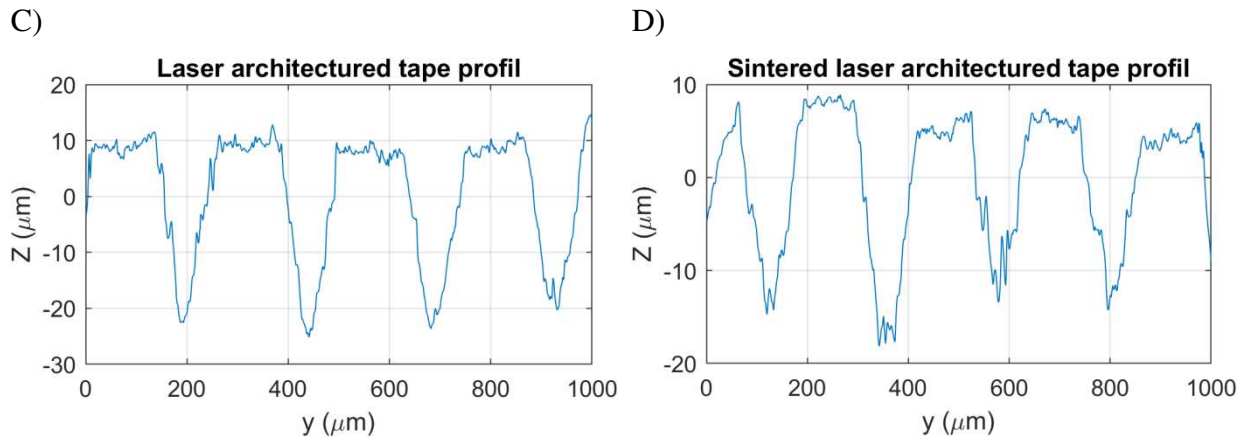
Figure III - 27 Architecturation by laser engraving of green tapes. A) Green tape 3D; B) Sintered tape 3D; C) Green tape profile; D) Sintered tape profile

The first goal of the investigation is to verify if the patterns are persistent during the sintering and eventually characterize the impact of this process on the geometrical parameters. The same methodology as in the previous subchapter is used to calculate those parameters which are reported in Table III – 14.

Table III - 14 Pertinent Z values of the green tape (figure III – 27 A and C) and the sintered ceramic (Figure II – 27 B and D)		
	Tape (µm)	Ceramic (µm)
Mean (Z)	0.00	0.00
Std (Z)	11.42	7.25
Absolute Min	-46.86	-21.72
Mean (Z<mean (Z))	-13.24	-7.77
Std (Z<mean (Z))	7.68	4.58
Mean (min (95% of values)	-28.6	-16.93
Absolute Max	35.05	20.11
Mean (Z>mean (Z))	7.84	5.26
Std (Z>mean (Z))	7.68	4.58
Mean (max (95% of values)	23.2	14.42
ΔZ (mean)	21,07	13.03
Mean period	245	195

AEC	1.0527	1.0198

Due to the low AEC, we have discarded his architecturing method until further maturation. Nevertheless, the feasibility and the regularity of the patterns (figure III − 28) as well as the possibility to create new sophisticated architecture, and the combination of architecturing and cutting, provides a potential interest for further development.
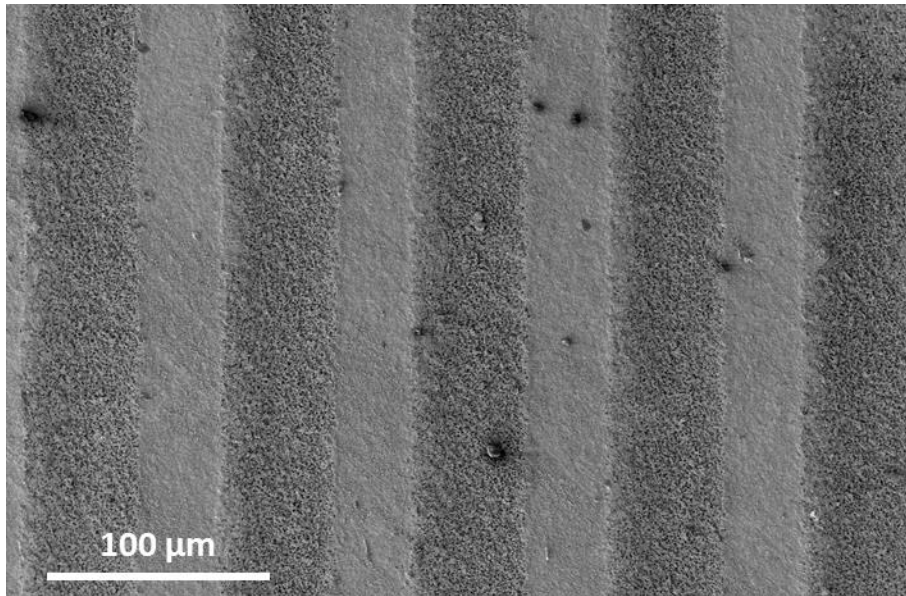
Figure III - 28 SEM image of sintered laser architectured tape

IV.   Conclusion and discussion

In this chapter focused on structural and chemical characterization we studied and reported several pertinent characteristics, necessary for the cell comparison helpful for the understanding of their behavior. On one hand, we characterized the cell components by scanning their microstructure, chemical distribution, and layer thickness.

IV.A. Components

On one hand, we characterized the cell components by scanning their microstructure, chemical distribution, and layer thickness for Type I and Type II cells.

IV.A.1. Type I cells

For Type I cells we saw that the electrolyte in both architectured and planar configuration presents a very favorable microstructure for the ionic conduction. Furthermore, the electrolytes are fairly thin (under 15 µm) which as Steele has published [2], should result in a low series resistance ($< 0.15 \ \Omega.cm^{-2}$) during the cell operation. The apparent electrolyte density and the lack of transversal cracks should ensure the gas tightness and electron insolation of the electrodes. This point will eventually be confirmed by the OCV value during the electrochemical measurements. The architecture seems to strengthen the mechanical stability of the cells because a lateral fracture can be observed through the electrolyte of the planar cell but is less present in the architectured one. . The thickness measurement of the electrolyte layer coupled with the architecture geometry study allows confirmation of the quasi equivalency between the architectured and planar cells.

The anode composition, in this case, has been optimized to promote the electronic phase percolation in the thick anode support layer. In both AS and AFL, the materials are homogeneously dispersed, and the cohesion with the electrolyte is well established. However, a degradation of the porosity is observed, which needs to be investigated and rectified as an optimized porosity is essential for the electrochemical reactions.

In this case study, the cathode presents two different layers: the cathode gas channel and the cathode functional layer. The architecturation is deployed at the cathode/electrolyte interface, and it is essential to have an adequate dispersion of the materials in order to study the impact of the interface geometry variation uniquely. The interface is entirely situated between the CFL and the electrolyte, which avoids any parasitic effects. A satisfactory wetting between the cathode and the electrolyte is observed. However, on one side of some patterns, we do observe holes. The position of these holes and their irregular distribution suggest that they may be artefacts caused by the polishing procedure.

Based on the reviewed characteristics of these cells, we may conclude that the architectured and planar cells are equivalent and should present similar electrochemical behavior. Thus, they are suitable for electrochemical performance analysis and comparison.

IV.B. Type II cells

A similar conclusion can be made as for the type I cells.

The electrolyte and the barrier layers present satisfactory microstructure in terms of grain size, density, and integrity. Although the grains size of the barrier layer is lower than the one of the electrolyte layer, the elevated conductivity of CGO is expected to compensate for this drawback. The barrier layer presents some cracks perpendicular to the interface. They are expected not to impact significantly the electrochemical performance of the cell because they do not traverse the electrolyte layer. However, these defects may cause complications in prolonged operation, and a durability test is necessary for these cells. The combined electrolyte and barrier layer thickness is slightly elevated (approximately 22 µm) which will impact the cell series resistance. The harmonic mean electrolyte thickness of the architectured cells is considered to aid the ASR and EIS interpretation.

The anode support and the anode functional layer in these cells do not present a material concentration gradient. Indeed, chronologically these cells were fabricated before the Type I cells and the consideration of the material optimization throughout the electrode was not yet taken into account. On the plus side, the porosity corresponds to one expected from the fabrication protocol and is optimized.

Again, due to the chronological position of the type II cell fabrication, the cathode presents inadequate materials dispersion. We observe CGO particle segregation which may hinder the equivalency between architectured and planar cells in the case of cathode/electrolyte interface modification. Thus, this interface modification was not studied here. A new cell fabrication with optimization of the anode and the cathode should be carried out in future works.

Based on the reviewed characteristics of these cells, we may conclude that they are pseudo-equivalent and should present similar electrochemical behavior. Thus, they are suitable for electrochemical performance analysis and comparison.

IV.C. Architecturation

In this subchapter, we have analyzed porous and dense ceramics architectured by two different methods which are laser engraving of green tape and the soft template method. The latter is preconized for the SOFC and microstructural results of its utilization can be studied in the

characterization of the components at the beginning of the chapter. Within this part of the chapter (II. Component characterization) as well as within the architecturation characterization part The SEM imaging reveals the microstructure of the architectured objects. The architectured electrolytes are as dense as the planar ones whereas the architectured anodes exhibit an adequate porosity. Thus, the architecturation is pertinent for SOFC application, and fabricated cells are suitable for electrochemical analysis.

Further detailed architecture characterization is established by optical profilometry. Due to the complexity of the patterns obtained with the soft template method, a numerical analysis protocol had to be developed and validated in this chapter. The numerical script developed in Matlab offers several useful options providing detailed information on the architecture parameters.

- AEC calculation: by using an elementary integration technique, the area expansion coefficient which is the ratio between the effective architectured surface area and the equivalent planar surface area can be calculated. The calculation technique is verified using objects presenting simple architectures such a rail or cubic geometry. The AEC calculated analytically is compared to the ones calculate numerically and the results are within an acceptable error (< 5%).
- Mean values and standard deviation. Different types of mean values of the z coordinates can be calculated as well as the standard deviation in respect to the mean values. Thus, we are capable to calculate an arithmetic and a harmonic mean value for the architecture thickness which are respectively 13.49 µm and 3.17 µm.
- Extrema analysis. The challenging extrema analysis is carried out by using the standard deviation from the mean low and the mean high values.

In this Chapter, we validate the type I and type II cells for electrochemical measurement and performance comparison. We have also characterized the interface architecturation obtained by original ceramics engineering techniques. This was achieved by the development and validation of numerical tools via Matlab.

[1]   C. Ni, M. Cassidy, and J. T. S. Irvine, 'Image analysis of the porous yttria-stabilized zirconia (YSZ) structure for a lanthanum ferrite-impregnated solid oxide fuel cell (SOFC) electrode', *Journal of the European Ceramic Society*, vol. 38, no. 16, pp. 5463–5470, Dec. 2018, doi: 10.1016/j.jeurceramsoc.2018.08.026.

[2]   B. C. H. Steele, 'Oxygen transport and exchange in oxide ceramics', *Journal of Power Sources*, vol. 49, no. 1, pp. 1–14, Apr. 1994, doi: 10.1016/0378-7753(93)01789-K.

[3]   'Standard deviation', *Wikipedia*. Nov. 18, 2020, Accessed: Nov. 22, 2020. [Online]. Available: https://en.wikipedia.org/w/index.php?title=Standard_deviation&oldid=989272416.

CHAPTER IV – SOFC characterization and performance analysis
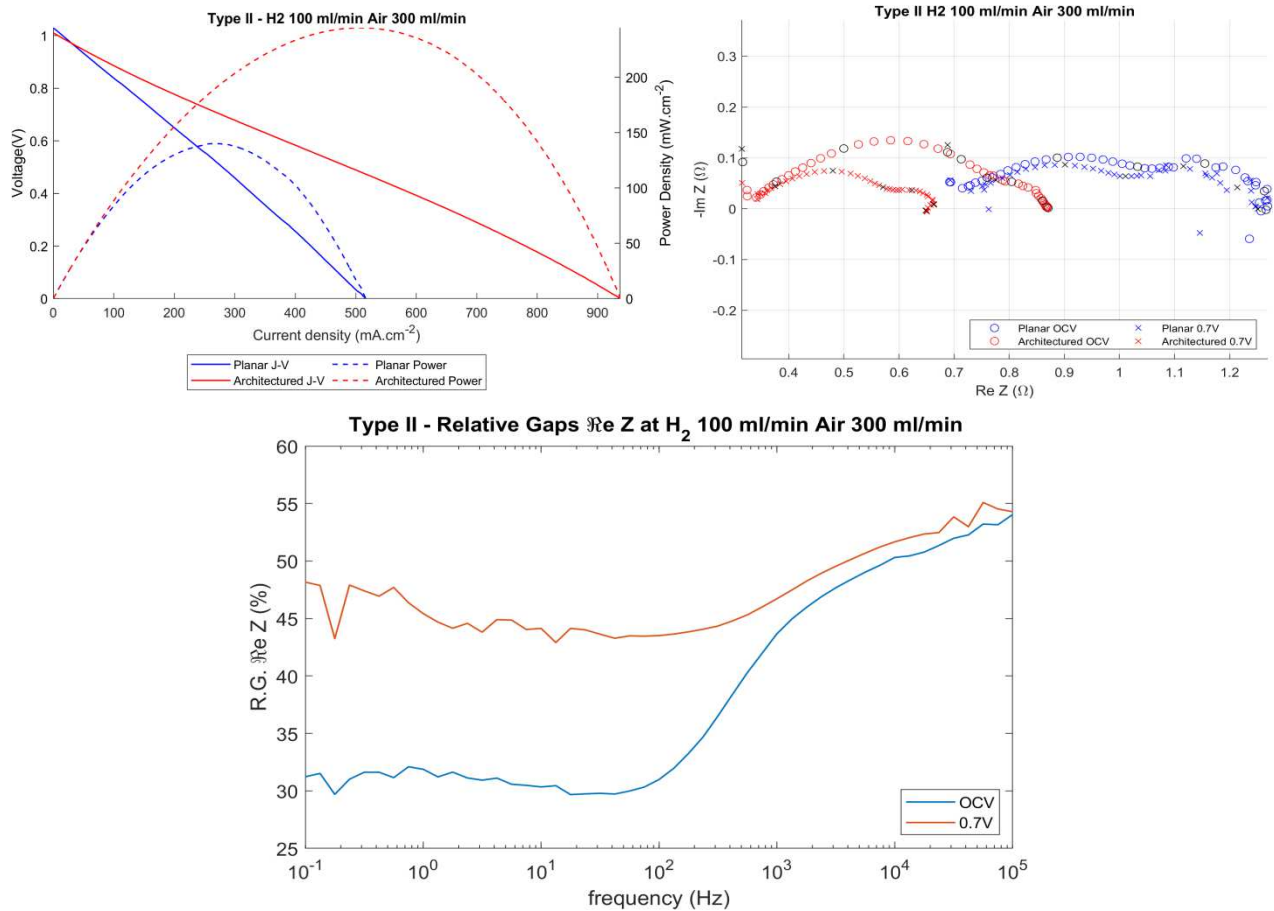
Chapter IV abstract

In this chapter, we carry out an electrochemical analysis on the fabricated Type I and Type II cells. A brief description of the techniques that are used can be found at the onset of the chapter. The first series of tests consists of polarization measurements in different gas conditions to study the electrical generation capability of the cells. Polarization measurement is a simple technique providing a direct quantification of the electrochemical performances of a fuel cell. The polarization curves of the architectured and planar cells are compared in order to investigate the influence of the architecturation on the current or power density (Figures IV – abstract – 1 and 2). For the second series of tests, Electrochemical Impedance Spectroscopy (EIS) in different gases and operating conditions is performed. EIS is a powerful and complex technique that provides an in-depth analysis of the cell operation. It can be used to reveal the contribution of the different phenomena occurring in the cell (charge and gas transport, electrochemical reactivity) that contribute to the global cell impedance. The EIS spectra of the architectured and planar cells are analyzed (Figures IV – abstract – 2 A and 3 A) and an innovative comparison method is used to isolate the contribution of the architecturation. This method consists of calculating the relative gap (R.G.) of the frequency-dependent resistivity of the cells (Equation 1) and studying the plot of the gaps as a function of the frequency (Figures IV – abstract – 2 B and 3 B).

Chapitre IV résumé

Dans ce chapitre, nous effectuons une analyse électrochimique sur les cellules de type I et de type II. Une brève explication des techniques utilisées est donnée en début de chapitre. La première série de tests consiste en des mesures de polarisation sous différentes atmosphères gazeuses afin d'étudier la capacité de production électrique des cellules. La mesure de la polarisation est une technique simple qui permet de quantifier directement les performances électrochimiques d'une pile à combustible. Les courbes de polarisation des cellules architecturées et planaires sont comparées afin d'étudier l'influence de l'architecture sur la densité de courant ou de puissance (figures IV - abstract - 1 et 2). Pour la deuxième série de tests, la spectroscopie d'impédance électrochimique (EIS) est effectuée dans différentes conditions de pression de gaz et de fonctionnement. L'EIS est une technique puissante et complexe qui permet une analyse

approfondie du fonctionnement de la cellule. Elle peut être utilisée pour révéler la contribution des différents phénomènes se produisant dans la cellule (transport de charge et de masse, réactivité électrochimique) et contribuant à l'impédance globale. Les spectres EIS des cellules architecturées et planaires sont analysés (Figures IV - abstract - 2 A et 3 A) et une méthode de comparaison innovante est utilisée pour isoler la contribution de l'architecture. Cette méthode consiste à calculer l'écart relative (R.G. = relative gap en anglais) de la résistivité des cellules en fonction de la fréquence (Equation 1) et à étudier le tracé des écarts en fonction de la fréquence (Figures IV - résumé - 2 B et 3 B).

$$R.G.(f_i) = \frac{Z'(f_i)_{planar} - Z'(f_i)_{architetured}}{Z'(f_i)_{planar}} \tag{1}$$
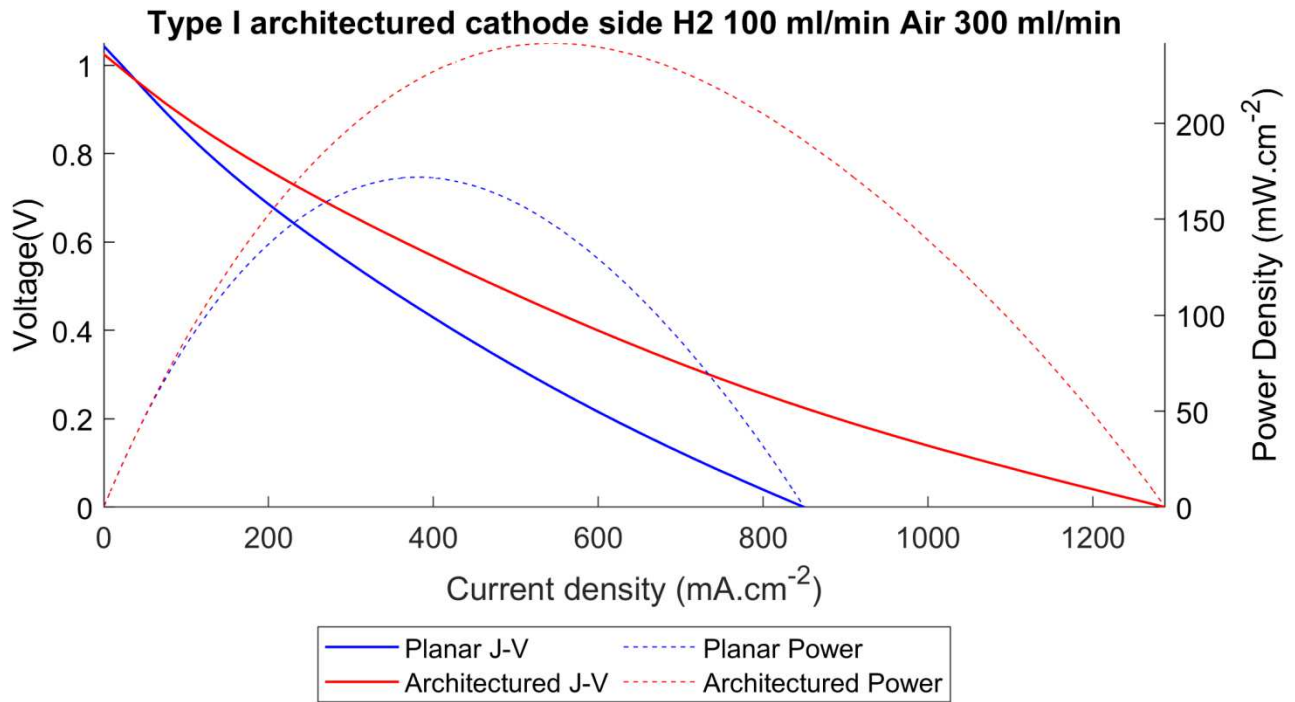
Figure IV - abstract - 1 Type I Polarization and density curves in reference gas conditions
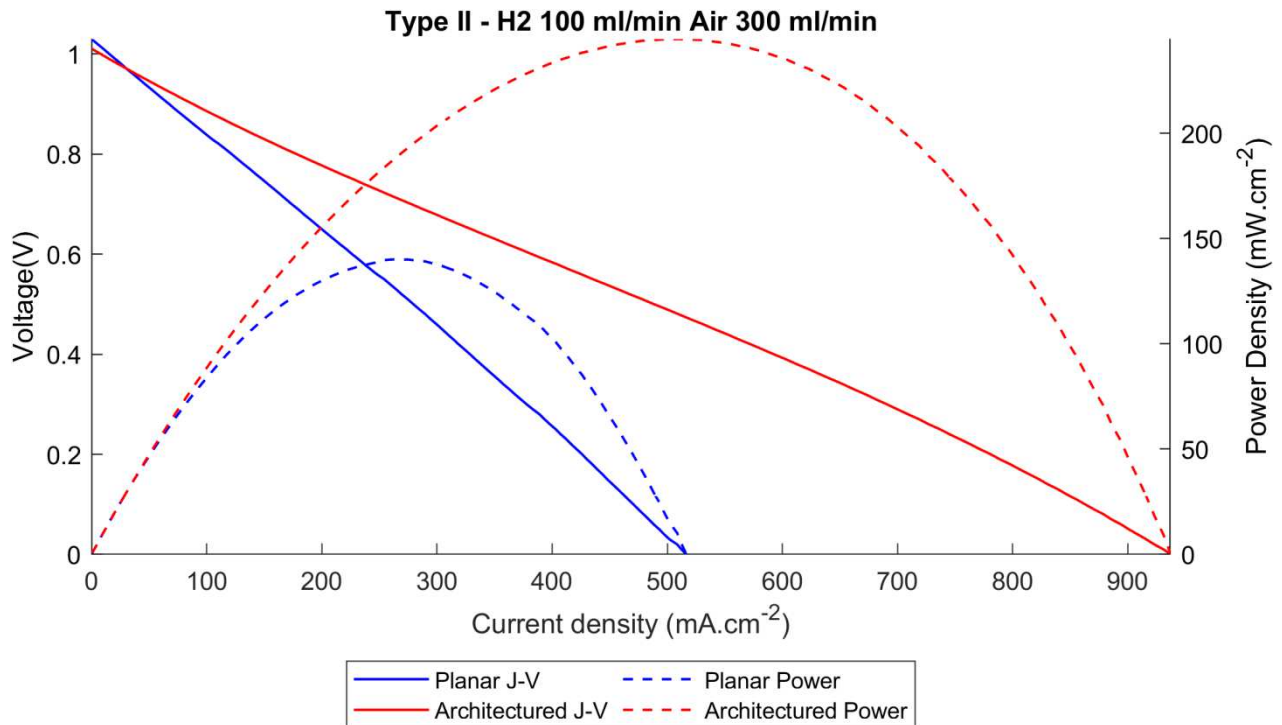
Figure IV - abstract - 2 Type II Polarization and density curves in reference gas conditions

171
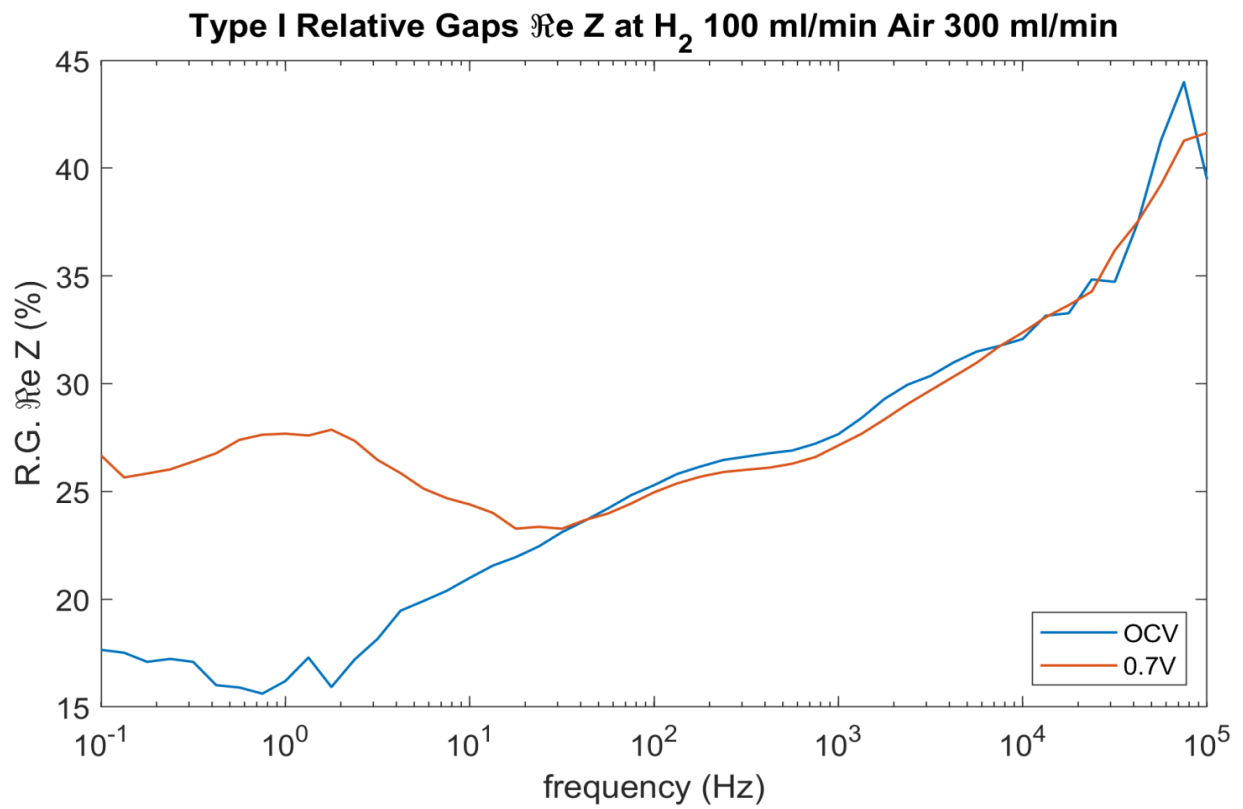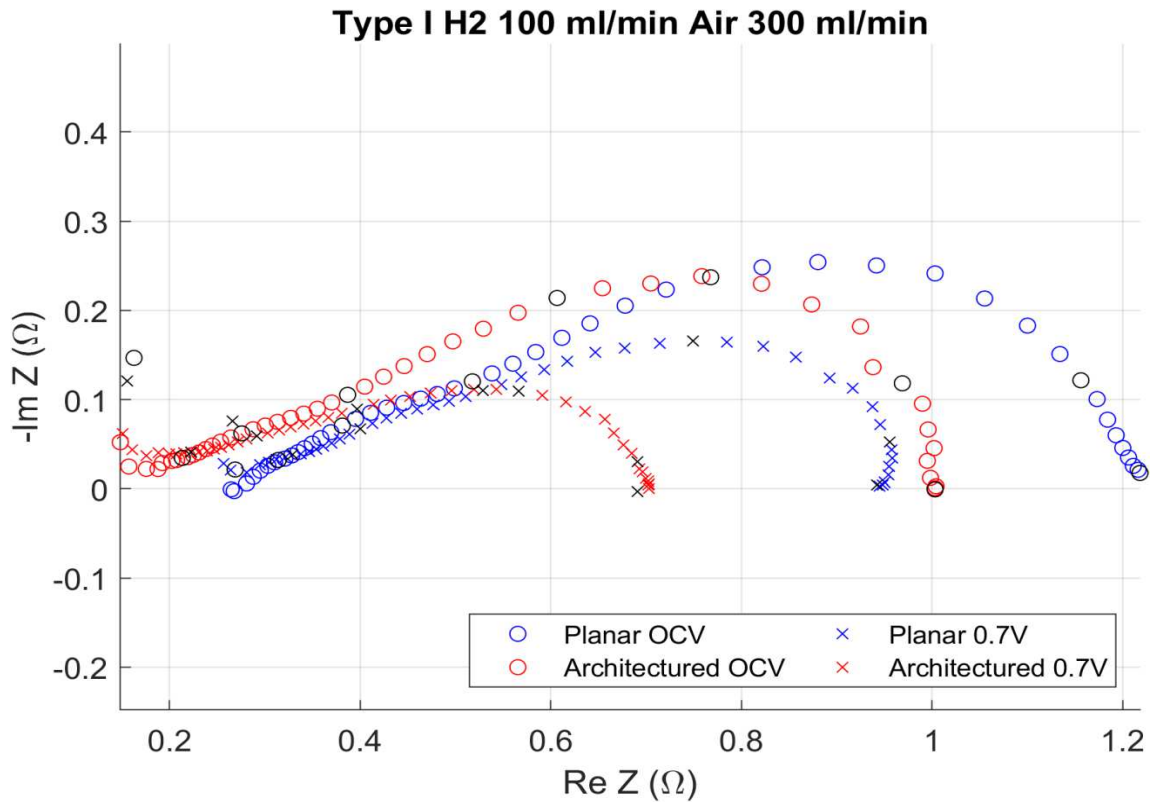
Figure IV - abstract - 3 Type I cells EIS in reference gas conditions and at OCV and 0.7 V. A)
Nyquist plots superimposition; B) Relative gap (R.G.) plots superimposition
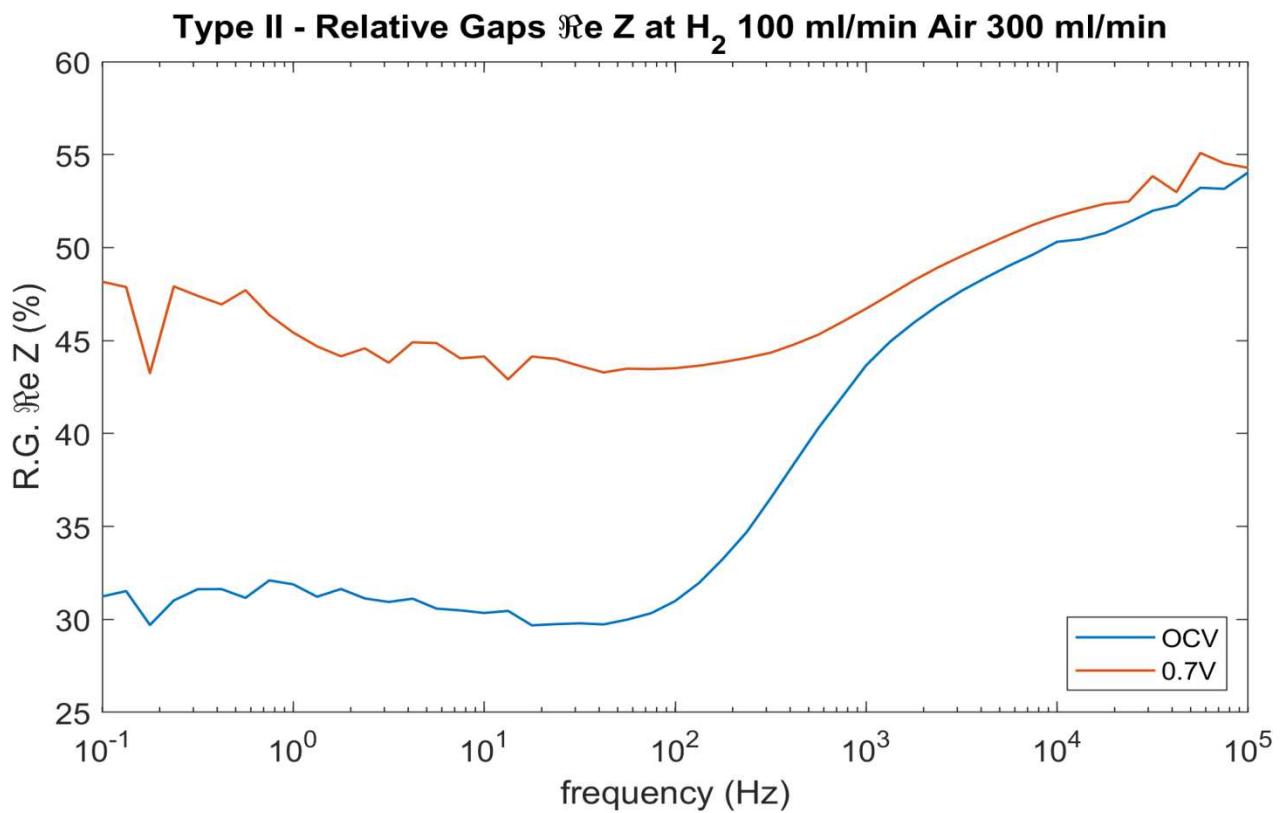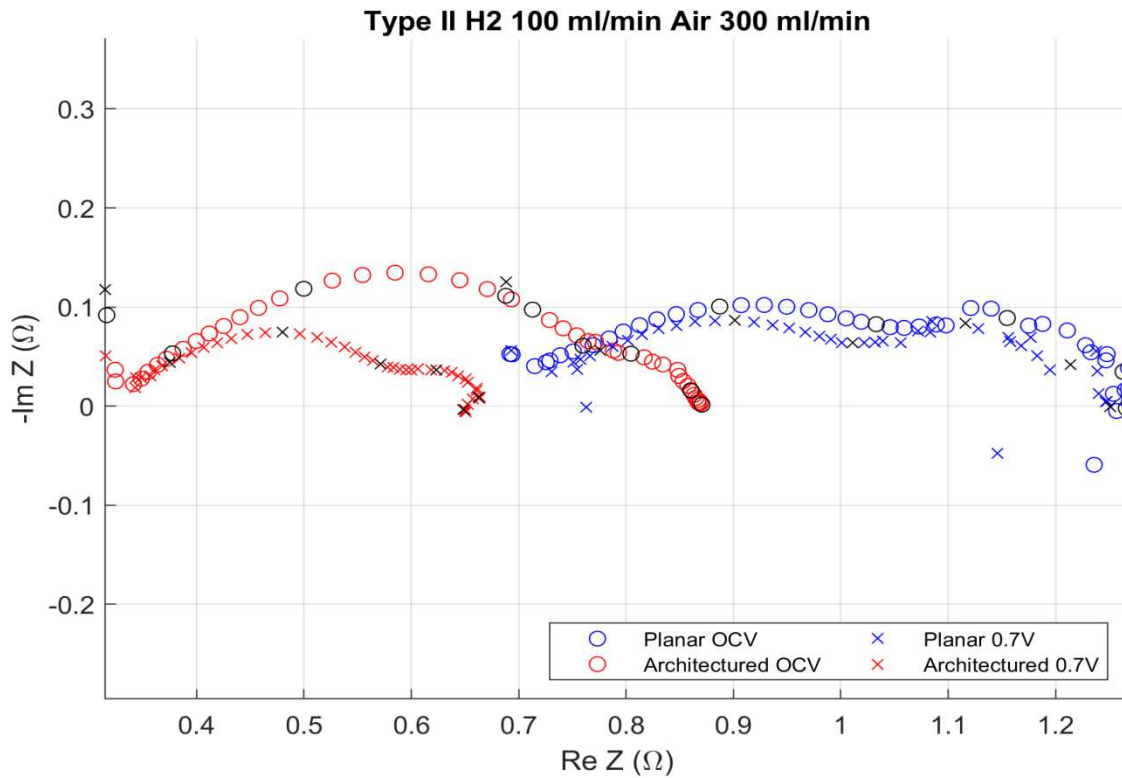
Figure IV - abstract - 4 Type II cells EIS in reference gas conditions and at OCV and 0.7 V. A)

Nyquist plots superimposition; B) R.G. plots superimposition

CHAPTER IV – SOFC characterization and performance analysis

Contents

List of figures

List of tables

177

I.   Introduction

In this chapter, a detailed electrochemical study of the fuel cells is established, based on a polarization analysis and electrochemical impedance spectroscopy (EIS). The objective is to compare the electrochemical performances of the architectured and equivalent planar cells. Additionally, the influence of the architecture on the cell properties (resistivity, catalysis, materials, and charge distribution) is evaluated. For this reason, measurements are carried out in different experimental conditions, and the results are superposed. An original and simplified method is proposed to indirectly study the EIS results and deduce the influence of the architecture by comparing the frequency associated resistivity of the cell pairs.

In the next section, we will describe the analysis methods used for the electrochemical study as well as a brief reminder of the measurement set-up. In the next two sections, Type I and Type II cells are analyzed first by polarization curve analysis followed by EIS.

II.   Analysis methods and set-up

II.A.   I/V

As it was mentioned in chapters I and II, the study of the I/V curve is the most direct way to measure the electrochemical performance of a fuel cell. Although it is a simple analysis technique, it offers a direct quantification of the ability to generate an electrical current at a given voltage and experimental conditions. Therefore, it represents a powerful tool to explore the variation of the cell performances in different conditions (variation of the temperature, gas partial pressures or flows) or between architectured and planar cells. The technique allows determining some important cell characteristics such as its OCV, its area-specific resistance (ASR), or its saturation current. In ideal conditions, OCV is close to the theoretical potential characteristic of the Redox couple (H_2/O_2 here). Thus, a variation from the theoretical potential can be linked to the gas tightness and electric insulation of the gases which indirectly informs on the integrity/impermeability of the electrolyte. The ASR is measured in the linear part of the polarization curve, where the ohmic overpotential is predominant. Hence, it is specific to the ohmic resistance of the cell not varying with current density. The saturation current is measured at 0 V, and it displays the maximum ability of the cell to generate an electronic flow, which is linked with the gas distribution properties and the number of active triple phase boundaries.

The cell voltage is as a function of the current (equation $IV-1$) represented by the polarization curve (figure $IV-1$)

$$E(i) = E_{rev} - \eta_{act,a} - \eta_{act,c} - \eta_{pol} - \eta_{conc,a} - \eta_{conc,c} \tag{1}$$
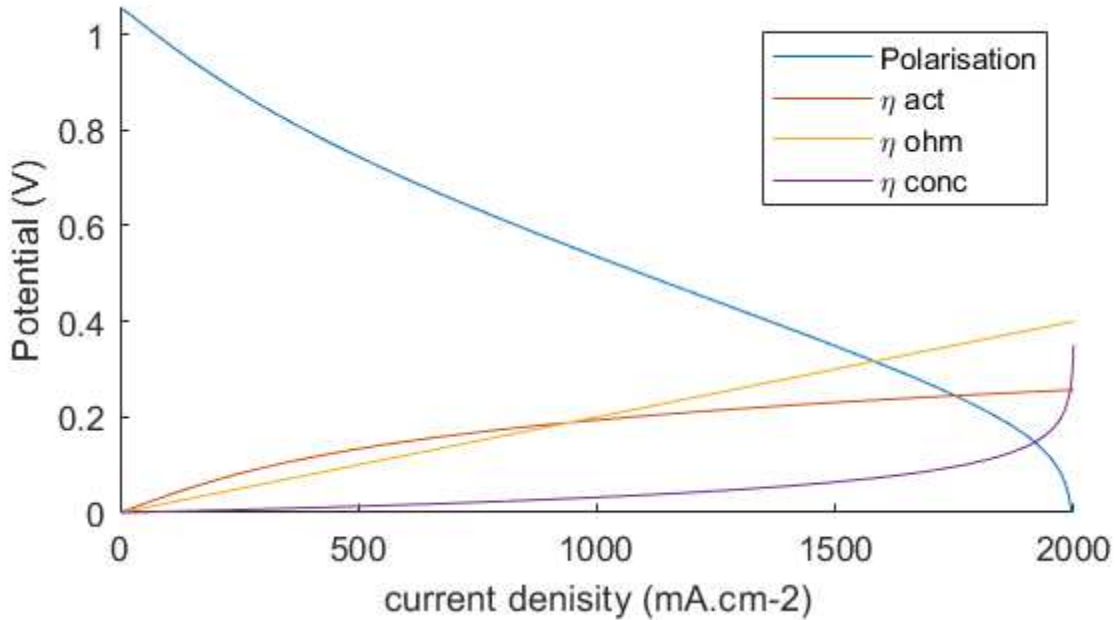
Figure IV - 1 Typical polarization curve with the contributions corresponding to the activation, ohmic, and concentration overpotentials

As mentioned, the architecturation is expected to impact the activation and the polarization overpotential. This will result in a modification of the slops of the curves and eventually their predomination domain.

II.B. Electrochemical Impedance Spectroscopy (EIS)

II.B.1. Introduction

EIS has become an essential characterization technique for fuel cells with close to 70% presence in modern scientific publications. Numerous excellent papers and books on theoretical description have been written by renowned authors such as Stoynov and Vladikova [1], Boukamp [2], Mogensen [3] or practical guidelines such as the one written by Ivers-Tiffée *et al.* [4] and by

Lasia[5]. The popularity of the technique is earned by the capacity to completely describe a complex electrical system, providing insight on its material characteristics and indirectly on its performances.

EIS is based on the well-known transfer function (TF), which is the ratio of an output and an input signal, as shown in Figure IV − 2. However, an electrochemical power source is nonlinear and therefore should be impossible to study via a TF. A solution is to minimize the perturbation amplitude in order to keep the steadiness of the currently investigated system state, ensuring local linearity. Hence, the principle is to study the response of the system to specter of AC signals with low frequency (typically several 10 mA or mV) with variating frequency. A wide frequency range is often necessary to completely describe the investigated system.

Input wave
(perturbation) x(t)

System

$$H(\omega) = \frac{Y(\omega)}{X(\omega)}$$

Output wave (response, measurement) y(t)
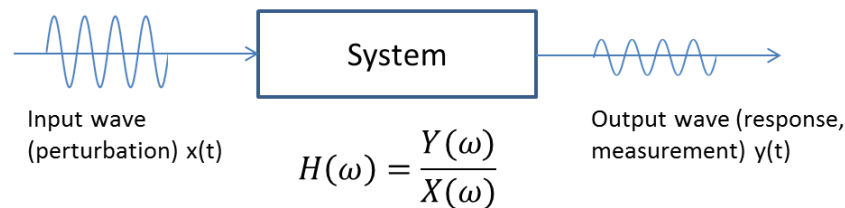
Figure IV - 2 Transfer function principle schematic. Where X(ω) and Y(ω) are the Fourier transformations of the input and output signals respectively, and H(ω) is the transfer function of the system.

If the input signal is a current and the output signal is a voltage, the TF is called an impedance and has the dimensions of a resistance.

The measurement frequencies are spaced on a logarithmic scale and defined by the maximal and minimal values as well as the number of points by decade. The response can be represented in two sets of coordinates and their respective graphic representation:

- Cartesian coordinates following the relation $Z(i\omega_i) = Z'(i\omega_i) + iZ''(i\omega_i)$ are plotted in a complex plane forming a Nyquist plot as shown in Figure IV − 3 A.
- Polar coordinates following the relation $Z(i\omega_i) = |Z_i|e^{i\varphi_i}$ where $|Z_i| = \sqrt{Z'(i\omega_i)^2 + Z''(i\omega_i)^2}$ and $\varphi_i = \arctan \frac{Z''(i\omega_i)}{Z'(i\omega_i)}$ represented by a Bode plot as shown in Figure IV − 3 B.

A)   B)
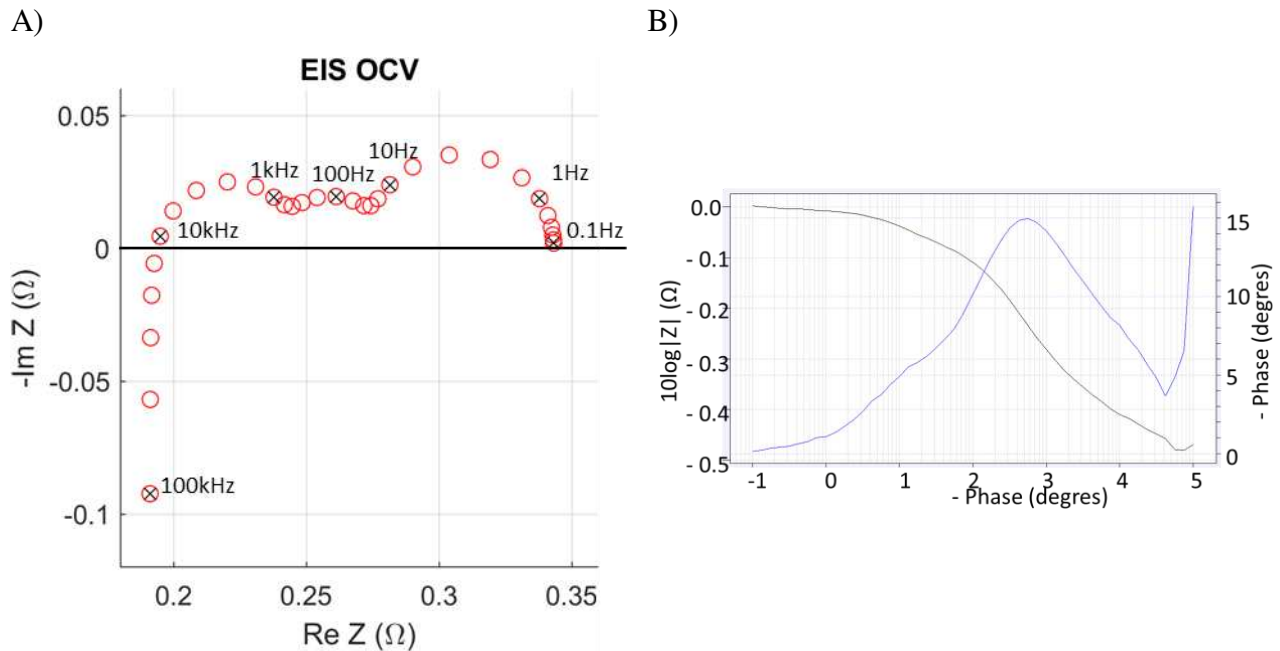
Figure IV - 3 EIS representations. A) Nyquist plot; B) Bode plot

The impedance analyzer measures the response of the probed system to the perturbation and not directly the phenomena occurring in this system. Thus a measurement interpretation is necessary to deduce the real system properties. For this, experimental data are usually fitted by a theoretical model based on the working hypothesis and the application of the complex nonlinear least-squares method. This fitting results in an identification of an equivalent electrical circuit corresponding to the diagram and allows determining the pertinent parameters.

A series or parallel combinations of simple electric elements such as resistance (R), capacity (C), or inductance (L) are used as a first-order approximation to describe homogeneous systems. Each of those elements can be linked to a physical phenomenon occurring in the cell.

Element	Symbol	Circuit representation	Impedance calculation	Associated phenomenon
Resistance	R		R	- Energy losses - Potential barrier - Electronic conductivity - Ionic conductivity
Capacitance	C		$\dfrac{1}{i\omega_i C}$	- Mass and charge accumulation - Dielectric polarization - Integral relation between parameters
Inductance	L		$i\omega_i L$	- Self-inductance

First-order reactions such as faradaic reactions or solid-state charge transport can usually be represented by a parallel combination of resistance and a capacitance described by the relation $Z(i\omega_i) = \frac{R}{1+\omega^2 t^2} - i\frac{\omega R T}{1+\omega^2 t^2}$ producing a semicircle with a diameter of R in the Nyquist plane.

For a more precise description of real and complex systems, a combination of the elementary elements may prove to be insufficient. In this case, more complex elements can be found as described below.

The constant phase element (CPE) was introduced to take into account any inhomogeneities or other frequency-dependent processes. It replaces the capacitance in the previously mentioned equivalent circuit and produces a flattened semicircle.

The second electrochemical element is the Warburg element (W) which is used to describe any diffusive processes.

Element	Symbol	Circuit representation	Impedance calculation	Associated phenomenon
Constant phase element	CPE (Q)	CPE	$\sigma\omega^{-0.5}(1-i)$	-Inhomogeneous processes - Overlapping of time constants
Warburg element	W	W	$A^{-1}(i\omega)^{-n}$	- Diffusion (Fick law)

II.B.2. Relative Gap method (R.G.) – a simplified comparison technique

EIS analysis of complete fuel cells remains challenging due to the complex structure and the overlapping of phenomena responses to the perturbation signal. Multiple studies have focused on the response of the components varying the experimental conditions, materials, and microstructure by carrying out measurements on complete symmetric cells. For an exhaustive components characterization, an in-depth EIS analysis needs to be performed, based on EIS spectra simulation by equivalent electric circuit method as well as by other methods such as differential impedance analysis. Many excellent papers and reviews can be found in the literature on EIS fundamentals [5], on porous components [6], and more precisely cathodes [7] [8] or anodes [9] as well as on dense oxygen conducting materials [10]. However, mastering these techniques requires long and continuous training focused on the comprehension of its subtleties.

In this work, we aim to compare architectured and planar cells and deduce the effect of the architecturation on a macroscopic scale. Thus, to avoid the formalism of the equivalent electric circuit identification, we propose a simplified comparison method inspired by the differential impedance analysis method.

This method consists of studying the R.G. between the frequency associated real part of the electrochemical impedance of the architectured and pseudo-equivalent planar cell (equation 1). For the validity of this method, the cell spectra need to be similar, i.e. to present the same number of arc responses. This approach is based on the fact that frequencies are usually representative of some given phenomenon, as reported for instance by Mauvy *et al* [11].

$$Relative\ Gap\ (f_i) = RG(f_i) = \frac{Z'(f_i)_{planar} - Z'(f_i)_{architetured}}{Z'(f_i)_{planar}} \qquad (2)$$

The R.G. as a function of the frequency allows evaluating the difference in resistivity of the compared cells at given experimental conditions. It shows us the variation of the resistivity of the architectured cell compared to the planar cell. The interpretation of the dependency evolution requires a basic understanding of the electrochemical impedance spectroscopy principles and the correspondence between the actual frequency and the occurring phenomenon as well as the corresponding cell element where the so-called phenomenon takes place.

To study the cells in static conditions and to probe uniquely the materials response, we study the EIS spectra at OCV condition. In this case, the R.G. describes the influence of the architecture on the components without electrochemical reactions between the electrodes. To analyze the catalytic properties of the components, we study the EIS spectra at operating conditions (0.7 V) during which the contribution characteristic to the electrochemical reactivity is also visible. Thus, to separate the influence of the architecture on the static materials and the catalytic properties, we study the difference between the R.G.s in these conditions ($R.G._{.0.7\,V}(f) - R.G._{.OCV}(f)$). The R.G. is also used to to compare the ASR as well as current and power density of the architectured and planar cells considering the planar cell values as the reference.

The separation of the electrodes contribution is more challenging as they both present gas and charge diffusion as well as electrochemical reaction. To separate their contribution, we have chosen to vary the gas concentrations.

Electrolyte

It is generally assumed that at high temperature, the electrolyte response to the EIS perturbation is equivalent to a series resistance which can be measured at high frequency. On the Nyquist plot, it is read at the beginning of the EIS spectrum.

Anode

A combined deconvolution and non-linear least squares (CNLS) fitting approach have been used by Sonn *et al*. [12] allowing identification frequency association of the processes occurring in Ni:YSZ anodes.

- At 30 – 20 kHz, the concerned process is the ion transfer in the YSZ matrix, and are consequently related to the triple-phase boundaries length
- Charge transfer reaction is observable at 8 - 2 kHz
- Gas diffusion processes response are observed at low frequencies below 200 Hz

Wagner *et* al. [13] also identify gas diffusion in the anode gas channel at frequencies close to 10 Hz.

In their publication on Electrochemical Impedance Modeling of a Solid Oxide Fuel Cell Anode Mohammadi *et al*.[9] identify two arcs corresponding to the electrochemical behavior (300 Hz – 35 kHz and gas diffusion (< 30 Hz) of the anodes. Furthermore, in thick electrodes (anode support for example), the appearance of a third arc is expected at low frequencies [14].

Cathodes

Although Type I and type II cell cathodes are composed of different materials, both are composites with an ion-conducting material and an electron or mixed ion-electron conducting material. As it is for the anode, the high frequencies arcs are associated with oxygen ions transfer in the ion-conducting phase ($O^{2-} + V_{\ddot{o}} \rightarrow O_o^{\times}$) as described by Kim *et al*. [15]. The authors lead a reflection on an intermediate frequency arc associated with an O^{2-} surface diffusion due to its low dependency on the pO_2 (proportional to $pO_2^{1/4}$). The low-frequency arc has a strong dependency on the pO_2 variation and is naturally associated with oxygen gas diffusion.

During their work on composite cathodes, Jørgensen *et al* [16] reported the presence of an arc with a time constant corresponding to 3-20 Hz. The authors associated it with a Gerisher-type impedance related to an electrochemical reaction coupled with surface diffusion and charge transfer.

Barbucci *et al.* [8] carry out a study in LSM:YSZ composite cathodes. They report the presence of at least two arcs and consequently physical phenomena in the 10 Hz – 40 kHz region related to ion transport and activation overpotential. The authors consider the concentration negligible in their study. An inductance effect is observed close to 1 Hz, which they associate with the adsorption of oxygen intermediate species (O^- and O^{2-}).

II.C.   Measurement set-up

In this work, a Fiaxell testing rig (Figure IV – 4 A) is used coupled with an IviumStat impedance spectrometer (Figure IV – 4 B) and a Brook Instruments debit flow meter (Figure IV – 4 C).

A)   B)
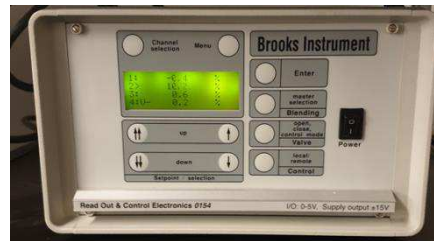
Figure IV - 4 Electrochemical measurements set-up. A) Fiaxell testing rig; B) Brook Instruments debit flow meter (figure II-38C)

The cell is placed between a nickel mesh at the anode side and a gold mesh at the cathode side, both having the role of current collectors. To ensure gas separation, aluminosilicate felts are shaped and positioned over the cell as shown in Figure IV – 5, and the excess gas is burned within the felt. Hence a local temperature gradient is possible and should be limited to avoid influencing the measurement, by temporary spacing successive measurements and controlling the gas flow.
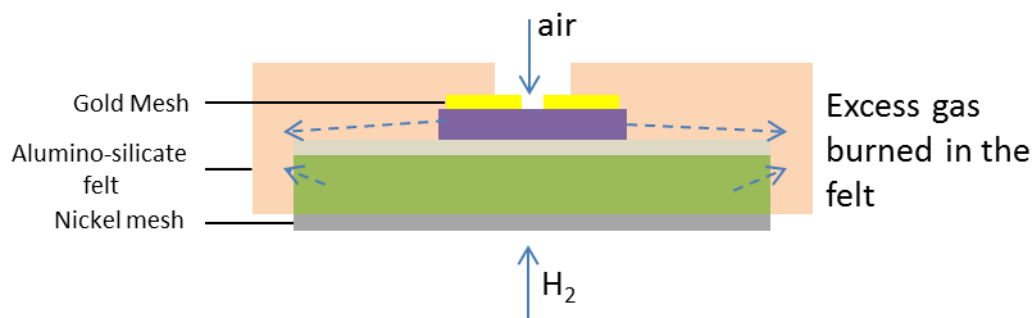
Figure IV - 5 Cell testing configuration schematic

III. Results

In this subchapter, we propose an electrochemical analysis of pairs of architectured and equivalent planar type I and type II cells.

In the previous chapter, we carried out a detailed characterization of the components of the cells including porosity, materials distribution, and thickness. The architecture obtained with the soft template method was also extensively characterized and the area expansion coefficient (AEC) was estimated to 28%.

The electrochemical performances of the cells are analyzed in variable gas flow, and partial pressure conditions and all measurements are carried out at a temperature **T = [792 – 804 °C]**. The electrical generation capacity of the cells is deduced from the polarization curves. Electrochemical impedance spectroscopy is carried out to promote a scientific understanding of the behaviour changes caused by the architecturation.

We anticipate that the architecturation should influence majorly three parameters of the fuel cell performances.

- The variation of the electrolyte thickness, which affects linearly (if homogeneous) the conductivity, should influence the overall ohmic overpotential of the cells. This contribution should remain unchanged with the gas conditions variation. This influence is characterized by electrochemical impedance spectroscopy and measuring the series resistance of the spectra.
- The increase of the exchange surface should increase the number of active triple phase boundaries, decreasing the overall activation overpotential.
- The penetration of the dense electrolyte within the porous electrodes should open new charge transport pathways and thus influencing the effective conductivity of the electrodes. Consequently, it should influence the overall ohmic polarization as well as the activation and concentration overpotential as it deploys new triple-phase boundaries closer to the gas diffusion channels.

The second and the third contributions can both be estimated by varying the reactant gas concentration during I-V or EIS measurements.

III.A. Type I

The Type I cells present an architecture at the cathode side and offer an insight into its influence on the oxygen electrode. As mentioned, we have chosen to present only this sample of this batch of Type I cells, due to the low porosity of the anode. We consider that pronounced architecturing on the anode/electrolyte interface would present inaccurate results as the architectures would cross the AFL and integrate the anode support. Thus, the drastic change in porosity and materials ratio would strongly influence the performance and the sole impact of the architecture would be difficult to estimate. However, practically speaking, a configuration with the electrolyte material passing through the AFL and ending in the anode support would be extremely interesting to increase the cell performances and should be considered in future works. Nonetheless, a slight curvature is observed on the anode/electrolyte side.

III.A.1.Components reminder

The characteristics of the cell components are reminded here in order to facilitate the link between microstructure, geometry and electrochemical performances. Cross-section SEM images are presented in Figure IV − 6 and the cell parameters are reported in Table IV − 1.

A)

B)
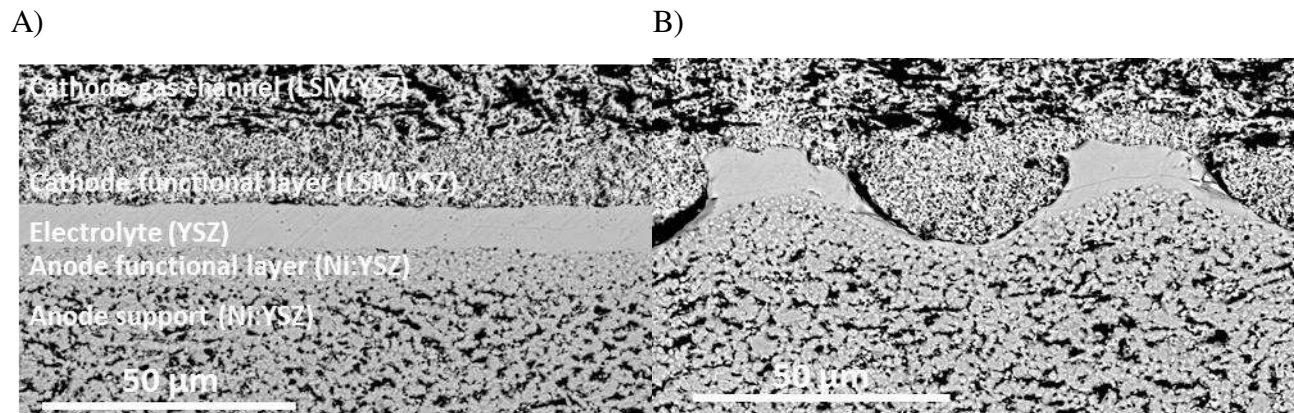
Figure IV - 6 Type I cross-section SEM observation. A) Planar cell; B) Cathode architectured cell (more detailed view in figure III − 3, page 125)

Table IV - 1 A) Type I cells parameters overview					
Component	Composition (Materials and volume ratio)	Porosity (%vol)	Thickness in the planar cell (µm)	Max thickness in the architectured cell (µm)	Min thickness in the architectured cell (µm)
Anode support	Ni:YSZ 44:56	27	334±5	334±5	334±5
AFL	Ni:YSZ 44:56	11	8.4	10.8	5.2
Electrolyte	YSZ	0	9.9	14.1	3.4
CFL	LSM:YSZ 50:50	34	15.5	21.4	5.4
CGC	LSM:YSZ 50:50	57	61±5	61±5	61±5
Table IV - 1 B) Harmonic mean value of the architectured electrolyte thicknesses					
	Planar	Min architectured	Harmonic mean[3] + min architectured	Ratio calculated architecture thickness vs planar thickness	
Electrolyte	9.9	3.4	6.57	0.33	

---

[3] Harmonic mean : $H = \dfrac{n}{\sum_{i=1}^{n}\frac{1}{z_i}}$

In this subchapter, we study the polarization curves of the Type I pair of cells under different gas conditions, accompanied by the corresponding power density curves. In Figure IV – 7, the curves in reference gas flow condition with humidified H_2 (97% H_2 + 3% H_2O) flow of 100 ml/min and synthetic air (20% O_2) flow of 300 ml/min are shown.
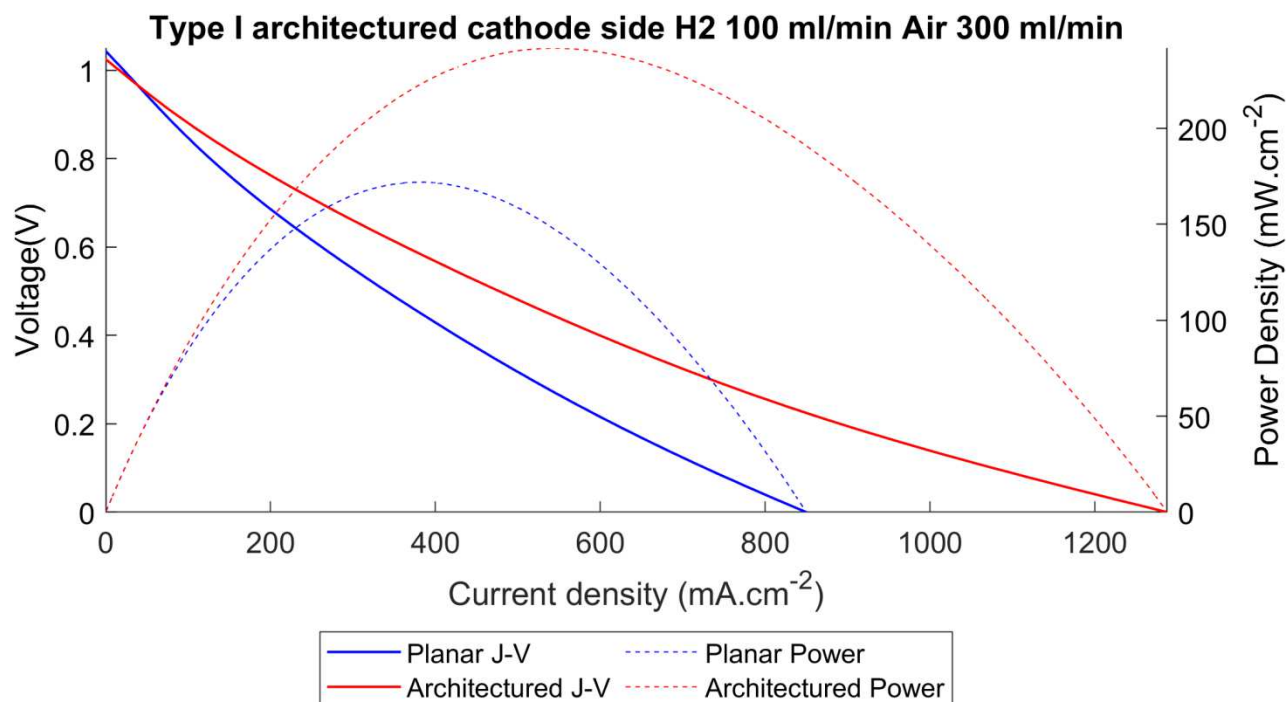
Figure IV - 7 Type I Polarization and density curves in Reference gas conditions

The first characteristic to be observed is the OCV values which in both cases are adequate (1.02 V for the architectured cell and 1.04 for the planar cell).

The potentiometry of the cells (variation of the imposed potential) reveals a superior current density of the architectured cells and consequently a superior power density. The maximum power density, as well as the corresponding current density, potential, and ASR, are reported in table IV – 2. In table IV – 3, we report the same characteristic with respect to an operational voltage fixed in this study at 0.7 V. In both cases, we calculate the ratio $P_{architectured}/P_{planar}$ in order to evaluate the effect of the architecture on the global cell performances.

Table IV - 2 Type I cell remarkable values with respect to the maximum power density using humidified H2 – air				
	Potential (V)	Current density (mA.cm^{-2})	ASR (Ω.cm^2)	Power density (mW.cm^{-2})
Planar	0.45	382.2	1.17	172
Architectured	0.44	549.4	0.80	241.7
R.G. (%)	2	44	32	40.5

Table IV - 3 Type I cell remarkable values with respect to the operating conditions (0.7 V) using humidified H2 – air				
	Potential (V)	Current density (mA.cm^{-2})	ASR (Ω.cm^2)	Power density (mW.cm^{-2})
Planar	0.7	190.2	3.68	133.2
Architectured	0.7	260	2.69	182
R.G. (%)	0	36.7	27	36.7

A significant increase of the electrochemical performances, demonstrated by the difference in the maximum power generation, is visible during this test. This increase in performance is superior to the AEC (= 28%), which means that in addition to deploying a larger exchange surface area, the architecture influences other cell parameters as mentioned previously. The variation of the ASR is consistent with the electrolyte thickness variation, calculated in the previous chapter (33%).

The polarization curves present a particular concave shape showing that the cells have no apparent limiting current. Thus, the gas concentration is not a limiting factor even at higher current densities. The shape of the curve is characteristic of a predominance of the activation overpotential. To further investigate the impact of the microstructural parameters such as the porosity and the architecture on the electrochemical performances, a study of the current and power density evolution is conducted under different gas conditions as shown in figures IV – 8 and 9.

A)

Type I Cath. side Ar/H2 (5%) 100 ml/min Air 300 ml/min

B)

Type I Cathode side H2 50 ml/min Air 300 ml/min

C)

Type I Cathode side H2 100 ml/min O2 300 ml/min
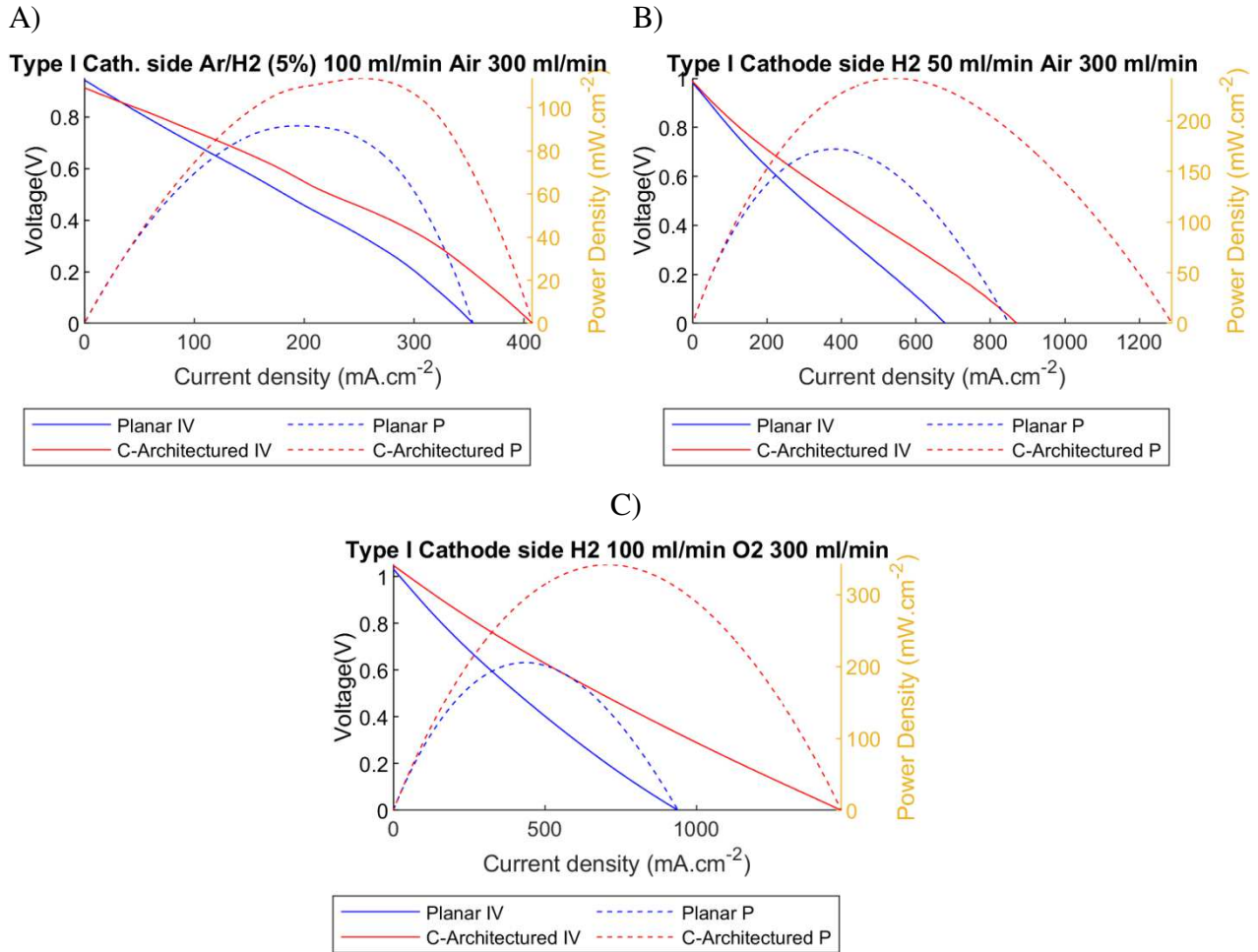
Figure IV - 8 Polarization curves in variable gas conditions A) Ar/H2 (5% H2) – Air; B – H2 (halved gas flow) – Air; C – H2 – O2

We hypothesize that, due to the low porosity of the anode layers, the anodic active TPB concentration is impaired and the performances of both planar and architectured cells are limited. The lack of a visible concentration overpotential shows that the reactant gases are not entirely consumed due to the inaccessibility of the anodic TPBs. This hypothesis can be supported by lowering the H_2 concentration but maintaining the same gas flow as shown in Figure IV – 8A. In this figure, the cells are tested using a mixture of humidified mixture of Argon and Hydrogen with a 5 % H_2 concentration.

Several important details can be noted. Firstly, the shape of the I-V curves is changed, and a concentration overpotential slope is visible as predicted. However, the slope remains very slowly decreasing, although the fuel concentration is drastically lowered. This agrees with the hypothesis that a limiting factor of the cell performances is the concentration of active anodic TPB caused by the insufficient porosity. Furthermore, the change in the slope at higher current densities can also be associated with a change in the internal resistance of the cell. As the concentration of hydrogen is critical, a partial reoxidation could occur due to the presence of oxygen ions as well as setup related oxygen gas leaks. This hypothesis is further investigated in the next subchapter.

In these gas condition conditions, the maximum power density is increased from 91.61 $mW.cm^{-2}$ for the planar configuration to 113.66 $mW.cm^{-2}$ for the architectured configuration which corresponds to 24%. Even in this stringent experimental condition, the architectured cell remains more efficient than the planar one and the performance augmentation is close to the area expansion coefficient (AEC = 28%). However, we observe uniform evolution of the current density generation when the concentration of hydrogen is lowered from 97% to 5%. The decrease of the current density at 0.7 V for the planar cell is 48.5 % (from 190 $mA.cm^{-2}$ to 98 $mA.cm^{-2}$) and for the architectured cell is approximately 52 % (from 260 $mA.cm^{-2}$ to 126 $mA.cm^{-2}$). Thus, as expected, the architecturation has a limited impact on the phenomena occurring in the anode. The second interesting observation is that the OCV values are considerably lowered compared to the ones measured in the recommended conditions (0.94 for the planar cell and 0.91 for the architectured cell) but remain close to the theoretical value corresponding to the condition (0.95 V).

Table IV - 4 Type I cell remarkable values with respect to the maximum power density using humidified Ar/H_2 – air				
	Potential (V)	Current density ($mA.cm^{-2}$)	ASR ($\Omega.cm^2$)	Power density ($mW.cm^{-2}$)
Planar	0.47	194.91	2.41	91.61
Architectured	0.45	252.58	1.78	113.66
R.G. (%)	4.2	29.6	26.1	24.1

Table IV - 5 Type I cell remarkable values with respect to the operating conditions (0.7 V) using humidified Ar/H$_2$ – air				
	Potential (V)	Current density (mA.cm^{-2})	ASR (Ω.cm^2)	Power density (mW.cm^{-2})
Planar	0.7	97.93	7.15	68.55
Architectured	0.7	125.87	5.56	88.11
R.G. (%)	0	28.5	22.2	28.5

In Figure IV – 8 B, we wish to study the impact of the fuel gas flow on the performances of the cells. For this, we use humidified H$_2$ (3% H$_2$O) and lower the gas flow by a factor of 2 (50 ml/min). A concentration overpotential slope is again visible, which means that in addition to limiting the TPB concentration, the impaired porosity hinders also gas diffusion.

Figure IV – 8 C shows the polarization curves of the cells using humidified hydrogen fed to the fuel electrode and O$_2$ fed to the air electrode. The pertinent measured values are reported in tables IV – 6 and IV – 7.

Table IV - 6 Type I cell remarkable values with respect to the maximum power density using humidified H$_2$ – O$_2$				
	Potential (V)	Current density (mA.cm^{-2})	ASR (Ω.cm^2)	Power density (mW.cm^{-2})
Planar	0.47	437.37	1.107	205.56
Architectured	0.48	711.65	0.674	341.59
R.G. (%)	2	62.7	39.1	66.2

Table IV - 7 Type I cell remarkable values with respect to the operating conditions (0.7 V) using humidified H$_2$ – O$_2$				
	Potential (V)	Current density (mA.cm^{-2})	ASR (Ω.cm^2)	Power density (mW.cm^{-2})
Planar	0.7	237.42	2.95	166.19
Architectured	0.7	404.44	1.73	283.11
R.G. (%)	0	70.3	41.3	70.3

By using pure O_2 instead of air (20 % O_2), the cathode reactional capabilities are probed. We observe a substantial augmentation of the power density caused by the architecturation: 66% increase in the maximum power density and 70 % increase of the power density in operating conditions are measured. This is over twice the value of the AEC and significantly superior to the measurements using air instead of O_2 ($\left[\dfrac{P_{max,archi}}{P_{max,planar}}\right]_{H_2,Air} = 1.40$, $\left[\dfrac{P_{max,archi}}{P_{max,planar}}\right]_{H_2,O_2} = 1.70$). A complementary comparison can be made, studying the evolution of the performances of each cell with the change in the O_2 concentration. The increase of the current density at 0.7 V for the planar cell is 25 % (from 190 mA.cm^{-2} to 237 mA.cm^{-2}) whereas for the architectured cell is approximately 56 % (from 260 mA.cm^{-2} to 404 mA.cm^{-2}). Due to the condition in which this considerable augmentation of the current densities is observed, it can be associated with the increase in the catalytic properties caused by the architecture.

To summarize an overview of the I/V curves is presented in Figure IV – 9.
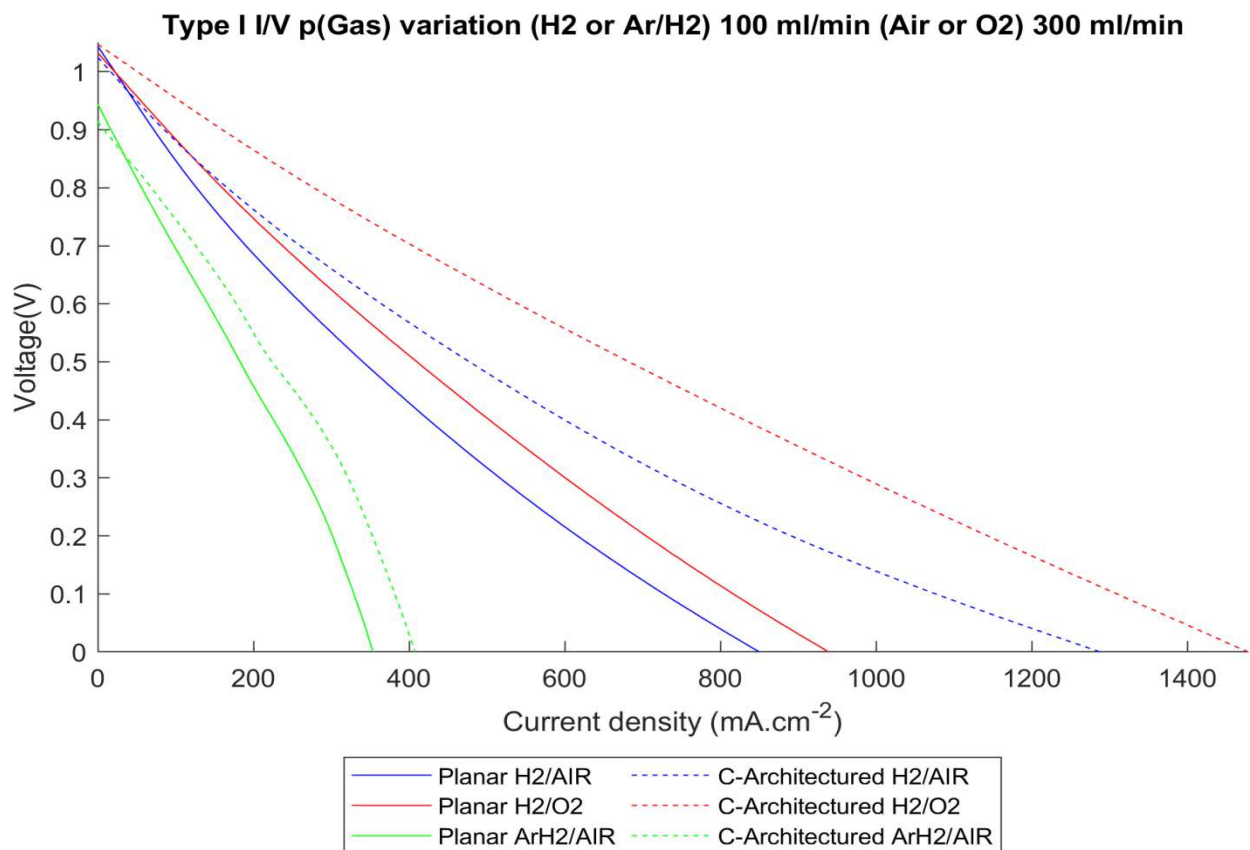
Table IV - 8 Type I polarization curves overview in variable gas conditions

The superimposition of the polarization curves in different conditions allows visualizing the evolution of the performance of the cells and comparing them. As mentioned, an impaired fuel consumption demonstrated by the presence of concentration overpotential slope when using 5% H_2 fuel and its absence when using the 97% H_2 fuel, limits the cell performance. Nevertheless, the architectured cell remains more performant than the planar one.

When using humidified H_2 as a fuel and O_2 at the cathode, the increase in the electrochemical performances (66-70%) is significantly superior to the AEC. Furthermore, the variation of the experimental conditions influences the performance ratios. Thus, we may conjecture that the architecture influences the electrochemical performances by acting on different properties. The contribution of the electrolyte thickness should remain constant with the variation in the gas conditions. Thus, we deduce that the difference in the power density ratios associated with the different gas conditions is caused by the influence of the architecturation on the electrode. A significant increase in the electrochemical performances, especially using pure O_2, was expected as the oxygen reduction reaction (ORR) is sluggish and improvement of the catalytic properties of the cathode is one of the most promising pathways of SOFC development.

To verify the suggested hypothesis, and to further understand the influence of the architecturation on the electrochemical performances we carry out an EIS study comparing the frequency associated resistance of the cells.

III.A.3.EIS

In this series of measurements, we proceed in the same manner as for the analysis of the I/V curves, by varying the reactant gas concentrations. The EIS measurements are carried out between 100 kHz and 0.1 Hz at either OCV condition using a galvanostatic measurement with 10 mA amplitude or at 0.7 V corresponding to the operating conditions using a potentiostat measurement with 10 mV amplitude. The objective is to separate the different contributions of the occurring phenomena from the global cell resistance.

In the following measurement procedure, we will display the Nyquist plots of the EIS measurement in the before mentioned condition. Ultimately, the interpretation will be based on the R.G. plots associated with the EIS measurements in those conditions. To obtain an absolute characterization of the fuel cells, a parametric study needs to be carried out. However, in this

work, we are interested in the relative variation of the electrochemical performances, and we will not focus on a parametric study of the EIS data.

III.A.3.a)   *Reference gas conditions*

In Figure IV – 9, we display every second frequency decade distribution on the Nyquist diagrams of the architectured and the planar cells at A) OCV and at B) at 0.7 V in the recommended gas flow and concentration conditions. For the sake of clarity, we will not display the frequencies in the next figures. We observe the expected mismatch of the series resistance between the architectured and the planar cells caused by the difference in the electrolyte thicknesses.

A)   B)
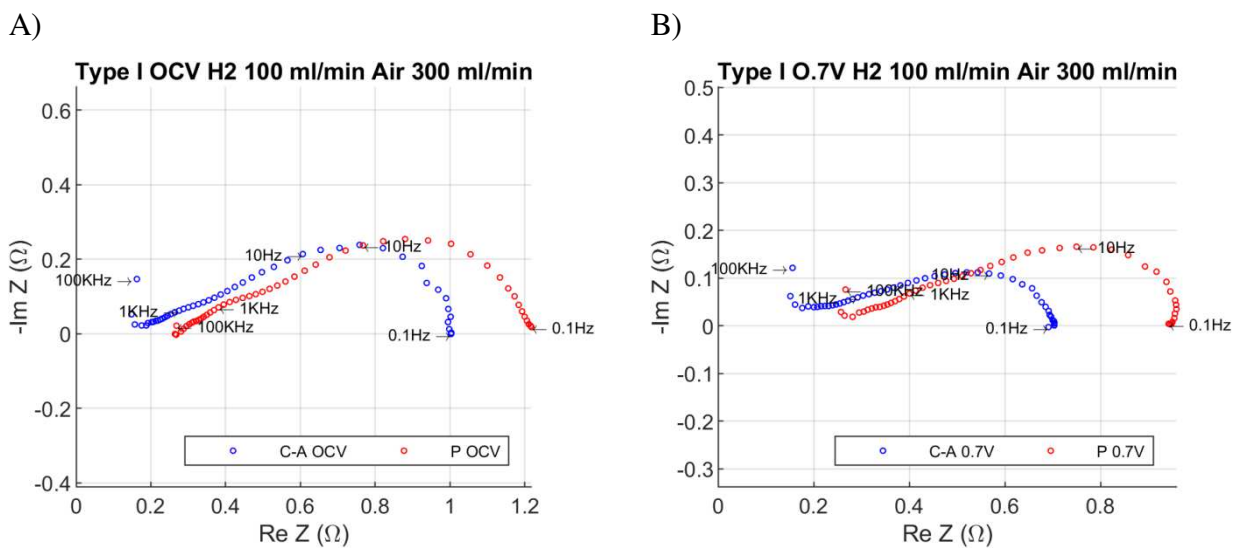
Figure IV - 9 Nyquist plot of Type I cells (C-A = cathode-architectured P = planar) in reference gas conditions displaying 1/2 frequency decades. A) At OCV; B) At 0.7 V

In figure IV – 10, we superimpose the plots for a more global overview of the test.
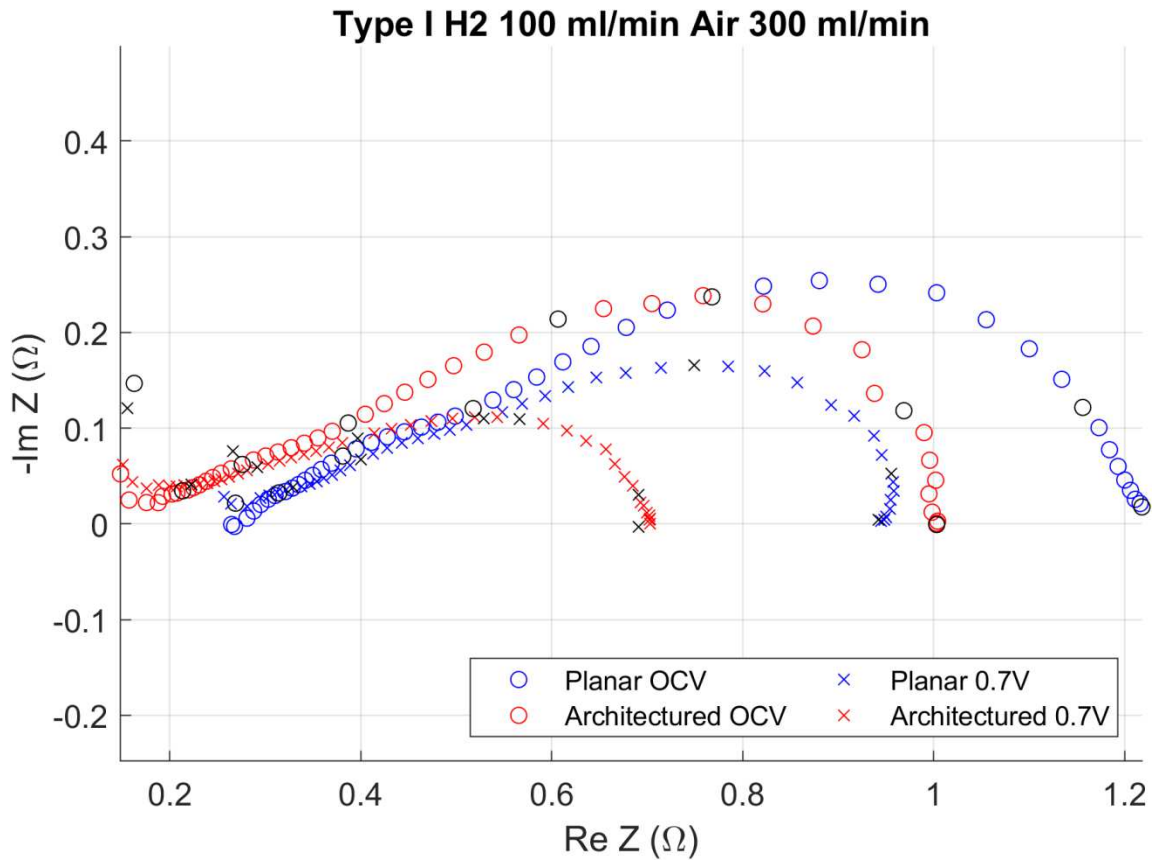
Figure IV - 10 Superimposition of the Nyquist plots of Type I cells in reference gas conditions

In Table IV – 9, we report the series resistance characteristic to the electrolyte resistance, as well as the overall resistance of the cells in the different test conditions (OCV and 0.7 V)

Table IV - 9 EIS Type I series and overall resistance values in reference gas conditions			
	Series R (Ω)	R_{total} (at OCV) (Ω)	R_{total} (at 0.7 V) (Ω)
Planar	0.26	0.95	0.7
Architectured	0.15	0.86	0.55
R.G. (%)	42.3	9.5	21.4

As predicted by the microstructural characterization, the electrolyte is significantly less resistant in the architectured cell. This is due to the variation of the thickness and the presence of very thin electrolyte zones. We proceed with a study of the R.G. plots as a function of the logarithm of the frequency as shown in figure IV – 11.
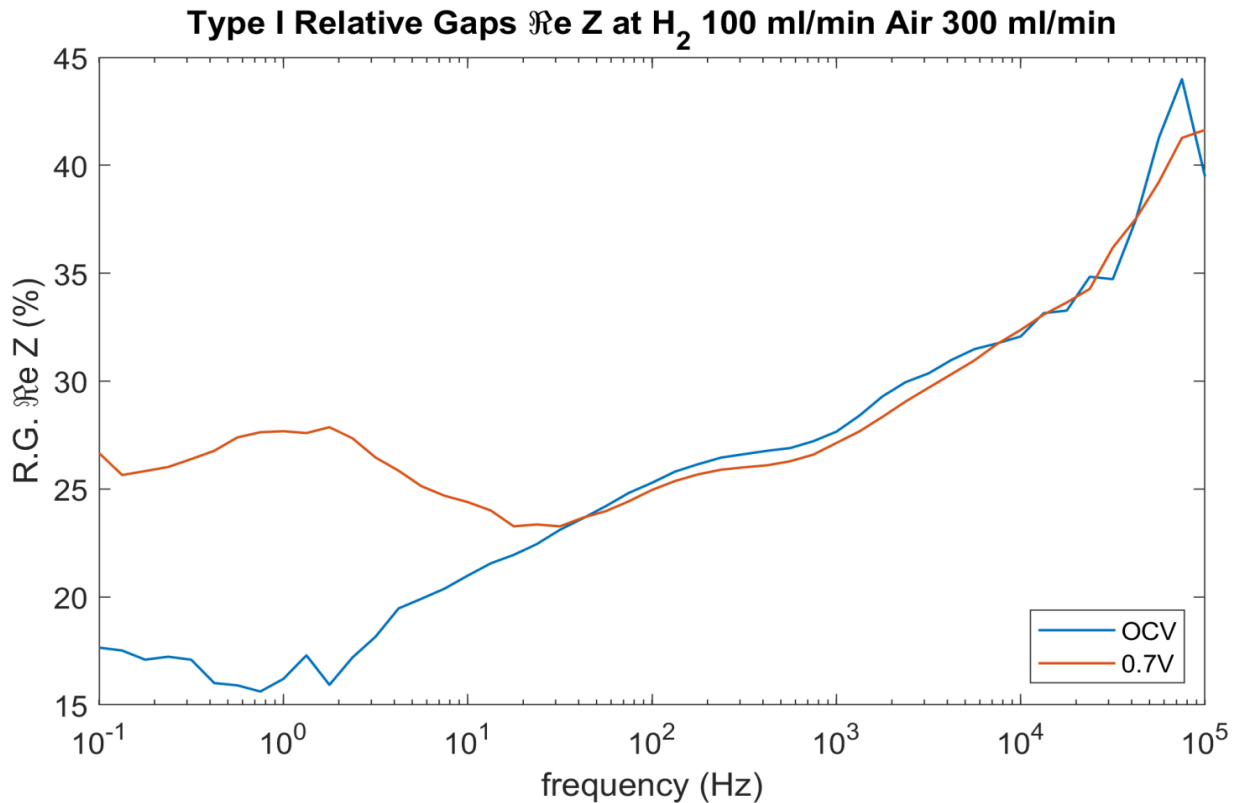
Figure IV - 11 Type I R.G. plots in reference gas conditions

Static conditions (at OCV)

In OCV conditions, the R.G. is steadily reduced as the frequency decreases. At high frequencies (>10 kHz) the resistivity of the architectured cell is approximately 42 % inferior to the one of the planar cell. It is generally accepted that this contribution of the EIS spectra is associated with the electrolyte materials response. Thus, we can deduce that the architectured electrolyte has an average resistance of 42 % lower than the one of the planar cell.

The R.G. remains elevated in the charge transfer associated domains (100 Hz – 50 kHz) with a linear decrease. This means that the architecture influences mostly the charge diffusion in the cell. However, at low frequencies [0.1 Hz ; 2 Hz], which are usually associated with gas diffusion phenomena, the OCV R.G. exhibits a 17% better gas diffusion in the architectured cells.

At operating conditions (0.7 V)

At 0.7 V, the R.G. has a similar behavior as in the OCV condition for frequencies higher than 30 Hz. As the frequency decreases to values lower than 30 Hz, the 0.7 V R.G. is increased and diverges from the OCV R.G. The difference between the gap in OCV and operating conditions demonstrates the influence of the architecture on the electrochemistry. This is in accordance with the work of Jørgensen *et al.* [16] where the response of the system is associated with a Gerischer-type impedance related to electrochemical reactions coupled with surface diffusion. Furthermore, the low frequencies are also associated with oxygen gas diffusion. As the cell operates, the oxygen is consumed and ultimately the diffusion is modified. Thus, by measuring the difference in the gaps, we could estimate that the architectured cells exhibit <u>8 to 12 % greater catalytic properties</u>.

In the next tests, we variate the gases concentrations in an attempt to identify the anode and the cathode contributions to the overall cell resistivity.

III.A.3.b)   pH$_2$ variation

In the first test, we superimpose the Nyquist plots of the cells using Ar/H$_2$ or H$_2$ as fuel gas. In Figure IV $-$ 12, we superimpose the Nyquist plots of the cells at OCV and 0.7 V, and in Table IV $-$ 10, we report the remarkable resistance values corresponding to the test.

A)

Type I - pH2 variation OCV

B)

Type I - pH2 variation 0.7V
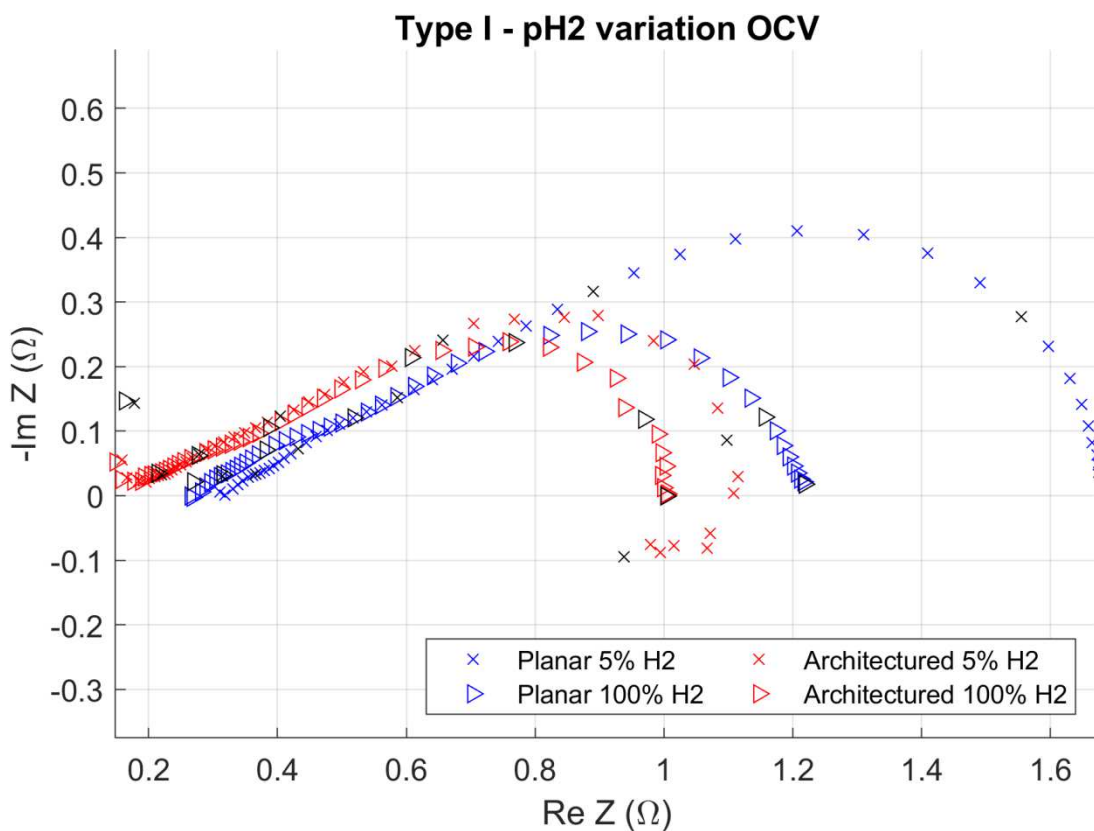
Figure IV - 12 Type I cells EIS with pH$_2$ variation. A) At OCV; B) At 0.7 V

Table IV - 10 EIS Type I series and overall resistance values with pH_2 variation						
	100 %			5 %		
	Series R (Ω)	Overall (OCV) (Ω)	Overall (0.7 V) (Ω)	Series R (Ω)	Overall (OCV) (Ω)	Overall (0.7 V) (Ω)
Planar	0.26	0.95	0.7	0.31	1.36	1.15
Architectured	0.15	0.86	0.55	0.16	0.97	1.07
R.G. (%)	42	9.5	21.4	48.4	28.7	7

We note that the series resistance R.G. is higher when using 5 % hydrogen. In these gas conditions, the resistance of the architectured cell is lower in OCV conditions than in the operating conditions, contrary to the resistivity measured in the reference gas conditions. This is most likely due to the hindered water management in the anode.

We observe a low-frequency inductive loop in the plot of the architectured cell in OCV condition. This loop is commonly related to the adsorption of intermediate oxygen species (O^{2-}, O^-) as reported by Barbucci *et al*. [8]. This effect may occur because the hydrogen concentration is low and possibly insufficient to oxidize the excessive oxygen in the felts leading to saturation. The loop is partially observed in the operating condition especially for the planar cell using hydrogen as fuel. Furthermore, the loop may be associated with water accumulation. However, it is registered at OCV, which means that no electrochemical activity is occurring and water should not be produced. A setup-related oxygen gas leaks could provoke a direct hydrogen and oxygen reaction resulting in water fabrication, hydrogen concentration decrease and consequently a partial reoxidation of the anode.

We proceed with studying the R.G. plots represented in Figure IV – 13.
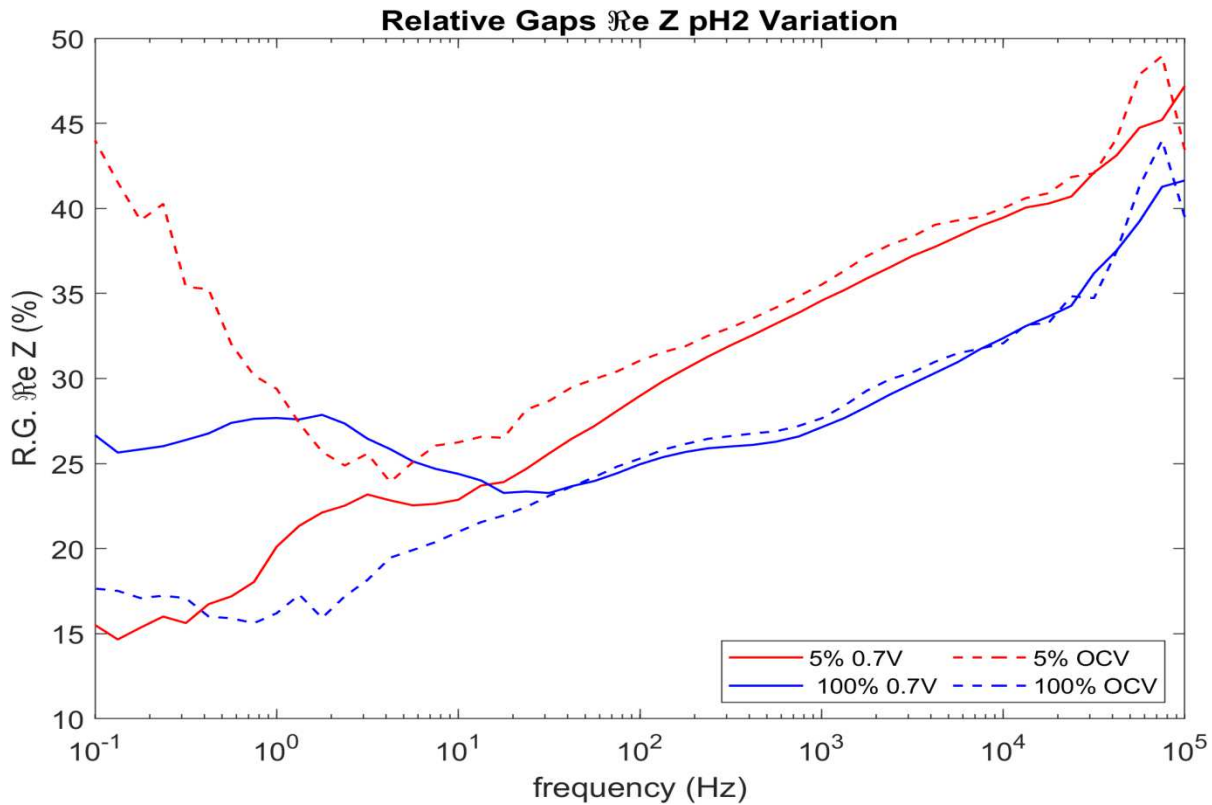
Figure IV - 13 Type I R.G. plots with variable pH$_2$

Although the architectured cell remains more efficient than the planar cell, the OCV and 0.7 V gaps are inverted when 5 % H$_2$ fuel gas is utilized. This is provoked by the weak water management exacerbated by the low porosity. Furthermore, the inversion of the position of the OCV plot in respect to the 0.7 V plot in these gas conditions, demonstrates that the resistance of the architectured cell is highly increased and brought closer to the one of the planar cell. This may be explained by the higher reactivity of the cell which leads to further H$_2$ depravation and consequently is more likely to present an anode reoxidation by the excess oxygen (ionic or gaseous). In these conditions, we observe the potential limits of the R.G. method in comparing EIS spectra which are not equivalent.

III.A.3.c)   pO$_2$ variation

In the next series of tests, we study the influence of the pO$_2$ variation on the cells and the influence of the architecture in these conditions. In Figure IV – 14 A and B, we superpose the Nyquist plots of the cells in the varying experimental condition and, in figure IV – 15, we summarize the R.G. plots.
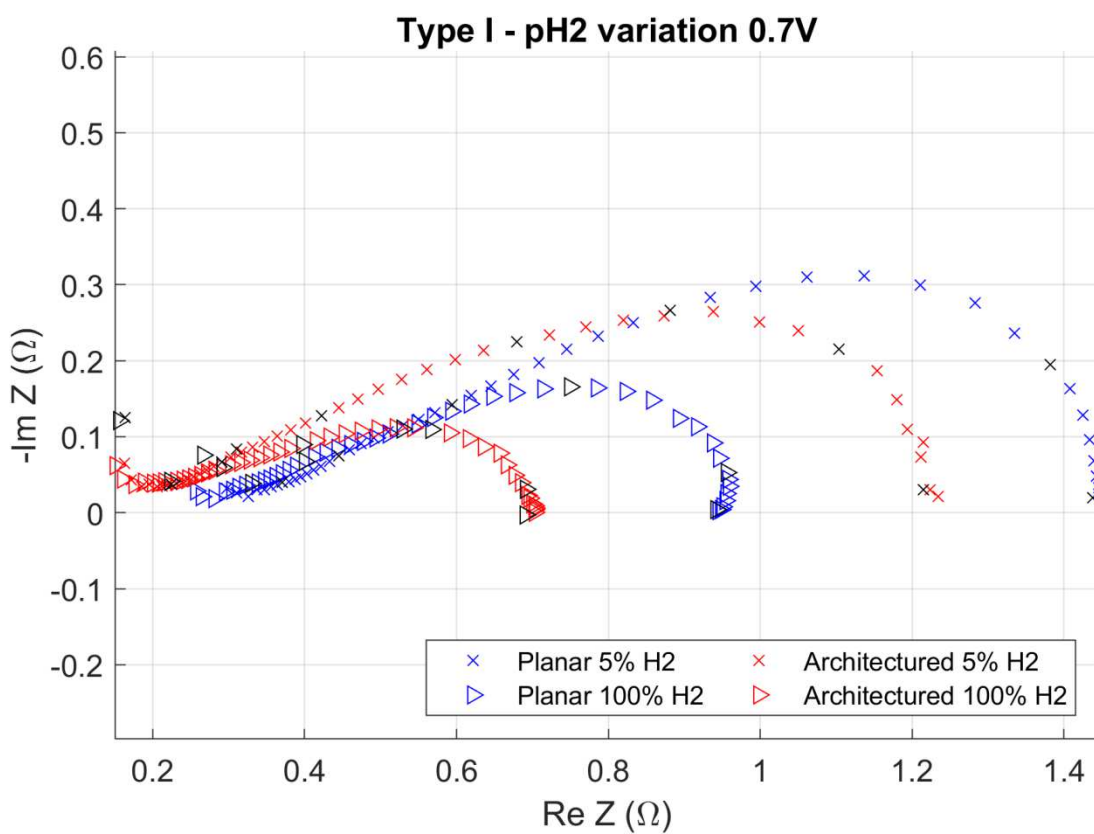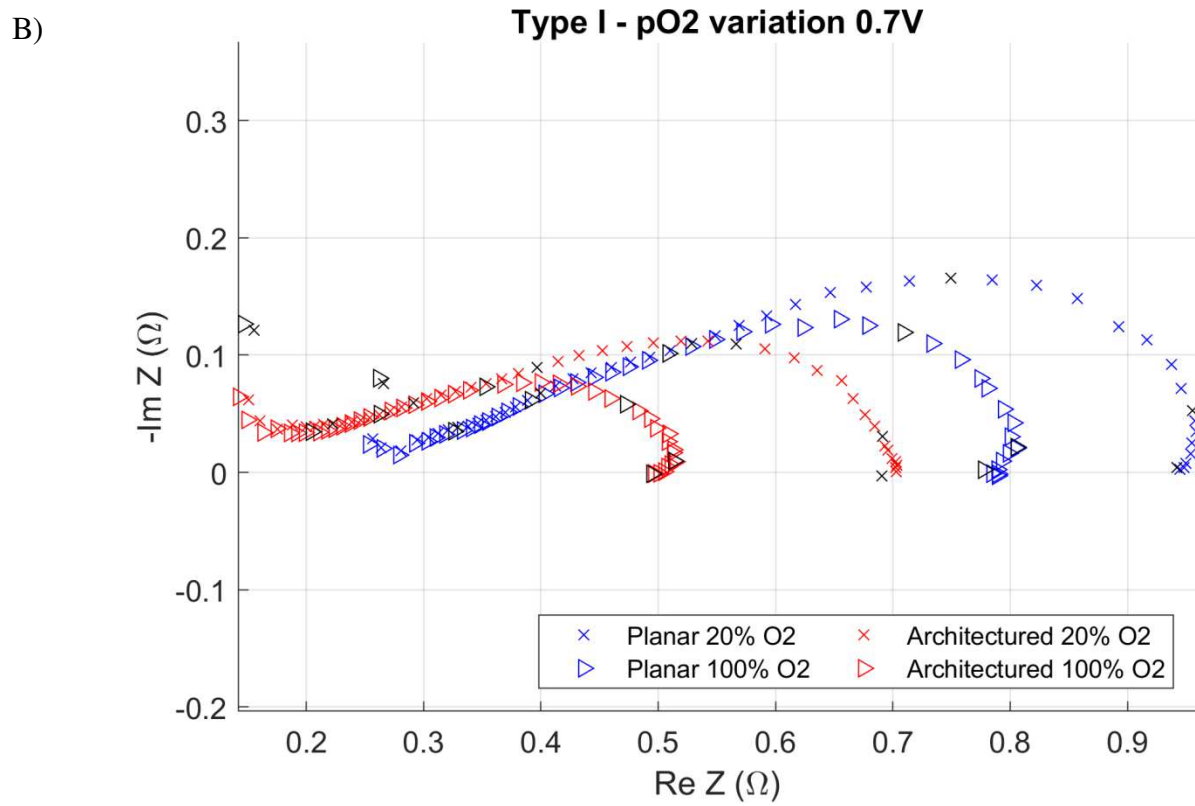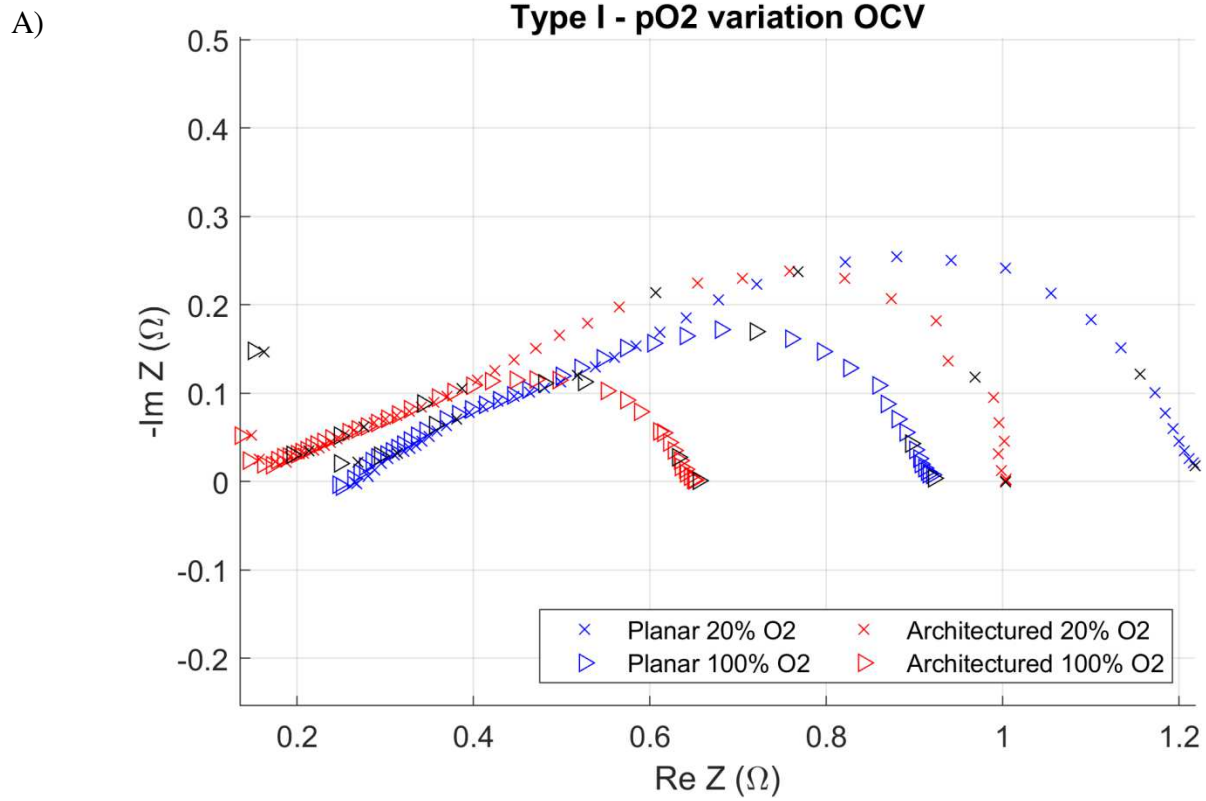
Figure IV - 14 Type I cells EIS with pO$_2$ variation. A) At OCV; B) At 0.7 V

Table IV - 11 EIS Type I series and overall resistance values with pO_2 variation						
	20 %			100 %		
	Series R (Ω)	R_{total} (at OCV) (Ω)	R_{total} (at 0.7 V) (Ω)	Series R (Ω)	R_{total} (at OCV) (Ω)	R_{total}(at 0.7 V) (Ω)
Planar	0.26	0.95	0.7	0.25	0.68	0.55
Architectured	0.15	0.86	0.55	0.14	0.52	0.37
R.G. (%)	42	9.5	21.4	44	23.5	32

The utilization of pure oxygen boosts considerably the electrochemical performances of the cells and in particular the ones of the architectured cell. The R.G. between the overall resistances of the pair of cells is greatly increased as expected as the architecture is deployed at the cathode/electrolyte interface. For further analysis, we proceed with studying the R.G.s in these conditions (Figure IV – 15).
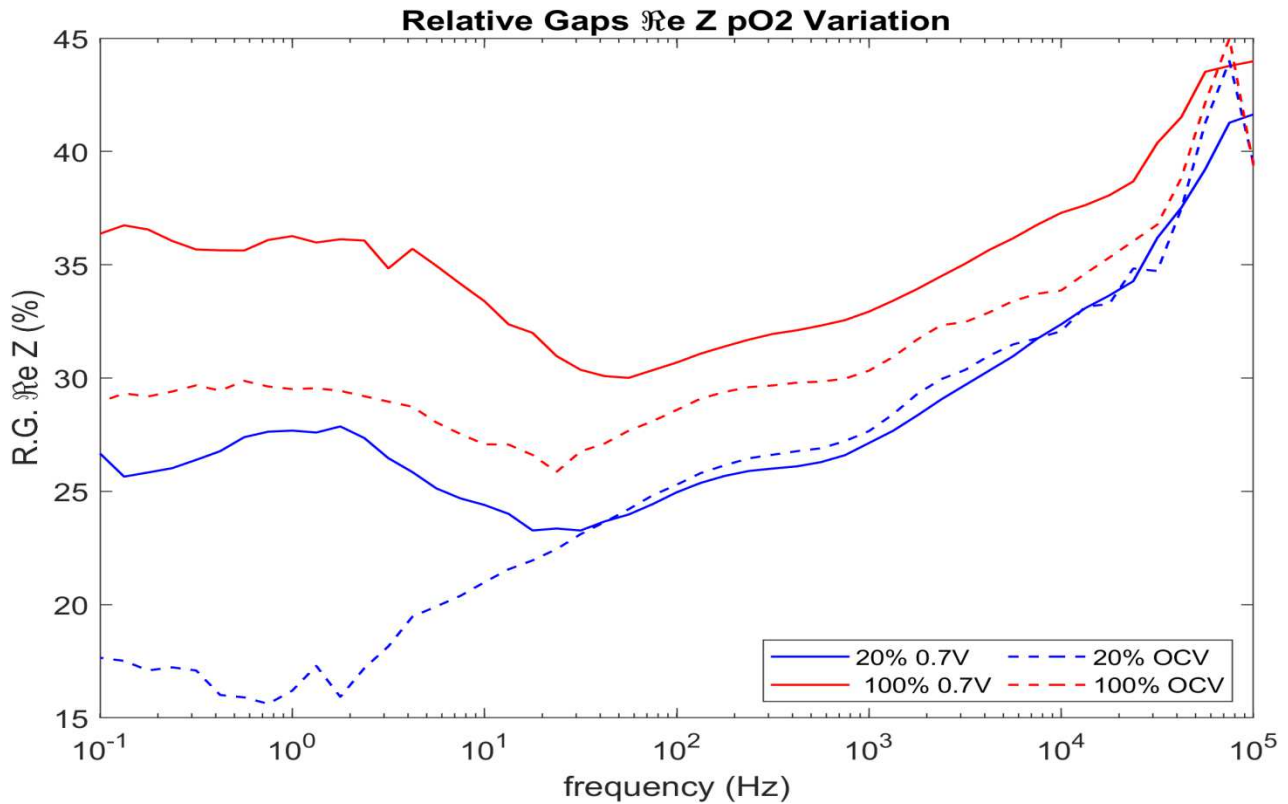
Figure IV - 15 Type I R.G. plots with variable pO_2

Static conditions (at OCV)

The measurements with varying the pO_2 are particularly insightful on the influence of the architecturation on the cathode/electrolyte interface. The R.G. plots using pure O_2 are superior to the ones using air in both OCV and 0.7 V conditions. Thus, the use of pure oxygen boosts the performance of the architectured cell compared to the planar one in every frequency domain. At high frequencies, we observe a significant increase in the conductivity of the YSZ matrix. This signifies that the penetration of dense electrolyte material within the porous cathode does open new ionic transport paths. Moreover, we observe an increasing difference between the OCV plots using O_2 and air in the low – intermediate frequencies [1 – 20 Hz] associated with the surface diffusion and charge transfer. Thus, we may deduce the increase in the transportation properties associated purely with the architecturation of the cathode/electrolyte interface by 6 to 8 %.

Operating conditions (at 0.7 V)

In the operation condition, a similar difference is observed between the air plot and the O_2 plot. The electrochemistry is boosted and the Gerischer-type impedance is strongly influenced by the architecture. We estimate a 5 to 7 % increase in the catalytic properties due to influence by the architecture.

III.B. Type II

Type II fuel cells are fabricated to demonstrate the feasibility of the architecturing method for the production of industrial cells. They are composed of anode support and functional layer, an electrolyte coated by a CGO barrier layer to separate it from a LSCF:CGO composite cathode. In this study and concerning this type of cells, we concentrate on the architecturing of the anode electrolyte interface.

The type II cells present an architecture at the anode/electrolyte interface and offer insight into its influence on the fuel oxidation.

III.B.1. Components reminder

An overview of the structural characteristics of the cells are presented in Figure IV – 16 and Table IV – 12.
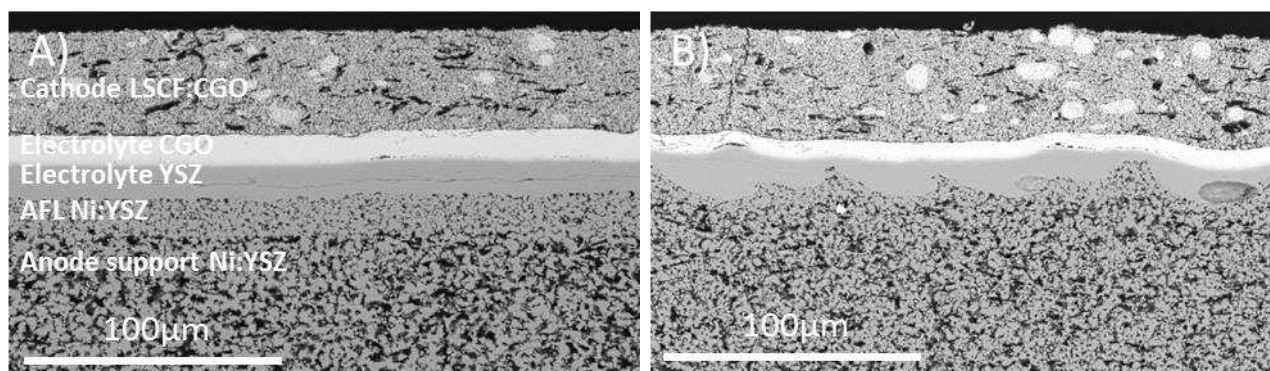
Figure IV - 16 Type II cross-section SEM observation. A) Planar cell and layer materials display; B) Architectured cell

Table IV - 12 A) Type II cells structural characteristics overview					
Component	Composition (Materials and volume ratio)	Porosity (%vol)	Thickness in the planar cell (µm)	Max thickness in the architectured cell (µm)	Min thickness in the architectured cell (µm)
Anode	Ni:YSZ 44:56	37	240 (+-5)	240 (+-5)	240 (±5)
AFL	Ni:YSZ 44:56	18.4	18.2	14 (±1.7)	5.7 (±1.8)
Electrolyte	YSZ	0	13.3	15 (±2.6)	5.4 (±0.9)
Barrier	CGO	0	11	7.2 (±0.7)	6.2 (±0.3)
Cathode	LSCF:CGO 50:50	28.7	38	44.6 (±0.7)	38 (±1.8)
Table IV - 12 B) Harmonic mean value of the architectured electrolyte thicknesses					
	Planar	Min architectured	Harmonic mean + min architectured		R.G. electrolyte thickness (%)
Electrolyte	13.3	5.4 (±0.9)	8.57		35.6
Barrier	11	6.2 (±0.3)	9.5		13.6

III.B.2. I/V

We begin the electrochemical analysis by studying the polarization curves of the cells. Figure IV – 17 shows the polarization and the associated power density curves in the standard condition which are humidified hydrogen (97% H_2 , 3% H_2O) and air (20% O_2).
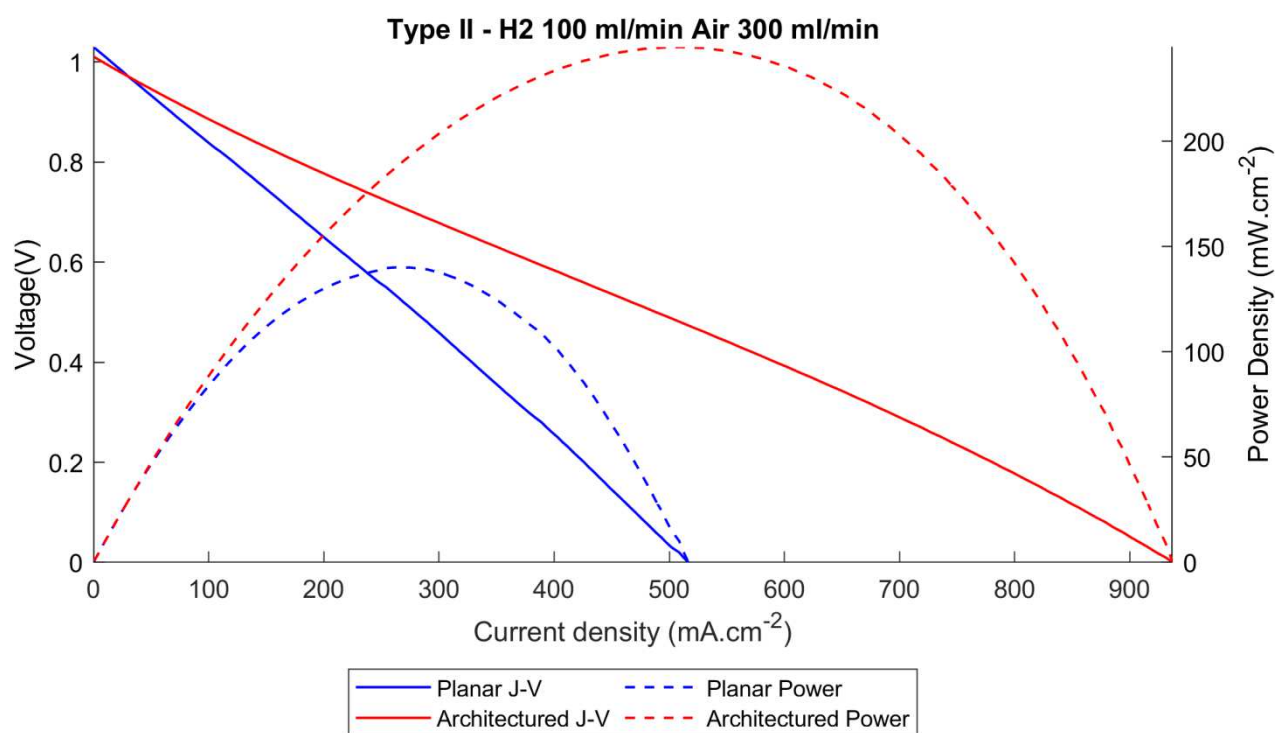
Figure IV - 17 Type II Polarization and density curves in reference gas conditions

Table IV - 13 Type II cell remarkable values with respect to the maximum power density using humidified H2 – air				
	Potential (V)	Current density (mA.cm^{-2})	ASR (Ω.cm^2)	Power density (mW.cm^{-2})
Planar	0.53	264.5	2.00	140.2
Architectured	0.49	499.5	0.98	244.8
R.G. (%)	7.5	88.9	51	74.6

Table IV - 14 Type II cell remarkable values at 0.7 V using humidified H2 – air				
	Potential (V)	Current density (mA.cm^{-2})	ASR (Ω.cm^2)	Power density (mW.cm^{-2})
Planar	0.7	173.9	4.0	121.7
Architectured	0.7	277.8	2.5	194.5
R.G. (%)	0	59.8	37.5	59.8

The architectured cell presents a slightly lower OCV than the planar cell, 1.01 V and 1.03 V respectively. This mismatch may be caused by leakage linked to the measurement set-up adjustments, as we do not observe perpendicular cracks within the electrolyte. In any case, both OCV values are above 1 V meaning that the gas tightness of the cell is satisfactory.

The I-V curves exhibit fairly regular shapes with low to none activation and concentration overpotential slopes. However, the concentration overpotential is more pronounced in the architectured cell starting from approximately 650 mA.cm^{-2}.

To quantify the effect of the architecture on the electrochemical performances of the fuel cells, we report the maximum power density as well as the corresponding current density, potential, and ASR in table IV – 13. In table IV – 14 we report the same characteristic with respect to an operational voltage fixed in this study at 0.7 V. In both cases, we calculate the ratio $P_{architectured}/P_{planar}$ in order to evaluate the effect of the architecture on the global cell performances.

Exceptional increases in the power density are observed in operating conditions (59.8% at 0.7 V), especially in the maximum values (74.6 %). The ratios between the power densities are far above the AEC. The variation of the ASR is consistent with the electrolyte and barrier thickness variation, calculated in the previous chapter (35.6% and 13.6% respectively). Similar to the protocol followed for the analysis of the type I cells, we will attempt to identify the influencing parameters by measuring the power generation and the electrochemical impedance response of the cells in different experimental conditions.

In figure IV – 18, the polarization curves and the associated power density curves using either Ar/H$_2$ fuel and air or using H$_2$ and O$_2$ are presented. They are complementary with the H$_2$ – air gas conditions presented previously (Figure IV – 17).

A)

B)
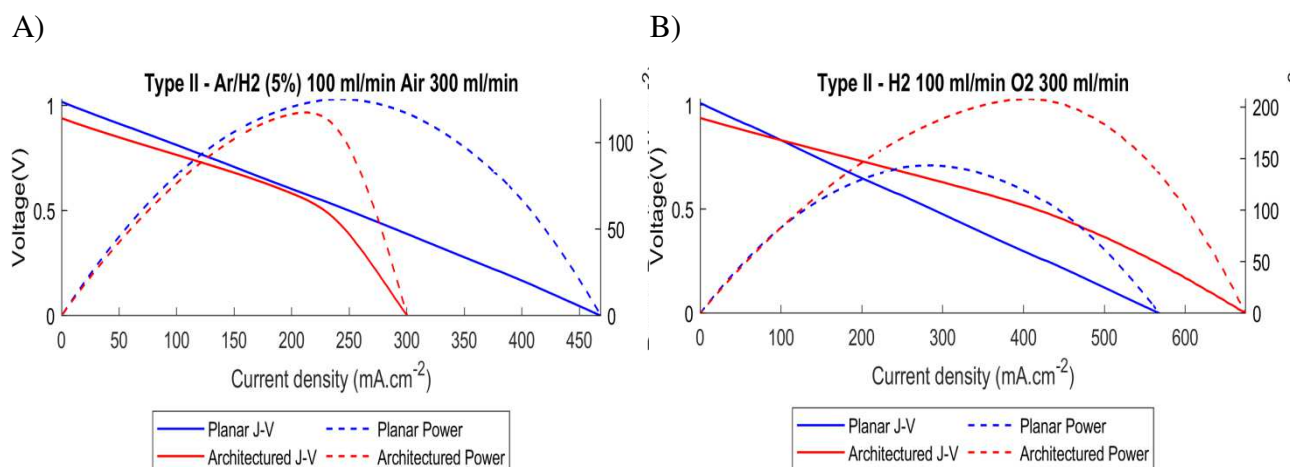
Figure IV - 18 Type II Polarization and density curves in variable gas conditions. A) Ar/H$_2$ (5%) – air; B) H$_2$ – O$_2$

Table IV - 15 Type II cell remarkable values with respect to the maximum power density using humidified Ar/H$_2$ (5% H$_2$) – air				
	Potential (V)	Current density (mA.cm^{-2})	ASR (Ω.cm^2)	Power density (mW.cm^{-2})
Planar	0.52	240.4	2.16	125.0
Architectured	0.55	213.3	2.58	117.3
R.G. (%)	5.8	- 11.3	- 19.4	- 6.2

Table IV - 16 Type II cell remarkable values at 0.7 V using humidified Ar/H$_2$ (5% H$_2$) – air				
	Potential (V)	Current density (mA.cm^{-2})	ASR (Ω.cm^2)	Power density (mW.cm^{-2})
Planar	0.7	153.5	4.56	105.7
Architectured	0.7	144.3	5.05	97.1
R.G. (%)	0	- 6	-10.7	-8.1

In both curves, we observe an important decrease of the OCV of the architectured cell. In these conditions, the molar ratio n(H$_2$) /n(O$_2$) is lower than in the reference gas conditions (figure IV – 17) and we think that a partial reoxidation of the anode occurs due to the excessive oxygen

injected into the system. This means that there are either microcracks in the electrolyte or "sealing" of the cell is inadequate.

We observe a severe slope change at higher current densities for the architectured cell which most likely is caused by the decrease of the fuel concentration and additionally a reoxidation of the anode. The effect on the resistivity of the cells is very visible in the Nyquist plot presented in figure IV - 25 where the cells are tested in operating conditions (0.7 V) and with different hydrogen concentrations. <u>This effect shows that in low hydrogen concentration, the architecturation of the anode/electrolyte side may prove to be counterproductive.</u>

Again to quantify the behavior of the cells in these conditions we report the usual parameters in Tables IV – 15 and 16

As mentioned, in figure IV – 18 B where the polarization and power density curves are measured in $H_2 - O_2$ gas conditions, we observe a lower OCV for the architectured cell. However, the ohmic overpotential slope is considerably lower and the architectured cell presents better performances under a certain voltage (0.91 V). The usual measurement values are reported in Tables IV – 17 and 18.

Table IV - 17 Type II cell remarkable values with respect to the maximum power density using humidified $H_2 - O_2$				
	Potential (V)	Current density (mA.cm^{-2})	ASR (Ω.cm^2)	Power density (mW.cm^{-2})
Planar	0.51	281.12	1.81	143.37
Architectured	0.51	407.73	1.25	207.94
R.G. (%)	0	45	30.1	45

Table IV - 18 Type II cell remarkable values at 0.7 V using humidified $H_2 - O_2$				
	Potential (V)	Current density (mA.cm^{-2})	ASR (Ω.cm^2)	Power density (mW.cm^{-2})
Planar	0.7	171.0	4.09	119.7
Architectured	0.7	229.6	3.05	160.7
R.G. (%)	0	34.3	25.4	34.3

Although the architectured cell presents a lower OCV and thus a lower "starting" point, it presents *in fine* a significant increase in the electrochemical performances and in particular in the maximum power density generation. We observe a concentration overpotential slope for the architectured cell in these conditions which is less pronounced when air is used. Thus, we deduce that the concentration overpotential is provoked on the anode side where the gas diffusion is slightly insufficient to cope with the gas consumption. As in the case with the usage of Ar/H$_2$ fuel, the generated water and the presence of gaseous oxygen can reoxidize locally the metallic nickel thus hindering the performances.

To summarize the study of the polarization curves, all of them are superposed in figure IV – 19.
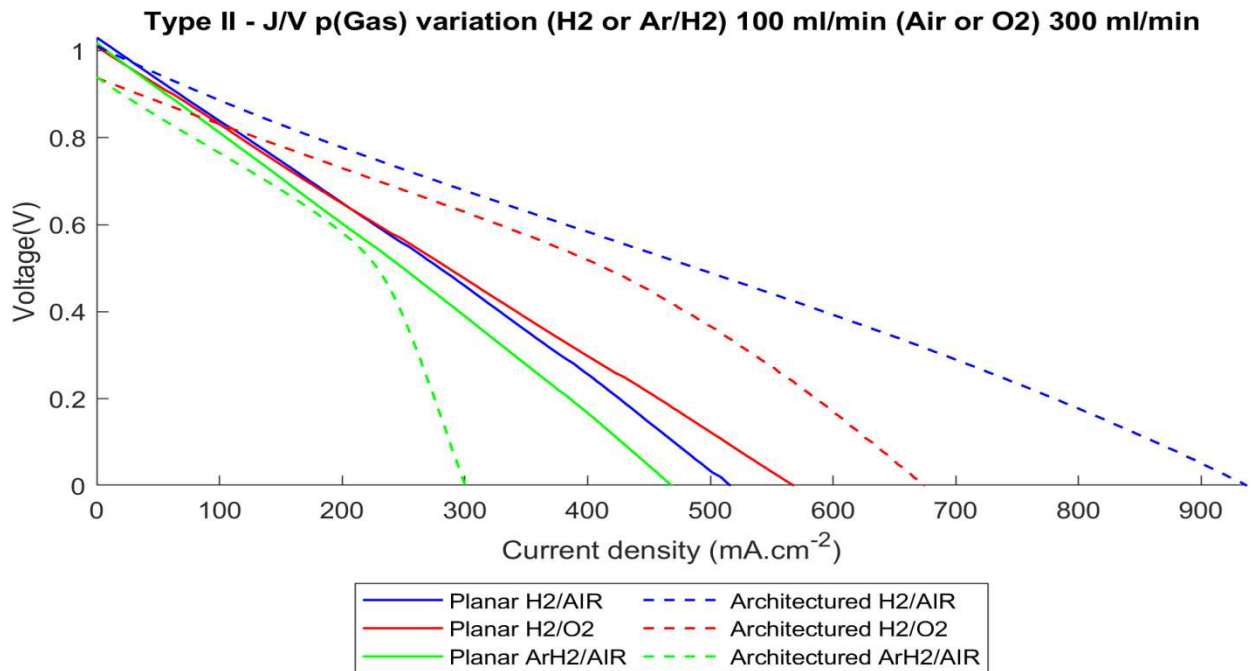
Figure IV - 19 Type II polarization curves measured in variable gas conditions

We conclude that in the case of architecturation of the anode/electrolyte interface, careful control of the gas concentrations is crucial to promote satisfactory results. The fuel gas distribution and water management can be a limiting factor of the cell operations.

To further understand the effect of the architecturation, we proceed with an electrochemical impedance spectroscopy analysis.

III.B.3.EIS

III.B.3.a) Reference gas conditions

In this subchapter, we propose an extensive EIS analysis interpreted with the R.G. method. As shown in figure IV - 20, the measurements are carried out in a frequency interval between 0.1 Hz and 100 kHz, and each cell is tested at OCV and in operating conditions (0.7 V) which allows us to differentiate the static cell behavior from the electrochemical one. Tests are performed in different concentrations of the reactant gases in order to isolate the anode and the cathode contributions to the overall impedance. Note that in the legends "A" refers to architectured cell and "P" to the planar cell.

A)

B)
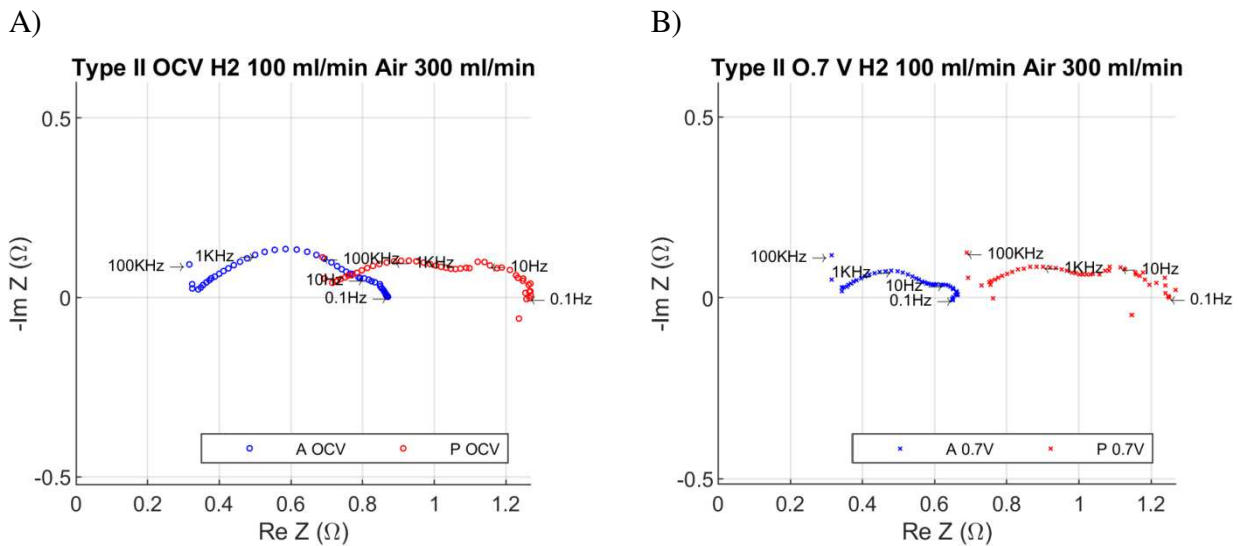
Figure IV - 20 Nyquist plot of Type II cells (A = architectured, P = planar) in reference gas conditions displaying 1/2 frequency decades. A) At OCV; B) At 0.7 V

During this first test, we wish to study the cells only in the reference gas conditions where humidified H_2 is fed to the anode, and air is fed to the cathode. The architectured and planar Nyquist plots realized in OCV and operation conditions are superposed.

The planar cell plots present some noise at low frequencies. Furthermore, both cells exhibit a high-frequency capacitive tail which can be associated with a manipulation error. However, due to its reproducibility, it should not hinder the spectra comparison.
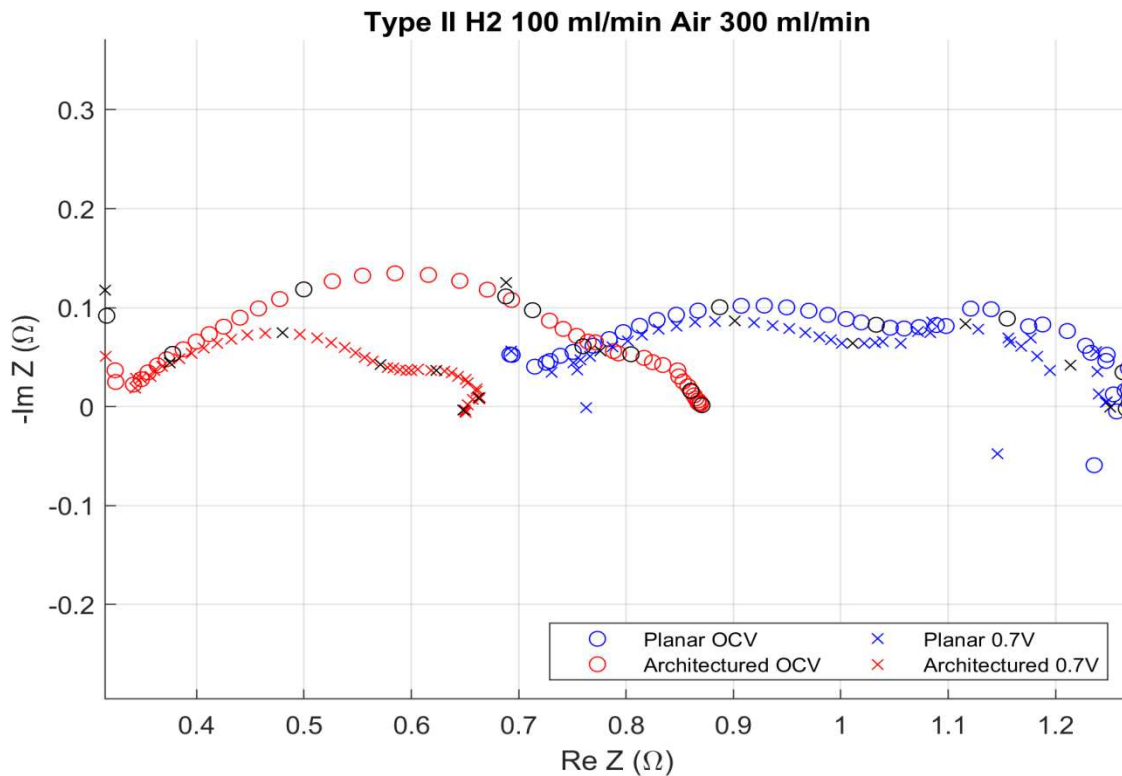
Figure IV - 21 Superimposition of the Nyquist plots of Type II cells in reference gas conditions

In Table IV – 19, we report the series resistance characteristic to the electrolyte resistance, as well as the overall resistance of the cells in the different test conditions (OCV and 0.7 V)

Table IV - 19 EIS Type II series and overall resistance values in reference gas conditions			
	Series R (Ω)	R_{total} (at OCV) (Ω)	R_{total} (at 0.7 V) (Ω)
Planar	0.71	0.58	0.58
Architectured	0.34	0.55	0.35
R.G. (%)	38	5.2	39

We note a drastic decrease in the resistance of the architectured cell with respect to the planar one at the operating condition.

We proceed by analyzing the R.G. between the frequency associated resistivity of the architectured and planar cells represented in Figure IV – 22.
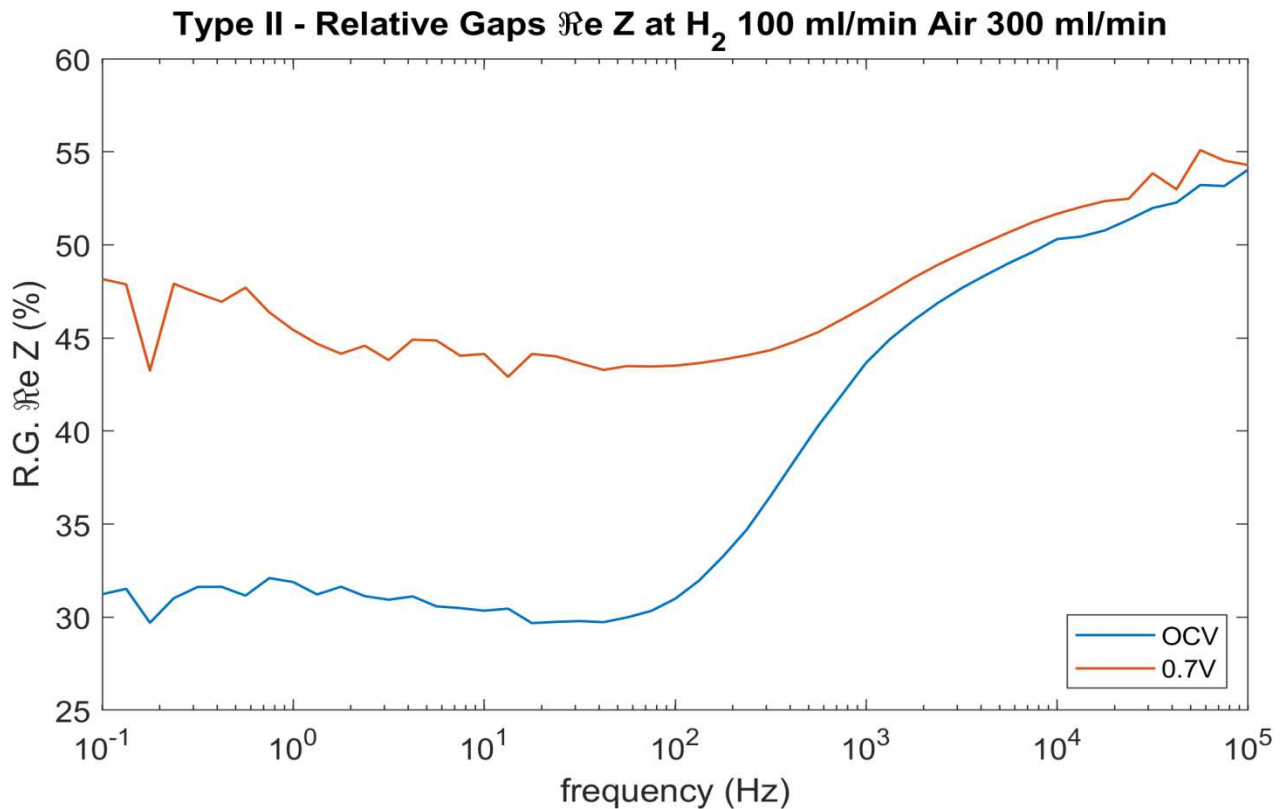
Figure IV - 22 R.G. plots of type II cells in reference gas conditions

Static condition (at OCV)

At OCV conditions, we observe a very important R.G. (49%) between the architectured and the planar cells. This difference in the resistivity of the cells is due to the variation of the electrolyte thickness.

In the interval between 40 Hz and 1000 Hz, which corresponds to the first large semicircle, a notable decrease in the R.G. is observable. These frequencies are related to the charge transfer and surface diffusion.

Below 20 Hz, the R.G. is stabilized and slightly increases (approximately 2%) with the decreasing frequencies. This effect is due to the presence of thinner zones of the AFL. As the AFL has a reduced porosity and pore size to promote higher TPB concentration, the gas diffusion is more challenging than in the anode support.

Operating conditions (0.7 V)

In this condition, the cell is operating and the electrochemical reactions occur within the electrodes.

As expected, at high frequencies the R.G. plot exhibits similar behavior as the one in OCV conditions.

In the operation condition, the drastic decrease in the gap plot in the frequency interval [30 – 1000 Hz] is significantly reduced. The charge transport and surface diffusion are dependent on the electrochemical activity of the cell. Furthermore, it has been reported that response at this interval of frequencies is related to electrochemical reactivity represented by a Gerisher-type impedance. The higher frequencies (above 100 Hz) are related to the anode Gerisher impedance and the lower ones to the cathode as the ORR is slower and the oxygen ions harder to diffuse. Thus, the catalytic properties of the anode are improved by the presence of the architecture [3 – 13 %] based on the interval [100 – 1000 Hz].

At low frequencies, we observe an increase in the gap plot. Furthermore, this increase is more important in these conditions than in the OCV condition. This effect can be explained with the presence of active triple phase boundaries, closer to the anode support. Thus, the hypothesis of new transportation pathways is verified.

For the rest of the chapter, we will present a superimposition of the Nyquist plots in either OCV or at operating conditions as shown in figure IV – 23 A and B respectively which will be followed by the R.G. plots superimposition as shown in figure IV – 24.

A)
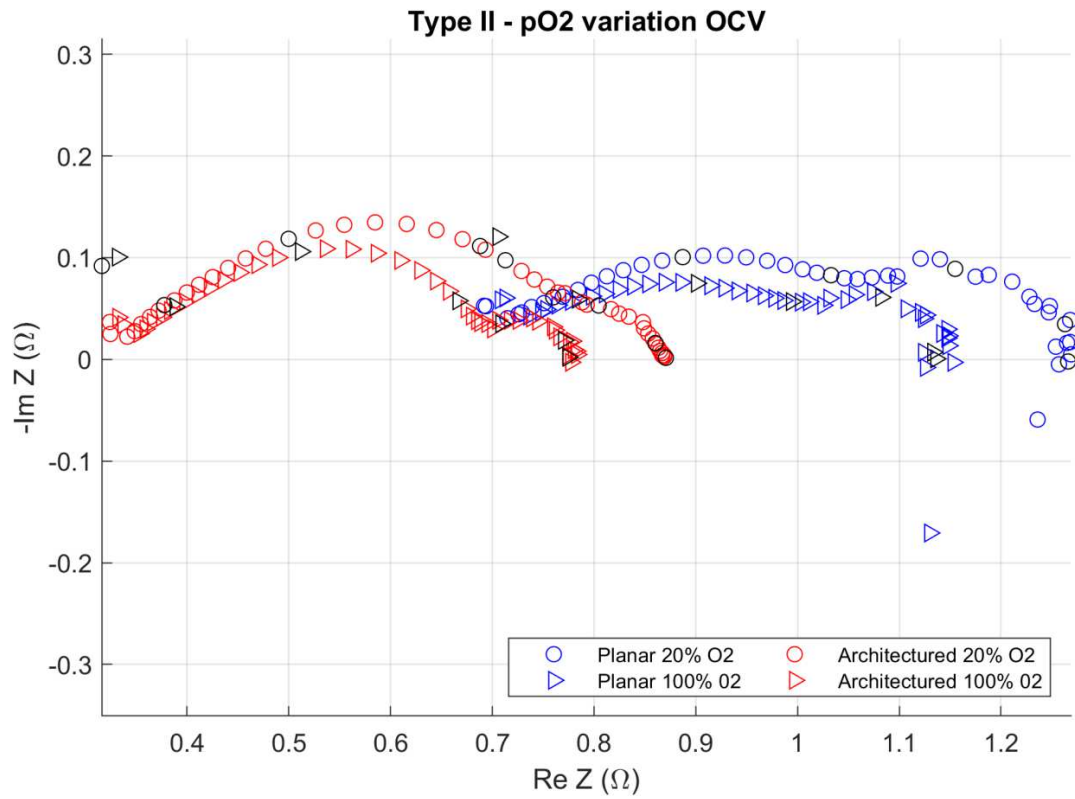
B)
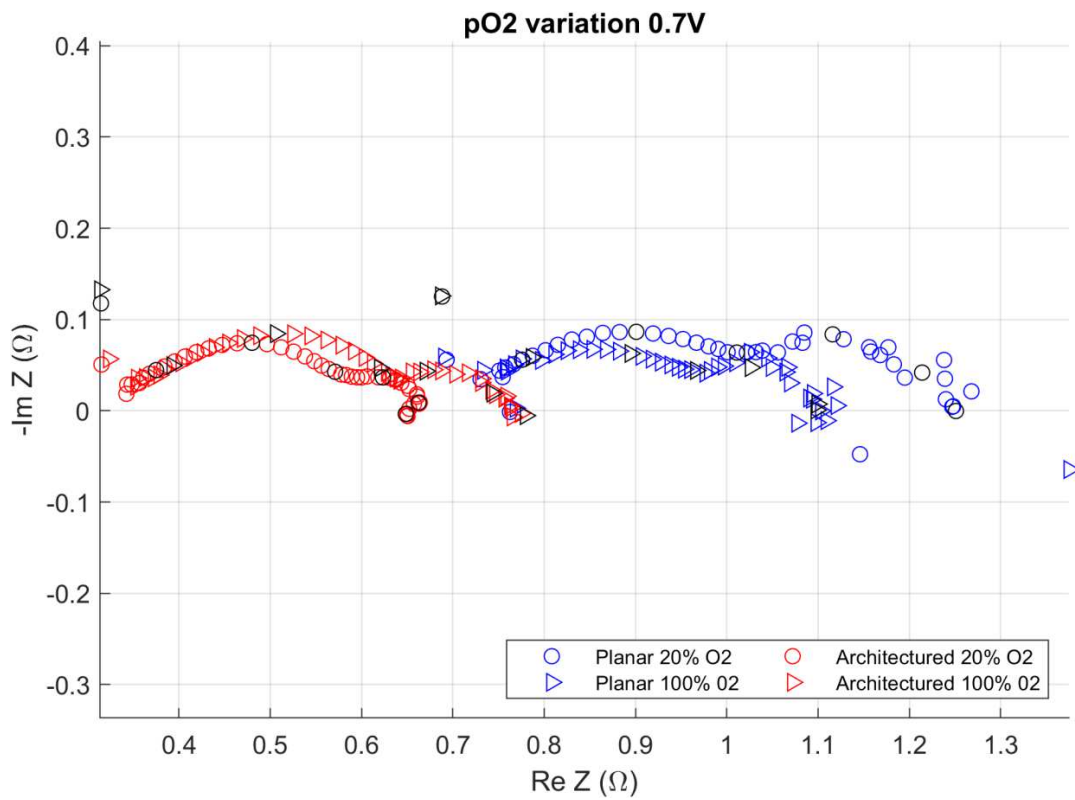
Figure IV - 23 Type II cells EIS with pO$_2$ variation. A) At OCV; B) At 0.7 V

The planar cells present a considerable noise at low frequencies (below 10Hz). Between 1Hz and 10 Hz, the response is related to the Gerisher impedance in which a contribution of a surface charge migration is present. However, the spectra shape seems to remain unchanged, presenting a large arc at intermediate frequencies (possibly englobing another smaller one close to 10kHz) and a smaller arc at lower frequencies which evolves significantly with the pO_2. It almost disappears at 20% O_2, especially in the architectured cells and in operating conditions. Based on the microstructural analysis where we observe CGO particle aggregation we propose the following hypothesis: it is possible to witness an oxygen ion accumulation on the surface of the aggregated CGO particles which would consequently locally modify the cathode conductivity. The effect is aggravated by the increase of the oxygen concentration and lowered by the higher oxygen consumption of the architectured cells.

An eventual gas mixing has been evocated during the analysis of the I-V curves. Such an occurrence would also hinder the gas diffusion by creating more water vapor especially for frequencies lower than 1 Hz as observed here. This is supported by the presence of a low-frequency loop. However, the noise is especially observable in the planar cells which present superior OCV than the architectured cells when using $H_2 - O_2$
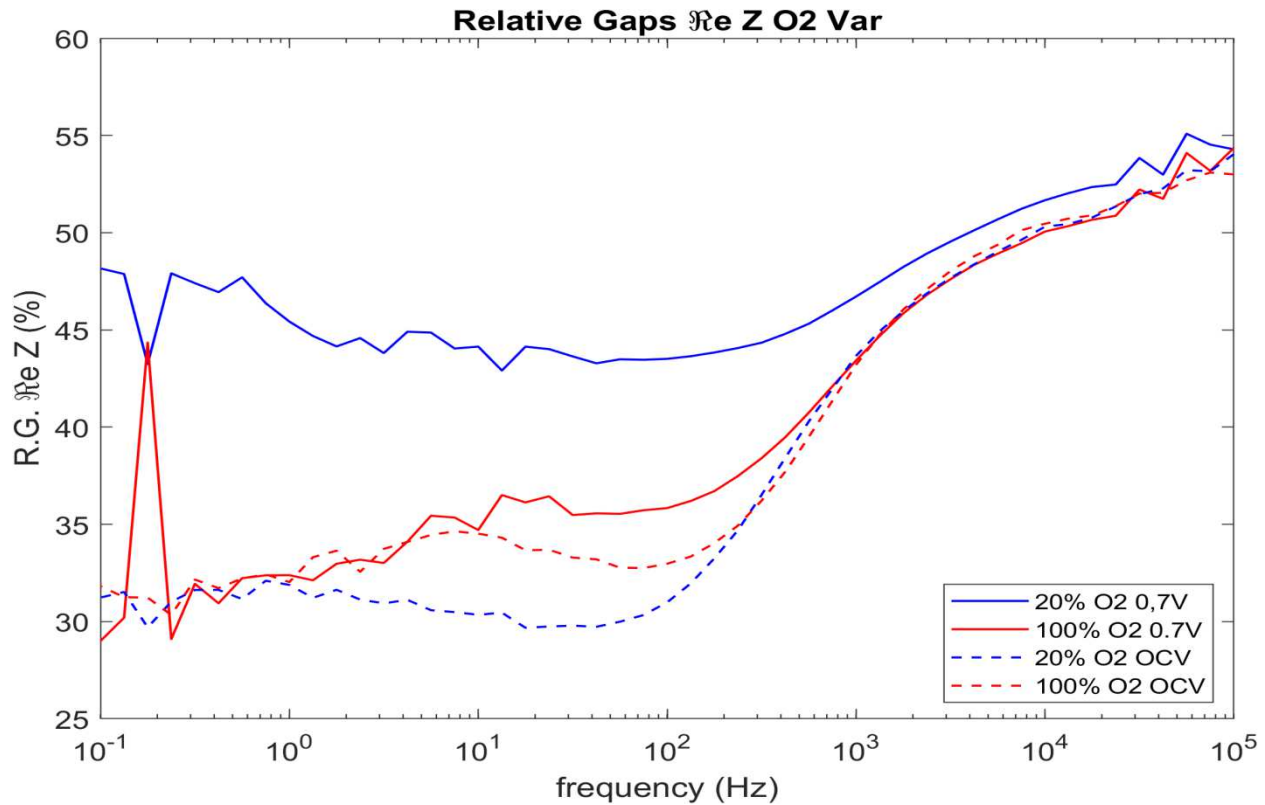
Figure IV - 24 Type II R.G. plots with variable pO_2

We observe that the architecturation impact in operating conditions is significantly lowered with the increase of the oxygen concentration. This effect was unexpected and contradictory to the electrochemical activity of the cell. The increase of the oxygen concentration should have a limited effect on the impact of the architecturation as the latter is deployed on the anode side. Thus, we suppose that the hindering effect is caused by the leakage of gaseous oxygen towards the anode side, where the fuel is consumed directly and the nickel is partially reoxidized

III.B.3.c)   pH2 variation

We saw that excessively low hydrogen concentration impairs drastically the performances and the measurements are rendered inconclusive. In Figure IV – 25, we demonstrate this by showing the Nyquist plots in operating conditions with humidified 1%, 10%, and 100% hydrogen. In addition to the plots shown at the beginning of the chapter, we can deduce a critical hydrogen concentration with which the cells can function properly. In this case, this concentration is 10%.
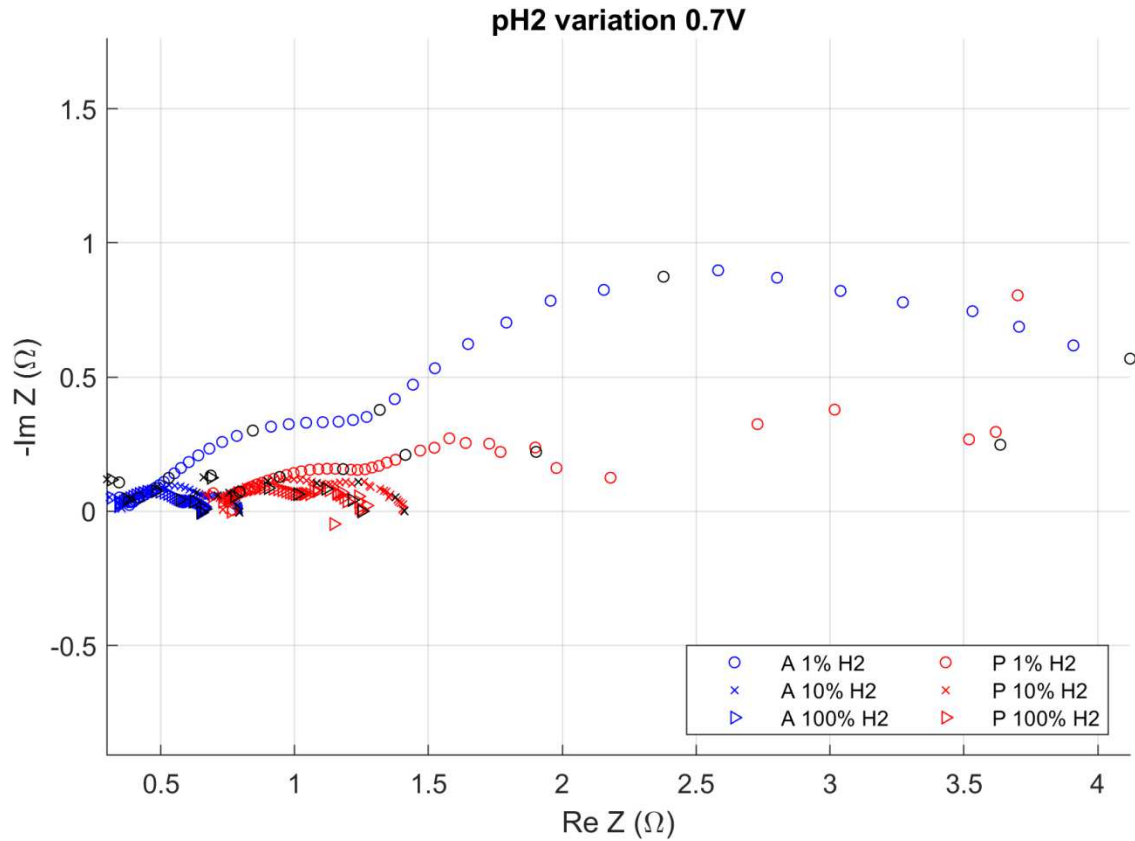
Figure IV - 25 Type II cells EIS with pH$_2$ including the 1% H$_2$ diagram variation at 0.7 V to demonstrate the divergence of the resistivity

The excessive resistance augmentation at lower frequencies renders the cells unusable in the selected conditions. Thus we proceed by using uniquely the humidified 10 and 100% hydrogen fuel gases.
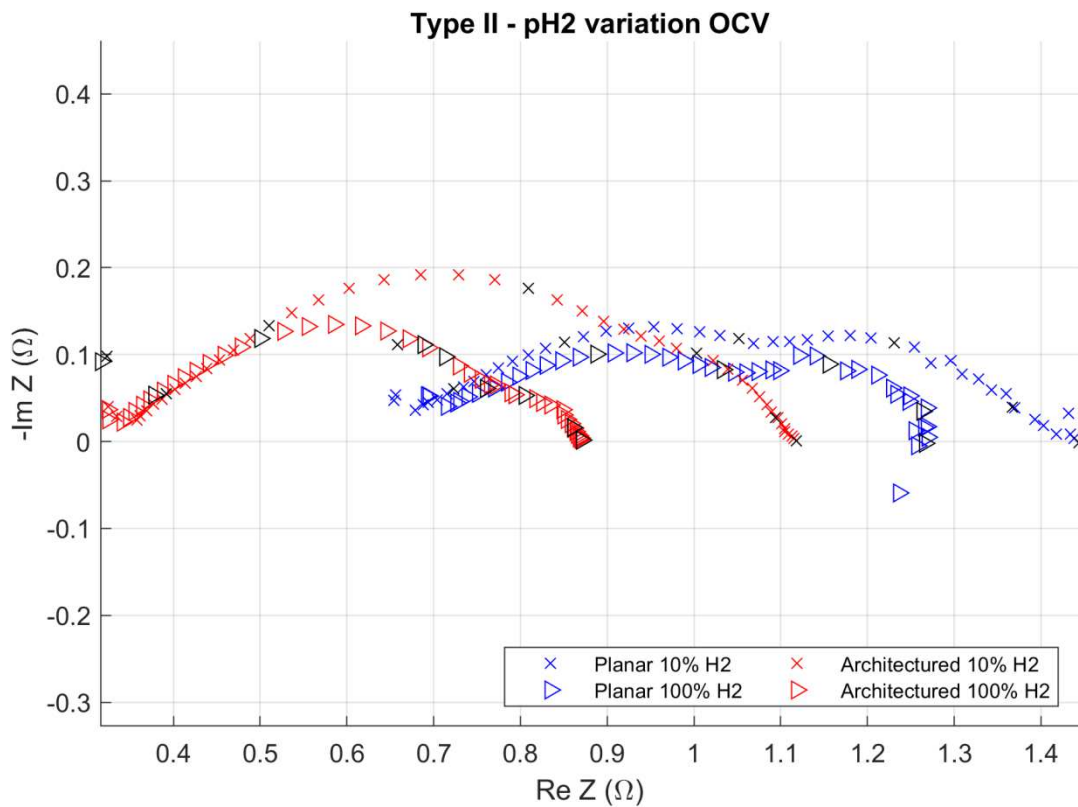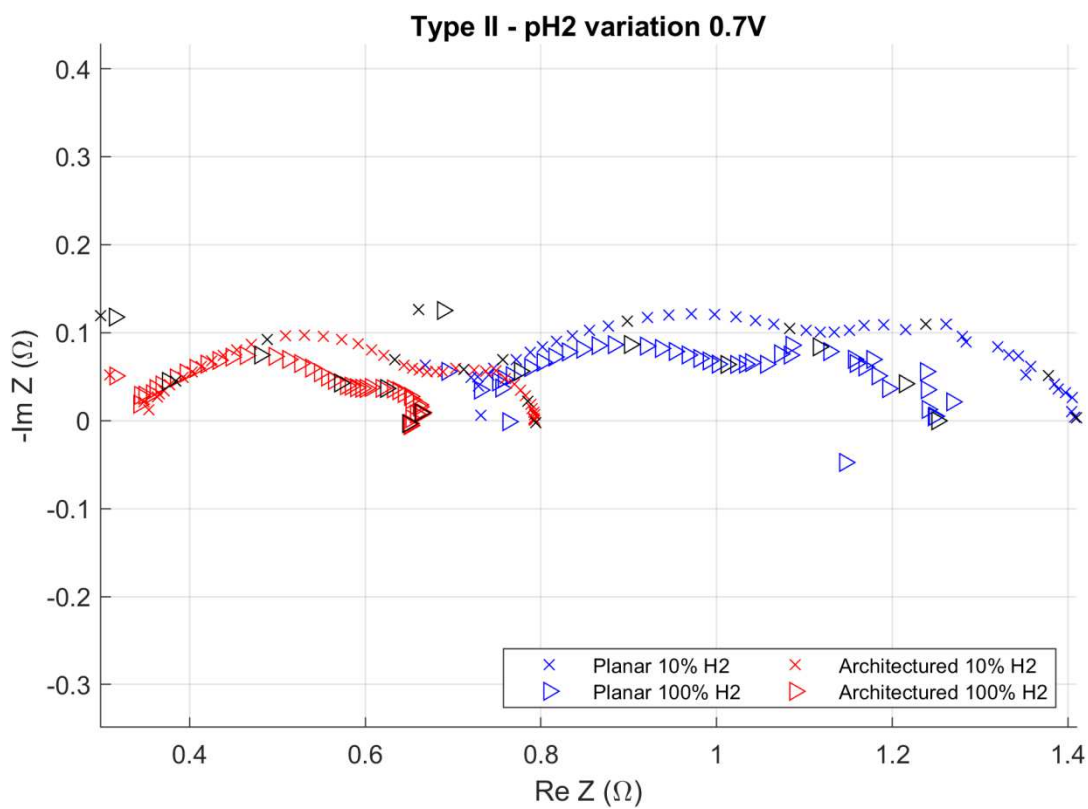
Figure IV - 26 Type II cells EIS with pH$_2$ variation. A) At OCV; B) At 0.7 V

The presence of noise at the low frequencies is again visible for the planar cell. However, it is considerably stabilized with respect to the measurements with pure oxygen.

In this example, we observe a significant retraction of the intermediated frequency arc (1000 Hz) when the hydrogen concentration is increased. This suggests that the anode catalytic contribution response is situated in this frequency domain. We proceed with the R.G. analysis.
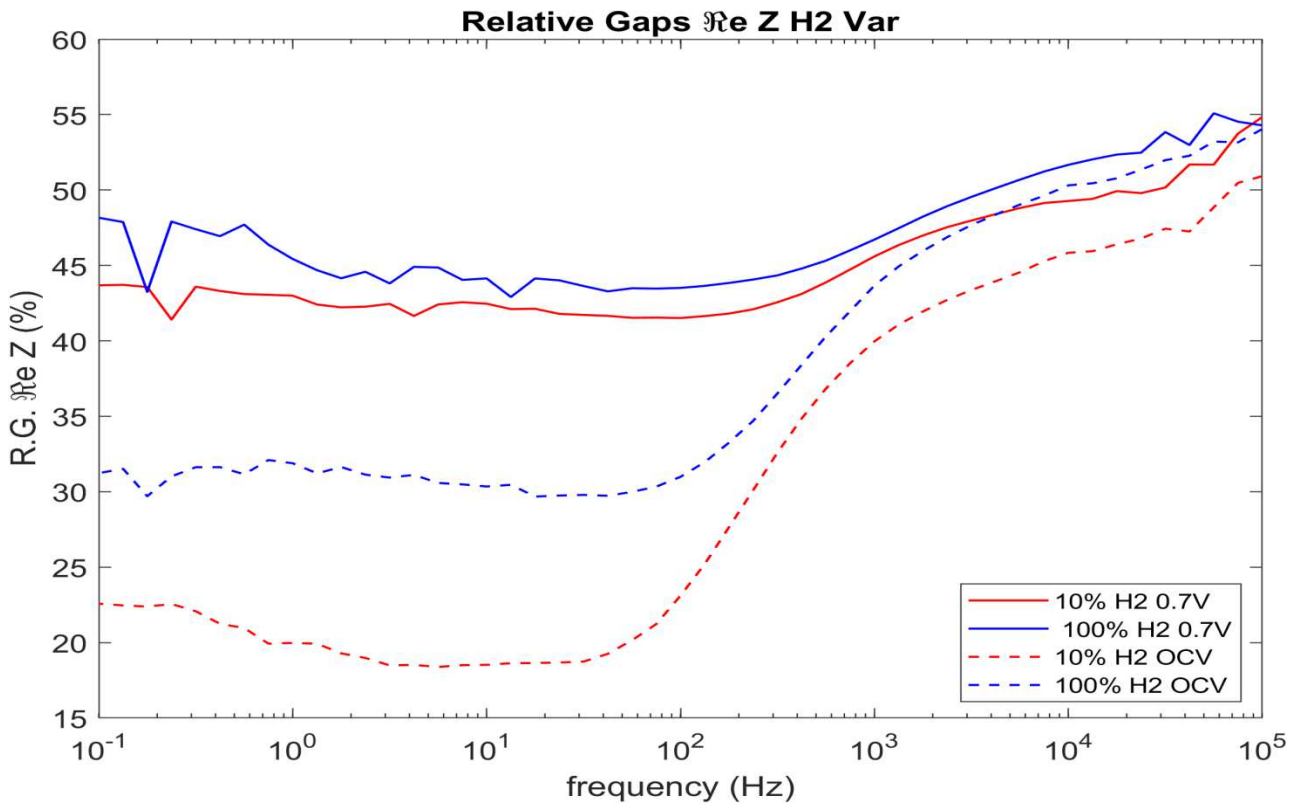
Figure IV - 27 Type II R.G. plots with variable pH$_2$

The two R.G. plots have similar behavior. However, we observe a severe gap between the ones measured in the OCV condition. At 10% hydrogen concentration the resistivity at lower frequencies of the architectured cell significantly closer to the one of the planar cell. In operating conditions, the same tendency is observed, although it is attenuated. The separation of the gas chambers being limited, the high concentration of hydrogen can provoke a burning of the gases in the felts and avoiding the excess oxygen to access near the anodic compartment. As we lower the hydrogen concentration the excessive oxygen can have increased penetration of the anode side and reoxidize partially the anode. We observe that the gap in OCV conditions and at high

222

frequency is considerably lower than the other plots. We believe that this is because of an increase in the electronic resistance of the anode due to this partial reoxidation. In operating conditions, the oxygen is consumed electrochemically and the excess oxygen is insufficient to reoxidize the anode as it is burned in the felts.

IV. Overview, conclusion and perspectives

In this chapter, we have carried out an extensive electrochemical characterization and analysis of two types of cells differentiated by cathode materials, microstructure, and architecturation location. Thus, a multitude of interesting and insightful pieces of information has been obtained on the effect of the architecture on the electrochemical behavior of the cells as well as their performances.

IV.A. Analysis methodology

In the first subchapter, we describe the analysis procedure. We use two complementary methods which are polarization curves study and electrochemical impedance spectroscopy. Due to the complexity and the multitude of phenomena occurring in a complete cell, it is necessary to perform a multitude of measurements in different gas and electrochemical conditions. This allows us to deduce the different contributions of the overall polarization or impedance spectra.

Important knowledge and references necessary for the interpretation of the EIS results are provided. However, a parametric study by EIS can be challenging and requires thorough experience and considerable time and effort to master it.

R.G. method

To bypass this requirement and still obtain the needed information, we have developed a simplified interpretation method inspired by already existing techniques such as differential impedance analysis (DIA). We call this technique the "relative gap method" and it consists of studying the R.G. between the frequency dependent real parts of the impedance spectra of the pair of cells as shown in equation (2) that we recall here:

$$R.G.(f_i) = \frac{Z'(f_i)_{planar} - Z'(f_i)_{architetured}}{Z'(f_i)_{planar}}$$

We have developed a Matlab script to facilitate the EIS analysis, by shaping the raw data, drawing the desired figures, calculating the R.G.s, and constructing a graphic representation.

IV.B. Type I cells

Several important results can be summarized concerning the effect of the architecturation of the cathode/electrolyte interface in the Type I cells.

- The architecturation increases significantly the electrochemical performances of the cell (70% increase of the maximum power generation) the when using $H_2 - O_2$ gas pair. A sequence of tests variating the reactant gases concentrations demonstrates that the electrochemical performances are majorly enhanced at the cathode side.
- In addition to the effect of the lower electrolyte thickness, the architectured cell presents better catalytic and charge transport properties (Gerisher type impedance) due to architecture [8 – 12 %] based on the interval [2 – 30 Hz] in the operation conditions
- A critical hydrogen concentration exists below which the concentration overpotentials become too important and a local anode reoxidation occurs under the influence of the excessive water concentration exacerbated by the insufficient anode porosity. Moreover, the sealing of the cells using alumina felts is limited and reoxidation of the anode can be observed due to the setup related oxygen gas leaks. The EIS spectrum at OCV presents an inductive loop at low frequencies, which suggests the presence of water in the anode.

IV.C. Type II cells

Several important results can be summarized concerning the effect of the architecturation of the anode/electrolyte interface in the Type II cells.

- The architecturation increases significantly the electrochemical performances of the cell (75 % increase of the maximum power generation) in the right conditions
- In addition to the effect of the lower electrolyte thickness, the architectured cell presents a better catalytic and charge transport properties architecture [3 – 13 %] based on the interval [100 – 1000 Hz] in the standard operation conditions
- The poor cathode microstructure hinder the charge transfer due to the presence of segregated CGO particles

- Again as for the type I cells, a critical hydrogen concentration exists below which the concentration overpotentials become too important and a local anode reoxidation occurs under the influence of the excessive water concentration and the eventual presence of gaseous O_2

IV.D. Conclusion

The architecturing of SOFC presents a powerful strategy to increase their electrochemical performances. We have demonstrated that in two pairs of samples, different in materials, microstructure, number of layers, and architecture location, the architecturation of the electrode/electrolyte interface results in a significant performance augmentation. The cells presented in this document have a 60 % increase in the maximum power generation for the Type I cells and 75 % for the type II cells.

By developing an analysis methodology and tools allowing a rapid and visual interpretation of the analysis data we have provided insight on the effect of the architecture opening the road for more detailed and fine study.

IV.E. Perspectives

Several important tests remain to be performed in future works.

- Durability tests are crucial for the continuation of the study where the absolute durability of the cells can be study as well as the comparison between the architectured cell and the equivalent planar cell. In the previous chapter, we have emitted the hypothesis of a potential mechanical strengthening provided by the architectures similar to bridge pillars. In addition to the electrochemical durability tests, mechanical testing should be performed.
- The creation of new architectures and studying their impact on the cells can be an interesting study. In this chapter, we have suggested that a cell with a gradual porosity traversed by the architecture should present intriguing results.
- Architectures of other cell configuration such as IdealCell or Rigel, and the application of that analysis methodology is an attractive strategy that will potentially be deployed in our team (by Dr. Lemoine)

REFERENCES

[1]   Z. B. Stoynov and D. E. Vladikova, 'MEASUREMENT METHODS | Electrochemical: Impedance Spectroscopy', in *Encyclopedia of Electrochemical Power Sources*, J. Garche, Ed. Amsterdam: Elsevier, 2009, pp. 632–642.

[2]   N. Hildenbrand, B. A. Boukamp, P. Nammensma, and D. H. A. Blank, 'Improved cathode/electrolyte interface of SOFC', *Solid State Ionics*, vol. 192, no. 1, pp. 12–15, Jun. 2011, doi: 10.1016/j.ssi.2010.01.028.

[3]   M. Mogensen and S. Skaarup, 'Kinetic and geometric aspects of solid oxide fuel cell electrodes', *Solid State Ionics*, vol. 86–88, pp. 1151–1160, Jul. 1996, doi: 10.1016/0167-2738(96)00280-9.

[4]   D. Klotz, A. Weber, and E. Ivers-Tiffée, 'Practical Guidelines for Reliable Electrochemical Characterization of Solid Oxide Fuel Cells', *Electrochimica Acta*, vol. 227, pp. 110–126, Feb. 2017, doi: 10.1016/j.electacta.2016.12.148.

[5]   A. Lasia, 'Electrochemical Impedance Spectroscopy and its Applications', in *Modern Aspects of Electrochemistry*, B. E. Conway, J. O. Bockris, and R. E. White, Eds. Boston, MA: Springer US, 2002, pp. 143–248.

[6]   A. Lasia, 'Modeling of Impedance of Porous Electrodes', in *Modeling and Numerical Simulations*, M. Schlesinger, Ed. New York, NY: Springer New York, 2009, pp. 67–137.

[7]   J. Nielsen and J. Hjelm, 'Impedance of SOFC electrodes: A review and a comprehensive case study on the impedance of LSM:YSZ cathodes', *Electrochimica Acta*, vol. 115, pp. 31–45, Jan. 2014, doi: 10.1016/j.electacta.2013.10.053.

[8]   A. Barbucci, R. Bozzo, G. Cerisola, and P. Costamagna, 'Characterisation of composite SOFC cathodes using electrochemical impedance spectroscopy. Analysis of Pt/YSZ and LSM/YSZ electrodes', *Electrochimica Acta*, vol. 47, no. 13, pp. 2183–2188, May 2002, doi: 10.1016/S0013-4686(02)00095-6.

[9]   R. Mohammadi, M. Søgaard, T. Ramos, M. Ghassemi, and M. B. Mogensen, 'Electrochemical Impedance Modeling of a Solid Oxide Fuel Cell Anode', *Fuel Cells*, vol. 14, no. 4, pp. 645–659, 2014, doi: https://doi.org/10.1002/fuce.201300292.

[10]   D. Vladikova, G. Raikova, Z. Stoynov, H. Takenouti, J. Kilner, and St. Skinner, 'Differential impedance analysis of solid oxide materials', *Solid State Ionics*, vol. 176, no. 25, pp. 2005–2009, Aug. 2005, doi: 10.1016/j.ssi.2004.12.014.

[11]   F. Mauvy *et al.*, 'Electrode properties of Ln2NiO4 + δ (Ln = La , Nd , Pr) : AC Impedance and DC Polarization Studies', *J. Electrochem. Soc.*, vol. 153, no. 8, p. A1547, Jun. 2006, doi: 10.1149/1.2207059.

[12]   V. Sonn, A. Leonide, and E. Ivers-Tiffée, 'Combined Deconvolution and CNLS Fitting Approach Applied on the Impedance Response of Technical Ni⁄8YSZ Cermet Electrodes', *Journal of The Electrochemical Society*, vol. 155, no. 7, p. B675, 2008, doi: 10.1149/1.2908860.

[13]   N. Wagner, W. Schnurnberger, B. Müller, and M. Lang, 'Electrochemical impedance spectra of solid-oxide fuel cells and polymer membrane fuel cells', *Electrochimica Acta*, vol. 43, no. 24, pp. 3785–3793, Aug. 1998, doi: 10.1016/S0013-4686(98)00138-8.

[14]   T. Ramos, M. Søgaard, and M. B. Mogensen, 'Electrochemical Characterization of Ni/ScYSZ Electrodes as SOFC Anodes', *J. Electrochem. Soc.*, vol. 161, no. 4, p. F434, Feb. 2014, doi: 10.1149/2.045404jes.

[15]   J.-D. Kim *et al.*, 'Characterization of LSM–YSZ composite electrode by ac impedance spectroscopy', *Solid State Ionics*, vol. 143, no. 3, pp. 379–389, Jul. 2001, doi: 10.1016/S0167-2738(01)00877-3.

[16]   M. J. Jørgensen, S. Primdahl, and M. Mogensen, 'Characterisation of composite SOFC cathodes using electrochemical impedance spectroscopy', *Electrochimica Acta*, vol. 44, no. 24, pp. 4195–4201, Jul. 1999, doi: 10.1016/S0013-4686(99)00134-6.

CHAPTER V

Overview, Conclusion and perspectives

Fabrication

Characterization

Electrochemical analysis
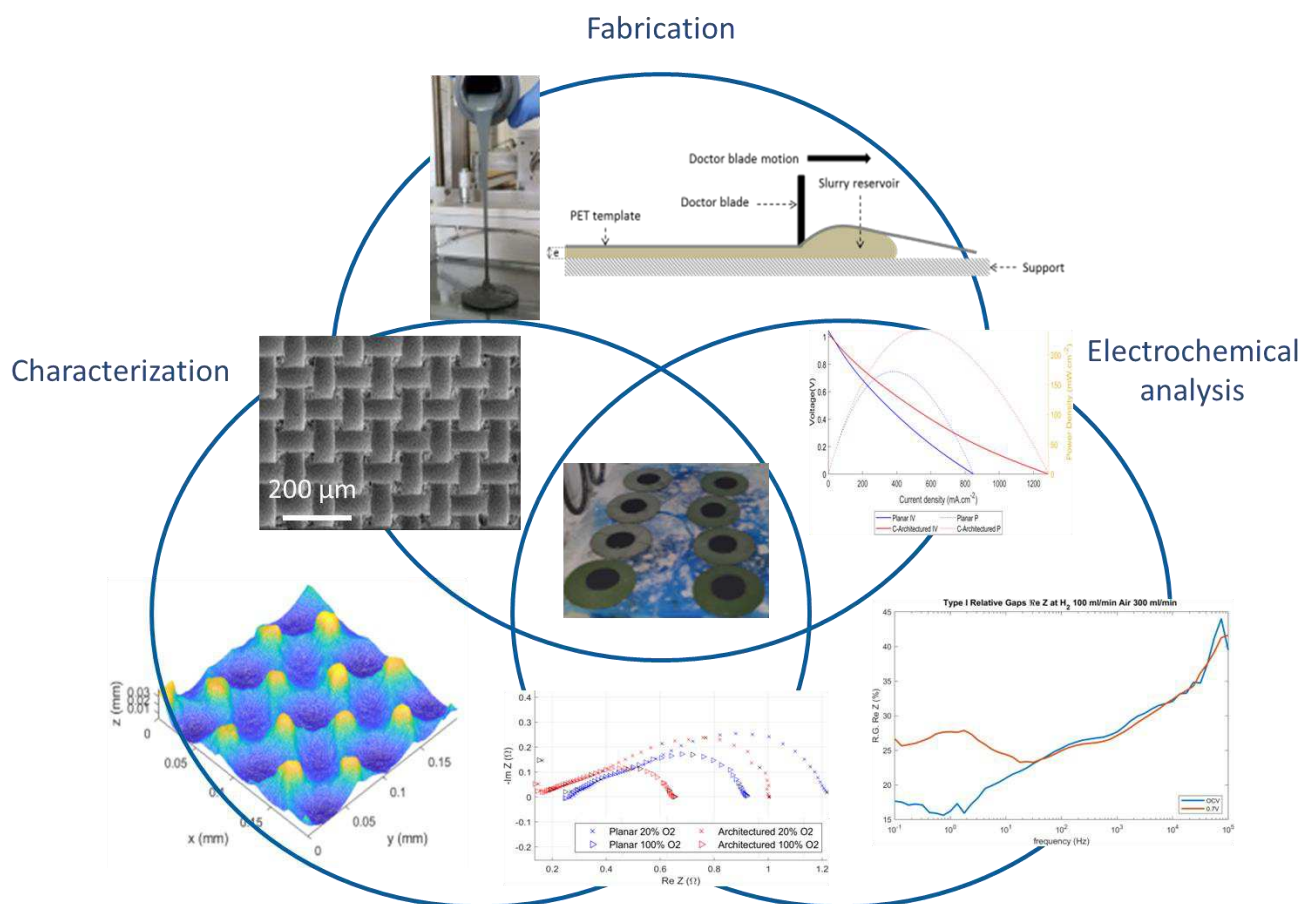
Chapter V abstract

The last chapter of this document offers an overview of the study and a review of the major results. In the first subchapter, we summarize the fabrication protocol followed by structural and chemical characterization of the obtained Type I and Type II fuel cells. In this part, we also provide hindsight of the results of the architecture topography measurements. Thus, a (conservative) equivalency of the planar and architectured cells is established considering two criteria:

- The same material environment (materials and microstructure) must be found at the interfaces of the planar and the architectured electrolytes
- The harmonic mean value of the thickness of the architectured electrolyte must be taken into account during the analysis of the electrochemical performances

The following subchapter summarizes the electrochemical analyses performed on the cells. Polarization measurements and EIS are used to study the electrochemical performances of the cells, to compare the architectured and planar ones. Finally, we isolate the influence of the architecturation on global impedance spectra by using an innovative comparison method based on the study of the relative gaps of the frequency-dependent resistance parts.

Following this procedure, we have established that the architecturation has a favorable influence on the electrochemical performances by strongly enhancing the catalytic capabilities of the electrodes as well as the charge transfer (and in particular the ion transfer) within the cell. The architecturation induces a 60 % increase of the maximum power density for the Type I cells and 75% for the Type II cells.

In the final subchapter, we provide a discussion on the perspectives which can be extracted from this work, such as further experiments and associated modeling.

Chapter V résumé

Le dernier chapitre de ce document offre une vue d'ensemble de l'étude et un résumé des principaux résultats. Dans le premier sous-chapitre, nous résumons le protocole de fabrication

suivi de la caractérisation structurale et chimique des piles à combustible de Type I et de Type II. Dans cette partie, nous donnons également un aperçu des résultats des mesures topographiques de l'architecture. Ainsi, une équivalence (conservatrice) des cellules planes et architecturées est établie sur la base de deux critères :

- Le même environnement matériel (matériaux et microstructure) doit être le même aux interfaces des électrolytes planaires et architecturés

- La valeur moyenne harmonique de l'épaisseur de l'électrolyte architecturé doit être prise en compte lors de l'analyse des performances électrochimiques

Le sous-chapitre suivant résume les analyses électrochimiques effectuées sur les cellules. Les mesures de polarisation et l'EIS sont utilisés pour étudier les performances électrochimiques des cellules, afin de comparer les cellules architecturées et planes. Enfin, nous isolons l'influence de l'architecture sur les spectres d'impédance globaux, en utilisant une méthode de comparaison innovante basée sur l'étude des écarts relatifs des parties de résistance dépendantes de la fréquence.

En suivant cette procédure, nous avons établi que l'architecture a une influence favorable sur les performances électrochimiques en ameliorant les capacités catalytiques des électrodes ainsi que les transferts de charges (et en particulier le transfert d'ions) dans la cellule. L'architecture induit une augmentation de 60 % de la densité de puissance maximale pour les cellules de Type I et de 75 % pour les cellules de Type II.

Dans le dernier sous-chapitre, nous présentons une discussion sur les perspectives qui peuvent être extraites de ce travail, telles que d'autres expériences couplées à une modélisation.

Chapter V Overview, conclusion and prospects

Contents

Figures

I. Introduction

The first objective of this work was to establish a simple, reliable, and cost-effective fabrication protocol for the production of cells with architectured or planar electrode/electrolyte interfaces. The second objective was to produce and test architectured fuel cells and to compare them to equivalent planar cells, in order to study the impact of the architecturation on the cell electrochemical performances. For this, two pairs of architectured and planar cells were fabricated, allowing measuring the impact of the architecture with varying materials, microstructure, and architecture location.

A summary of the fabrication protocol and the characterization of the architecturation obtained by the soft template method can be found in subchapters II – A and B. Subchapters II – C and D will provide an outline of the characteristics of the cells Type I and II respectively.

The characterization procedures will allow us to compare the architectured and planar cells and establish their equivalency. For this, we consider the following criteria:

- Mean global electrolyte thickness of the architectured cells equal or superior to the one of the planar cells
- The same material environment (materials and microstructure) at the interfaces of the planar and the architectured electrolytes

In subchapter III we will discuss the results of the electrochemical analysis as well the comparison of the performances of the cells. A discussion over the perspectives and the potential future studies is presented in part IV.

II. Fabrication protocol and characterization

This subchapter is an outline of the fabrication protocol and the structural analysis of the cells obtained with it.

II.A. Fabrication protocol

To meet the fabrication protocol requirements, the number of used techniques has been lowered to a minimum. Thus, the well-known tape casting technique has been used for the fabrication of

each cell component shaped by punching or laser cutting. A diagram of the protocol used to fabricate complete cells can be found in figure V – 1.
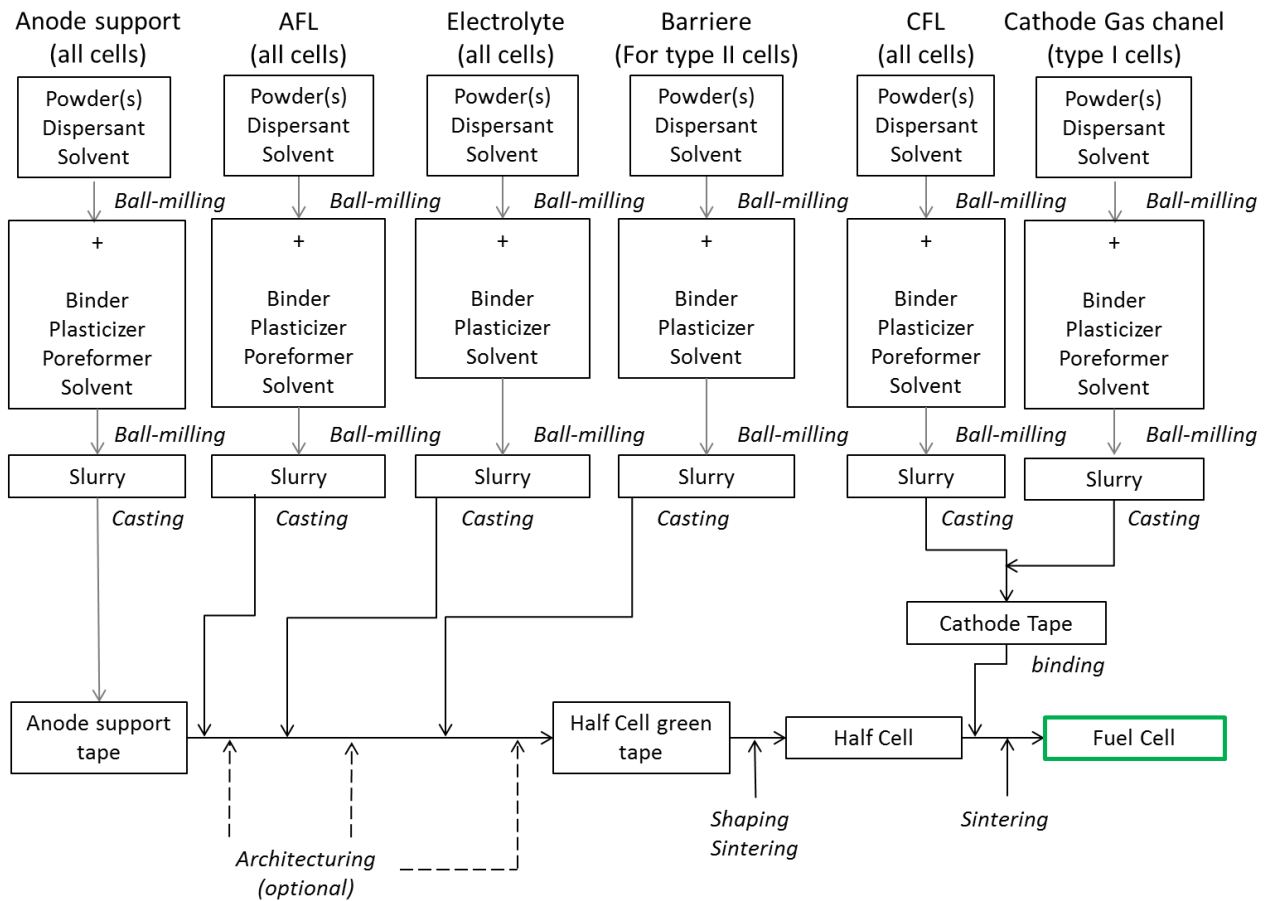
Figure V - 1 (reproduced from chapter II) Fabrication protocol overview

By using a low number of techniques, the fabrication time, materials, equipment, and know-how necessary to carry on the fabrication are reduced, making the protocol simple and cost and logistic - effective. Furthermore, tape casting allows the fabrication of high area surface green tapes with significant reproducibility. The architecturation is established using a slight modification of the original technique by applying a soft template between the doctor blade and the slurry, which results in a pattern implementation during the drying process. An explicative schematics and photography are shown in figure V – 2.
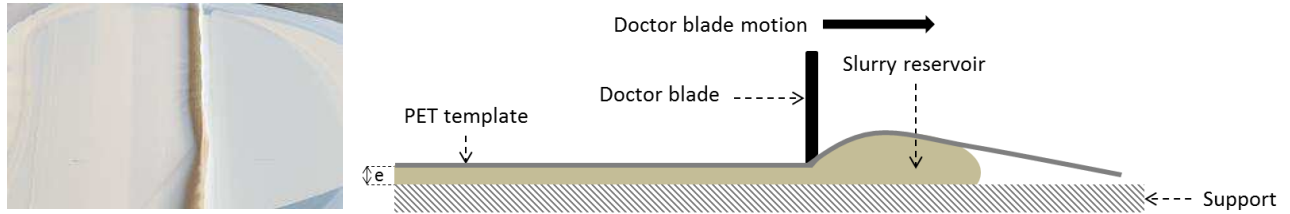
Figure V - 2 (reproduced from chapter II) Soft template architecturation method. A) green tape architecturing using a PET1500 fabric; B) Principle schematic

The protocol is validated by optical and electron microscopy, and if the integrity of the cells is confirmed, they are tested electrochemically.

II.B. Architecturing

In this subchapter, we summarize the results obtain using the soft template method, which is preconized for the SOFC fabrication in this work due to its simple application and its low influence on the microstructure of the components. In figure V – 3, an architecturation of an anode tape (A) is covered by an electrolyte layer which penetrated the "valley" shapes presenting satisfactory wetting.
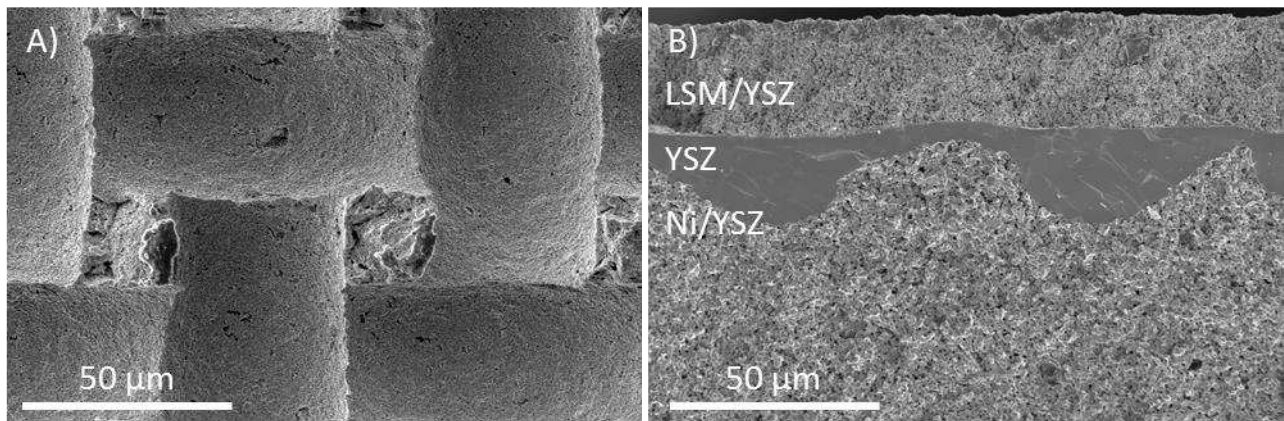
Figure V - 3 (reproduced from chapter III) Architectured sintered open surface: Anode open surface with a porous microstructure; B) Architectured anode-electrolyte interface

We can observe that the anode remains porous whereas the electrolyte is dense. The microstructural preservation can be observed in the application of the architecturation method on the electrolyte in order to expand the cathode/electrolyte interface as shown in figure V – 4.
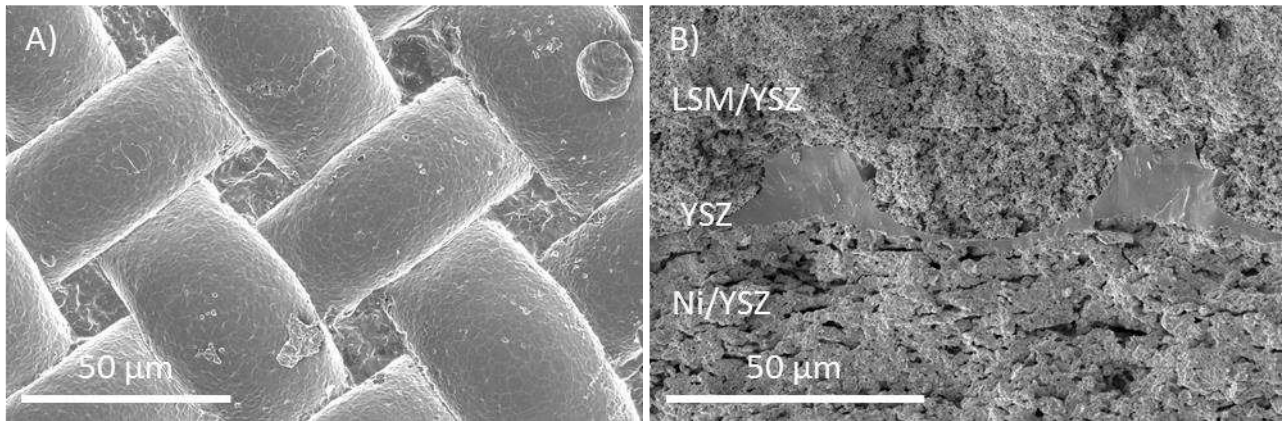
Figure V - 4 (reproduced from chapter III) Architectured sinter electrolyte: A) Electrolyte open surface with a dense microstructure; B) Architectured cathode-electrolyte interface

Detailed architecture characterization is established by optical profilometry. Due to the complexity of the patterns obtained with the soft template method, a numerical analysis protocol had to be developed and validated in this chapter. The numerical script developed with Matlab offers several useful options providing detailed information on the architecture parameters and visual representation (figure V – 5).

- AEC calculation: by using an elementary integration technique, the area expansion coefficient, which is the ratio between the effective architectured surface area and the equivalent planar surface area, can be calculated. The calculation technique is verified using objects presenting simple architectures such a rail or cubic geometry. The AEC calculated analytically is compared to the ones calculate numerically and the results are within an acceptable error (< 5%).

- Mean values and standard deviation. Different types of mean values of the z coordinates can be calculated as well as the standard deviation in respect to the mean values. Thus, we are able of calculating a mean value for the electrolyte thickness which is 13.49 µm

- Extrema analysis. The challenging extrema analysis is carried out by using the standard deviation from the mean low and the mean high values.
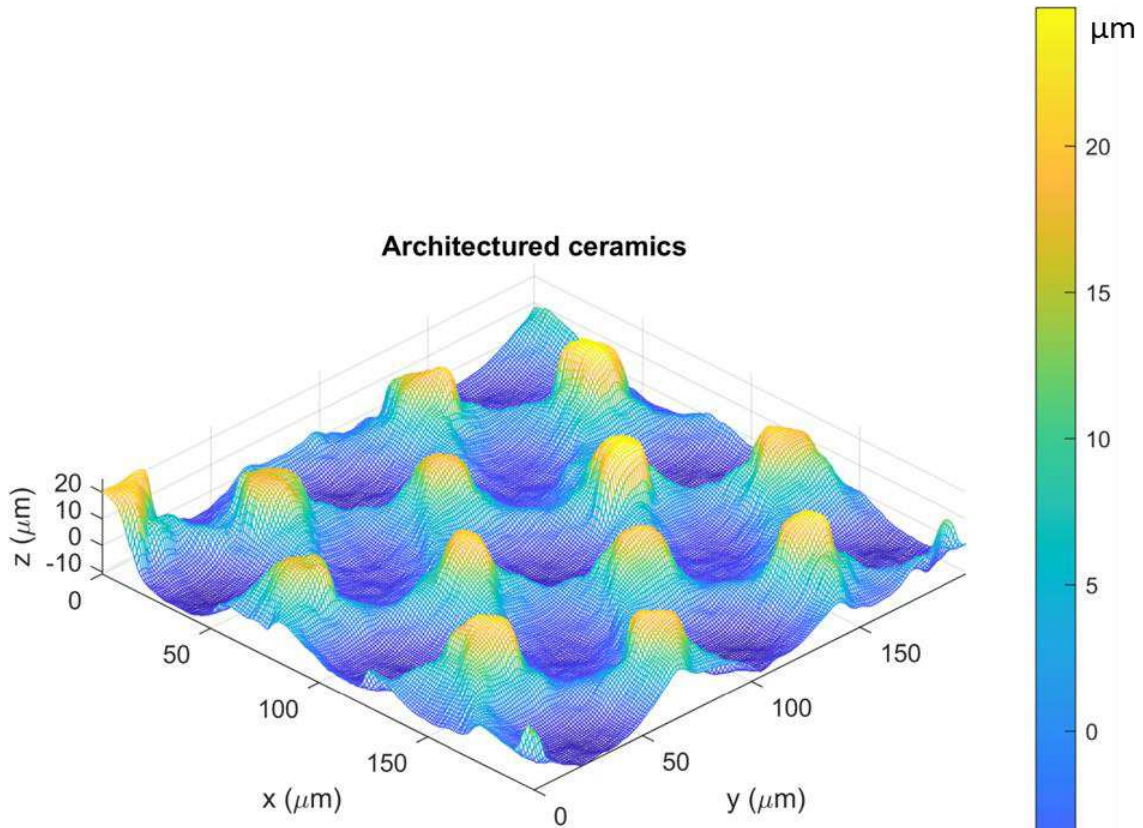
AEC = 1.28
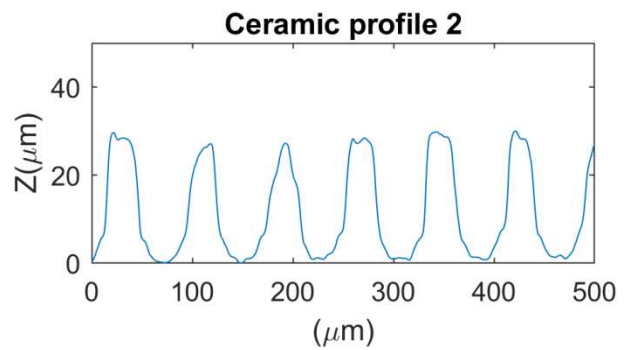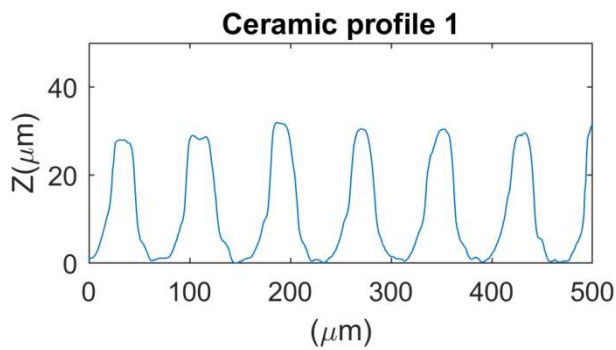
Figure V - 5 (reproduced from chapter III) High scale (200 µm) 3D representation of sintered ceramic architecture A) 3D mesh representation of 200x200mm surface; B and C) Perpendicular profiles passing through "valleys" and 'mountains"

Interesting architecturation results have been obtained by using laser engraving on green ceramic tapes, which have been sintered afterward. In figure V – 6, we show an example of an engraving of an anode tape. This method of architecturation represents an interesting alternative for the architecturing due to the possibility to create diverse patterns with controlled depth as well as the possible combination of the architecturation and cutting procedures. However, in this work, we did not fabricate functional cells using this method. Besides, it leads to the loss of some material, which does not constitute a very sustainable approach.
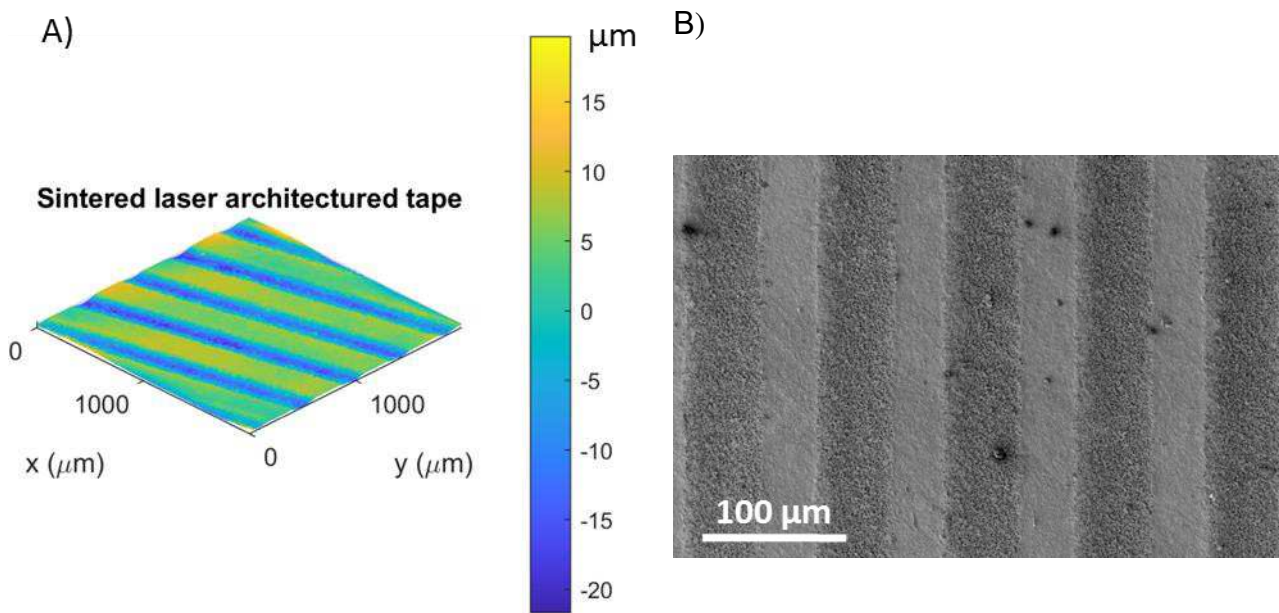
AEC = 1.02

Figure V - 6 Architecturation of an anode tape by laser engraving. A) Profilometry representation B) SEM of the architectured free surface

The next subchapter is focused on structural and chemical characterization we studied and reported several pertinent characteristics, necessary for the cell comparison helpful for the understanding of their behavior. On the one hand, we characterized the cell components by scanning their microstructure, chemical distribution, and layer thickness. On the other hand, we characterized the cell components by scanning their microstructure, chemical distribution, and layer thickness for Type I and Type II cells.

II.C.   Type I cells

Type I cells are formed by an anode support composed of an Ni:8YSZ cermet with a 44:56 volume ratio and with elevated porosity (> 35%), and the anode functional layer has intermediate porosity of approximately 20 – 25 %. The electrolyte is composed of dense 8YSZ film. The cathode functional layer is composed of LSM:8YSZ composite with a 50:50 volume ratio and intermediate porosity (~20 – 25 %), whereas the cathode gas channel layer has a higher porosity of approximately 35 – 40 %. These cells allow visualizing the impact of the architecture on cells with graduated electrodes and with adequate intrinsic performances.
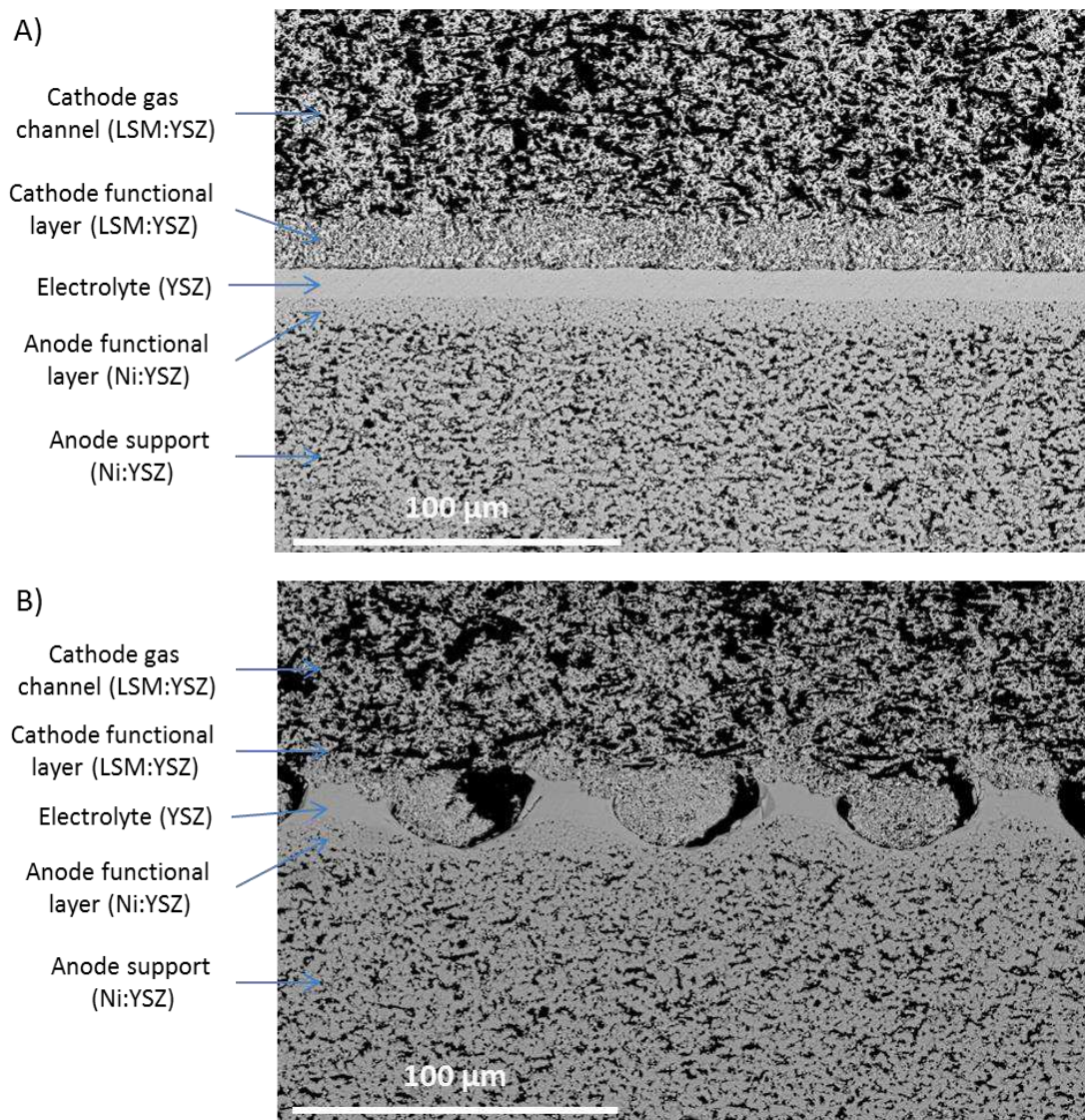
Figure V - 7 Type I cross-section observation; A) Planar cell; B) Architectured cell (cathode/electrolyte interface)

For Type I cells, we saw that the electrolyte in both architectured and planar configuration presents a very favorable microstructure for the ionic conduction. The important grain size with respect to the layer thickness and consequently, the low grain boundary concentration has been demonstrated to lower the layer resistivity. Furthermore, the electrolytes are fairly thin (under 15 µm) which results in a low series resistance (< 0.30 Ω) during the cell operation. The apparent electrolyte density and the lack of transversal cracks ensure the gas and electron insulation of the two sides of the cell. The OCV value will eventually confirm this point during the electrochemical measurements. The architecture seems to strengthen the mechanical stability of the cells since a lateral fracture can be observed through the electrolyte of the planar cell but is less present in the architectured one. The thickness measurement of the electrolyte layer coupled with the architecture geometry study allows confirming the quasi equivalency between the architectured and planar cells.

The anode composition, in this case, has been optimized to promote the electronic phase percolation in the thick anode support layer. In both AS and AFL, the materials are homogeneously dispersed, and the cohesion with the electrolyte is well established. However, a degradation of the porosity is observed, which needs to be investigated and rectified as an optimized porosity is essential for the electrochemical reactions.

In this case study, the cathode presents two different layers: the cathode gas channel and the cathode functional layer. The architecturation is deployed at the cathode/electrolyte interface, and it is essential to have an adequate dispersion of the materials in order to study the impact of the interface geometry variation uniquely. The interface is entirely situated between the CFL and the electrolyte, which is one of the criteria for the equivalency of the cells. A satisfactory wetting between the cathode and the electrolyte is observed. However, on one side of some patterns, we do observe holes. The position of these holes and their irregular distribution suggest that they may be artefacts caused by the polishing procedure.

In conclusion, the Type I cells present adequate components characteristics. The equivalency criteria, which are the same material environment at the interface for the architectured and planar cells as well as the consideration of the harmonic mean value of the electrolyte thickness are

satisfied. Thus, the cells should present a similar electrochemical behavior and are validated for electrochemical performance comparison.

II.D.   Type II cells

Type II cells have the same anode and electrolyte composition and microstructure as type I cells. Additionally, a dense barrier layer is cast over the electrolyte composed of CGO10. The cathode material, in this case, is an LSCF:CGO composite and the porosity is approximately 20-25 %. Type II cells are fabricated to demonstrate the feasibility and pertinence of the architecturing on commercial cells.
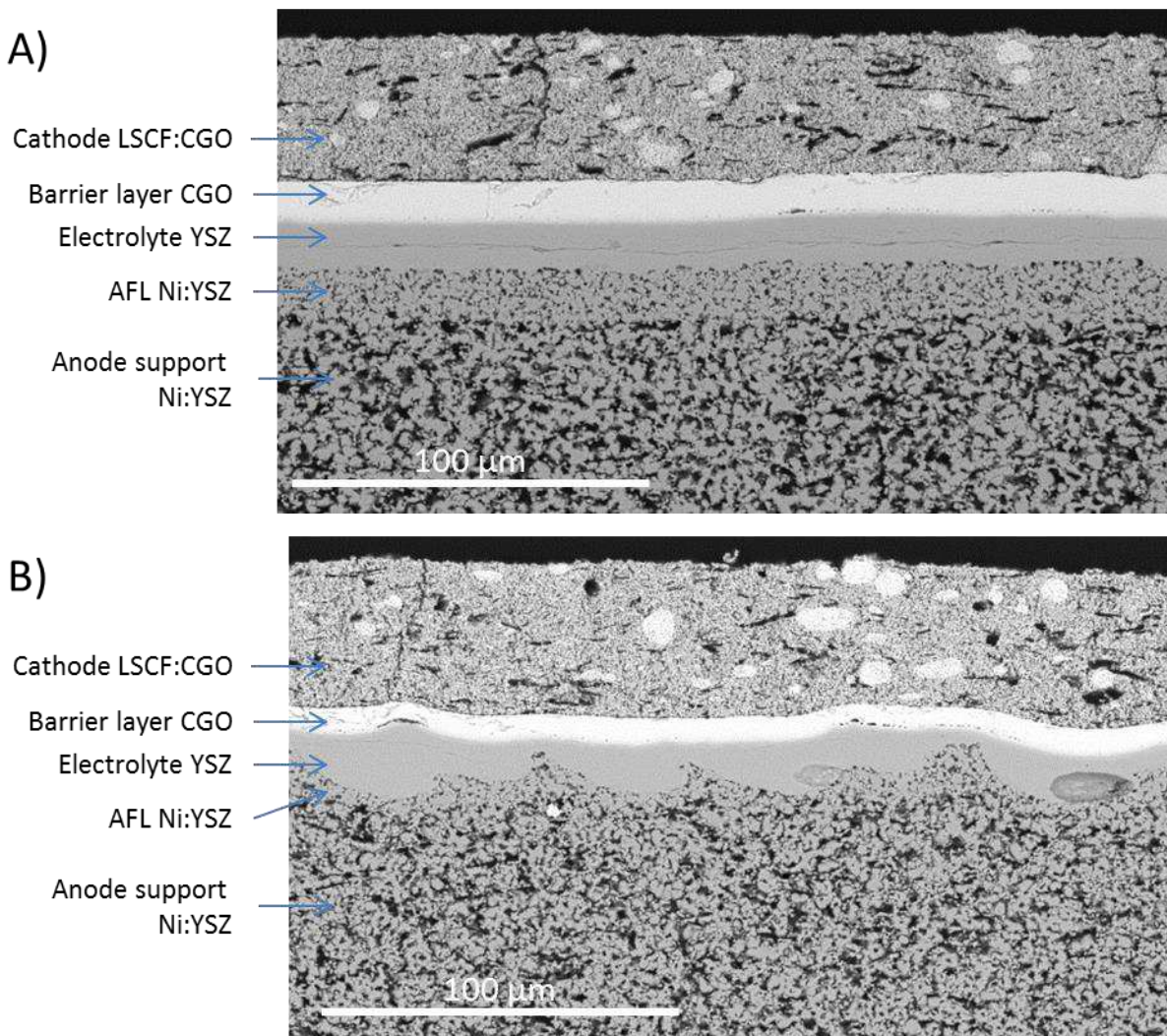
Figure V - 8 Type II cross-section observation: A) Planar cell; B) Architectured cell

The electrolyte and the barrier layers present satisfactory microstructure in terms of grain size, density, and integrity. Although the grain size of the barrier layer is lower than the one of the electrolyte layer, the elevated conductivity of CGO is expected to compensate for this drawback. The barrier layer presents some cracks perpendicular to the interface. They are expected not to impact the electrochemical performance of the cell significantly because they do not traverse the electrolyte layer. However, these defects may cause complications in prolonged operation, and a durability test is necessary for these cells. The combined electrolyte and barrier layer thickness is slightly elevated (approximately 22 µm), which will impact the cell series resistance. The difference between the harmonic mean electrolyte thicknesses of the architectured and planar is considered during the polarization and EIS analyses.

The anode support and the anode functional layer in these cells do not present a material concentration gradient. Indeed, chronologically these cells were fabricated before the Type I cells and the consideration of the material optimization throughout the electrode was not yet taken into account. On the plus side, the porosity corresponds to the expected by the fabrication protocol and is optimized.

Again, due to the chronological position of the type II cell fabrication, the cathode presents inadequate materials dispersion. We observe CGO particle segregation which may hinder the equivalency between architectured and planar cells in the case of cathode/electrolyte interface modification. Thus, this interface modification was not studied here. A new cell fabrication with optimization of the anode and the cathode should be carried out in future works.

In conclusion, the Type I cells present adequate components characteristics. The equivalency criteria which are the same material environment at the interface for the architectured and planar cells as well as the similar mean electrolyte thickness are satisfied. Thus, the cells should present a similar electrochemical behavior and are validated for electrochemical performance comparison.

II.E.   Conclusion

The characterization procedure of the architecture and the fuel cells presents several interesting points.

- The soft template architecturation method allows deploying a regularly patterned architecture at both anode/electrolyte and cathode/electrolyte interfaces. It preserves the microstructure of the concerned layers and persists during the sintering process. The area expansion coefficient obtained with this method is 1.28, which means that the architectured surface area is 28 % larger than the planar one.

- The two types of fuel cells produced by the fabrication protocol present satisfactory characteristics such as porosity, electrolyte electronic insulation and gas tightness, layer thickness, and layer cohesion. Furthermore, an equivalency between the planar and the architectured cells is established based on two criteria: the same material environment at the interface and similar mean electrolyte thickness or superior one for the architectured cells.

III. Electrochemical analysis

III.A. Method

In the first subchapter, we describe the analysis procedure. We use two complementary methods which are polarization curves study and electrochemical impedance spectroscopy. Due to the complexity and the multitude of phenomena occurring in a complete cell, it is necessary to perform a multitude of measurements in different gas and electrochemical conditions. This allows us to deduce the different contributions of the overall polarization or impedance spectra.

Important knowledge and references necessary for the interpretation of the EIS results are provided. However, a parametric study by EIS can be challenging and requires thorough experience and considerable time and effort to master it.

Relative gap method

To bypass this requirement and still obtain the needed information, we have developed a simplified interpretation method inspired by already existing techniques such as differential impedance analysis (DIA). We call this technique the "relative gap method", and it consists of studying the relative gap between the frequency dependent real parts of the impedance spectra of the pair of cells as shown in equation (IV - 2) that we recall here:

$$R.G.(f_i) = \frac{Z'(f_i)_{planar} - Z'(f_i)_{architetured}}{Z'(f_i)_{planar}}$$

III.B. Type I cells

The Type I cells present an architecture at the cathode side and offer an insight into its influence on the oxygen electrode. As mentioned, we have chosen to present only this sample of this batch of Type I cells, due to the low porosity of the anode. We consider that pronounced architecturing on the anode/electrolyte interface would present inaccurate results as the architectures would traverse the AFL and integrate the anode support. Thus, the drastic change in porosity and materials ratio would strongly influence the performance and the sole impact of the architecture would be difficult to estimate. However, practically speaking, a configuration with the electrolyte material passing through the AFL and ending in the anode support would be extremely interesting to increase the cell performances and should be considered in future works. Nonetheless, a slight curvature is observed on the anode/electrolyte side.

Figure V - 9 Type I Polarization and density curves in reference gas conditions

Figure V - 10 A) Superimposition of the Nyquist plots of Type I cells in reference gas conditions

B) Superimposition of the relative gap plots of Type I cells in reference gas conditions

III.C. Type II

Type II fuel cells are fabricated to demonstrate the feasibility of the architecturing method for the production of industrial cells. They are composed of anode support and functional layer, an electrolyte covert by a CGO barrier layer to separated it from an LSCF:CGO composite cathode. In this study and concerning this type of cells, we concentrate on the architecturing of the anode electrolyte interface.

The type II cells present an architecture at the anode/electrolyte interface and offer insight on its influence on fuel oxidation.
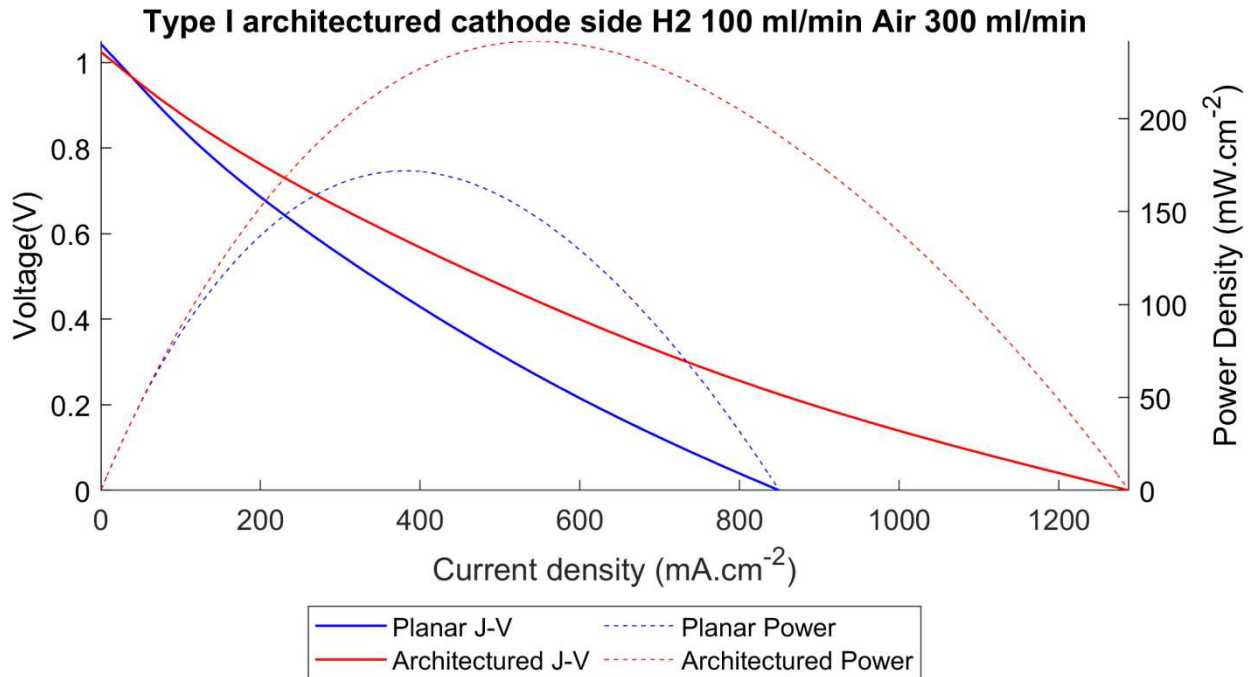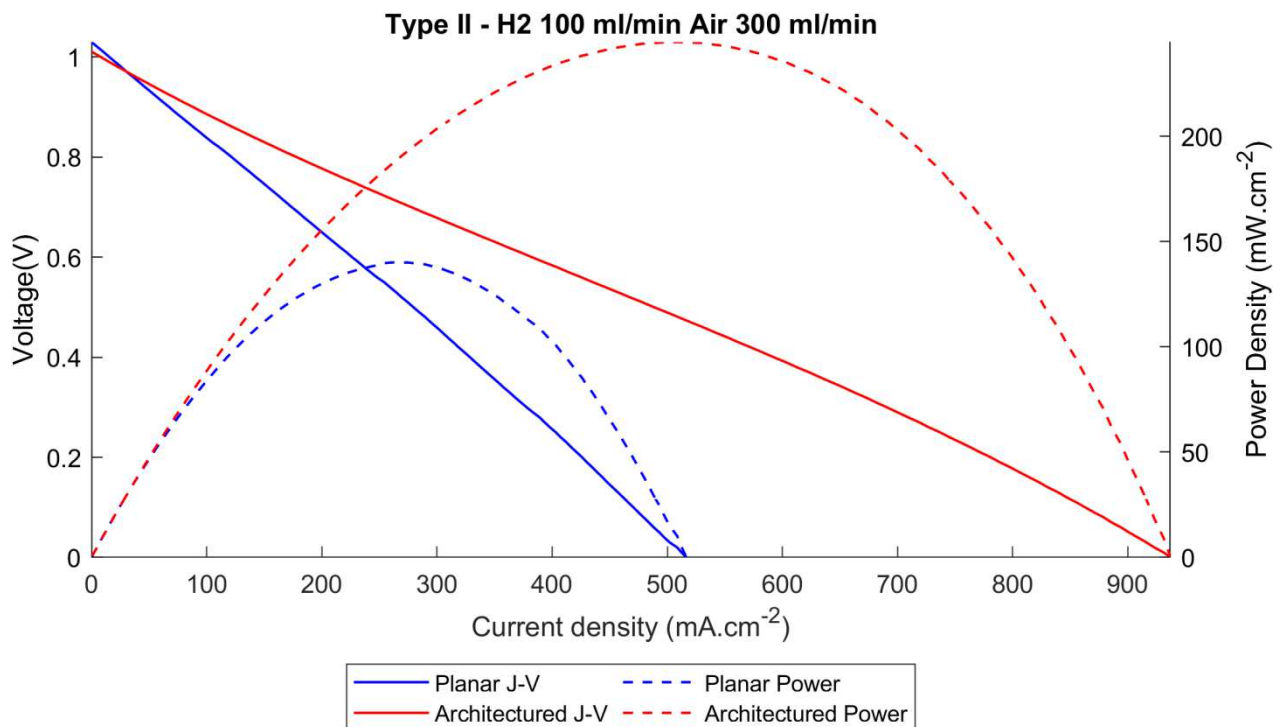

Figure V - 11 Type II Polarization and density curves in Reference gas conditions
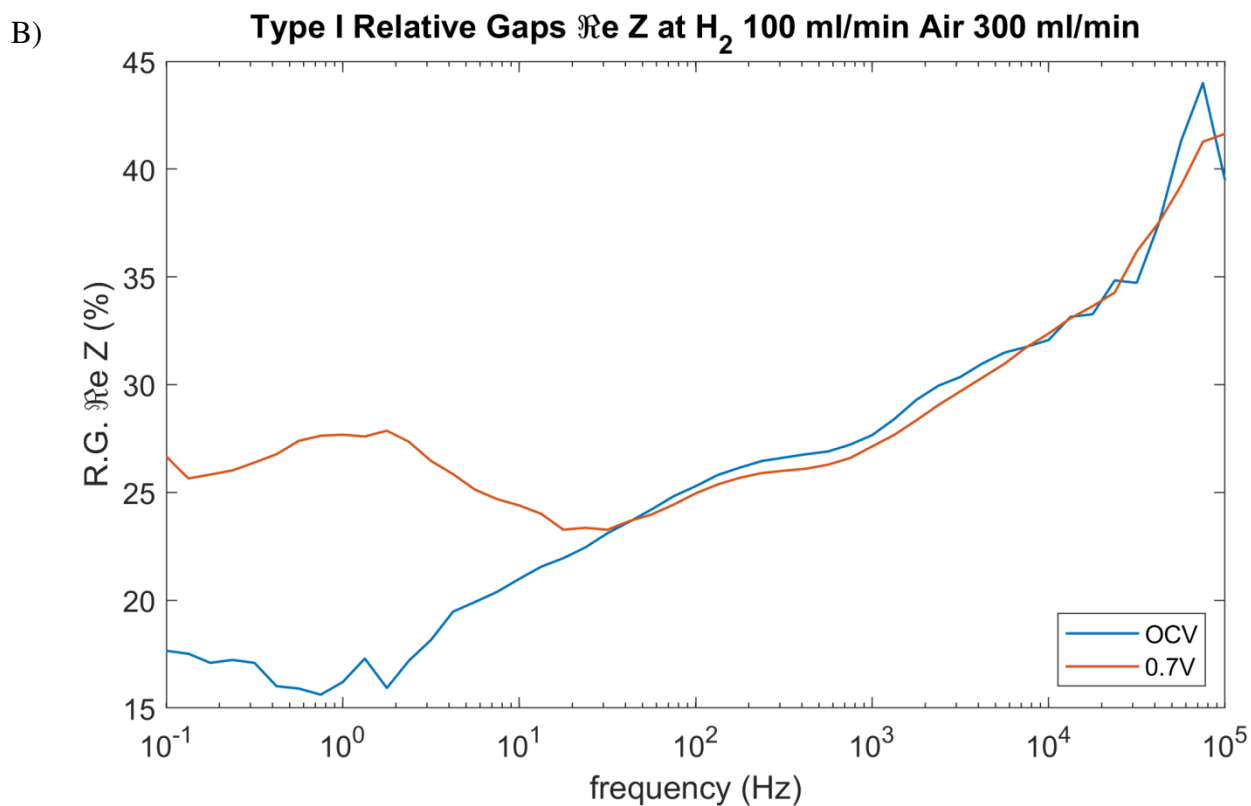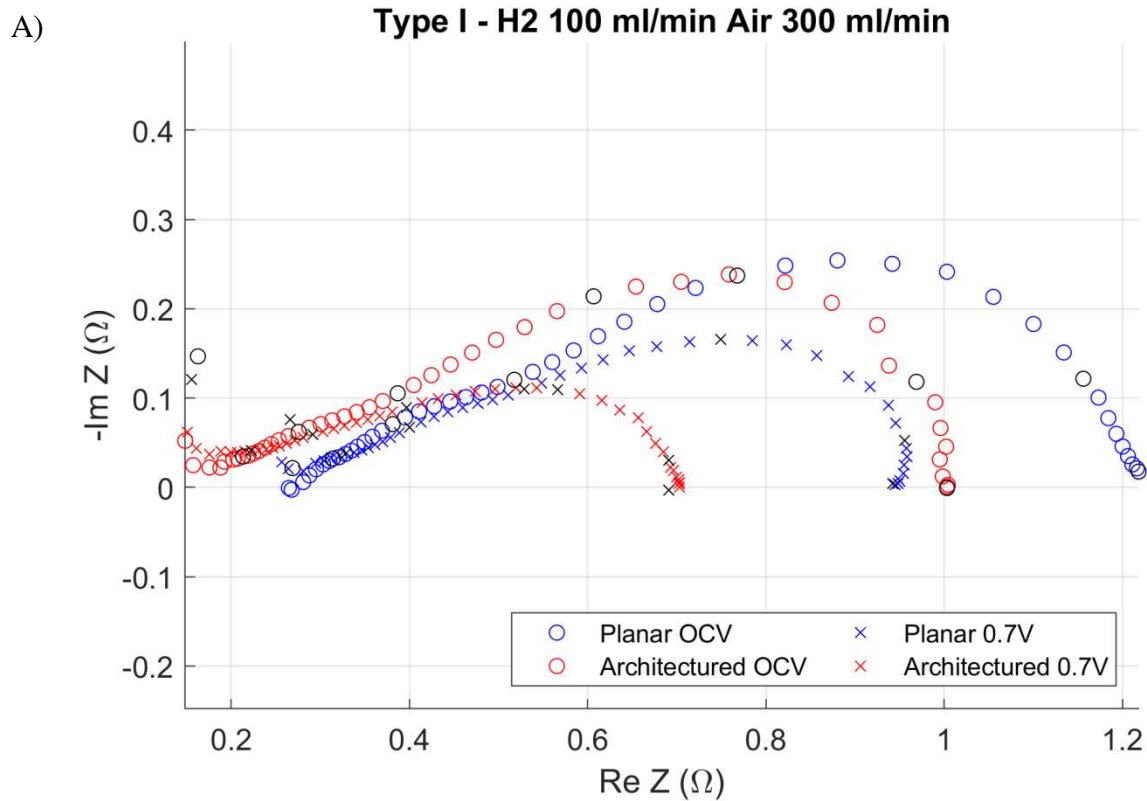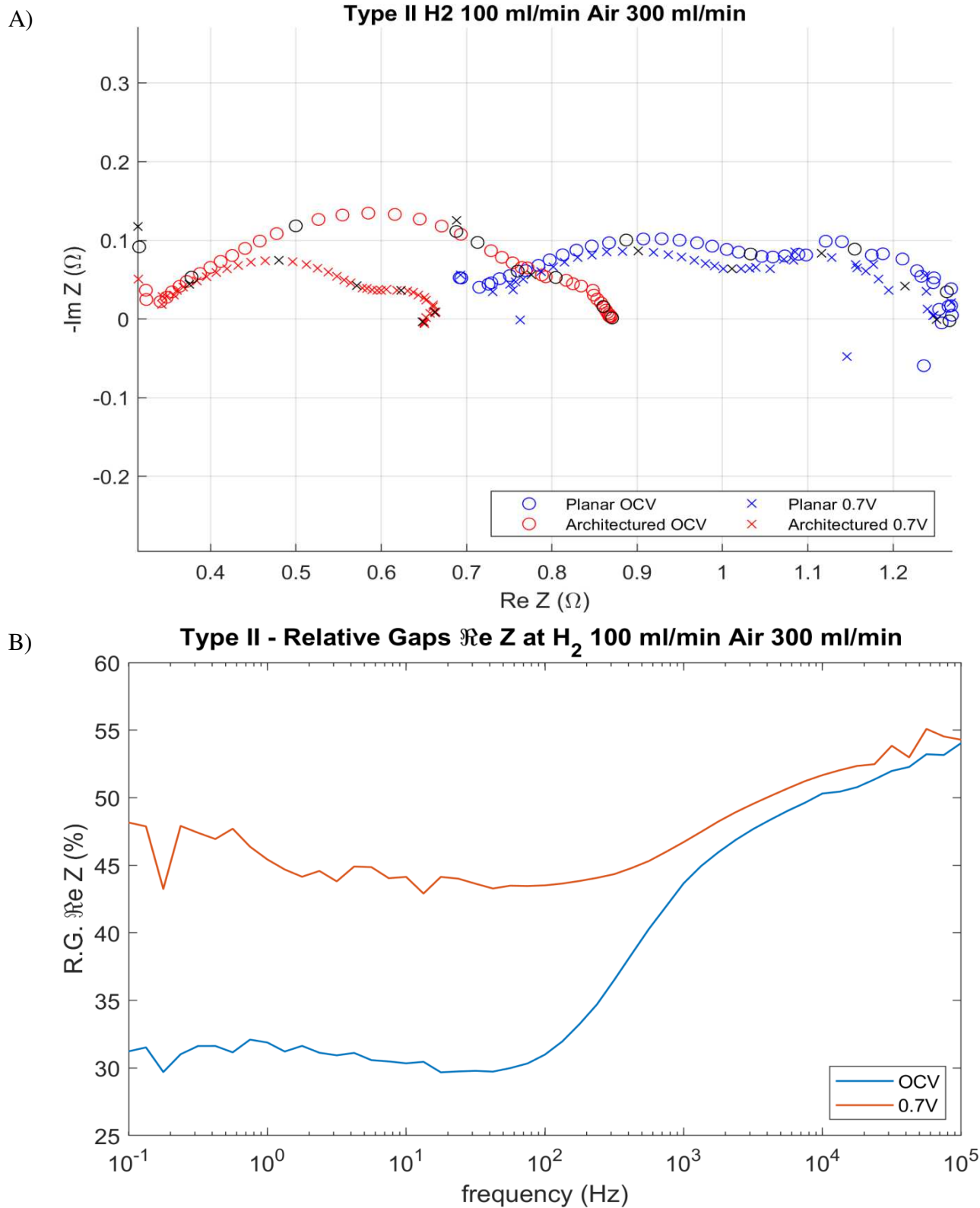
Figure V - 12 A) Superimposition of the Nyquist plots of Type I cells in Reference gas conditions

B) Superimposition of the relative gap plots of Type I cells in Reference gas conditions

IV.   General conclusion

In this work, we have established an industrial fabrication protocol for a single fuel cell with architectured and planar electrode/electrolyte interfaces. In this protocol, the well-known tape casting technique has been slightly modified in order to deploy a regular architecture allowing to obtaining 28 % of surface area expansion compared to the planar surface. The method is tested on porous and dense layers with excellent results. Subsequently, we have demonstrated that in two pairs of samples, different in materials, microstructure, number of layers, and architecture location, the architecturation of the electrode/electrolyte interface results in a significant performance augmentation. The cells presented in this document have a 60 % increase in the maximum power generation for the Type I cells and 75 % for the Type II.

By developing an analysis methodology and tools allowing a rapid and visual interpretation of the analysis data we have provided insight on the effect of the architecture opening the road for more detailed and fine study.

Thus, the architecturation has a significant impact on the cell performance by provoking an important increase in the current and power density. We have demonstrated that this increase has several contributions which we have isolated by using the analysis protocol.

- The variation of the electrolyte thickness is responsible for an important lowering of the overall cell resistance of the architectured cell. This contribution has been calculated by using the harmonic mean thickness of the electrolyte and has been measured using the relative gap method.
- A sequence of measurements using different gas concentrations and operation conditions allowed us to isolate the impact of the architecture on the catalytic and conductivity properties of the cells.

Thus we may conclude that the architecturing of SOFC presents a powerful strategy to increase their electrochemical performances.

- The architecture enhances the catalytic capabilities of the electrodes
- The architecture enhances the charge transport properties of the cells

V. Perspectives

V.A. Complementary experiments

In this project, we aimed to fabricate architectured and planar cells with good performances. Thus, we elaborated cells with gradual porosity in the electrodes. However, we realized that the varying position of the interface and its distance from the gas channel layers (anode support, cathode gas channel), may influence the effect of the architecturation on the performances. Although it is exactly this complex effect that is aimed at, because the industrial cells would present these characteristics, testing on simple fuel cells would promote a better understanding of the architecturation effect.

Thus, complementary tests on Type O (Figure V – 13) cells composed of a Ni:YSZ anode support, YSZ electrolyte, and LSM:YSZ cathode will present an interesting addition to the project work.
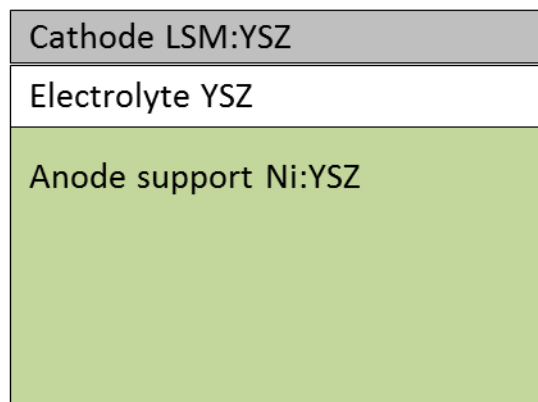
Figure V - 13 Type O planar cell schematic

Unfortunately, due to the Covid19 pandemic, these tests could not be carried out during the current Ph.D. work.

V.B. Durability test

Durability tests are essential for further pursuing the industrialization of the thus fabricated cells. The usual durability tests allow following the decrease of the performances (in %) for intervals of time over 1000h.

We have emitted a hypothesis that the architecturation may present a mechanical stabilization of the cells due to the penetration of the dense electrolyte in the porous electrode. This penetration may act as bridge pillars helping to reduce the risks of delamination or breaking. However, the presence of geometric singularities may provoke the contrary effect and fragile the cell.

The durability testing should be associated with mechanical tests such as tensile or fatigue.

V.C.   Ideal cell/ Rigel application

The fabrication process and the analysis methodology can be adapted for different types of fuel cell designs. As an example, we propose the IdealCell concept developed in previous studies by our team [1], [2]. In this work, a combination of oxygen conducting SOFC and proton-conducting cells is established using a central porous membrane with a mixt ion, proton, and electron conduction.   Thus, architecturation effects can be cumulated by applying the interface modification on both compartment.

This work is currently carried out by Dr. Lemoine during the project HYTREND.

V.D.   Modeling

One of the secondary objectives of this project is the development of a numerical model allowing to simulate the operation of architectured fuel cells. Based on previous work established by Delloro *et al.* [3], and Chesnaud *et al.* [4], we were able to obtain interesting but insufficient results on the gas, current, and ionic potential distribution and they are not presented in this document.

[1]   A. S. Thorel *et al.*, 'Proof of Concept for the Dual Membrane Cell I. Fabrication and Electrochemical Testing of First Prototypes', *J. Electrochem. Soc.*, vol. 160, no. 4, pp. F360–F366, Jan. 2013, doi: 10.1149/2.051304jes.

[2]   A. Thorel, 'Cellule de pile à combustible haute température à conduction mixte anionique et protonique', Mar. 17, 2005.

[3]   F. Delloro and M. Viviani, 'Simulation study about the geometry of electrode-electrolyte contact in a SOFC', *Journal of Electroceramics*, vol. 29, no. 3, pp. 216–224, Nov. 2012, doi: 10.1007/s10832-012-9766-8.

[4]   A. Chesnaud *et al.*, 'Corrugated Electrode/Electrolyte Interfaces in SOFC: Theoretical and Experimental Development', *ECS Trans.*, vol. 78, no. 1, pp. 1851–1863, May 2017, doi: 10.1149/07801.1851ecst.

[5]   D. Arnošt and P. Schneider, 'Dynamic transport of multicomponent mixtures of gases in porous solids', *The Chemical Engineering Journal and the Biochemical Engineering Journal*, vol. 57, no. 2, pp. 91–99, Apr. 1995, doi: 10.1016/0923-0467(94)02900-8.

ANNEX

I.   Fuel Cell types

Based on the functioning temperature, elements material composition and charge carrier, fuel cells can be separated into several types briefly described in table 1 (inspired by [1]). Depending on the application limitations some fuel cells would be preferred to others. For example for transportation (automobiles, trucks, tractors, etc), low-temperature fuel cells would be the optimal choice based on their lighter built and low heat generation. As for stationary application (industry, housing) intermediate to high-temperature fuel cells represent a more viable alternative thanks to high efficiency and power density (average from $100mW/cm^2$ to $2W/cm^2$).

Table Annex - 1 Fuel cell types				
Fuel cell	Working temperature	Charge carrier	Typical fuel	Electrolyte material
Direct methanol fuel cell (DMFC)	50-120	H^+	Liquid methanol/water	Naflon®
Proton exchange membrane fuel cell (PEMFC)	70 - 200	H^+	Hydrogen	Polymer membrane Naflon®
Alkaline fuel cell (AFC)	<80	OH^-	Hydrogen	Alkaline solution (KOH_{aq}) Anion exchange membrane
Phosphoric acid fuel cell (PAFC)	150-200	H^+	Hydrogen	Concentrated phosphoric acid (H_3PO_4)
Molten carbonate fuel cell (MCFC)	600-650	CO_3^{2-}	Hydrogen Methane	Molten alkaline carbonate

Proton conducting fuel cell (PCFC)	400-650	H^+	Hydrogen Methane	H^+ conducting ceramic (BYZ)
Solid oxide fuel cell (SOFC)	600-1000	O^{2-}	Hydrogen Methane	O^{2-} conducting ceramics (YSZ, CGO)

II.   SOFC configurations

Different configurations of SOFC can be found varying the geometry of the cell (flat, tubular) or the mechanical supporting element (anode, electrolyte, cathode, metal). A brief description of some of the configurations can be found in Table Annex 2.

Table Annex - 2 SOFC geometries	
Configuration	Representation
Flat, Metal supported	
Flat, Anode supported	
Flat, Electrolyte supported	
Flat Cathode supported	
Tubular	

Every cell configuration is completed with a current collector and gas diffusion layer at the electrodes called interconnect Figure Annex 1.

A)	B)
Figure Annex - 1 Example of cell stacking [2] A) Flat cell stack B) Tubular design	
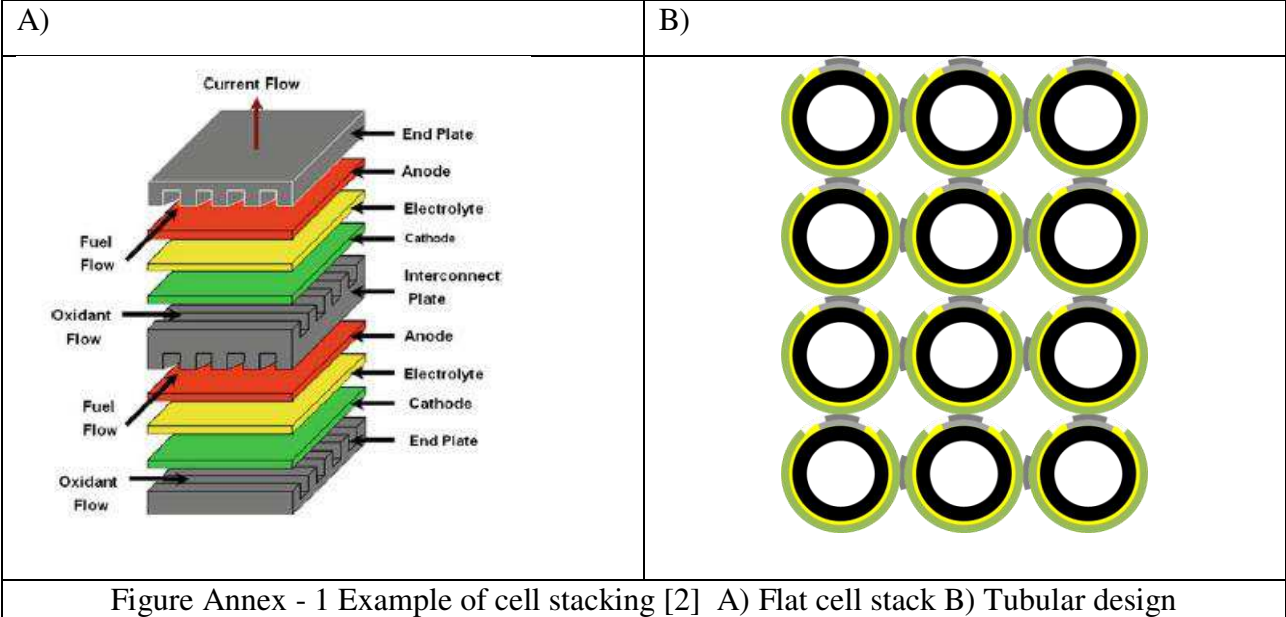
III. Slurries composition

III.A. Anode

Table Annex - 3 Anode support composition					
	Density	%wt	%vol in slurry	%vol in green tape	% vol in solid
YSZ	5,9	15,0	3,6	11,6	26,3
NiO	6,7	24,7	5,2	16,9	38,4
PEG	1,1	2,6	3,3	10,7	0,0
PVB	1,1	8,8	11,2	36,6	0,0
Terpineol	0,9	1,8	2,6	8,6	0,0
Carbon black	2,2	7,5	4,8	15,6	35,3 (porosity)
Solvant	0,8	39,6	69,4	0,0	0,0

Table Annex - 4 Anode functional layer composition					
	density	%wt	%vol in slurry	% vol in solid	%vol in green tape
YSZ	5,9	16,2	3,732	40,7	13,7
NiO	6,7	26,7	5,437	59,3	20,0
PEG	1,1	2,9	3,438	0	12,7
PVB	1,1	9,5	11,773	0	43,4
Terpineol	0,9	1,9	2,773	0	10,2
Solvant	0,8	42,8	72,847	0	0,000

III.B. Electrolyte and barrier

Table Annex - 5 Electrolyte composition					
	density	%wt	%vol in slurry	% vol in solid	%vol in green tape
YSZ	5,9	42,7	9,7	100	37,2
PEG	1,1	2,6	3,1	0	12,0
PVB	1,1	8,8	10,7	0	41,1
Terpineol	0,9	1,8	2,5	0	9,7
Solvant	0,8	44,1	73,9	0	0,000

Table Annex - 6 Barrier composition					
	density	%wt	%vol in slurry	% vol in solid	%vol in green tape
PEG	1,1	2,6	3,2	0	12,9
PVB	1,1	8,8	10,9	0	44,1
Terpineol	0,9	1,8	2,6	0	10,4
Solvant	0,8	44,1	75,2	0	0,000
CGO	7,2	42,7	8,1	100	32,7

III.C. Cathodes

Table Annex - 7 Cathode gas channel layer (Type I cells) composition					
	density	%wt	%vol in slurry	% vol in solid	%vol in green tape
YSZ	5,9	7,7	1,8	15,6	6,1
PEG	1,1	3,1	3,8	0,0	12,7
PVB	1,1	8,8	11,1	0,0	37,3
Terpineol	0,9	2,2	3,3	0,0	11,0
Carbon black	2,2	4,4	2,8	23,9	9,3 (porosity)
Solvant	0,8	40,7	70,3	0,0	0,0
LSM	6,5	33,0	7,0	60,6	23,7

Table Annex - 8 Cathode functional layer (Type I cells) composition					
	density	%wt	%vol in slurry	% vol in solid	%vol in green tape
YSZ	5,9	20,0	4,5	50,3	16,6
PEG	1,1	3,0	3,6	0,0	13,2
PVB	1,1	9,6	11,6	0,0	42,5
Terpineol	0,9	2,2	3,1	0,0	11,4
Solvant	0,8	43,5	72,7	0,0	0,0
LSM	6,5	21,7	4,5	49,7	16,4
TOTAL	32,4	100,0	100,0	100,0	100,0

Table Annex - 9 Cathode functional layer (Type II cells) composition					
	density	%wt	%vol in slurry	% vol in solid	%vol in green tape
PEG	1,1	2,6	3,2	0,0	12,4
PVB	1,1	8,7	10,8	0,0	42,5
Terpineol	0,9	1,7	2,6	0,0	10,0
Solvant	0,8	43,5	74,5	0,0	0,0
LSCF	6,2	21,7	4,8	53,7	18,8
CGO	7,2	21,7	4,1	46,3	16,2

[1]   O. Z. Sharaf and M. F. Orhan, 'An overview of fuel cell technology: Fundamentals and applications', *Renewable and Sustainable Energy Reviews*, vol. 32, pp. 810–853, Apr. 2014, doi: 10.1016/j.rser.2014.01.012.

[2]   S. C. Singhal, 'Solid Oxide Fuel Cells: Past, Present and Future', in *Solid Oxide Fuels Cells: Facts and Figures: Past Present and Future Perspectives for SOFC Technologies*, J. T. S. Irvine and P. Connor, Eds. London: Springer London, 2013, pp. 1–23.

RÉSUMÉ

Dans ce travail, nous avons établi un protocole de fabrication industrielle pour réaliser des cellules de piles à combustible avec interfaces électrode/électrolyte architecturées, ou planes. Nous avons démontré que pour deux types d'échantillons, différents par les matériaux, la microstructure, le nombre de couches et l'emplacement de l'architecture, l'architecture de l'interface électrode/électrolyte entraîne une augmentation très significative des performances. Les mesures de polarisation et l'EIS sont utilisées pour étudier les performances électrochimiques des cellules, ainsi que pour comparer les cellules architecturées et les cellules planes. Nous isolons l'influence de l'architecture sur les spectres d'impédance globaux en utilisant une méthode de comparaison innovante basée sur l'étude des écarts relatifs des parties de résistance dépendantes de la fréquence. Ainsi, l'architecture a une influence favorable sur les performances électrochimiques en améliorant les capacités catalytiques des électrodes ainsi que le transfert de charges (et en particulier le transfert d'ions) dans la cellule. L'architecture induit une augmentation de 60 % de la densité de puissance maximale pour les cellules de Type I et de 75 % pour les cellules de Type II.

MOTS CLÉS

Piles à combustible à oxyde solide (SOFC), Hydrogène, stockage d'énergie, ingénierie des interfaces, matériaux céramiques

ABSTRACT

In this work, we have established an industrial fabrication protocol for single fuel cells with either architectured or planar electrode/electrolyte interfaces. We have demonstrated that in two types of samples, differing in materials, microstructure, number of layers, and architecture location, the architecturation of the electrode/electrolyte interface results in a highly significant performance increase. Polarization measurements and EIS are used to study the electrochemical performances of the cells, to compare the architectured and planar ones. We isolate the influence of the architecturation on global impedance spectra by using an innovative comparison method based on the study of the relative gaps of the frequency-dependent resistance parts. Thus, the architecturation has a strongly favorable influence on the electrochemical performances by enhancing the catalytic capabilities of the electrodes as well as the charge transfer (and in particular the ion transfer) within the cell. The architecturation induces a 60 % increase of the maximum power density for the Type I cells and 75% for the Type II cells.

KEYWORDS

Solide Oxide Fuel Cells (SOFC), Hydrogen, energy storage, Interface engineering, ceramic materials